

A STUDY OF REACTIVE FLOW OF POLYPROPYLENE
IN SINGLE- AND TWIN-SCREW EXTRUDERS

by

David Bryan Strutt

A thesis
presented to the University of Waterloo
in fulfilment of the
thesis requirement for the degree of
Doctor of Philosophy
in
Chemical Engineering

Waterloo, Ontario, Canada, 1998

© David Strutt 1998



National Library
of Canada

Acquisitions and
Bibliographic Services

395 Wellington Street
Ottawa ON K1A 0N4
Canada

Bibliothèque nationale
du Canada

Acquisitions et
services bibliographiques

395, rue Wellington
Ottawa ON K1A 0N4
Canada

Your file Votre référence

Our file Notre référence

The author has granted a non-exclusive licence allowing the National Library of Canada to reproduce, loan, distribute or sell copies of this thesis in microform, paper or electronic formats.

The author retains ownership of the copyright in this thesis. Neither the thesis nor substantial extracts from it may be printed or otherwise reproduced without the author's permission.

L'auteur a accordé une licence non exclusive permettant à la Bibliothèque nationale du Canada de reproduire, prêter, distribuer ou vendre des copies de cette thèse sous la forme de microfiche/film, de reproduction sur papier ou sur format électronique.

L'auteur conserve la propriété du droit d'auteur qui protège cette thèse. Ni la thèse ni des extraits substantiels de celle-ci ne doivent être imprimés ou autrement reproduits sans son autorisation.

0-612-32860-0

BORROWERS' PAGE

The University of Waterloo requires the signatures of all persons using or photocopying this thesis. Please sign below, and give address and date.

**A STUDY OF REACTIVE FLOW OF POLYPROPYLENE
IN SINGLE- AND TWIN-SCREW EXTRUDERS**

ABSTRACT

This work brings together extruder flow simulations, peroxide-initiated reactive degradation of polypropylene (PP), and mixing efficiency analysis of flows. A steady-state, reactive extrusion process model incorporating the controlled degradation reaction is presented, in both a differential model formulation and a reduced dimension macroscopic formulation for self-wiping co-rotating twin-screw (CSCO) extruder systems. The differential formulation is solved using the finite element method for a single-screw extruder system, and both formulations are solved for CSCO extruder systems. Simulation results for both reactive and non-reactive PP flows are obtained, to study the effects of the reaction and other processing parameters on the model predictions of the extruders' behaviour, as well as on the mixing ability of the flows within their channels, as characterized by the area and flow mixing efficiencies. For the single-screw extruder system, it is demonstrated that the mixing abilities of the channel flows are very similar to those of two-dimensional flows, on the basis of average flow efficiencies along the channels. Both pressure-to-drag flow ratio and the channel aspect ratio are found to have a significant influence on these values. For the twin-screw extruder system, it is demonstrated that the mixing abilities of the flows in fully-filled forward conveying screw element channels are again similar to those of two-dimensional flows. The average flow efficiencies in the intermeshing region are less than those in the translation region, due to extensional flows caused by the channel shift. The pressure-to-drag flow ratio is found to have a significant influence on the flow efficiencies in the translation region of the channels, and the magnitude of the channel shift in the intermeshing

region is found to influence the values there. Also for the twin-screw system, the macroscopic composite process model for CSCO extrusion is solved, yielding profiles of average values of the process degrees of freedom along the extruder axis. Predicted PP extrudate molecular weights for reactive extrusion simulation runs at 6 levels of peroxide addition at one screw speed and mass throughput level are found to compare closely with measured molecular weights for the same conditions. A response surface of average residence times against screw speed and mass throughput is found using the results of a residence time distribution experiment on a laboratory scale CSCO extruder. The regression model is found to show significant lack of fit, particularly at high average residence times. By performing simulations for the same conditions as the experiments, it is demonstrated that the macroscopic twin-screw extrusion process model can accurately predict polymer average residence times in a co-rotating twin-screw extruder. Finally, several recommendations for future work are made.

ACKNOWLEDGEMENTS

I would like to thank Dr. Costas Tzoganakis and Dr. Thomas Duever for supervising me in this work, and also for suggesting the topics of investigation. The financial support of the Ontario Centres for Materials Research (now known as Materials and Methods Ontario) and Mr. and Mrs. Walter Strutt are also appreciated.

TABLE OF CONTENTS

ABSTRACT	(iv)
ACKNOWLEDGEMENTS	(vi)
TABLE OF CONTENTS	(vii)
LIST OF TABLES	(x)
LIST OF FIGURES	(xi)
NOMENCLATURE	(xv)
CHAPTER 1: INTRODUCTION AND OBJECTIVES	
1.1 Reactive Extrusion	1
1.2 Process Modeling and Simulation	4
1.3 Objectives	7
1.4 Outline of Dissertation	8
CHAPTER 2: SINGLE- AND TWIN-SCREW EXTRUSION	
2.1 Introduction	10
2.2 Single-Screw Extruders	10
2.3 Twin-Screw Extruders	18
2.3.1 Closely-Intermeshing Self-Wiping Co-Rotating Twin-Screw Extruders	20
CHAPTER 3: MACROSCOPIC MODELING AND STEADY-STATE SIMULATION OF CONVENTIONAL AND REACTIVE EXTRUSION IN CSCO EXTRUDERS	
3.1 Introduction	28
3.2 Literature Review	30
3.2.1 Self-Wiping Screw Profile	30
3.2.2 Macroscopic Modeling of Melt Conveying in Conveying Screw Elements	31
3.2.3 Macroscopic Modeling of Melt Conveying in Kneading Block Elements	38
3.2.4 Modeling of Solids Conveying and Melting	40
3.2.5 Composite Macroscopic Models of Modular CSCO Extruders	43
3.2.6 Modeling of Reactive Extrusion of Polypropylene With Peroxide-Initiated Degradation	45
3.3 CSCO Extrusion Process Model	46
3.3.1 Solids Melting	47
3.3.2 Melt Conveying and Pressurization	49
3.3.3 Material Distribution in Extruder Channels	58

3.3.4 Melt Temperature Change	59
3.3.5 Peroxide-Initiated Controlled Degradation of Polypropylene	62
3.4 Simulation Program	66
3.4.1 Inputs	67
3.4.2 Inner Loop	70
3.4.3 Outer Loop	72
3.5 Simulation Procedure and Results	74
3.5.1 Material Properties	74
3.5.2 Screw and Barrel Geometries	78
3.5.3 Simulations of Conventional Extrusion of Polypropylene	80
3.5.4 Sensitivity Analysis of Predicted Average Residence Times in Conventional Extrusion	90
3.5.5 Simulations of Peroxide-Initiated Controlled Degradation of Polypropylene - Part I	91
3.5.6 Simulations of Peroxide-Initiated Controlled Degradation of Polypropylene - Part II	100
3.6 Discussion	105
3.6.1 Simulation Predictions	105
3.6.2 Simulation Algorithm Problems	106
3.6.3 Process Model Weaknesses	107

CHAPTER 4: RESPONSE SURFACE ANALYSIS OF EXPERIMENTAL AVERAGE RESIDENCE TIMES IN A CSCO EXTRUDER

4.1 Introduction	113
4.2 Literature Review	114
4.3 Response Surface Analysis Theory	117
4.4 Procedures	119
4.4.1 Experimental Procedure	119
4.4.2 Data Analysis	122
4.4.3 Computer Simulation	126
4.5 Results and Discussion	126
4.5.1 Experimental Average Residence Times	126
4.5.2 Variances of Experimental Residence Time Distributions	129
4.5.3 Experimental Response Surface	130
4.5.4 Model Diagnostics	134
4.5.5 Simulation Results and Response Surface	136

CHAPTER 5: FINITE ELEMENT METHOD SIMULATION AND MIXING ANALYSIS OF POLYMER MELT FLOW IN A SINGLE-SCREW EXTRUDER CHANNEL

5.1 Introduction	141
5.2 Literature Review	143
5.2.1 Finite Element Method Simulation of Melt Conveying in Single-Screw Extruders	143

5.2.2 Theoretical Analysis of Laminar Mixing in Melt Conveying in Single-Screw Extruders	144
5.3 Theory	146
5.3.1 Model Equations	146
5.3.2 Mixing Efficiencies	148
5.4 Simulation Procedure	154
5.4.1 Model Parameter Values	154
5.4.2 Finite Element Method Details	160
5.4.3 Calculations and Iterative Procedure	170
5.5 Results and Discussion	172
5.5.1 First Channel Geometry - Degree of Freedom Profiles	172
5.5.2 Second Channel Geometry - Degree of Freedom Profiles	189
5.5.3 Mixing Efficiency Analysis - Flow Efficiencies	196
5.5.4 Mixing Efficiency Analysis - Area Efficiencies	210
5.5.5 Discussion	211
 CHAPTER 6: FINITE ELEMENT METHOD SIMULATION AND MIXING ANALYSIS OF POLYMER MELT FLOW IN A CSCO EXTRUDER CONVEYING SCREW ELEMENT CHANNEL	
6.1 Introduction	215
6.2 Literature Review	216
6.3 Theory	219
6.4 Simulation Procedure	220
6.4.1 Model Parameter Values	220
6.4.2 Finite Element Method Details	222
6.4.3 Calculations and Iterative Procedure	237
6.5 Results and Discussion	238
6.5.1 First Channel Geometry - Degree of Freedom Profiles	238
6.5.2 Second Channel Geometry - Degree of Freedom Profiles	259
6.5.3 Mixing Efficiency Analysis - Flow Efficiencies	260
6.5.4 Discussion	270
 CHAPTER 7: CONCLUSIONS AND RECOMMENDATIONS	
7.1 Conclusions	276
7.2 Recommendations	280
REFERENCES	282

LIST OF TABLES

Table 3.1	Material Data for Simulations	75
Table 3.2	Power-Law Parameter Values of Virgin KF6100 PP	77
Table 3.3	Extruder Geometry Data for Simulations	81
Table 3.4	Element Geometry Data for Two Screw Elements in Conventional Extrusion Screw Configuration	81
Table 3.5	Conventional Extrusion Simulation Operating Conditions and Results of Interest	85
Table 3.6	Sensitivity Analysis Results	92
Table 3.7	Reactive Extrusion Simulation Operating Conditions and Results of Interest	96
Table 3.8	Comparison of Experimental and Simulation Results for Reactive Extrusion Runs	103
Table 4.1	Extruder Average Residence Time Experiment Data	121
Table 4.2	Actual and Computed Tracer Masses	128
Table 4.3	Analysis of Variance Table	135
Table 4.4	Residence Time Distribution Run Simulation Results	137
Table 5.1	Screw and Channel Geometry Data for Simulations	155
Table 5.2	Polypropylene Property Data for Simulations	155
Table 5.3	Operating Conditions for Simulations	159
Table 5.4	Maximum Inlet Peroxide Levels for Non-Uniform Distributions	167
Table 5.5	First Channel Geometry Simulation Results	173
Table 5.6	Particle Pathline Data for First Channel Geometry	187
Table 5.7	Second Channel Geometry Simulation Results	190
Table 5.8	Particle Pathline Data for Second Channel Geometry	195
Table 5.9	Simulation Results for Additional Runs	203
Table 6.1	Screw and Element Geometry Data for Simulations	221
Table 6.2	Operating Conditions for Simulations	221
Table 6.3	Finite Element Mesh Data	229
Table 6.4	Mass Flow Rates Across Barrel Surface Sections in First Half of Intermeshing Region	233
Table 6.5	Simulation Results	239
Table 6.6	Particle Pathline Data for First Channel Geometry	258
Table 6.7	Simulation Results for Additional Runs	267

LIST OF FIGURES

Figure 1.1	Reactive Extrusion System	3
Figure 1.2:	Reactive Extrusion Process Model	6
Figure 2.1	Single-Screw Extruder	11
Figure 2.2	Extruder Screw Geometry	11
Figure 2.3	Cutaway View of Single-Screw Extruder	13
Figure 2.4	Melting of Solid Bed in Plastication Zone	13
Figure 2.5	Single-Screw Extruder Example Temperature Profiles	14
Figure 2.6	Single-Screw Extruder Example Pressure Profiles	14
Figure 2.7	Screw and Die Characteristic Curves	16
Figure 2.8	Down-Channel Velocity Profiles	16
Figure 2.9	Transverse Circulation Streamlines	17
Figure 2.10	Polymer Particle Streamline in Screw Channel	17
Figure 2.11	Twin-Screw Extruder Screws	19
Figure 2.12	Self-Wiping Profile Cross-Sections	21
Figure 2.13	Fluid Shift in Intermeshing Region of Conveying Screw Element	23
Figure 2.14	Partially-Filled Screw Channel	23
Figure 2.15	Kneading Block Element	25
Figure 2.16	Material Motion in CSCO Extruder	25
Figure 2.17	Independent Channel Flow in CSCO Extruder	25
Figure 2.18	CSCO Extruder Example Pressure and Filling Level Profiles	27
Figure 2.19	CSCO Extruder Example Temperature Profiles	27
Figure 3.1	Self-Wiping Screw Profile for Bilobal Screws	32
Figure 3.2	Self-Wiping Screw Channel Cross-Section	32
Figure 3.3	Groove Model Geometry	34
Figure 3.4	Solids Melting Model Assumed Particle Packing	51
Figure 3.5	Dimensionless Screw Characteristic Curves for One-Dimensional Flow of Power-Law Fluid	51
Figure 3.6	Leakage Flow Material Balance	54
Figure 3.7	Kneading Block Section Highlighting Radial Gaps	57
Figure 3.8	Polypropylene Chain Scission Reaction Mechanism	64
Figure 3.9	Simulation Algorithm Flow Chart	68
Figure 3.10	Flow Curves of Polypropylene Resins	77
Figure 3.11	Power-Law Indices of Degraded Samples at 210°C	79
Figure 3.12	Power-Law Consistency Indices of Degraded Samples at 210°C	79
Figure 3.13	Screw Configuration for Conventional Extrusion Simulations	82
Figure 3.14	Degree-of Fill Profiles for Conventional Extrusion Simulations	87
Figure 3.15	Cumulative Average Residence Time Profiles for Conventional Extrusion Simulations	87
Figure 3.16	Average Melt Pressure Profiles for Conventional Extrusion Simulations	89

Figure 3.17	Average Melt Temperature Profiles for Conventional Extrusion Simulations	89
Figure 3.18	Screw Configuration for Reactive Extrusion Simulations	93
Figure 3.19	Relative Weight-Average Molecular Weight Profiles for Reactive Extrusion Simulations	98
Figure 3.20	Average Melt Pressure Profiles for Reactive Extrusion Simulations	98
Figure 3.21	Average Melt Temperature Profiles for Reactive Extrusion Simulations	101
Figure 3.22	Experimental and Predicted Extrudate Molecular Weights	104
Figure 4.1	Second-Order Central Composite Design Operating Points	118
Figure 4.2	Benzophenone Infrared Transmittance Spectrum	123
Figure 4.3	Isotactic PP Infrared Transmittance Spectrum	123
Figure 4.4	Benzophenone Absorbance Calibration Curve	125
Figure 4.5	Standard Deviations of Experimental Residence Time Distributions	131
Figure 4.6	Dimensionless Variances of Experimental Residence Time Distributions	131
Figure 4.7	Experimental Extruder Average Residence Time Response Surface	133
Figure 4.8	Experimental Extruder Average Residence Time Contours	133
Figure 4.9	Regression Model Residual Plot	135
Figure 4.10	Comparative Average Residence Time Plot	137
Figure 4.11	Extrusion Process Model Predicted Average Residence Time Response Surface	139
Figure 4.12	Extrusion Process Model Predicted Average Residence Time Contours	139
Figure 5.1	Stretching of an Interfacial Area Element	150
Figure 5.2	Power-Law Consistency Index Regression Formula Plot	157
Figure 5.3	Power-Law Index Regression Formula Plot	157
Figure 5.4	First Channel Geometry Finite Element Mesh	162
Figure 5.5	Second Channel Geometry Finite Element Mesh	163
Figure 5.6	Inlet Velocity Profiles For Different Pressure-to-Drag Flow Ratios	167
Figure 5.7	Barrel Peroxide Addition Patterns	169
Figure 5.8	Random Peroxide Addition Patterns	169
Figure 5.9	Average Temperatures for First Channel Geometry	176
Figure 5.10	Average Pressures for First Channel Geometry	176
Figure 5.11	Average Peroxide Conversions for First Channel Geometry	179
Figure 5.12	Average Peroxide Levels With No Peroxide Decomposition For First Channel Geometry	179
Figure 5.13	Average Relative Molecular Weights for First Channel Geometry	181
Figure 5.14	Velocity Vectors in Cross-Section for First Channel Geometry	183
Figure 5.15	Pressures in Cross-Section for First Channel Geometry	183
Figure 5.16	Normal Velocities in Cross-Section for First Channel Geometry	184
Figure 5.17	Temperatures in Cross-Section for First Channel Geometry	184
Figure 5.18	Peroxide Weight Fractions in Cross-Section for First Channel Geometry	186
Figure 5.19	Relative Weight-Average Molecular Weights in Cross-Section for First Channel Geometry	186

Figure 5.20	Particle Pathlines for First Channel Geometry	187
Figure 5.21	Average Peroxide Levels With No Peroxide Decomposition for Second Channel Geometry	192
Figure 5.22	Velocity Vectors in Cross-Section for Second Channel Geometry	193
Figure 5.23	Normal Velocities in Cross-Section for Second Channel Geometry	193
Figure 5.24	Particle Pathlines for Second Channel Geometry	195
Figure 5.25	Flow Efficiencies in Cross-Sections Perpendicular to the Screw Axes	197
Figure 5.26	Flow Efficiencies in Cross-Sections Perpendicular to the Screw Flights . . .	197
Figure 5.27	Average Flow Efficiencies for First Channel Geometry for Runs at Both Peroxide Levels	199
Figure 5.28	Average Flow Efficiencies for First Channel Geometry for Runs at Both Screw Speeds	199
Figure 5.29	Average Flow Efficiencies for First Channel Geometry for Runs With No Peroxide	201
Figure 5.30	Average Flow Efficiencies for First Channel Geometry for Runs With Uniform Peroxide Distribution	201
Figure 5.31	Average Flow Efficiencies for First Channel Geometry for Runs With Barrel Peroxide Distribution	202
Figure 5.32	Average Flow Efficiencies for First Channel Geometry for Runs With Random Peroxide Distribution	202
Figure 5.33	Average Flow Efficiencies for Second Channel Geometry for Runs at Both Peroxide Levels	205
Figure 5.34	Average Flow Efficiencies for Second Channel Geometry for Runs at Both Screw Speeds	205
Figure 5.35	Average Flow Efficiencies for Second Channel Geometry for Runs With No Peroxide	207
Figure 5.36	Average Flow Efficiencies for Second Channel Geometry for Runs With Uniform Peroxide Distribution	207
Figure 5.37	Average Flow Efficiencies for Second Channel Geometry for Runs With Barrel Peroxide Distribution	208
Figure 5.38	Average Flow Efficiencies for Second Channel Geometry for Runs With Random Peroxide Distribution	208
Figure 6.1	First Channel Geometry Finite Element Mesh	224
Figure 6.2	First Channel Geometry Cross-Section Meshes	225
Figure 6.3	Second Channel Geometry Finite Element Mesh	228
Figure 6.4	Vector Plots of Velocities on Inlet Plane	235
Figure 6.5	Barrel and Random Peroxide Addition Patterns	235
Figure 6.6	Average Temperatures for First Channel Geometry	243
Figure 6.7	Average Pressures for First Channel Geometry	243
Figure 6.8	Average Peroxide Conversions for First Channel Geometry	246
Figure 6.9	Average Peroxide Levels With No Peroxide Decomposition For First Channel Geometry	246

Figure 6.10	Average Relative Weight-Average Molecular Weights for First Channel Geometry	251
Figure 6.11	Velocity Vectors in Cross-Section for First Channel Geometry	253
Figure 6.12	Pressures in Cross-Section for First Channel Geometry	253
Figure 6.13	Normal Velocities in Cross-Section for First Channel Geometry, $Q_P/Q_D=0$.	254
Figure 6.14	Normal Velocities in Cross-Section for First Channel Geometry, $Q_P/Q_D=-0.25$	254
Figure 6.15	Temperatures in Cross-Section for First Channel Geometry	255
Figure 6.16	Peroxide Weight Fractions in Cross-Section for First Channel Geometry ..	255
Figure 6.17	Relative Weight-Average Molecular Weights in Cross-Section for First Channel Geometry	257
Figure 6.18	Particle Pathlines for First Channel Geometry	258
Figure 6.19	Flow Efficiencies in Cross-Section for First Channel Geometry, $Q_P/Q_D=0$.	261
Figure 6.20	Flow Efficiencies in Cross-Section for First Channel Geometry, $Q_P/Q_D=-0.25$	261
Figure 6.21	Average Flow Efficiencies for First Channel Geometry for Runs with Different Peroxide Distributions	265
Figure 6.22	Average Flow Efficiencies for First Channel Geometry for Runs at Both Screw Speeds	265
Figure 6.23	Average Flow Efficiencies for First Channel Geometry for Runs With No Peroxide - 1	266
Figure 6.24	Average Flow Efficiencies for First Channel Geometry for Runs With No Peroxide - 2	266
Figure 6.25	Average Flow Efficiencies for Second Channel Geometry	267

NOMENCLATURE

a	Centreline separation of screws, m
A	Infrared radiation absorbance
A_{Free}	Twin-screw extruder open area for flow in lateral cross-section, m ²
A_S	Specific area stretch, dimensionless
b	Single-screw extruder channel width, m
\bar{b}	Twin-screw extruder average channel width, m
b_{Max}	Twin-screw extruder maximum channel width, m
b_{Thread}	Length of flight for leakage flow calculation, m
Br	Brinkman number, dimensionless
c_p	Polymer melt specific heat capacity, J kg ⁻¹ °C ⁻¹
C	Molar concentration, kmol m ⁻³
d	Ordinary derivative
D	Rate-of-deformation tensor, s ⁻¹
D_p	Polymer pellet hydraulic diameter, m
D_R	Single-screw extruder screw root diameter, m
D_S	Screw outer diameter, m
e	Single-screw extruder flight thickness, m
e_{Max}	Twin-screw extruder flight width, m
E	Residence time distribution function, s
f	Channel degree-of-fill, dimensionless
f_p	Peroxide free radical initiation efficiency, dimensionless

F	Geometry correction factor, dimensionless - eqn. (3.8)
F	F distribution critical value - eqn. (4.12)
F_S	Solid volume fraction, dimensionless
Gz	Graetz number, dimensionless
h	Twin-screw extruder channel depth based on self-wiping profile, m
\bar{h}	Twin-screw extruder average channel depth based on self-wiping profile, m
h_{Max}	Twin-screw extruder maximum channel depth, m
H	Single-screw extruder channel depth, m
ΔH_F	Polymer heat of fusion, J kg ⁻¹
i	Number of screw flights
I	Free radical initiator molecule - eqn. (3.26)
I	Peroxide concentration in polymer melt, kmol m ⁻³ - eqn. (3.27)
I	Infrared light intensity - eqn. (4.5)
k	Number of parallel flow channels
k_C	Absorbance ratio calibration constant, dimensionless
k_D	Peroxide thermal decomposition rate constant, s ⁻¹
K	Power-law consistency index, Pa s ⁿ
K_{0T}	Temperature independent part of power-law consistency index, Pa s ⁿ
L	Axial length, m
\dot{m}	Mass flow rate, kg s ⁻¹
m_0	Molecular weight of polymer repeating unit, kg kmol ⁻¹
\bar{M}_N	Number-average molecular weight, kg kmol ⁻¹

\bar{M}_w	Weight-average molecular weight, kg kmol ⁻¹
\bar{M}_z	Z-average molecular weight, kg kmol ⁻¹
n	Power-law index, dimensionless - eqn. (3.31)
n	Unit normal orientation vector to interfacial area element, or component thereof - eqn. (5.4)
\hat{n}	Eigenvector of rate-of-deformation tensor (principal direction)
n_0	Frequency of screw rotation, min ⁻¹
N_p	Number of solid polymer particles in a unit volume of lattice, m ⁻³
P, p	Polymer melt pressure, Pa - eqn. (3.8)
P	Polymer molecule - eqn. (3.26)
P_{Die}	Melt pressure at diehead, Pa
P_{Input}	Specific mechanical power input to fluid, W m ⁻³
Q	Volumetric flow rate, m ³ s ⁻¹ - eqn. (3.3)
Q	Coordinate transformation matrix, dimensionless - eqn. (5.5)
Q_0, Q_1, Q_2, Q_3	Moments of polymer molecular weight distribution, kmol m ⁻³
Q_P/Q_D	Pressure-to-drag flow ratio, dimensionless
r_D	Throttle ratio, dimensionless
r_p	Polymer solid pellet hydraulic radius, m
R	Peroxide molecule fragment - eqn. (3.26)
R	Specific reaction rate, kmol m ⁻³ s ⁻¹ - eqn. (5.2)
R, r	Radius, m - eqn. (3.37)
R^2	Square of the multiple correlation coefficient, dimensionless

s_R	Radial flight gap width, m
s_{Rep}^2	Sample variance of average residence times from centre point replicate runs, s^2
t	Screw pitch, m - Fig. 2.2
t	Student-t distribution critical value - eqn. (4.4)
t^*	Residence (Lagrangian) time, s
\bar{t}_R	Average residence time, s
T	Melt temperature, °C
T_B	Barrel surface temperature, °C
T_{Bulk}	Polymer melt temperature in bulk of fluid, °C
T_M	Polymer fusion temperature, °C
\bar{v}_Z	Average speed of flow in downchannel direction, $m\ s^{-1}$
V, v	Speed, $m\ s^{-1}$
\dot{V}	Volumetric flow rate, $m^3\ s^{-1}$
V_ϕ, v_0	Tangential speed of barrel in groove model system, $m\ s^{-1}$
w	Weight fraction
x	Distance in cross-channel direction, m - Fig. 3.2
x	Dimensionless independent variable - eqn. (4.1)
x	Generic coordinate, m
X	Solid bed width, m - Fig. 2.4
X	Treatment level matrix - eqn. (4.2)
y	Distance in channel depth (radial) direction, m
Z, z	Distance in downchannel (helical axis) direction, m

Greek Symbols

α	Specific rate of stretching of interfacial area element, s^{-1}
β	Exponential temperature dependence factor of viscosity, $^{\circ}C^{-1}$ - eqn. (3.31)
β	Regression model parameter, s - eqn. (4.1)
β	First eigenvalue ratio, dimensionless - eqn. (5.9)
γ	Second eigenvalue ratio, dimensionless
$\dot{\gamma}$	Shear strain rate, s^{-1}
$\dot{\gamma}$	Rate of strain tensor, s^{-1}
Δ	Change in quantity
δ	Sample thickness, m
ϵ	Extinction coefficient, $m^2 kmol^{-1}$ - eqn. (4.5)
ϵ	Random error in average residence time, s - eqn. (4.1)
ζ	Dimensionless downchannel length
η	Shear viscosity, Pa s
η_A	Area efficiency, dimensionless
η_F	Flow efficiency, dimensionless
θ	Angle, rad - eqn. (3.1)
θ	Dimensionless temperature - eqn. (3.23)
λ	Polymer melt thermal conductivity, $W m^{-1} ^{\circ}C^{-1}$ - eqn. (3.19)
λ	Eigenvalue of rate-of-deformation tensor, s^{-1} - eqn. (5.5)
ξ	Dimensionless channel depth
$\pi_{\dot{\gamma}}$	Dimensionless flow rate

π_p	Dimensionless pressure gradient
ρ	Polymer melt density, kg m ⁻³
ρ_{Bulk}	Polymer bulk solid density, kg m ⁻³
ρ_S	Polymer solid density, kg m ⁻³
σ^2	Variance of experimental residence time distribution, s ²
τ	Shear stress, Pa
ϕ_S	Screw helix angle, rad
ϕ	Screw tip angle, rad
ϕ_1, ϕ_2	Coefficients of approximation equation for screw characteristic curve, dimensionless
χ	Dimensionless quantity in power-law index hyperbola formula
Ψ	Stream function
ω	Wavenumber, cm ⁻¹
Ω	Intermeshing angle of screws, rad
∇	Differential operator, m ⁻¹
∂	Partial derivative

Subscripts/Superscripts/Other Symbols

<i>B</i>	Benzophenone
<i>Die</i>	For die
<i>Ele</i>	Entire element
<i>F</i>	Free channel region
<i>i</i>	Index

<i>I</i>	Intermeshing region
<i>I</i>	Initiator (peroxide)
<i>I</i>	First scalar invariant of tensor
<i>II</i>	Second scalar invariant of tensor
<i>In</i>	Entering value
<i>LM</i>	Log mean
<i>Max</i>	Maximum value
<i>Melt</i>	For molten polymer
<i>Min</i>	Minimum value
<i>Out</i>	Exiting value
PP	Polypropylene
<i>Solid</i>	For solid polymer
<i>X</i>	Cross-channel direction
<i>Y</i>	Channel depth (radial) direction
<i>Z</i>	Downchannel (helical axis) direction
<i>X',Y',Z'</i>	FIDAP global coordinate system axis directions
0	Value for polymer structural unit
0	Value at start of region
0	Radical molecule
1	Value at end of region
[]	Concentration

- ‘ Corrected or transformed value
- Mean value
- || Absolute value
- ^ Estimate
- <> Adiabatic average

Abbreviations

CRPP	Controlled rheology polypropylene
CSCO	Closely-intermeshing self-wiping co-rotating
D	Dimension
DOF	Degree of freedom
FAN	Flow analysis network
FEM	Finite element method
MWD	Molecular weight distribution
PDF	Pressure-to-drag flow
PP	Polypropylene
PSM	Position of start of melting
PSMMIN	Earliest possible position of start of melting
REX	Reactive extrusion
RTD	Residence time distribution
SSE	Single-screw extruder
TSE	Twin-screw extruder

CHAPTER 1

INTRODUCTION AND OBJECTIVES

1.1 Reactive Extrusion

Screw extrusion is an important unit operation in polymer processing. Indeed nearly all polymers pass through an extruder at least once in their journey from the polymerization reactor to the finished product. In simplest terms, screw extruders are polymer pumps with the additional capacity to melt the material which they are fed. Screw extruders are comprised of one or more Archimedean screws rotating in a heated barrel, to which are fed either solid or molten polymer and which deliver a molten homogenized polymer to a die at a desired pressure for the purpose of shaping into a final product. The greatest strength of screw extruders results from the intense shearing environment created within the flow channels of the screws, which makes it possible for extruders to continuously process highly viscous materials such as polymer melts without the need for solvents, resulting in significant reductions in raw material and equipment costs.

Due to the inherent process economy gained by combining production and processing steps in one, extruders are increasingly finding use as continuous polymer reactors. In this process known as reactive extrusion (REX), the synthesis or modification of a polymeric material occurs simultaneously with melting, mixing, and pumping within the extruder. Extruders offer other important advantages over conventional stirred tank and batch reactors types as well, such as better control over the material residence time distribution (RTD) through variation of operating conditions and screw configurations. Residence time is also generally lower in a screw extruder than in a batch reactor for the same reaction, and so long exposure of material to high temperatures that can cause thermal degradation is greatly avoided (Tzoganakis, 1989). The flow patterns

created within the screw channels also give extruders good mixing characteristics resulting in better temperature control and mass transfer capacity in viscous materials than conventional reactor types (Todd, 1992). Because of their design, screw extruders also allow stage-feeding of reactive agents for polymer modification processes, which permits several reaction steps to be completed in one piece of equipment. Figure 1.1 shows a schematic representation of an extruder in a reactive extrusion application (Tzoganakis, 1989).

An industrially important application of REX is the peroxide-initiated reactive degradation of polypropylene (PP). Polypropylene is a thermoplastic of great commercial importance, due to its numerous desirable properties which make it suitable for a wide variety of consumer and industrial products. The strengths of PP include excellent chemical resistance, and the lowest density and highest melting point of the volume thermoplastics, which have contributed to its broad application in injection molding and in films, fibres, and filaments (Cheng, 1995). The conventional polymerization process for the synthesis of PP employs a Ziegler-Natta catalyst system, which results in a polymer with a high molecular weight and a broad molecular weight distribution (MWD) due to the broad distribution of active sites on the catalyst. Molten PP resins with these characteristics are usually difficult to process due to their high elasticity and viscosity. To improve the processing characteristics of the material, a post-reactor process known as controlled degradation is performed in an extruder. A peroxide free radical initiator is added to the polymer melt stream, and in the high temperature conditions of the extruder the peroxide molecules thermally decompose into free radicals which initiate a random scission of the polymer chains. Longer polymer chains have a higher probability of being attacked by the peroxide radicals, and so a general decrease of the molecular weight of the polymer and a narrowing of the MWD

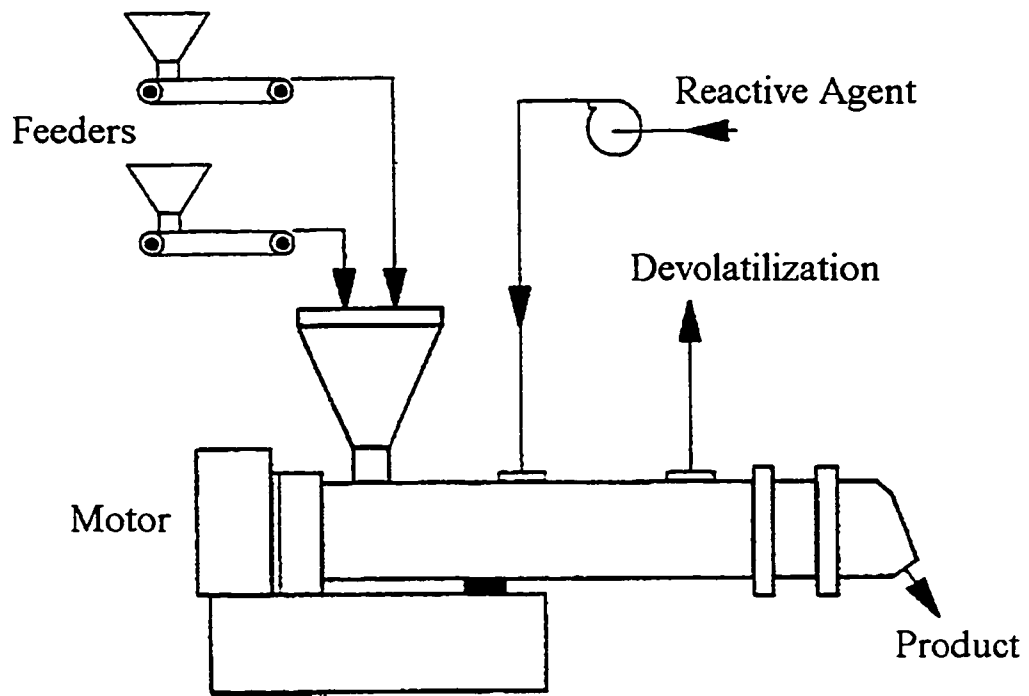


Figure 1.1: Reactive Extrusion System

result (Krell et al., 1994). By controlling the amount of peroxide initiator injected into the system, PP grades with tailor-made molecular and rheological properties can be produced. Such resins are referred to as controlled rheology polypropylenes (CRPPs).

1.2 Process Modeling and Simulation

Process modeling of conventional (non-reactive) extrusion over the last 30 years has led to a tremendous increase in the understanding of the operation of both single- and twin-screw extruders. The models incorporate descriptions of the extruder geometry, along with formulations of the conservation equations for mass, momentum, and energy, with corresponding boundary conditions. The influence of the material being processed is incorporated through its physical properties as well as the constitutive equations describing its rheological behaviour. The earliest modeling efforts used simplified geometries and assumed simple materials in isothermal flow; gradually over time these simplifications have been replaced with more realistic assumptions, and thus the operation of true systems has been more closely represented. However, the added complexities mean that for processes of engineering interest closed-form analytical solutions to extruder process models are not available.

In reactive extrusion systems, the presence of chemical reactions is an additional complication. The contributions of the reactions to the process model are in the form of the conservation equations of the reacting species, as well as the reaction rate expressions. The kinetics of the effect of the reactions on the polymer molecular structure must also be specified, along with the dependence of the parameters of the fluid constitutive equation on molecular structure. In REX systems then, the viscosity of the polymer melt combines the simultaneous effects of the

deformation and temperature fields and the chemical reactions. Mathematically, the consequence of this is coupling between the momentum, energy, and species conservation equations. A schematic representation of the reactive extrusion process model showing the different process factors along with interactions is shown in Figure 1.2.

As indicated above, for complicated conventional and reactive extrusion problems, the model equations can only be solved numerically. Such simulations yield steady-state profiles of the system degrees of freedom (velocity components, temperature, pressure, and species concentrations) at calculation nodes throughout the system geometry. With the proliferation of cheap and increasingly powerful digital computers over the recent past, and the increased availability and sophistication of simulation software for these machines, simulations are an increasingly important tool in extrusion process design and analysis. The greatest benefit of the use of simulation studies in process design is the capability to optimize designs quickly and cheaply by investigating design options on a computer rather than in a laboratory.

Another benefit of simulations is that the solution of the complete set of field variables in a system allows other variables of interest giving more insight into the system operation to be computed. Among such variables are the area and flow efficiencies, which characterize the instantaneous mixing conditions at each point in a flow. The area efficiency measures how an infinitesimal element of a material interface at a point is oriented relative to the direction of the maximum rate of stretch, and the flow efficiency indicates the efficiency with which the flow field converts the input mechanical power into the best deformation conditions for mixing. Together the values of these two quantities separate out the different factors that contribute to effective mixing (Zerafati and Bigio, 1994).

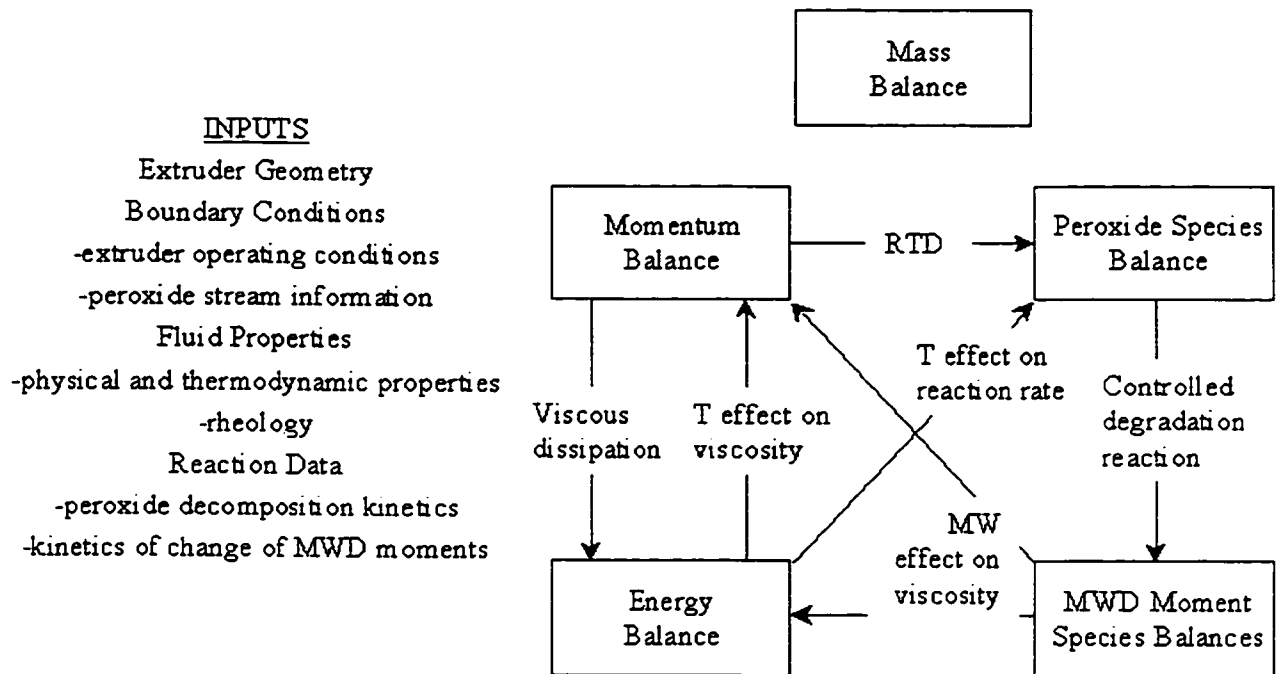


Figure 1.2: Reactive Extrusion Process Model

1.3 Objectives

The objective of this dissertation is to present and solve steady-state reactive extrusion process models of single-screw extrusion and twin-screw extrusion in self-wiping co-rotating twin-screw extruders, for the peroxide-initiated reactive degradation of PP. These models are extensions of existing non-reactive process models, with the model additions being based on published kinetic models of the controlled degradation reaction, and the temperature and molecular weight dependence of the rheology of PP. For a single-screw extruder system the model will be expressed and solved as a differential formulation, and for twin-screw extruder systems the model will be expressed as both a differential formulation and a reduced dimension macroscopic formulation. The macroscopic model has the advantage that it allows a complete twin-screw extruder to be simulated, with incorporation of the complete set of thermophysical phenomena that occur within (along with the chemical reaction), but has the disadvantage that it only returns average values of the degrees of freedom (DOFs) along the extruder axis direction. The differential models have the disadvantage that due to the considerable computational demands they impose, only a short length of an extruder can be simulated at a time, but the benefit is that the complete profiles of the process DOFs are computed within the considered domains.

A numerical solution algorithm for the twin-screw extruder macroscopic model is written in the C programming language, and simulations are carried out for both reactive and non-reactive flows of a PP resin in the same extruder, but with different screw configurations. The objective of this is to examine the effect of changing specified operating conditions and peroxide addition levels on the predictions of the extruder behaviour. Predicted extrudate molecular weights are also compared to published experimental values for one set of operating conditions and several

peroxide levels. Experimental average residence times are then acquired for a non-reactive process using a laboratory scale co-rotating twin-screw extruder, and are compared to predicted times for the same system using the simulation program.

For the single- and twin-screw differential models, numerical solutions are carried out using the finite element method with the commercial computational fluid dynamics package FIDAP. REX processes are simulated in conveying screw elements for both extruder systems, with channel geometry, operating conditions and peroxide level and addition pattern varied. The simulation results are analyzed to examine the effect of the degradation reaction on the flows at the microscopic scale, with particular emphasis on the effect on mixing conditions as indicated by the area and flow efficiencies.

1.4 Outline of Dissertation

Chapter 2: The geometry and operation of single-screw extruders are discussed, with description of the thermodynamic and hydrodynamic phenomena that take place within them. Twin-screw extruders are then introduced, with identification of the different classes. The geometry and operation of one class, self-wiping co-rotating twin-screw extruders, are described in more detail.

Chapter 3: A macroscopic steady-state process model for conventional and reactive extrusion in self-wiping co-rotating twin-screw extruders is presented, followed by a description of the numerical solution algorithm for the problem. Simulation results are presented and discussed. Predicted extrudate molecular weights for peroxide-initiated controlled degradation of polypropylene are compared to published results

for one system.

- Chapter 4: An experimental investigation into the effect of operating conditions on the average residence time in a non-reactive PP flow in a self-wiping co-rotating twin-screw extruder is described. Response surface analysis techniques are utilized to determine a regression model between the average residence time and the operating conditions. A regression model based on simulated average residence times for the same system is also developed, and the two are compared.
- Chapter 5: A differential process model for controlled degradation of PP in a single-screw extruder is presented, and the details of the finite element method numerical solution are given. Simulation results for a channel section are presented, including results of the mixing efficiency analyses of the flows.
- Chapter 6: The reactive extrusion process model presented in Chapter 5 is solved numerically using the finite element method for a channel in a forward conveying screw element of a self-wiping co-rotating twin-screw extruder. Simulation results are again presented, including results of the mixing efficiency analyses of the flows.
- Chapter 7: The primary results of the dissertation are summarized, and recommendations for future work presented.

CHAPTER 2

SINGLE- AND TWIN-SCREW EXTRUSION

2.1 Introduction

Screw extruders in industrial use can be grouped into two major classes: single- and twin-screw extruders. The distinction, of course, is made on the basis of whether the extruder has one or two screws. In this chapter the geometry and operation of both classes of screw extruder are described.

2.2 Single-Screw Extruders

Single-screw extruders (SSEs) have been the major continuous processing machines of the thermoplastics industry since their development in the latter years of the 19th century (White, 1990). Figure 2.1 shows a schematic of a typical single-screw extruder (Middleman, 1977). The polymer to be processed enters the extruder through the feed hopper (generally as pellets or powder), and is carried toward the die in the channels of the screw. Figure 2.2 shows a diagram of the geometry of the extruder screw (Middleman, 1977). The important geometric parameters are the helix angle ϕ_s , the channel width b , the channel depth H , the flight thickness e , the screw pitch t , the radial flight clearance s_R , and the screw root diameter D_R . The Figure exaggerates the flight clearance relative to the channel depth.

Figure 2.3 shows a cutaway view of a single-screw extruder showing the functional zones and the state of the polymer in each (Agassant et al., 1991). In the feed zone of the extruder the solid polymer particles are compressed together in the screw channel to form a solid bed of material. At the start of the next extruder section, the plastication (melting) or compression zone,

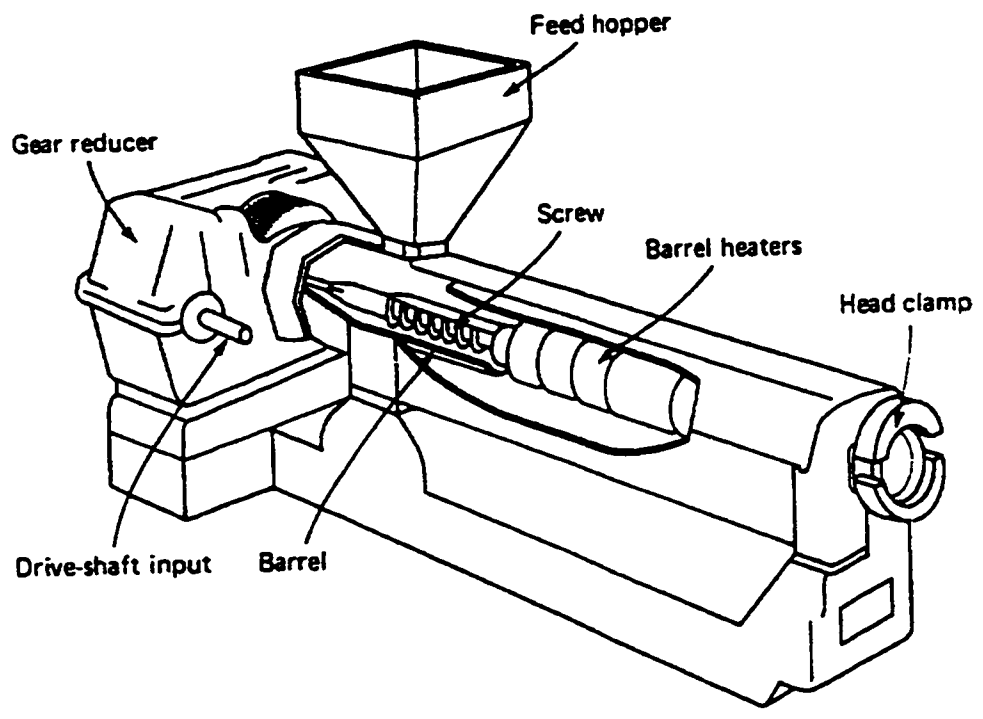


Figure 2.1: Single-Screw Extruder

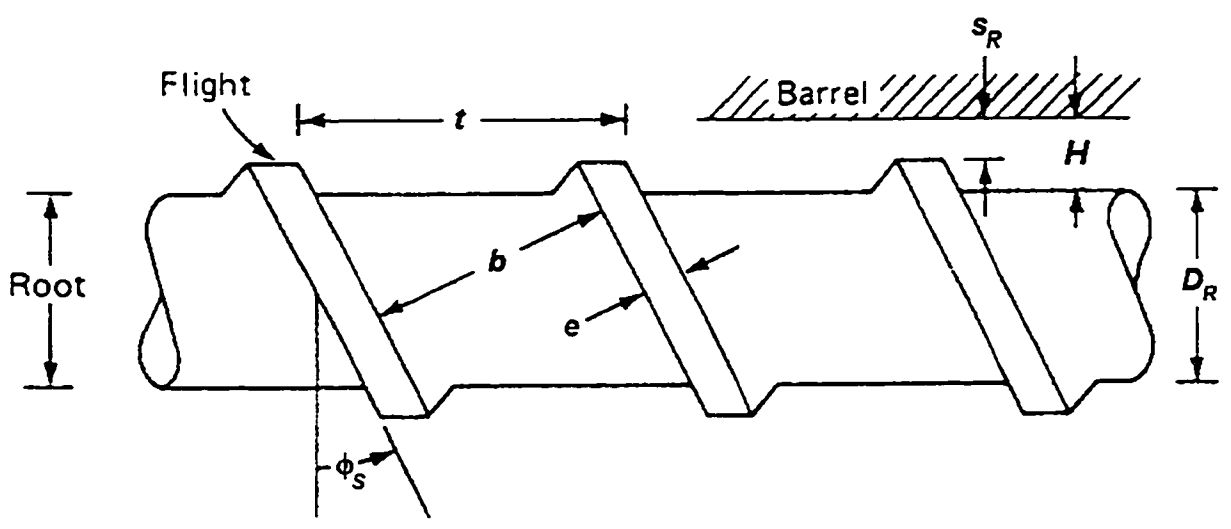


Figure 2.2: Extruder Screw Geometry

the barrel heaters cause a thin film of molten polymer to form in the gap between the solid bed and the barrel wall. The melt film is subjected to intense shearing in the thin gap, and due to the extremely high viscosities of molten polymers high rates of viscous dissipation result. The generated heat melts the solid bed within a short distance of the start of melting. Figure 2.4 illustrates how the solid bed width changes along the length of a screw channel in the plastication zone (Agassant et al., 1991). In the last zone of the extruder, the metering zone, the polymer melt flow is stabilized in the shallow screw channels, and finally the material passes out through the die on the end of the machine.

Figure 2.5 shows typical temperature profiles along the length of a SSE for three different screw speeds (Agassant et al., 1991). The profiles show steady rise in the material temperature along the length of the extruder, due to the continuous action of viscous dissipation. In SSEs, the screw speed and throughput are not independent, and so the curves for higher screw speed also correspond to higher throughput. The profiles show that temperatures are higher for higher screw speeds since viscous dissipation is more intense; this occurs even in spite of the dilution effect of the increased throughput. Figure 2.6 shows pressure profiles along the length of a SSE for three different screw speeds (Agassant et al., 1991). It shows that the melt pressure peaks at an intermediate position in the extruder (within either the compression or metering zones), and drops over the remaining extruder length to the die. As with temperatures, higher screw speeds yield higher pressures. This is a consequence of the larger pressure drop required to drive the higher throughput through the extruder die.

In the operation of single-screw extruders, the operating conditions of the greatest importance are the throughput and the screw speed. As mentioned above, they are coupled to one

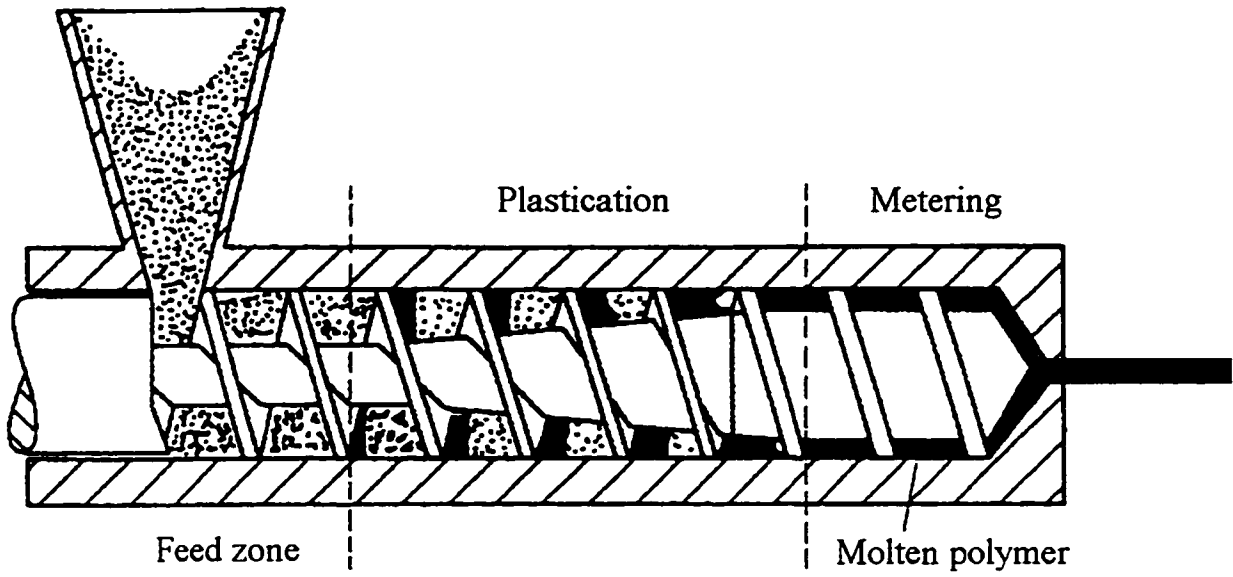


Figure 2.3: Cutaway View of Single-Screw Extruder

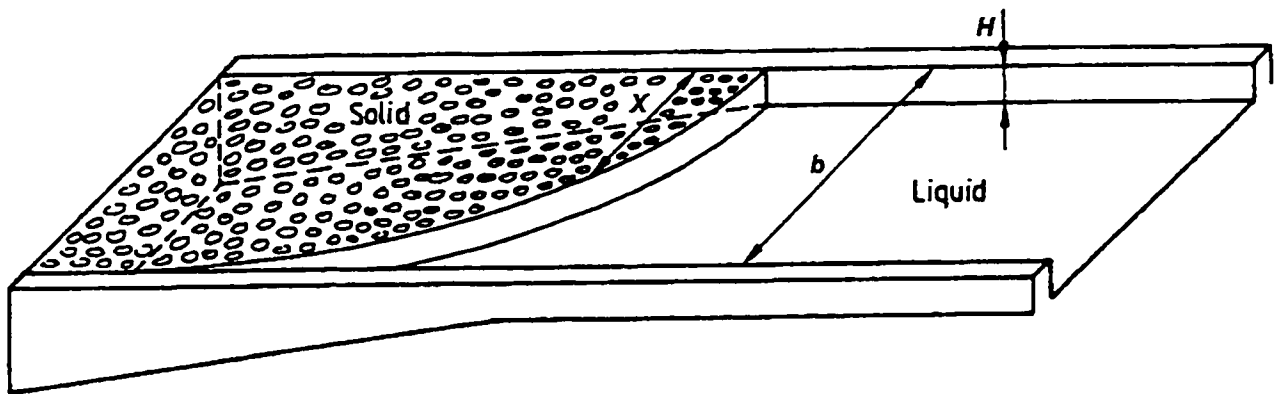


Figure 2.4: Melting of Solid Bed in Plastication Zone

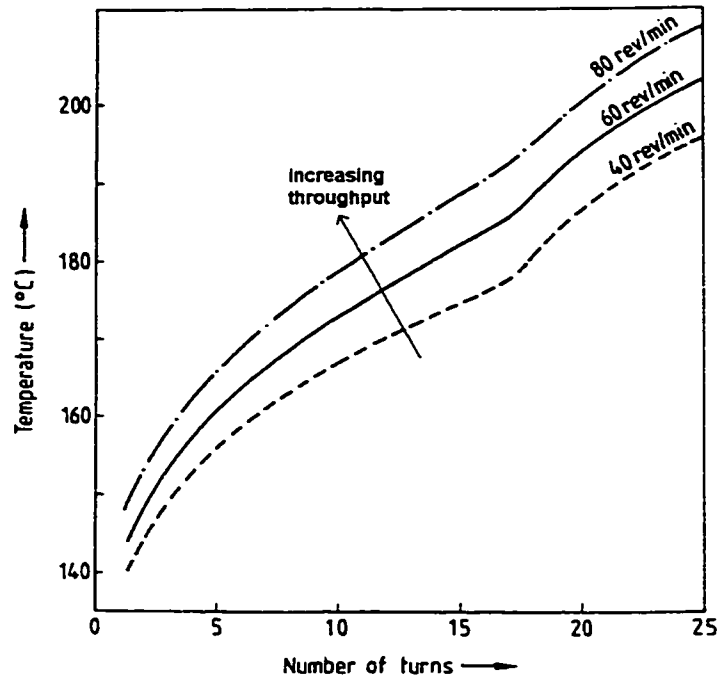


Figure 2.5: Single-Screw Extruder Example Temperature Profiles

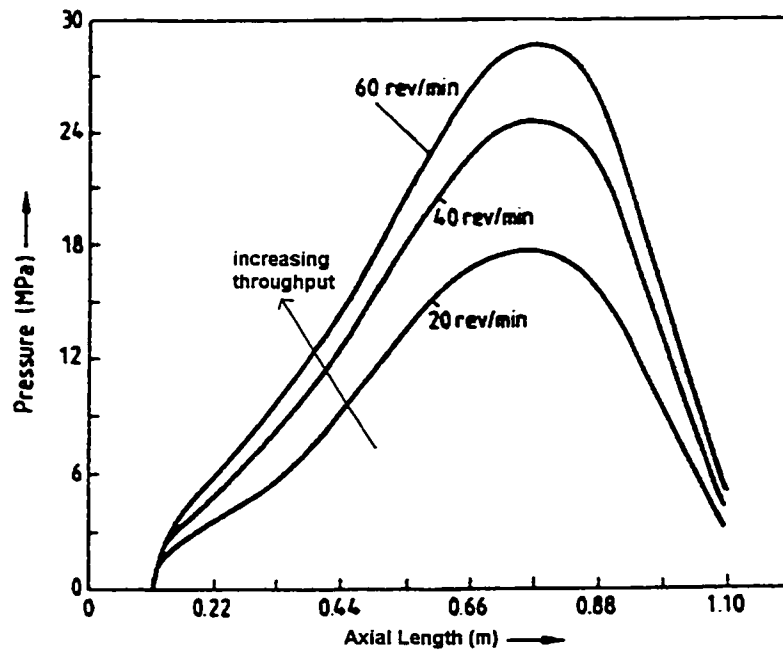


Figure 2.6: Single-Screw Extruder Example Pressure Profiles

another in an indirect manner through the influence of the die. A high resistance die will result in a lower throughput at a given screw speed than a low resistance die. The other important consideration is the pressurization capacity of the extruder itself. The relationship between the throughput and pressure drop in a die is known as the die characteristic equation, and similarly the relationship between throughput and diehead pressure for an extruder (at a given screw speed) is known as the screw characteristic equation. Since the die and extruder are coupled at the diehead, at this point the pressures in each are equal. Hence, if the screw characteristic and die characteristic curves are plotted on the same diagram of throughput against relative pressure, the point at which they cross will be the operating point of the extruder, with coordinates of the throughput and diehead pressure. Figure 2.7 shows such a plot, with die characteristic curves for both a low and a high resistance die (Agassant et al., 1991).

In SSEs, the polymer melt is conveyed along the screw channels parallel to the screw flights. Since the screw flights are inclined to the direction of the tangential velocity of the screw, the drag force exerted by the barrel on the polymer melt has both down-channel and cross-channel components. The down-channel velocity profile is a drag flow profile with a superposed pressure profile. Figure 2.8 shows four such profiles, for different pressure conditions (Rauwendaal, 1986). In the fourth profile, corresponding to closed discharge (i.e. zero throughput), the drag flow and pressure backflow balance each other. The cross-channel profile also has drag and pressure flow components; due to the presence of the screw flights what results is a recirculating flow. Figure 2.9 shows a diagram of the closed streamlines (Wang and White, 1989). The particle motion that results from the combination of these two velocity profiles is a helical flow within the screw channel. This is known as “helix within a helix” flow. Figure 2.10 shows a diagram of this

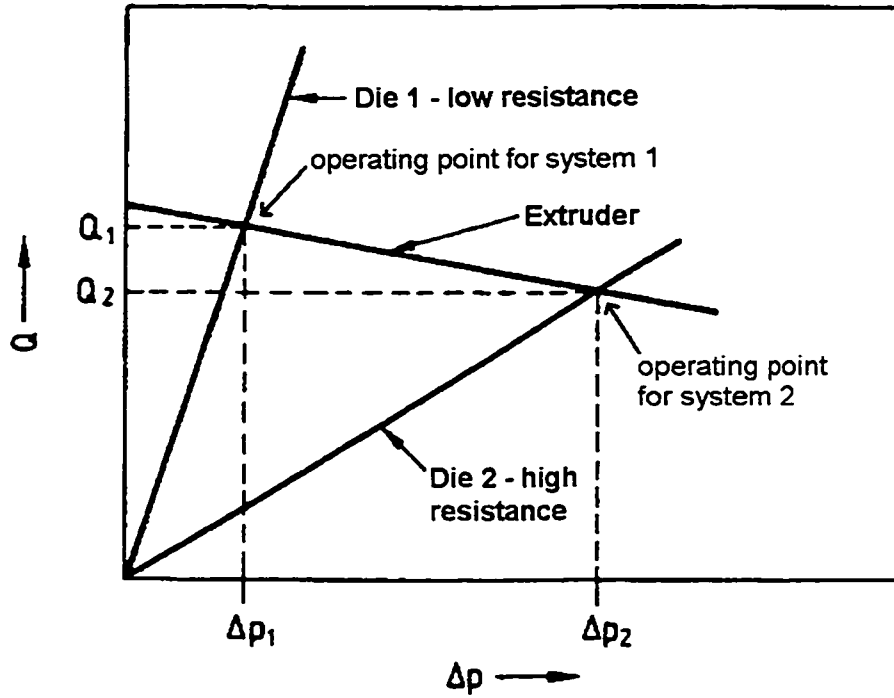


Figure 2.7: Screw and Die Characteristic Curves

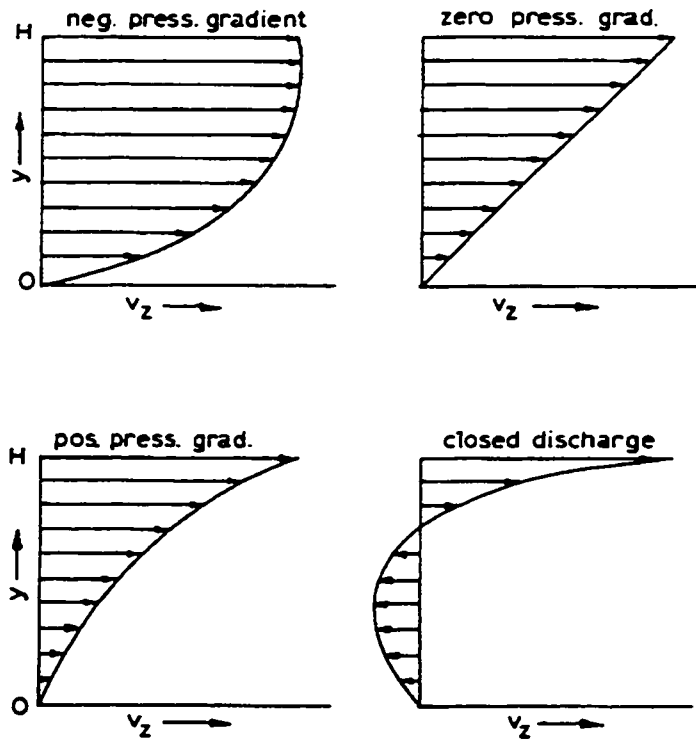


Figure 2.8: Down-Channel Velocity Profiles

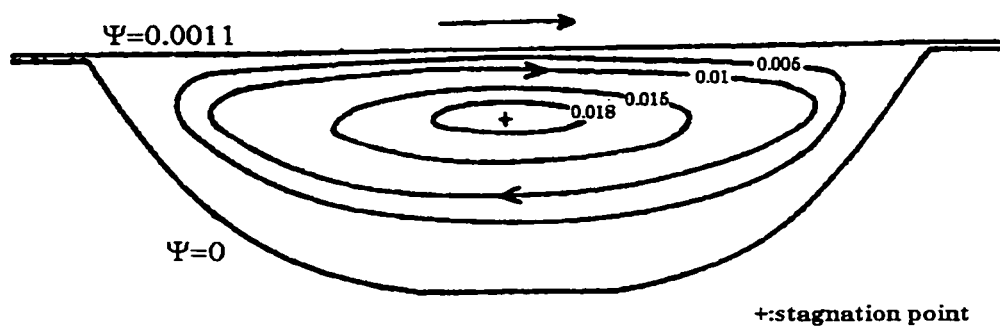


Figure 2.9: Transverse Circulation Streamlines

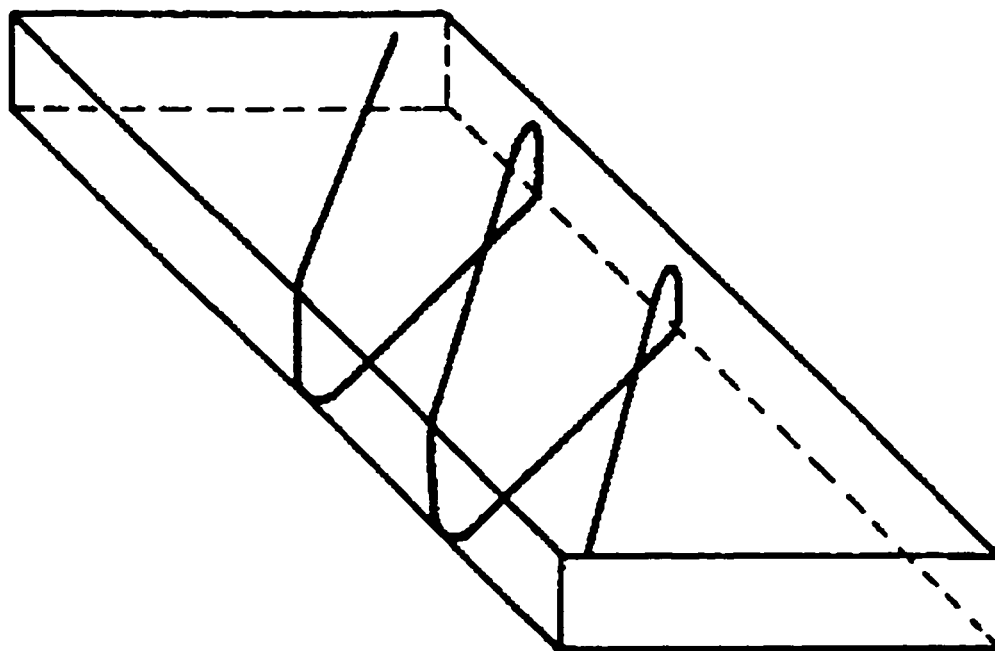


Figure 2.10: Polymer Particle Streamline in Screw Channel

(Agassant et al., 1991). It should be noted that the information presented in Figures 2.8 to 2.10 are shown from a frame of reference embedded in the screw, from which the screw appears stationary and the barrel turning.

2.3 Twin-Screw Extruders

Twin-screw extruders (TSEs) are extruders with two screws of the same diameter, which turn side-by-side within the extruder barrel at the same speed. In recent years, twin-screw extruders have come into increasingly wider use in applications such as mixing, blending, compounding of thermoplastic polymers, devolatilization, and reactive extrusion. TSEs offer greater control over RTD and mixing than single-screw extruders and have superior heat and mass transfer capabilities (Tzoganakis, 1989). There are three major classes of twin-screw extruders, with the classification based on the relative direction of turning of the screws and whether or not the screws intermesh with one another. Figure 2.11 shows a section of screws for each of the three major TSE classes, illustrating the relative position and orientations of the screws (Rauwendaal, 1986). Beginning at the top, the screws in Figure 2.11 are from a co-rotating fully-intermeshing TSE, a counter-rotating intermeshing TSE, and a counter-rotating non-intermeshing TSE. All boast good mixing characteristics, large melting capacity, good devolatilization capacity, and good control over residence times. With twin-screw extruders modular design is also possible, whereby the screws are custom built using different screw elements configured along a screw shaft in such a way as to meet the requirements of the application at hand. An unlimited number of different configurations are possible for such screws.

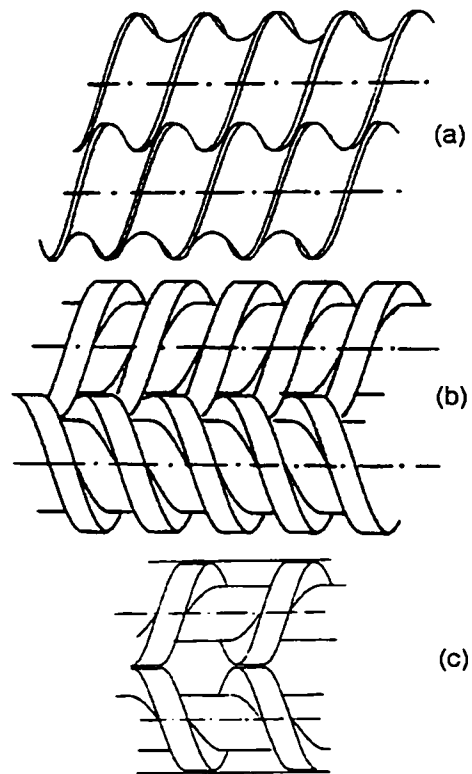


Figure 2.11: Twin-Screw Extruder Screws
(a) co-rotating fully-intermeshing
(b) counter-rotating intermeshing
(c) counter-rotating non-intermeshing

2.3.1 Closely-Intermeshing Self-Wiping Co-Rotating Twin-Screw Extruders

Of particular interest is the fully-intermeshing co-rotating twin-screw extruder, or CSCO (for Closely-intermeshing Self-wiping CO-rotating) extruder. Because of the special design of its screws, the CSCO extruder has the unique attribute that with every complete screw turn the entire surface of each screw is wiped by the other, thus eliminating the possibility of dead spots in which material could collect and degrade. This feature leads to narrower RTDs in CSCO extruders than in SSEs, making them particularly attractive for use with thermal and shear sensitive materials (Sakai et al., 1987). Combined with the control over average residence times permitted by modular screw design, the self-wiping feature of CSCO extruder screws also makes the machines very attractive for reactive extrusion applications, since a narrow RTD leads to greater product homogeneity (Uhland and Wiedmann, 1994). Figure 2.12 illustrates the self-wiping cross-section screw profile for single-, double-, and triple-flighted screws (also known as monolobal, bilobal, and trilobal screws) (Dreiblatt and Eise, 1991). The difference between the three screw profiles is that as the number of flights increases, the average channel depth decreases, resulting in lower conveying capacity and higher average shear rates.

CSCO extruders use a variety of different screw element types, the principal ones being conveying elements and kneading blocks. Conveying elements are the normal screw elements as shown in Figure 2.11 (a), and can be either forward or reverse conveying, depending on their orientation. Forward conveying elements generally cause an increase in melt pressure; reverse conveying elements do the opposite. The conveying characteristics of forward conveying elements are similar to those of single-screw extruder screws, since both have open channels in the direction of flow and transport material by mechanisms of drag and pressure flow. One important distinction

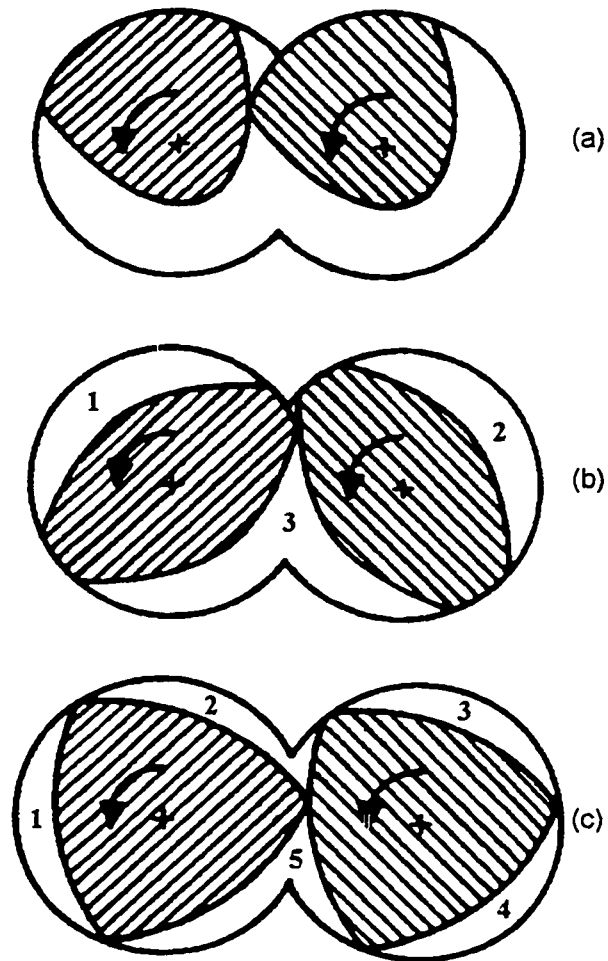


Figure 2.12: Self-Wiping Profile Cross-Sections

- (a) monolobal screws
- (b) bilobal screws
- (c) trilobal screws

of the flow mechanism in CSCO conveying screw elements comes from the flow field disturbance at the centre of the intermeshing region of the screw elements, in which the fluid undergoes a zig-zag motion in passing from one screw to the next. This effect is displayed in Figure 2.13 (with the channel geometry unwrapped and projected onto a plane), and is due to the presence of the flight of one screw in the channel of the other in the intermeshing region (see Figure 2.11 (a)). The effect can be neglected in screws for which the screw flight width is small compared to the channel width. Another major difference in the conveying behaviour of CSCO extruders is that in their operation throughput and screw speed are independent. The consequence of this is that starved feeding is possible, in which regions of the screws are only partially-filled with material, and subsequently are at atmospheric pressure. Figure 2.14 illustrates where the polymer accumulates in a conveying screw element channel under these conditions (Rauwendaal, 1986). The free surface in the channel is assumed to be parallel to the helical axis of the channel.

Kneading blocks are special mixing elements comprised of several discs staggered at an angle to one another. Forward staggering results in the kneading blocks having positive pressurization capacity, reverse staggering results in the opposite. Neutral staggering (given by a 90° angle-of-stagger) is also possible. The motion of the kneading discs causes intense shearing and has a chopping effect on the material stream. Most of the dispersive mixing (melt homogenization and solids breakup) and melting that occurs within the extruder takes place in kneading blocks. Figure 2.15 shows a set of kneading discs which are forward staggered at a 45° angle (Yang and Manas-Zloczower, 1992). Note that the element cross-sections still show the self-wiping profile. The arrows indicate where the material emerges from the element. Radial gaps are created between consecutive screw tips by the staggering of the discs, through which material

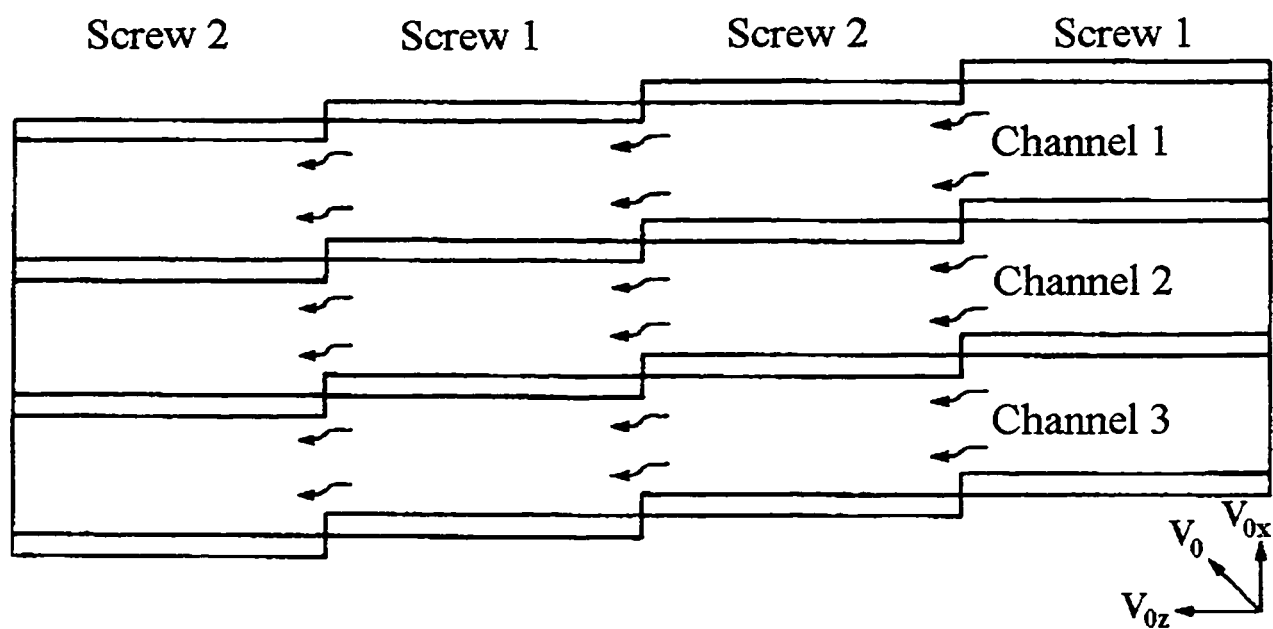


Figure 2.13: Fluid Shift in Intermeshing Region of Conveying Screw Element

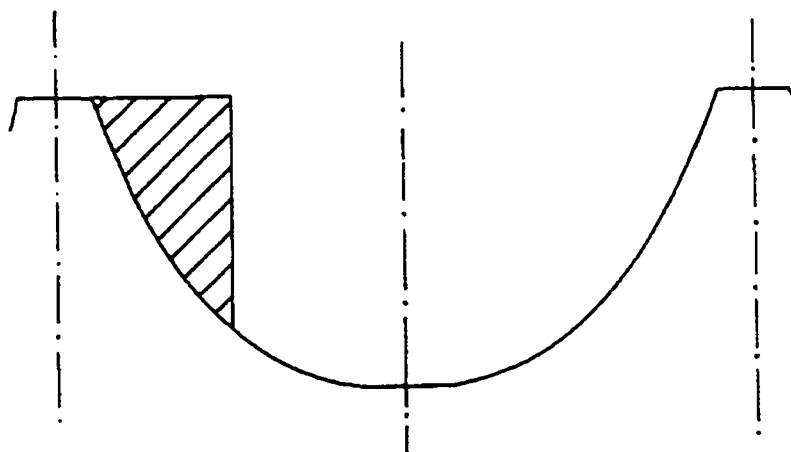


Figure 2.14: Partially-Filled Screw Channel

will leak under pressure, and thereby increase back-mixing. In normal screw configurations a reverse conveying screw element is placed downstream of a kneading block element, to act as a flow restriction and maintain fully-filled conditions within the kneading block.

A characteristic feature of material transport in CSCO extruders is the circumferential ‘figure-eight’ motion of the material as it passes back and forth between the screws while being conveyed along the extruder axis direction. This motion is illustrated in Figure 2.16, and occurs because the tight intermeshing between the screws results in essentially complete transfer of material from one screw to the other across the intermeshing region (White, 1990). For multi-flighted (i.e. bilobal or trilobal) screws, this motion leads to the creation of a number of essentially independent co-axial down-channel flows in the extruder. Figure 2.17 highlights the material of one such flow in an extruder with bilobal screws (Rauwendaal, 1986). The number of independent flows is 3 for extruders with bilobal screws and 5 for systems with trilobal screws; Figure 2.12 (b) and (c) show the chambers through which the flows would travel, separated from each other by the screw flights and barrel walls.

Profiles of the conditions inside a typical CSCO extruder in plasticating extrusion operation are presented in Figures 2.18 and 2.19, along with the corresponding screw configuration (Potente et al., 1994). The screw is made up of conveying elements, with a kneading block region in the middle followed by a reverse conveying screw element. Figure 2.18 shows the pressure and filling level profiles along the extruder length for three screw speeds (at the same throughput) as two families of three curves each. The upper family of curves is for the filling level; the solid curves are for the lowest screw speed. The Figure shows that the melt pressure only becomes greater than zero in the regions where the filling level is unity, and also that higher screw speeds lead to lower

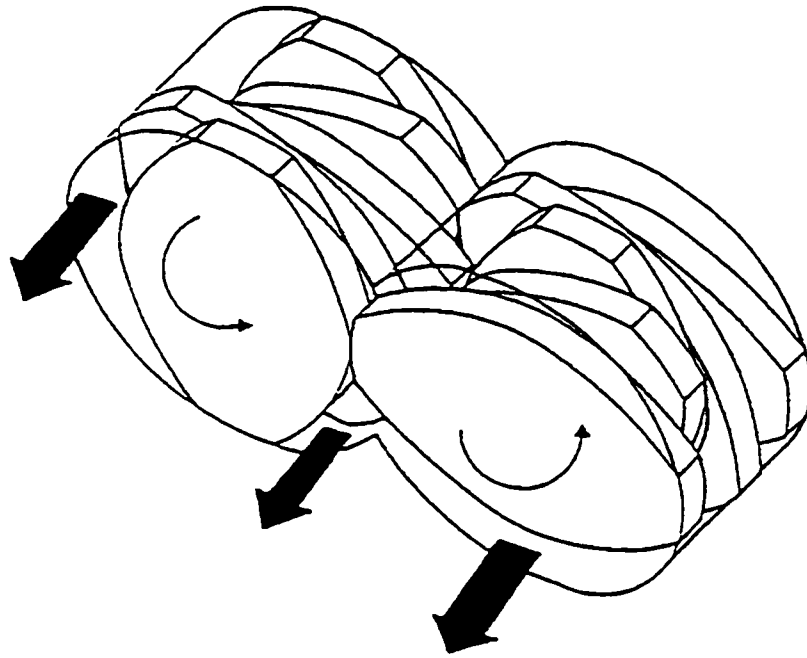


Figure 2.15: Kneading Block Element

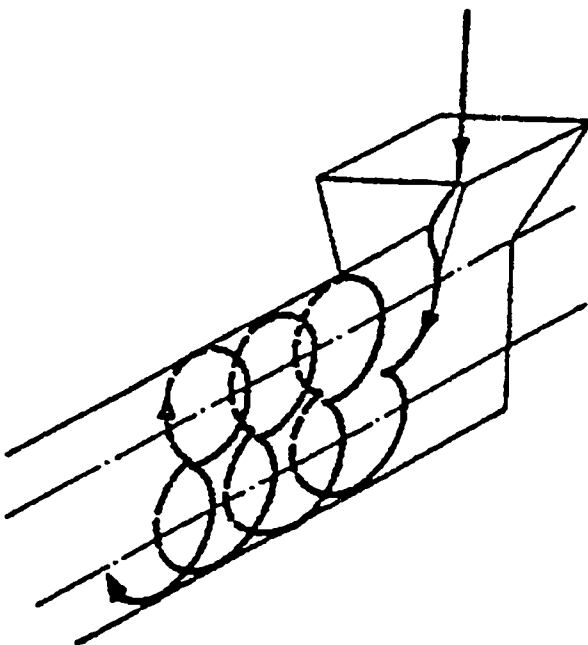


Figure 2.16: Material Motion in CSCO Extruder

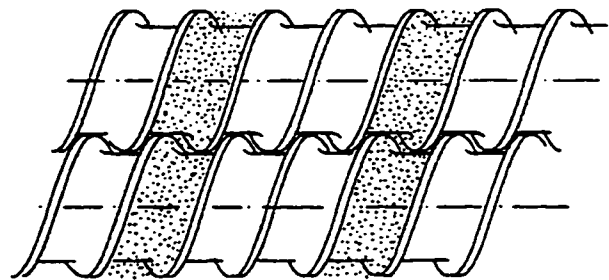


Figure 2.17: Independent Channel Flow in CSCO Extruder

overall filling. Figure 2.19 shows melt temperature profiles for the same systems. The curves show that most of the temperature growth occurs in the kneading block region, where shearing is most intense. The curves also show that the melt temperature is not as strongly affected by screw speed as it is in single-screw extruders.

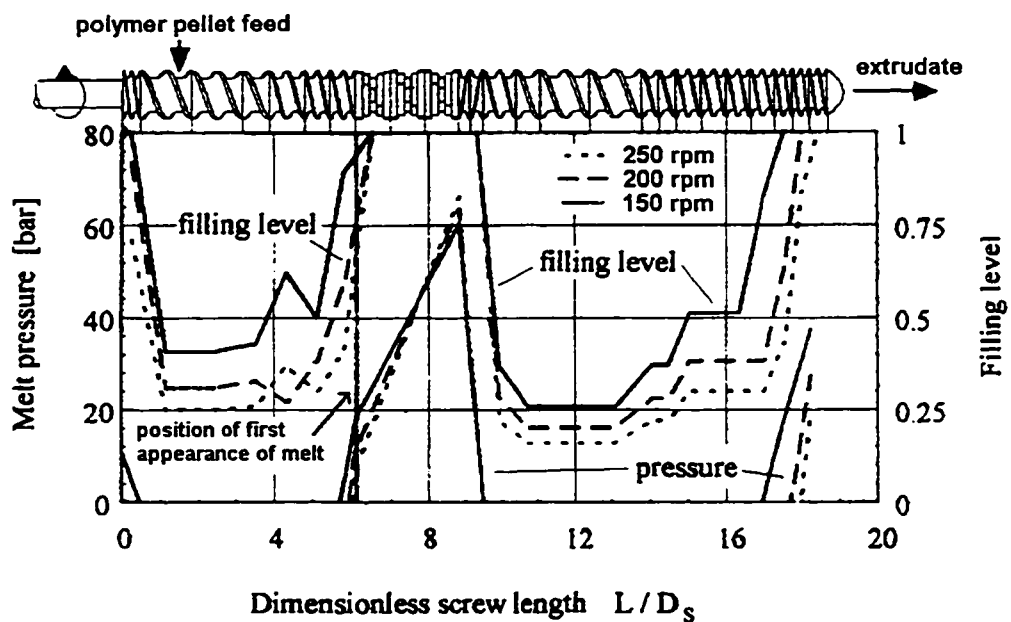


Figure 2.18: CSCO Extruder Example Pressure and Filling Level Profiles

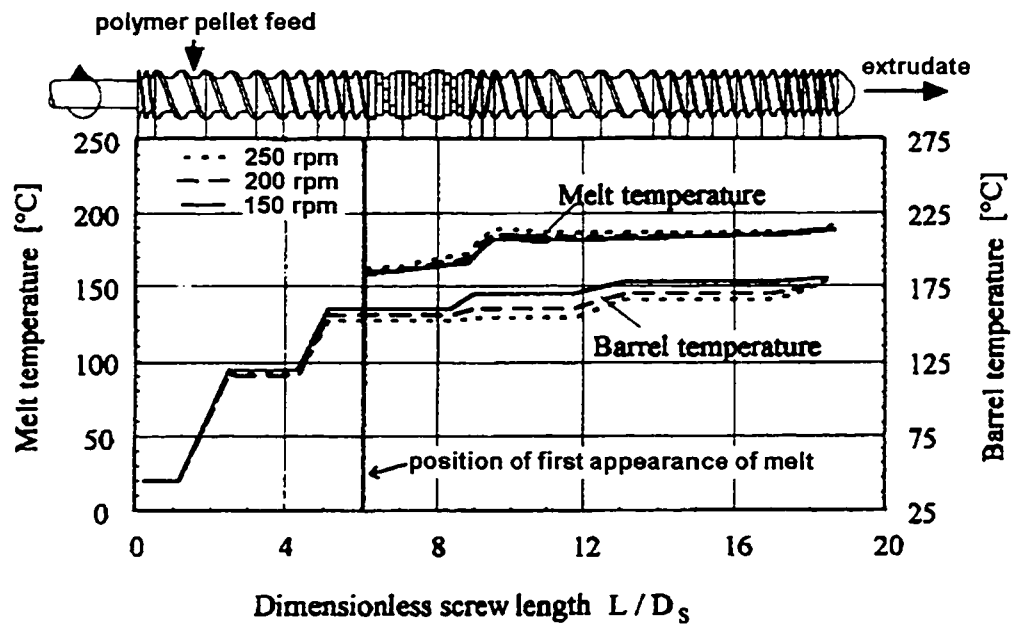


Figure 2.19: CSCO Extruder Example Temperature Profiles

CHAPTER 3

MACROSCOPIC MODELING AND STEADY-STATE SIMULATION OF CONVENTIONAL AND REACTIVE EXTRUSION IN CSCO EXTRUDERS

3.1 Introduction

CSCO extruders are very complicated machines, in both design and function. They are versatile in application, as the number of parameters in their design and operation is large. Even for systems with fixed screw cross-section geometry, the number of different configurations the extruder can assume is almost unlimited, due to the modular design of CSCO extruder screws. The configuration of the extruder barrel can also be varied, by the addition of barrel sections with ports for injection of additives or removal of volatiles. In operation, both screw speed and throughput can be independently varied, along with the extruder barrel temperature distribution, and the material being processed can be changed. The number of thermophysical phenomena taking place within the extruder screw channels is also large, including solids conveying, melting, melt conveying and pressurization, heat transfer, and also possibly chemical reaction. The complexity of these interrelated phenomena make it difficult to know in advance what the effect of changing one or several system and process parameters will be on the extruder performance. Even empirical characterization is insufficient to quantify these effects, as only a finite number of different possibilities can be examined. As such, the need exists for composite models covering all the phenomena occurring within CSCO extruders, along with numerical algorithms for their solution.

Composite models of polymer flow within CSCO extruders assemble the complete process models for flow within screw elements for the entire machine. The elemental process models describe the thermophysical phenomena taking place within the screw channels, and include the

element geometries, the physical and rheological properties of the material being processed, and the kinetics of any chemical reactions taking place within the melt phase. Limitations on computing power and memory capacity require that for a complete modular CSCO extruder to be simulated, such composite models must be macroscopic (or reduced dimension) in that they only compute average values of the process degrees of freedom along the extruder axis direction. To date, proposed models have all been for steady-state extrusion, thus leaving out the additional complication of time variability. The numerical simulation algorithms to solve composite CSCO extrusion models perform the calculations to solve the model equations following the sequence of elemental geometries specified by the screw configuration, employing iterative techniques to simultaneously solve the coupled flow phenomena. The algorithms permit the computation of the effects on the performance of an extruder of changing the screw configuration, changing operating conditions, and changing the material being processed, as well as potentially the addition of a chemical reaction to the flow.

The development of composite models for CSCO extrusion is difficult, due to the need to model the numerous phenomena taking place within the extruder elements. This must be done for both conveying screw elements and kneading block elements, which exhibit quite different flow patterns. The problem is further complicated by the complex self-wiping screw element geometry, by the coupling of the different flow phenomena within the screw channels, and by the complex fluid rheology. As such, it is only within the most recent decade that such models have begun to appear in the literature. In this chapter, the published literature on the different approaches taken to steady-state macroscopic modeling of non-reactive polymer flows within CSCO extruder screw elements and complete modular machines is reviewed. The few papers on reactive extrusion of PP

with peroxide-initiated degradation are also mentioned. One of the extruder composite models is selected as the basis for a simulation algorithm, and this model is outlined, with descriptions of the equations for the different process phenomena presented. A model extension for the peroxide-initiated controlled degradation of PP is also given. The numerical solution algorithm derived from the extended composite model is described, along with the C program written to execute the algorithm. Simulation results for both a non-reactive and a reactive system using the same PP resin and extruder, but different screw configurations, are presented. For the non-reactive system, a sensitivity analysis of predicted average residence times against several model parameters is presented, and for the reactive system, predictions of extrudate molecular weights for several levels of peroxide addition are compared to published experimental values. Discussion of the process model then follows, with emphasis on its weaknesses and their impact on the model predictions.

3.2 Literature Review

3.2.1 Self-Wiping Screw Profile

Publication of the mathematical description of the shape of the self-wiping screw profile for CSCO extruder screws by Booy (1978) represented the passage of the first major hurdle to the modeling of CSCO extrusion, that of the complicated screw geometry. Figure 3.1 shows the self-wiping screw geometry along with the principal geometric parameters, for bilobal screws at a centreline separation distance $a = 0.85D_s$. With both screws rotating in the same direction at the same angular velocity, in every complete turn each screw fully wipes the surface of the other. In Figure 3.1 the inner circles are the screw roots, the bold outer lines are the barrel walls, and the connecting curves between the two are the edges of the screw flights cut by the viewing plane

perpendicular to the screw axis. The shaded regions represent the area available for flow. The variation in the channel depth between the screw root and the tip of the screw flight is given by the following expression:

$$h(\theta | 0 \leq \theta \leq \Omega) = \frac{1}{2}D_s(1 + \cos \theta) - \sqrt{a^2 - \frac{1}{4}D_s^2 \sin^2 \theta}; \quad \begin{aligned} \frac{1}{2}D_s < a < D_s \\ \Omega &= 2 \cos^{-1} \frac{a}{D_s} \\ \Omega + \phi &= \frac{\pi}{i} \end{aligned} \quad (3.1)$$

Figure 3.2 shows the cross-section perpendicular to the screw flights of a channel with the self-wiping profile. The Figure shows the the principal geometric quantities that describe the channel cross-section, which are the channel width b_{Max} , the maximum channel depth h_{Max} , the flight width e_{Max} , and the radial flight clearance s_R .

3.2.2 Macroscopic Modeling of Melt Conveying in Conveying Screw Elements

The self-wiping screw profile was first used in the modeling of polymer melt flow in conveying screw elements, for which the first significant paper was that of Denson and Hwang (1980). In this study, screw characteristic curves of flow rate against down-channel pressure gradient were determined from first principles for Newtonian isothermal flow in channels of different pitches, by solving the equation of motion for down-channel flow using the finite element method. Leakage flows through the flight clearances between adjacent channels were included in the model, but the channel shift in the intermeshing region was neglected. In modeling the conveying capacity of the screw element, two model simplifications taken from single-screw

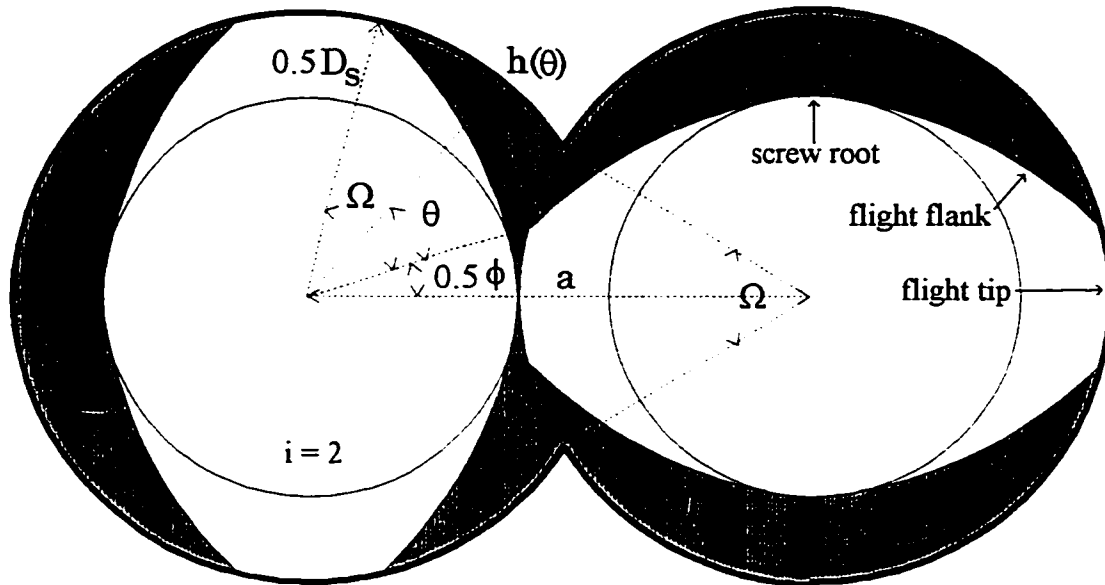


Figure 3.1: Self-Wiping Screw Profile for Bilobal Screws

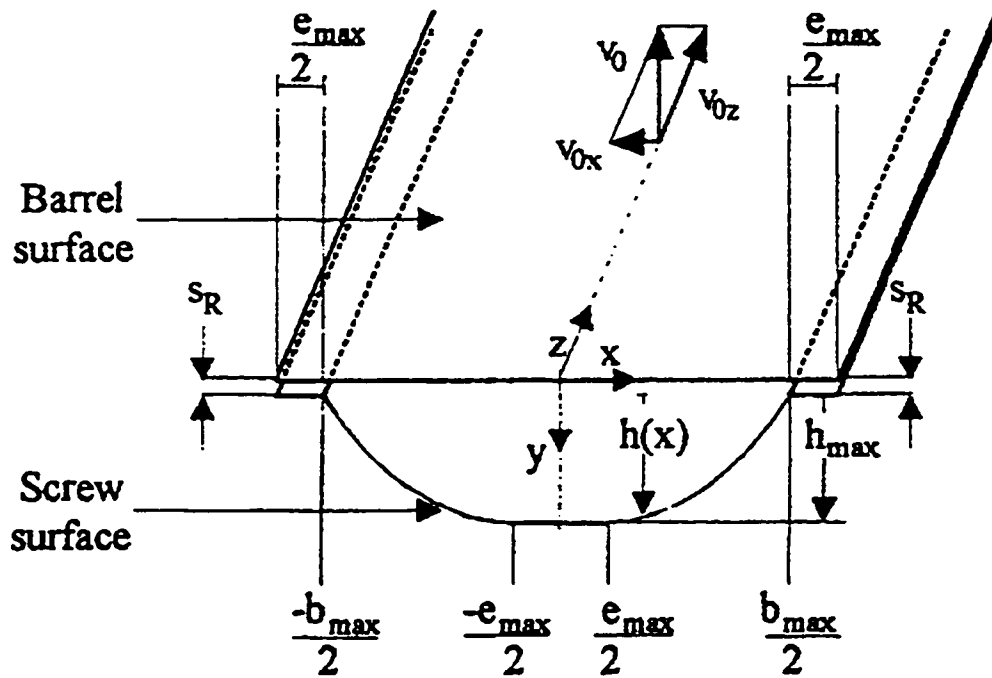


Figure 3.2: Self-Wiping Screw Channel Cross-Section

extrusion modeling were employed. The first was a kinematic reversal assumption by which the polymer flow is modeled from a frame of reference embedded in the screw, from which perspective the screw appears stationary and the barrel turning in the opposite direction at the screw angular velocity. The second assumption was that the screw channels and the barrel surface can be “unwrapped”, that is laid out flat and projected onto adjacent planes. The resulting model (known as the groove or flat plate model) is a flat plate sliding over a series of parallel channels aligned at an angle to the plate velocity, within which the polymer moves. These two assumptions are only applicable to systems in which the screw and barrel curvatures can be neglected, i.e. for screws with small ratios of channel depth to screw diameter. Figure 3.3 shows a schematic representation of the groove model geometry (White, 1990).

Szydowski and White (1987) expanded the work of Denson and Hwang (1980) by considering the effect of the cross-channel pressure gradient and the channel shift in the intermeshing region on the flow in a conveying screw element. The equations of motion for down-channel and cross-channel flow were solved simultaneously by a control volume technique known as the flow analysis network (FAN) method (Tadmor et al., 1974). Screw characteristic curves were computed for both forward and reverse conveying elements, including for the geometries considered by Denson and Hwang (1980). Comparisons with the results of Denson and Hwang (1980) showed excellent agreement. To further investigate the effect of the intermeshing region channel shift, simulations were carried out for forward conveying elements with increasingly larger flight widths. Results showed that the wider the flight relative to the channel, the greater the dissipation of the developed pressure in the element, since the flight in the channel acts as a flow restriction. However, significant pressure losses in the intermeshing region were not found until

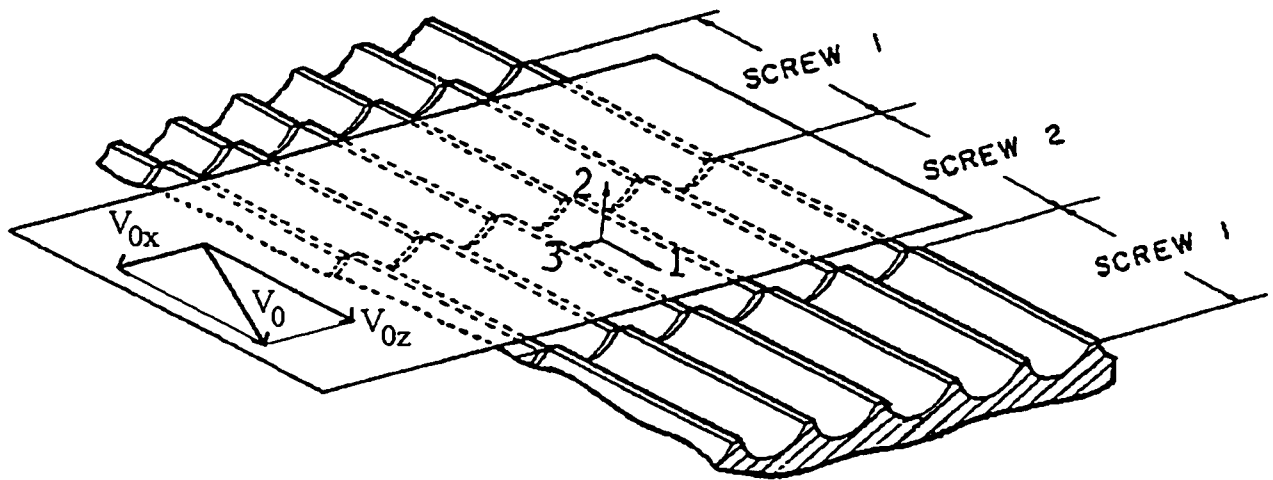


Figure 3.3: Groove Model Geometry

the flight width exceeded half the maximum channel width.

Wang and White (1989) extended previous models to non-Newtonian flow, by considering isothermal power-law fluid flow in conveying screw elements. Screw characteristic curves were computed both by a modified FAN method (with fluid viscosity a function of the down-channel and cross-channel velocity gradients) and by a conventional finite element method (with fluid viscosity a function of all velocity gradients) for comparison. The results showed a difference of no more than 10% between the two methods (the modified FAN method had the advantage of requiring much less computer time). The screw curves indicated a sharp decrease in pumping capability as the power-law coefficient decreased. It was concluded that shearing in directions parallel to channel cross-sections can be neglected in calculating the pumping characteristics of conveying screw elements for non-Newtonian fluids in CSCO extruder channels.

Wang et al. (1989) considered isothermal power-law fluid flow in reverse conveying screw elements, and presented screw characteristic curves for the elements. Results were analogous to those for forward conveying elements, in that as the power-law coefficient decreased the pressure dissipation capacity of the elements decreased sharply. The effects of the intermeshing region channel shift and the size of the radial flight clearance on the pumping capacity of forward conveying elements for isothermal power-law fluids was also examined. Results indicated that decreasing the flight clearance increases pumping capacity, due to a drop in leakage over the screw flight tips, and that as found in Szydlowski and White (1987), the effect of the tip width on conveying capacity is small up to a value of half the maximum channel width.

Potente et al. (1990) took a different approach from previous authors to modeling the conveying capacity of CSCO conveying screw elements. Here the authors directly extended

existing relations between dimensionless flow rate and pressure gradient for isothermal flow of power-law fluids in SSE screws, to CSCO forward conveying screw elements, taking advantage of the similarity of conveying characteristics between the two systems. The relations are simple algebraic expressions which approximate numerically determined screw characteristic curves in dimensionless form for SSE screws. They take the following form:

$$\pi_v = \phi_1 - \phi_2 \pi_p \quad (3.2)$$

Here π_v and π_p are the dimensionless flow rate and pressure gradient respectively. The coefficients ϕ_1 and ϕ_2 are functions of the screw element geometry and the fluid power-law parameters. The form of the equation expresses the opposing actions of drag and pressure flows, with drag flow (represented by the first term on the right-hand side) working to move material downstream and pressure backflow (represented by the second term) opposing this. The approximation equations were derived for two-dimensional (2D) channel flow (i.e. including the cross-channel component); the rounded self-wiping channel profile was represented as a rectangular profile with depth equal to the true average channel depth; and in calculating the total pressure change in an element the presence of a screw flight in the intermeshing region was modeled as a reduction in the channel width there. The authors performed experimental studies to compare measured melt pressures in a CSCO extruder with predicted values, and found the agreement between the two to be quite good.

In Potente et al. (1994), the authors extended their model further, by accounting for the effect of leakage flows over the screw flights on the pressure development in the flow of power-law fluids in conveying screw element channels. This was done by representing the net throughput at any axial position in the extruder as the sum of flows parallel and perpendicular to the screw

flights. The flow in the flight clearance region between the tops of the screw flights and the barrel surface was modeled as one-dimensional (1D) flow (i.e. with no transverse circulation component). The authors also presented an approximation equation for the conveying performance of reverse conveying elements, in the same form as equation (3.2).

Huneault and Dumoulin (1994) took another markedly different approach to modeling melt conveying in CSCO conveying screw element channels, one which used more realistic boundary conditions for computation of the flow field in the channels. Their basic argument was that the conventional groove model assumption for modeling melt flow in CSCO screw element channels fails to capture the true effect of the intermeshing region channel shift on pressure development. In reality, the melt flow in the extruder results from a combination of positive displacement of the channel volume, drag flow in the upstream direction due to screw rotation, and pressure flow due to pressure differences. For an observer standing in the intermeshing region and advancing with it as the screws rotate, the flow is clearly going backward. Thus, the flow restriction in the intermeshing region restrains the backwards drag and pressure flows, and hence leads to an increase in pumping capacity, not a decrease as predicted by the groove model with the screws stationary and the barrel moving. The throughput across a lateral cross-section (perpendicular to the extruder axis) is equal to the positive displacement rate due to the translation of the channel free volume minus the upstream flow rate in the moving frame of reference:

$$Q_{Net} = \frac{n_0}{60} t A_{Free} - k Q_{Back} \quad (3.3)$$

The authors presented the results of fully three-dimensional finite element simulations of flow of Newtonian and power-law fluids in curved screw channels with rectangular profiles, including

flow through an intermeshing region between two channels with flow reorientation and a channel shift of either zero or half the channel width. The flow reorientation was not found to have a significant effect on pressure growth, but the screw element with the shifted channel geometry was found to have significantly higher pressurization capacity than the element without the channel shift, around 25% higher for both Newtonian and non-Newtonian fluids. Unfortunately, the authors did not go so far as to present approximation equations for their screw characteristic curves covering different screw helix angles and material power-law indices, so the promising results of this paper cannot be applied in a macroscopic composite model of CSCO extrusion.

Michaeli et al. (1995) presented a model for reactive melt extrusion in a CSCO extruder with screws comprised only of forward conveying screw elements. The reactions examined involve bulk polymerization from monomer, and the flow was modeled as non-isothermal and non-Newtonian, with the viscosity a function of molecular weight, temperature, and shear rate. The conveying model was an extension of that for SSEs, with the channel shift in the intermeshing region neglected and leakage flows over the screw flights included but assumed to not affect velocity profiles within the channels. An energy balance was performed on the melt stream, accounting for viscous dissipation in the bulk, heat exchange with the barrel wall, and released heat of reaction. An ideal pipe reactor model was used for modeling residence time in the extruder, for calculation of the conversion profile.

3.2.3 Macroscopic Modeling of Melt Conveying in Kneading Block Elements

Due to the greater complexity of the flow mechanisms in kneading block elements, until the late 1980's their modeling treatment was almost entirely neglected. Szydlowski et al. (1987)

first addressed the problem, examining isothermal creeping flow of a Newtonian fluid in a kneading block element. The pressure and flow distributions in the different gaps between the individual discs were computed for various angles-of-stagger by a modified FAN approach. Results indicated that the staggering of the kneading discs creates a helical channel resembling that of a poorly designed screw section, with a comparatively large pitch and gaps in the channel flights (i.e. the radial gaps between discs due to stagger) through which leakage flows occur.

White and Szydlowski (1987) summarized the pumping performance of kneading block elements by means of equivalent screw characteristic curves. These showed that pressure development is much weaker in kneading disc assemblies than in conventional conveying screw elements. Also, as the number of discs in a kneading block is increased, the pumping capacity of the element is increased.

Wang et al. (1989) extended the previous results to isothermal power-law fluid flow in kneading block elements. They found that as the material power-law index was reduced, pressure fields were much reduced in intensity, and in the same way as for conveying screw elements, the pumping capacity of kneading block elements decreased. The effect of the angle-of-stagger was also examined, with the result obtained that pumping capacity decreases with increasing angle-of-stagger, which is commensurate with the accompanying increase in the size of gaps for leakage flows.

Potente et al. (1994) modeled the conveying capacity of kneading blocks by taking advantage of the conclusion of Szydlowski et al. (1987) that kneading blocks can be represented as equivalent screw elements. Leakage flows through the radial gaps between adjacent kneading discs were accounted for in their model by assuming a larger radial flight clearance in the

equivalent screw element. The screw pitch was calculated from the angle-of-stagger, the number of discs and the disc thickness in the kneading block, and the increase in the radial flight clearance was found by summing the areas available for the leakage flows between the discs and averaging the total over the equivalent flight length.

Michaeli and Grefenstein (1996) modeled the conveying capacity of kneading block elements by representing the element as having both a main and a back conveying channel (representing the leakage flows), each with different pitches and cross-section areas.

3.2.4 Modeling of Solids Conveying and Melting

The modeling of solids transport and melting in CSCO extruders has only recently begun to receive full treatment in the literature. The first solids melting model to appear in the literature was that of Potente et al. (1994). The authors extended the analogy between the operation of SSEs and CSCO extruders one step further, and assumed that the characteristic contiguous solids melting mechanism that is observed in SSEs (as shown in Figure 2.4) also exists in tightly intermeshing co-rotating twin-screw extruders. The well known Tadmor melting model for tracking the change in the solid bed width along the helix was modified to account for the rounded self-wiping channel profile. The authors made no allowance for the flow rearrangement and enhanced shearing that take place in the kneading block sections of an extruder.

Bawiskar and White (1995) dispelled the assumed melting mechanism of the above authors, in their examination of the melting of polyethylene pellets in a modular CSCO extruder with a central kneading block section. The experiments were performed by running the extruder to steady-state, stopping the screws, allowing the machine to cool, and then removing the screws

and stripping the solidified polymer off the screws for inspection. The primary result was that the melting occurring in the kneading block regions of the extruder differs considerably from melting in single-screw extruder screw channels. When forward staggering was used on the kneading discs, a central pellet bed was observed which moved along the screw helices and rapidly shrank. The surrounding melt exhibited much shorter residence times in the extruder than the pellet bed, leading the authors to hypothesize that the tips of kneading discs block the progression of portions of the solid bed, resulting in higher residence times in the kneading block region and faster melting. For neutral and reverse staggering of the kneading discs, melting was observed to take place even sooner than for forward staggering, due to increased filling levels, and no pellet bed was observed to form.

Potente and Melisch (1996) described similar experiments examining melting of polyethylene and polypropylene pellets in a CSCO extruder. They too reported observing unmelted compacted solid particles dispersed within a melt matrix in the kneading block section of their machine. Following from this observation, they presented a mathematical model of the melting of pellet form polymers, which assumes the solid particles to be spheres uniformly distributed in the polymer melt. Melting is considered to begin at the position where the solid particles, in their tightest packing, are completely surrounded by melt, and then viscous dissipation within the melt drives the melting process to completion. The model allows the polymer pellet radii to be computed against down-channel position. Calculated solid volume fractions were compared to experimentally determined values for two systems, and the model was found to adequately reproduce the true system behaviour.

Bawiskar and White (1995) also examined conveying mechanisms of solid polymer pellets,

in flow visualization experiments of a starved-fed CSCO extruder in a custom-made transparent barrel. In regions of conveying screw elements, the conveying mechanism was seen to be primarily forced conveyance, with the pellets being transported in the upper intermeshing region of the screws for low feed rates or high screw speeds. At higher feed rates or lower screw speeds, the material began to overflow the upper intermeshing region in the direction of screw rotation into the lower screw channels. The conveying regime ended when the pellets fused together after being softened by heat conducted from the barrel surface. The fused masses moved helically through the screw channels while being pushed ahead by forced conveyance, until a kneading block element was reached and the screws became fully-filled.

Potente et al. (1996) presented the first mathematical model for solids conveying in a CSCO extruder. The authors described three different solids transport regimes in conveying screw elements at increasing throughputs, each characterized by its own material distribution pattern in the screw channels. The transport mechanism was forced conveyance, and even at conditions of maximum throughput the screw channels remain only partially-filled. The detailed model presented by the authors permits calculation of the maximum conveying capacity of the feed zone of an extruder, the torque requirements of the different transport regimes, and even the solid pressure distributions that arise within the compressed zones of material accumulation. Experimental measurements of maximum conveyable material throughputs were reported for an extruder using several different materials, screw speeds, and screw pitches, and predicted values were found to correlate well with these parameters.

3.2.5 Composite Macroscopic Models of Modular CSCO Extruders

The ultimate objective of the modeling of the individual process phenomena that take place in a CSCO extruder is to be able to combine the individual models into a composite model completely describing the macroscopic processing performance of the extruder. To date only steady-state process models have been proposed; no transient models of flow phenomena in co-rotating twin-screw extruders have been published.

The first CSCO extruder composite model was given by White and Szydowski (1987), for the isothermal conveyance of a Newtonian melt in a modular twin-screw extruder comprised of forward and reverse conveying screw elements and kneading block elements. Working backwards from the die, with the throughput held constant between consecutive elements, the pressure change across each element was calculated by the element characteristic equation, represented by the authors as an algebraic relationship between throughput, screw speed, and pressure change. Gauge pressure values of zero indicated starvation (i.e. partial-filling) in the corresponding elements.

Wang et al. (1989) proposed a composite model of isothermal melt extrusion of a viscous power-law fluid, with the calculation algorithm the same as above, only with the pumping capacities of the extruder elements computed numerically using the modified FAN approach to solving the momentum balance equation. Results for a filling level experiment on a complete modular twin-screw extruder were given, and the predicted locations of the onset of complete filling from a simulation of the system were found to fall close to the positions actually observed. White et al. (1990) provided further results of filling level experiments for comparing with simulation results from the above model. The actual filling profiles were compared to predictions for three different screw configurations and two different materials (at single values of screw speed

and throughput) and agreement was found to be quite good.

Chen and White (1994) described a composite process model for non-isothermal power-law flow in a CSCO extruder with multiple feeds and vents. The throughput at any position in the extruder was the sum of feed rates through all upstream feed ports less the sum of removal rates through all upstream vents. The fluid viscosity was taken as temperature dependent, and a stream enthalpy balance was used as the energy balance equation, with terms for heat conduction from the barrel and viscous dissipation included. The temperature profile was coupled to the pressure and filling level profiles through the temperature dependent fluid viscosity, and so an iterative solution procedure was employed. Simulation results for a range of model parameter values were observed to qualitatively correspond to expectations.

The most complete published composite process model for CSCO extrusion to date is that of Potente et al. (1994), which covers plasticating non-isothermal extrusion of a material with power-law melt rheology in a modular extruder. The model allows computation of pressure, filling level, temperature, and melting profiles within the extruder. The solids melting model is a modified Tadmor contiguous solids model, which since publication has been shown to be incorrect. The melt conveyance model is based on Potente et al. (1990), and accounts for the effects of leakage flows over the screw channel flights and the channel shift in the intermeshing region. The filling level profile is calculated by assuming that in partially-filled screw sections the fraction of free volume occupied by the melt is equal to the fraction the throughput is of the drag flow capacity of the element. The temperature profile is calculated by an energy balance on the melt stream, which accounts for viscous dissipation in the bulk and conduction between the melt and the barrel wall, but does not consider the contribution of leakage flows. The temperature

dependence of the viscosity again necessitated an iterative solution algorithm, in which the pressure, filling level and melting profiles were all computed using the temperature profile from the previous iteration, following which the temperature profile was recalculated. Comparison between calculated and experimental values of pressure and temperature in an extruder showed reasonable agreement.

3.2.6 Modeling of Reactive Extrusion of Polypropylene With Peroxide-Initiated Degradation

Publications in which extruder process models are extended to include chemical reaction are rare in the literature. A fully-predictive mathematical model for controlled degradation of PP in a plasticating single-screw extruder was given in Tzoganakis et al. (1988a). The model is based on a free radical kinetic mechanism for the peroxide-initiated degradation reaction and on conventional plasticating extrusion theory. Solids conveying, melting, melt pumping, and reaction phenomena were combined, and interactions between flow pattern and mass and heat transfer fields via the residence time distribution and the chemorheology of the reactive melt were considered. For a given REX system, the model can predict the extruder throughput, profiles of pressure, temperature, and molecular weight along the screw channels, and the residence time distribution. Model predictions were shown to be in satisfactory agreement with experimental data from runs on an extruder at several peroxide levels and screw speeds.

For CSCO extruders, the first publication to appear in the literature dealing with modeling of PP peroxide-initiated reactive degradation processes was that of Kim and White (1997). The authors extended the composite process model of Chen and White (1994) for non-isothermal

extrusion of a power-law melt to include the degradation reaction. Their model included a kinetic model for the reaction, as well as for thermal degradation of PP. The solution procedure was described in which the extent of the degradation reaction in each screw element was calculated from the average residence time and temperature there. It was claimed that the melt viscosity in each element was computed using the molecular weight profile generated by the reaction calculations, yet data on the molecular weight dependence of the fluid rheological parameters were not given, and the effect of the reaction on the calculated degree of freedom profiles in the extruder was not demonstrated. In fact, in the PhD dissertation of the first author (Kim, 1996) on which the paper was based, there was no mention whatsoever of the coupling of the reaction routine calculations to the computations of the other process DOFs. This claim, therefore, is doubtful. Computed molecular weight profiles were given for simulations using four different screw configurations, four peroxide throughputs, and five screw speeds. The observed trends conformed to expectations, but predicted extrudate molecular weights were found to consistently overshoot experimental values.

3.3 CSCO Extrusion Process Model

The two major composite macroscopic process models for non-reactive CSCO extrusion are those of J.L. White and co-workers at the University of Akron, Ohio, and that of H. Potente and co-workers at the University of Paderborn, Germany. Between the two of these, the choice was made to use the latter model, since it is the most complete and the best documented in the open literature, and in particular for calculating the conveying capacity of screw elements, it is the easiest to implement, thus reducing the possibilities for errors. The composite model outlined in

this section is principally based on that of Potente et al. (1994), and covers plasticating non-isothermal extrusion of a power-law material, with extensions to include leakage flows over the screw flight tips in fully-filled zones, the contribution of the radial flight clearance to total channel depth, and the effect on melt flow of the presence of unmelted solids in the screw channels in the plastication zone. A kinetic and chemorheological model of peroxide-initiated controlled degradation of PP is also included. The complete model, when solved, yields profiles of average values of pressure, filling level, melt temperature, solid volume fraction, and PP molecular weight along the extruder axis for a modular CSCO extruder. The models for the different process phenomena are outlined in the following subsections, along with equations for calculating the different degree of freedom profiles. The basic assumption behind all models is the applicability of the groove model, that is that the curvature of the screws and barrel can be neglected, and the screws viewed as stationary and the barrel moving. As well, in each model the polymer melt is modeled as a purely viscous fluid, and the rounded self-wiping channel profile in the channel cross-section perpendicular to the screw flights (shown in Figure 3.2) is replaced by a rectangular profile with the same channel width and cross-section area.

3.3.1 Solids Melting

The melting model used is based on the dispersed solids melting model for pellet form solids of Potente and Melisch (1996). The basic assumptions of the model are that the solid particles are perfect spheres of equal radius at every cross-section position, arranged in a lattice with cubic face-centred packing. Hot melt fills the interstitial spaces between the particles, and the heat source of viscous dissipation in the melt provides the energy to melt the solids. Interaction of

temperature fields between adjacent particles is neglected, i.e. an undisturbed temperature field is assumed to exist in the melt around each particle, with the melt just at the fusion temperature at the particle surface and at the bulk temperature at infinite distance from the particle surface. Sensible heating of the solid particles from their entering temperature to the fusion temperature is also neglected. The mathematical model allows calculation of the diminishing particle radii and solid volume fraction along the channel direction.

The equation for the change of particle radius in the helical direction is derived by setting the heat flux at the particle surface from the melt phase (calculated by differential energy balance) equal to the rate of enthalpy increase per unit surface area in the particle by melting, and solving for the unknown downstream particle radius in terms of the known upstream value. The resultant equation is (see the Nomenclature for a description of each variable):

$$r_{P1} = r_{P0} - \frac{\lambda}{\rho c_P} \frac{b_{Max}(\bar{h} + s_R)}{[\dot{V}_{Z,Melt}/(1-F_S)]r_{P0}} \ln \left[\frac{\rho c_P (T_{Bulk} - T_M)}{\rho_S \Delta H_F} + 1 \right] \Delta z \quad (3.4)$$

Here $\dot{V}_{Z,Melt}$ is the melt volumetric flow rate in the channel, and F_S the solid volume fraction. The position of the start of melting is defined as the first position downstream of the feed port where the channel becomes completely filled and the barrel temperature exceeds or equals the material fusion temperature. It is assumed that at this point the melt just fills the spaces between the solid particles at their original sizes.

The solid volume fraction profile along the extruder axis is computed from the particle radius profile. At the position of the start of melting, the solids fraction is found by consideration of the packing of the spheres in the screw channel, as shown in Figure 3.4, with simplifications to account for the rounded channel profile. The initial solids fraction is also corrected for the non-

spherical particle shape by using the solid bulk density. Downstream of this point, the solids fraction is found by dividing the total volume of the modeled solid particles by the open channel volume, and again correcting for the particle shape:

$$F_S = \left(\frac{N_P}{\Delta z} \right) \frac{4\pi r_P^3}{3b_{Max}(\bar{h} + s_R)} \cdot \frac{\rho_{Bulk}}{0.74\rho_S} \quad (3.5)$$

3.3.2 Melt Conveying and Pressurization

The melt pumping capacity of fully-filled conveying screw elements and kneading blocks in conveying power-law melts is modeled as in Potente et al. (1994), using algebraic equations which approximate families of screw characteristic curves determined for different power-law index values and element helix angles. As previously mentioned, the original screw characteristic curves were determined by numerical solution of the equations of motion for isothermal viscous flow of a power-law fluid in the channels of single-screw extruders. The assumptions made in the modeling were as follows:

- incompressible fluid
- fully-developed, steady laminar flow
- no body forces or fluid inertia
- no slip between fluid and channel walls
- rectangular channel cross-sections
- large channel aspect ratio

The last assumption allows the effect of the screw flights on the velocity profiles in the channels to be neglected. The result is that the flow in the channel cross-section is modeled as two-

dimensional parallel flow between the barrel and screw root surfaces, with the down- and cross-channel velocity profiles independent of cross-channel position. This is known as the lubrication approximation, because of its utility in the modeling of lubrication systems (Middleman, 1977).

The screw characteristic curve approximation equations are extended for use with CSCO extruder screw elements by representing the rounded self-wiping channel profile as a rectangular profile having the average channel depth, and by adding a factor of geometry to the definition of the dimensionless flow rate to account for the reduction in channel width in the intermeshing region due to the presence of a screw flight there. Figure 3.5 shows the shape of numerically determined dimensionless screw characteristic curves for different values of the power-law index for a particular screw geometry, with the assumption of one-dimensional flow (i.e. no cross-channel flow) (Potente et al., 1990). The curves for 2D flow are of a similar shape, only they do not all cross the line of $\pi_p=0$ at $\pi_{\dot{\gamma}}=1$. As can be seen, the curves for power-law indices close to 1 are essentially linear over the entire range of $\pi_{\dot{\gamma}}$ values shown, and even for lower values of n the curves are linear in the central region of the graph, around $\pi_{\dot{\gamma}}=1$. The Potente approximation equations for these curves simply express dimensionless flow rate as a linear function of dimensionless pressure gradient, with the slope and intercept coefficients calculated from the material power-law index and the screw element helix angle. For 2D flow the equation is:

$$\pi_{\dot{\gamma}} = \phi_1 - \phi_2 \pi_p, \quad \phi_1 = \frac{0.3486(1-n) + (0.5229 + 0.4455n) \left(2 - \cos \phi_S - \frac{1 - \cos \phi_S}{n^{0.94} \cos^{1-n} \phi_S} \right)}{\cos^{1-n} \phi_S} \quad (3.6)$$

$$\phi_2 = \frac{0.5229 + 0.4455n}{n^{0.94} \cos^{2(1-n)} \phi_S} \quad 0 < n \leq 1 \quad 0 < \phi_S < \pi/2$$

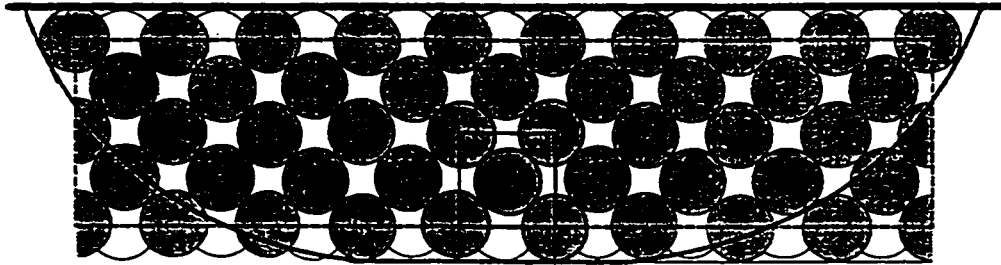


Figure 3.4: Solids Melting Model Assumed Particle Packing

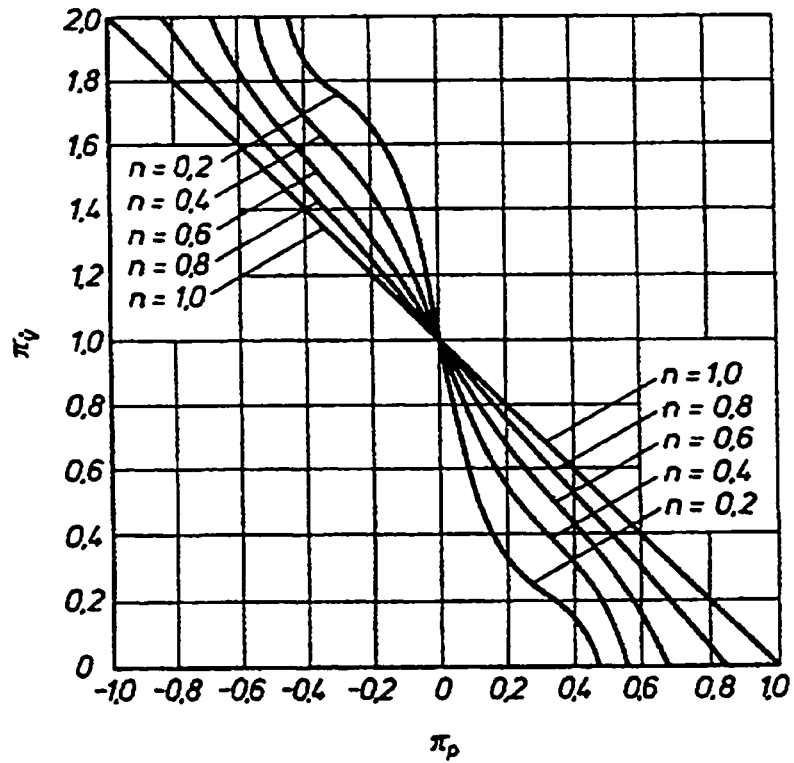


Figure 3.5: Dimensionless Screw Characteristic Curves for One-Dimensional Flow of Power-Law Fluid

The ranges of applicability of equation (3.6) are:

$$\begin{aligned}
 0.2 < n < 0.5: \quad & 0.3 < \pi_{\dot{v}} < 1.7 \\
 0.5 < n \leq 1: \quad & 0.1 < \pi_{\dot{v}} < 1.9 \\
 \frac{a}{D_s} \geq 0.85 \quad & \frac{t}{D_s} \leq 1.6
 \end{aligned} \tag{3.7}$$

The limit on the ratio of the centreline separation of the screws to the screw diameter is the condition for applicability of the groove model, i.e. that curvature can be neglected.

The definitions of $\pi_{\dot{v}}$ and π_p in equation (3.6) differ depending on whether the equation is applied to the flow inside or outside the intermeshing region, or to the entire channel of a screw element. These definitions are:

$$\begin{aligned}
 \text{a) Free channel zone: } \pi_{\dot{v}} &= \frac{\dot{V}_{Z,Melt}}{\frac{1}{2} v_{0Z} b_{Max} (\bar{h} + s_R) (1 - F_S)} & \pi_p &= \frac{(\bar{h} + s_R)^{1-n} \cdot \Delta p_F}{6K v_{0Z}^n (1 - F_S) Z_F} \\
 \text{b) Intermeshing zone: } \pi_{\dot{v}} &= \frac{\dot{V}_{Z,Melt}}{\frac{1}{2} v_{0Z} (b_{Max} - e_{Max}) (\bar{h} + s_R) (1 - F_S)} & \pi_p &= \frac{(\bar{h} + s_R)^{1-n} \cdot \Delta p_I}{6K v_{0Z}^n (1 - F_S) Z_I} \\
 \text{c) Screw element} & : \pi_{\dot{v}} = \frac{\dot{V}_{Z,Melt}}{\frac{1}{2} v_{0Z} b_{Max} (\bar{h} + s_R) (1 - F_S)} F & \pi_p &= \frac{(\bar{h} + s_R)^{1-n} \cdot \Delta p_{Ele}}{6K v_{0Z}^n (1 - F_S) Z_{Ele}}
 \end{aligned} \tag{3.8}$$

$$F = \frac{Z_F + Z_I \frac{b_{Max}}{b_{Max} - e_{Max}}}{Z_F + Z_I} \quad \Delta p_{Ele} = \Delta p_F + \Delta p_I \quad Z_{Ele} = Z_F + Z_I$$

The definitions for the screw element follow from defining the total pressure change over the element as the sum of the changes in the free channel and intermeshing regions. The presence of the radial flight clearance above the channel is reflected as an increase in the mean channel depth beyond that given by integrating the self-wiping profile of equation (3.1) over the cross-section perpendicular to the flights. The term $(1 - F_S)$ represents the effective reduction in the channel cross-

section area for melt flow due to the presence of unmelted solids.

In calculating the total pressure change over a screw element, equation (3.8 (c)) is used, along with a material balance across the screw channels to calculate $\dot{V}_{Z,Melt}$, the melt volumetric flow rate in the channel parallel to the flights. The material balance is performed on a triangular prism section of the groove system, with faces perpendicular to the channel, parallel to the screw flight, and perpendicular to the extruder axis, shown in Figure 3.6 as the triangle ABC (Potente et al., 1994). The equation obtained is:

$$\dot{m} = k\dot{m}_Z \mp \dot{m}_X \quad (3.9)$$

The negative leading sign is for forward conveying screw elements, and the positive sign for reverse conveying elements. What this equation shows is that the effect of leakage flows in forward conveying screw elements is to increase the channel flow rate \dot{m}_Z , leading to a reduction in the pressurization capacity of the elements as part of the pumping effort is wasted. In reverse conveying elements the effect is just the opposite, with leakage flows decreasing the channel flow rate, which reduces the pressure drop necessary over the element to achieve a certain throughput as less material must be driven through the channels against the direction of drag flow.

In expanding equation (3.9), the leakage flows are modeled as 1D pure melt flows directed perpendicular to the screw flights, with a drag flow component from the barrel velocity component in that direction, and a pressure component due to the pressure gradient across the flights. The leakage flow rate \dot{m}_X is found by writing the approximation equation for 1D flow across the flight clearance (Potente et al., 1994):

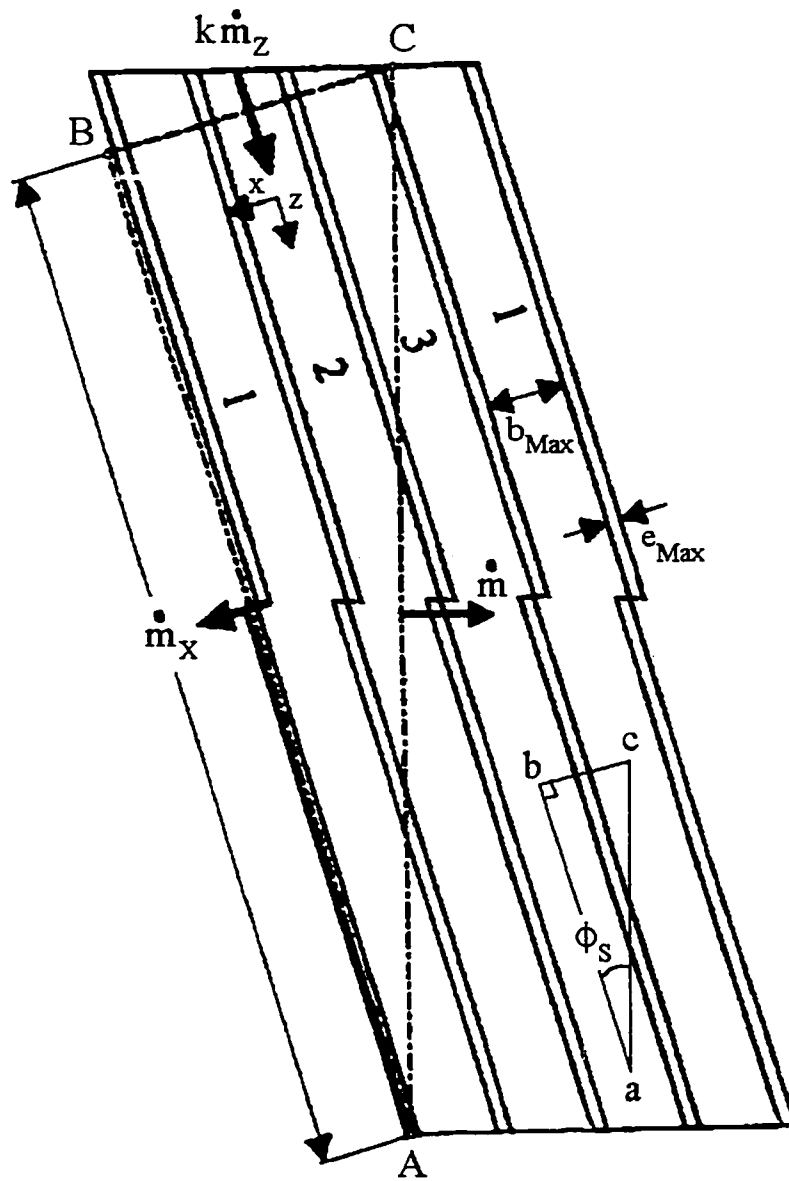


Figure 3.6: Leakage Flow Material Balance

$$\pi_{\dot{V}_{Gap}} = 1 - \frac{\pi_{P_{Gap}}}{n_{Gap}^{0.94}}, \quad \pi_{\dot{V}_{Gap}} = \frac{\dot{m}_X / \rho}{\frac{1}{2} v_{0X} b_{Thread} s'_R}, \quad \pi_{P_{Gap}} = \frac{(s'_R)^{1-n_{Gap}} \cdot \Delta p_X}{6K_{Gap} v_{0X}^{n_{Gap}} e_{Max}} \quad (3.10)$$

For kneading block elements the radial flight clearance used here is corrected to include the contribution from the radial gaps between adjacent kneading discs. The pressure difference across the flight clearance, Δp_X , is considered to arise because of the difference in axial positions between the channel cross-sections separated by the flight. The pressure in each cross-section is modeled as being uniform, and so pressure in the channels is a function of down-channel position only. Looking at the smaller triangle **abc** in Figure 3.6, Δp_X is the pressure difference between points b and c; the pressure at point c is the same as at point a, at the same axial position. Hence Δp_X can be expressed in terms of the free channel pressure gradient:

$$\Delta p_X = \mp \frac{\Delta p_F \cdot b_{Max} + e_{Max}}{Z_F \cdot \tan \phi_S} \quad (3.11)$$

Next the mass flow rate in the channels is expanded by expressing it as the sum of the solid and melt flow rates:

$$\dot{m}_Z = \rho_S \dot{V}_{Z,Solid} + \rho \dot{V}_{Z,Melt} = \left(\rho_S \frac{F_S}{1-F_S} + \rho \right) \dot{V}_{Z,Melt} \quad (3.12)$$

The melt flow rate in the channel is expanded using equation (3.6) and the dimensionless quantity definitions for the free channel region from equation (3.8 (a)):

$$\dot{V}_{Z,Melt} = \frac{1}{2} v_{0Z} b_{Max} (\bar{h} + s_R) (1 - F_S) \left[\Phi_1 - \Phi_2 \frac{(\bar{h} + s_R)^{1-n}}{6K v_{0Z}^n (1 - F_S)} \cdot \frac{\Delta p_F}{Z_F} \right] \quad (3.13)$$

Equation (3.9) is expanded using equations (3.10) to (3.13), yielding a long equation in one unknown, the free channel pressure gradient $\Delta p_F / Z_F$. Once this is calculated, $\dot{V}_{Z,Melt}$ is found from

equation (3.13), and then this value is substituted into the following equation, found by solving equation (3.6) for the pressure change, using the dimensionless quantity definitions for the screw element from equation (3.8 (c)):

$$\Delta p_{Ele} = \frac{6Kv_{0Z}^n(1-F_S)}{(\bar{h}+s_R)^{1-n}\phi_2} \left[\phi_1 - \frac{\dot{V}_{Z,Melt}}{\frac{1}{2}v_{0Z}b_{Max}(\bar{h}+s_R)(1-F_S)} F \right] Z_{Ele} \quad (3.14)$$

Equation (3.14) shows directly that an increase in the channel melt flow rate reduces the pressurization capacity of a conveying screw element.

The above results also apply to reverse conveying screw elements, only different definitions are used for the screw characteristic curve approximation equation coefficients (Potente et al., 1994):

$$\phi_1 = -\frac{0.31+0.69n}{n} e^{1-n} \quad \phi_2 = \frac{e^{1-n}}{n} \quad (3.15)$$

These coefficients are generic, for any element helix angle. As can be seen in equation (3.15), ϕ_1 is always negative, so for the dimensionless flow rate in equation (3.6) to be positive, the dimensionless pressure gradient must always be negative, meaning the pressure drops along the element.

The conveying capacity of kneading blocks is calculated by representing them as equivalent screw elements with comparatively large screw pitches, calculated from the disc angle-of-stagger, the number of discs and the disc thickness, and with large radial flight clearances to reflect the large leakage flows in the radial gaps between the discs. Figure 3.7 shows part of an end-on view of a kneading block element with four bilobal discs staggered at an angle of 45°, showing the radial gaps between the discs (Potente et al., 1994). The increase in the radial flight clearance of

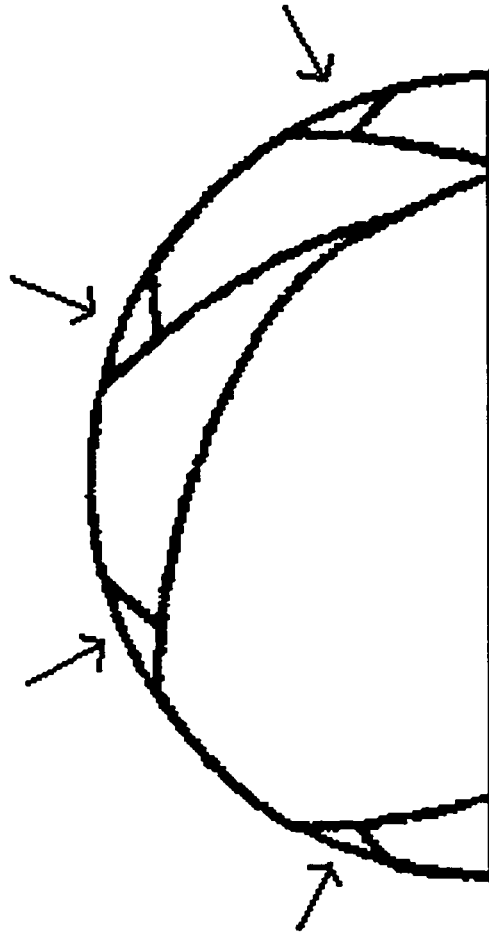


Figure 3.7: Kneading Block Section
Highlighting Radial Gaps

the equivalent screw element is found by summing the areas of the radial gaps and dividing this by the total length of the screw element flight outside the intermeshing region.

3.3.3 Material Distribution in Extruder Channels

The distribution of material in the extruder channels is indicated by the filling level profile, which shows the fractional approach to complete filling at each axial position in the extruder. The degree-of-fill of a screw element is computed differently depending on whether the element is in the solids conveying or melt conveying zone of the extruder. In the solids conveying zone, following from Bawiskar and White (1995) and Potente et al. (1996), the transport mechanism is assumed to be forced conveyance, and so the filling level is the minimum possible value, which gives the minimum residence time in the element. The degree-of-fill is calculated as the solids volumetric throughput divided by the volume swept by the screw flights per second:

$$f_{Min} = \frac{\dot{m}/\rho_{Bulk}}{(n_0/60)tA_{Free}} \quad (3.16)$$

The pressure dependence of the solids bulk density is ignored here.

In the melt conveying zone, the degree-of-fill is computed in elements for which the pressure at both ends is found to be atmospheric, which indicates partial-filling. The degree-of-fill is found by dividing the dimensionless flow rate in the element by the maximum possible dimensionless flow rate for pure drag flow (Potente et al., 1994):

$$f = \frac{\pi_{v_{Etc}}}{\phi_1} \quad (3.17)$$

Definitions are taken from equations (3.6) and (3.8 (c)). The possibility of leakage flows over the

screw flights is ignored for partially-filled zones, and so from equation (3.9) the melt flow rate in the channel is given by:

$$\dot{V}_{Z,Melt} = \frac{\dot{m}/k}{\rho_s \frac{F_s}{1-F_s} + \rho} \quad (3.18)$$

3.3.4 Melt Temperature Change

The melt temperature profile in the screw channels is computed by solution of an energy balance on the channel flow, following Potente et al. (1994) and Potente and Melisch (1996), which accounts for heating from the barrel surface and heat generation by viscous dissipation in the melt. The channel flow is modeled as plug flow in the down-channel direction only, and no cross-channel temperature gradients are considered to exist. A differential energy balance is performed over a fluid element of differential length in the helical axis direction, differential depth, and width equal to the effective channel width. Consideration of solids in the channel is minimized - they are assumed to affect the cross-section area available for flow of the melt, but not the temperature profile in the melt. The effect of the melting of the solids is deferred for later consideration. The resulting equation (with boundary conditions) is:

$$\rho c_p \bar{v}_z \frac{\partial T}{\partial z} = \lambda \frac{\partial^2 T}{\partial y^2} + \eta \bar{\dot{\gamma}}^2 \quad \begin{array}{l} T|_{y>0, z=0} = T_0 \\ T|_{y=0, z>0} = T_B \\ T|_{y=\infty, z>0} = T_0 \end{array} \quad (3.19)$$

Here the fluid viscosity is assumed constant, and so the length of channel over which equation (3.19) can be applied is limited. The boundary conditions specify that at the inlet to the screw channel the temperature profile is uniform, and that downstream of the inlet the fluid temperature

profile perpendicular to the barrel surface develops as in a semi-infinite space, with the temperature fixed at the barrel value at the channel top, and remaining at the initial value at infinite depth.

The plug flow velocity is calculated based on entering conditions:

$$\bar{v}_Z = \frac{\dot{V}_{Z,Melt,0}}{\bar{b}(\bar{h}+s_R)(1-F_{SO})} \quad (3.20)$$

The average channel depth and width in equation (3.20) are the equivalent rectangular dimensions of the filled portion of the channel cross-section, computed from the channel self-wiping profile and consideration of the position of the melt free surface in the channel. In this way allowance is made for the filling level profile in the calculations. Equation (3.20) also includes the effect of the presence of unmelted solids on the effective open channel area for melt flow.

The value of the average shear rate used in equation (3.19) is the nominal shear rate in the channel for pure drag flow, which is also used in the computation of the fluid viscosity from the power-law equation. This shear rate is:

$$\bar{\dot{\gamma}} = \frac{v_0}{\bar{h}+s_R} \quad (3.21)$$

This approach differs from that of Potente and Melisch (1996), who assumed that unmelted solids in the channel increase the average shear rate by reducing the effective average channel depth by a fraction equal to the solid volume fraction in the channel. This is equivalent to saying that the solids affect the melt as if they adhered to the screw surface in a continuous solid bed. This, however, contradicts published visualization results for the motion of solids in the plastification zone of CSCO extruders, including those of the same authors. The solid particles probably do

cause an increase in the mean channel shear rate, but in an unknown way, so the effect is neglected here.

Equations (3.20) and (3.21) are substituted into equation (3.19), and then the result is expressed in terms of dimensionless variables to yield:

$$\frac{\partial^2 \theta}{\partial \xi^2} - Gz \frac{\partial \theta}{\partial \zeta} = -Br \quad \begin{array}{l} \theta|_{\xi>0, \zeta=0} = \theta_0 \\ \theta|_{\xi=0, \zeta>0} = 0 \\ \theta|_{\xi=\infty, \zeta>0} = \theta_0 \end{array} \quad (3.22)$$

Here Gz and Br represent the Graetz and Brinkman numbers respectively. The variable definitions are:

$$\theta = \frac{T - T_B}{T_B}, \quad \xi = \frac{y}{\bar{h} + s_R}, \quad \zeta = \frac{z}{Z}, \quad Gz = \frac{\rho c_p \dot{V}_{Z, Melt, 0} (\bar{h} + s_R)}{\lambda b Z (1 - F_{S0})}, \quad Br = \frac{K v_0^{1-n} (\bar{h} + s_R)^{1-n}}{\lambda T_B} \quad (3.23)$$

Equation (3.22) has a known analytical solution. The area average melt temperature at the end of a screw channel section is found by integrating this solution over the channel cross-section:

$$\bar{\theta} = \theta_0 \left[1 - \operatorname{erfc} \left(\frac{1}{\sqrt{4\zeta/Gz}} \right) - \sqrt{\frac{4\zeta}{\pi Gz}} (1 - e^{-\frac{1}{4\zeta/Gz}}) \right] + \frac{Br}{6} \sqrt{\frac{4\zeta}{\pi Gz}} \left[\left(1 + \frac{4\zeta}{Gz} \right) e^{-\frac{1}{4\zeta/Gz}} - \frac{4\zeta}{Gz} \right] + \frac{Br}{4} \frac{4\zeta}{Gz} - \left(\frac{Br}{6} + \frac{Br}{4} \frac{4\zeta}{Gz} \right) \operatorname{erfc} \left(\frac{1}{\sqrt{4\zeta/Gz}} \right) \quad (3.24)$$

Melt temperature calculations using equation (3.24) are begun at the end of the element in which melting is assumed to begin, according to the solids melting calculation routine. The fusion temperature of the polymer is taken as the initial melt temperature.

In the plastication zone of the extruder, the mean melt temperature given by equation (3.24) is further modified to account for the melting that takes place along the channel length of consideration. The effect of the melting process on the melt temperature is twofold, both from the

absorption of the heat of fusion by the solids in melting, and by the consequent addition of (relatively cold) melt at the polymer fusion temperature to the stream. It is assumed that the melting that takes place in the channel section takes place instantaneously as the stream crosses the exit plane of the section, and so a stream enthalpy balance is performed on the two-phase streams on opposite sides of the plane, with the exiting melt temperature represented by a mixing cup temperature. The result is:

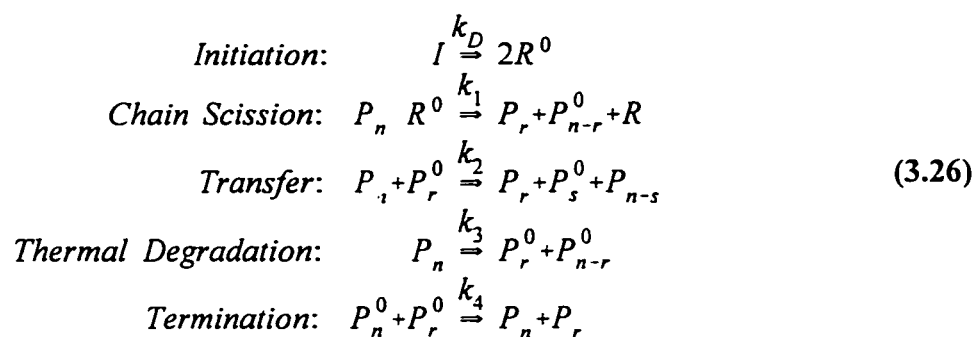
$$T'_Z = \frac{\rho_S \frac{F_{Sl}}{1-F_{Sl}} + \rho}{\rho_S \frac{F_{S0}}{1-F_{S0}} + \rho} \left(T_Z - T_M + \frac{\Delta H_F}{c_P} \right) + T_M - \frac{\Delta H_F}{c_P} \quad (3.25)$$

3.3.5 Peroxide-Initiated Controlled Degradation of Polypropylene

As mentioned before, when a peroxide free radical initiator is added to the polymer melt stream in the channels of a CSCO twin-screw extruder, in the high temperature conditions of the extruder the peroxide molecules are thermally decomposed into free radicals which initiate a random scission of the polymer chains. Longer polymer chains have a higher probability of being attacked by the peroxide radicals, and so a general decrease of the molecular weight of the polymer and a narrowing of the MWD result. This has the effect of reducing the polymer viscosity and elasticity, and thereby improving its processing characteristics. To model the effect of the peroxide on the rheological parameters of the PP, what are needed are the degradation reaction mechanism, a complete kinetic model for the reaction process, and correlations relating the dependence of the melt rheological parameters on the MWD of the polymer. Each of these is described in the

paragraphs below.

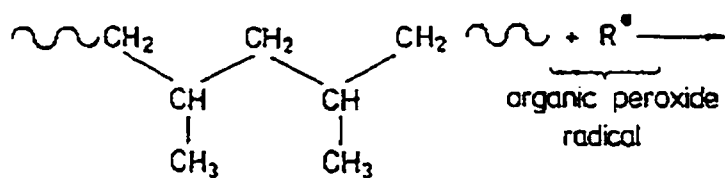
The generally accepted chemical mechanism for the chain scission reaction is shown in Figure 3.8 (Fritz and Stohrer, 1986). A peroxide radical first abstracts preferentially a tertiary hydrogen atom of the polymer main chain. The formed radical centre on the polymer chain is unstable due to steric hindrance from the methyl side group and as a result a molecular chain division (or β -scission) reaction takes place which creates a polymer molecule of smaller chain length. The complete free-radical mechanism of peroxide-initiated degradation of PP is given below (Tzoganakis et al., 1988b):



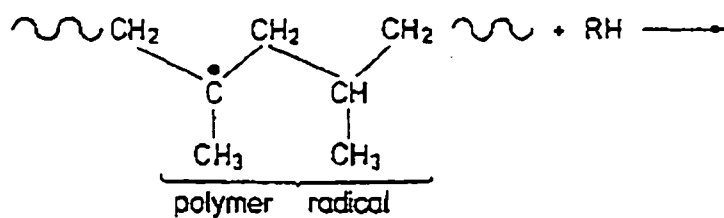
If a stabilizing agent has been added to the polymer, then the transfer reaction may be omitted from the mechanism. Also, the thermal degradation reaction is known to only be significant at high temperatures, greater than 240°C (Fritz and Stohrer, 1986).

The kinetic model for the degradation process comes from writing balances on all the species in equation (3.26). What results is an extremely large set of coupled nonlinear differential equations. The solution procedure considered here is that of Tzoganakis et al. (1988b), which involves simplifying the species balances by neglecting the contributions of the transfer and thermal degradation reactions, introducing definitions of the moments of the polymer and polymer

Radical attack



Hydrogen abstraction



Degradation (β - scission)

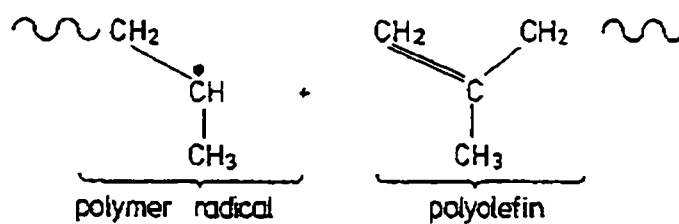


Figure 3.8: Polypropylene Chain Scission Reaction Mechanism

radical distributions to reduce the dimensions of the equation system, and assuming that the radical concentrations do not change with time (the stationary state hypothesis) to further reduce the number of equations. What results is a compact system of coupled differential equations in the peroxide concentration and the polymer MWD moments that can be solved numerically:

$$\begin{aligned}
 \frac{dI}{dt} &= -k_D I \\
 \frac{dQ_0}{dt} &= 2f_p k_D I \frac{Q_1 - 3Q_0}{Q_1 - Q_0} \\
 \frac{dQ_1}{dt} &= -2f_p k_D I \frac{2Q_0}{Q_1 - Q_0} \\
 \frac{dQ_2}{dt} &= 2f_p k_D I \frac{-Q_3/3 + Q_1/3 - 2Q_0}{Q_1 - Q_0}
 \end{aligned}
 \quad Q_i = \sum_{n=2}^{\infty} n^i [P_n]; \quad i=0,1,2 \quad (3.27)$$

The closure method of Hulbert and Katz (1964) is used to correlate the third moment of the polymer MWD, Q_3 , with the first three moments of the distribution:

$$Q_3 = \frac{2Q_2}{Q_1 Q_0} (2Q_2 Q_0 - Q_1^2) \quad (3.28)$$

Once the moment equations are solved, the average molecular weights of the polymer can be calculated by:

$$\begin{aligned}
 \bar{M}_N &= m_0 Q_1 / Q_0 \\
 \bar{M}_W &= m_0 Q_2 / Q_1 \\
 \bar{M}_Z &= m_0 Q_3 / Q_2
 \end{aligned} \quad (3.29)$$

The decomposition rate constant for the peroxide initiator is material dependent. In all simulations described in this chapter the peroxide data used is for 2,5-dimethyl-2,5-di-tert-butylperoxy hexane (Lupersol 101), a bifunctional dialkyl peroxide which is a low viscosity liquid at room temperature. The expression for its decomposition rate constant is (Tzoganakis et al.,

1988a):

$$k_D = 1.98 \times 10^{12} e^{-\frac{14947}{T-273.15}} \quad (3.30)$$

The half-life of the peroxide (the time for half the material in a sample to decompose) decreases rapidly above 200°C, from a value of 18.3 s at 200°C to 1.6 s at 240°C. The value of the peroxide efficiency (f_p in equation (3.27)) was determined to be approximately 0.6, by fitting the kinetic model equations given in equation (3.27) to experimental data from ampoule experiments at low peroxide concentrations (Tzoganakis et al., 1988b).

The final components of the degradation reaction model are correlations relating the dependences of the melt rheological parameters on the MWD of the polymer (i.e. the fluid chemorheology). For the PP resin that is to be simulated, samples of different extents of degradation must be prepared in the laboratory by treatment with increasing levels of peroxide in an extruder or batch mixer. The degraded samples as well as the virgin resin must then undergo molecular and rheological characterization. Molecular characterization involves measurement of the material MWD (most importantly the weight-average molecular weight), by a technique such as gel permeation chromatography. Rheological characterization is the experimental determination of the relationship between the shear viscosity of the molten material and shear rate, at several levels of temperature, using a device such as a capillary rheometer. With this data, regression formulas relating the power-law parameters of the PP melt to temperature and weight-average molecular weight can be generated.

3.4 Simulation Program

A computer program in the C language was written to solve the macroscopic composite

process model for the steady-state operation of a modular CSCO extruder presented in the previous section. Taking as inputs the extruder geometry and configuration, material hydrodynamic and thermodynamic properties, and operating conditions of the extruder, it computes profiles of average pressure, filling level, melt temperature, solid volume fraction, and PP weight-average molecular weight (for reactive extrusion application) along the extruder axis. The simulation algorithm is comprised of two nested loops: an inner loop, in which the pressure, filling level, temperature, and solid volume fraction profiles are computed consecutively in each iteration, and an outer loop, in which for PP reactive degradation processes the molecular weight profile of the polymer is computed for the extruder region downstream of the peroxide injection point, using the converged temperature and filling level profiles from the inner loop. Figure 3.9 shows a flow chart of the algorithm. Discussion of the major elements is given in the following subsections.

An important feature of the calculations is that they are carried out in an integer number of calculation zones within each screw element, each of which is assumed to behave as a separate screw element with the same channel geometry as the parent. The number of zones for each screw element is length dependent. This approach allows more precise positioning of where filling levels change in the elements, and also complies with the energy balance assumption that the length of channel over which temperature changes are computed is small.

3.4.1 Inputs

Program inputs are broken up into 3 categories: machine data, operating conditions, and material data. The machine data consists of the screw geometry and configuration, and the barrel configuration. The screw geometry parameters define the self-wiping cross-section profile: the

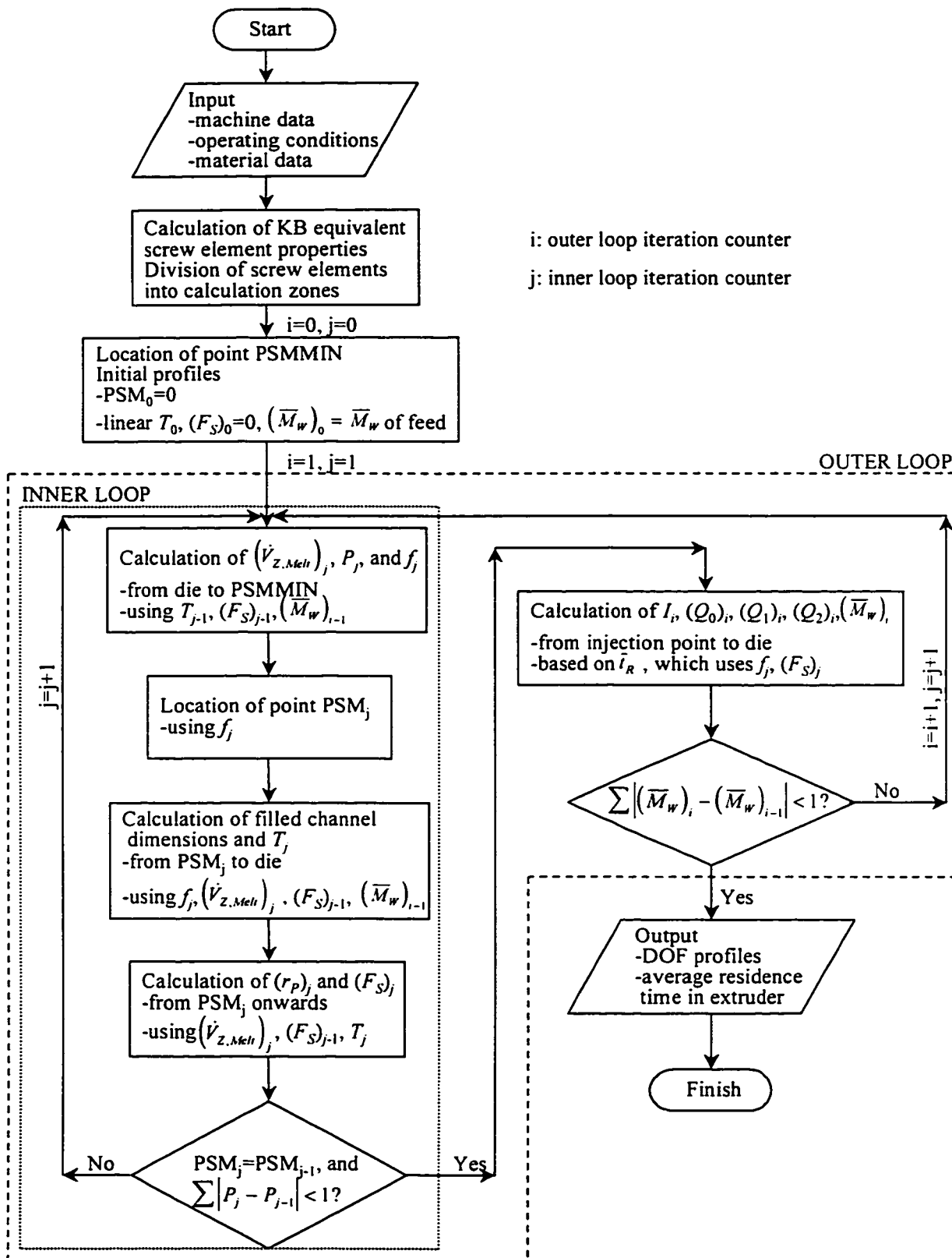


Figure 3.9: Simulation Algorithm Flow Chart

screw diameter D_s , the number of screw flights i , the radial flight clearance s_R , and either the centreline separation of the screws a or the maximum screw channel depth h_{max} . The barrel configuration data are the number and length of the barrel sections. The screw configuration data are the element-specific geometric parameters for the screw elements in order of their imagined placement, from the feed port position to the die. For conveying screw elements, these parameters are length in the screw axis direction L_{Ele} and screw pitch t . From these values, along with the global screw geometry parameters, the element helix angle ϕ_S , maximum channel width b_{Max} , flight width e_{Max} , down-channel length Z , and number of calculation zones are computed. For kneading block elements, the geometric parameters are axial length, number of discs, and angle-of-stagger between adjacent discs. From these values, again with the global screw geometry parameters, the geometric parameters of the equivalent screw elements are computed, along with values of the radial flight clearances corrected to represent the radial gaps between the discs.

The operating conditions of the extruder are the screw rotational speed n_0 , the mass throughput \dot{m} , the diehead pressure at the end of the screws P_{Die} , and the profile of barrel section temperature setpoints T_B . For reactive extrusion application, the number and position of liquid peroxide feed streams must also be specified, along with the stream feed rates, expressed as peroxide weight fractions in the polymer melt. Finally, the material data are the thermophysical and rheological parameters of the polymer: melt density ρ , solid density ρ_S , bulk solid density ρ_{Bulk} , solid pellet hydraulic diameter D_p , melt thermal conductivity λ , melt specific heat capacity c_p , fusion temperature T_M , heat of fusion ΔH_F , and for non-reactive extrusion application the three parameters n , K_{0T} , and β of the power-law fluid constitutive equation given below:

$$\eta = (K_{0T} e^{-\beta T}) \dot{\gamma}^{n-1} \quad (3.31)$$

For PP reactive extrusion simulations, the entering number- and weight-average molecular weights of the polymer must be given. The melt power-law parameters are calculated by resin-specific regression formulas from temperature and weight-average molecular weight. The formulas for each resin to be simulated must be incorporated directly into the program code.

3.4.2 Inner Loop

The inner loop of the algorithm computes the coupled pressure, filling level, temperature, and solid volume fraction profiles consecutively, and iterates the calculations until the pressure profile is converged. Prior to the first iteration of the loop, the earliest possible position of the start of melting (hereafter referred to as point PSMMIN) is found, which is the start of the first calculation zone downstream of the feed port at which the barrel temperature exceeds or equals the material fusion temperature. Upstream of this position is the solids conveying zone of the extruder, so the calculations in the inner loop are only carried out downstream of here. For the first iteration of the inner loop, an initial linear melt temperature profile is assumed, going from the fusion temperature at point PSMMIN to the final barrel section temperature setpoint at the die. Also, a zero initial solid volume fraction profile is assumed, as well as a constant initial weight-average molecular weight profile at the specified undegraded PP value.

The profiles of average melt pressures and average degrees-of-fill are computed first in the loop. The direction of the calculations is retrograde, beginning at the diehead, at which the pressure is known, and proceeding backwards to point PSMMIN. In each calculation zone, the average melt volumetric flow rate is found using equation (3.13), and the average melt pressure at the upstream end of the zone is found using equation (3.14). In these calculations, the values used for the melt

temperature, weight-average molecular weight, and solid volume fraction are averages for the zone in consideration, based on results from the previous inner and outer loop iterations. Since the conditions in the radial flight clearance are not known, the values for the melt power-law parameters there are approximated by values based on channel conditions. If pressures at both ends of the zone are zero, the average degree-of-fill in the zone is then found by equation (3.17), otherwise the channel is fully-filled so the degree-of-fill is 1. Finally, once point PSMMIN is reached, the actual position of the start of melting for the current inner loop iteration (point PSM) is located as the position of the upstream end of the first fully-filled calculation zone.

The average melt temperature profile is computed next, starting from the fusion temperature at point PSM, and proceeding in a prograde manner to the diehead melt temperature. For each calculation zone, if the degree-of-fill from the current inner loop iteration is less than 1, values of the average channel depth and width for the occupied portion of the channel are found. The average melt temperature at the downstream end of the zone is then calculated using equation (3.24), with melt power-law parameters based on the entering melt temperature and the average weight-average molecular weight in the zone from the previous outer loop iteration. The computed temperature is then corrected for solids melting using equation (3.25) and the solid volume fraction profile from the previous inner loop iteration. For PP reactive degradation simulations, it is assumed that the heat of reaction for the degradation process is negligible, and that the melt thermodynamic properties remain unchanged.

The solid volume fraction profile is updated last in the inner loop. Beginning at point PSM, the polymer pellet hydraulic radius is taken as the entering value, and the initial solid volume fraction is found by equation (3.5), using the channel dimensions at this point to find the imagined

solid particle packing density $N_p/\Delta z$. The calculations then proceed in a prograde manner towards the die, continuing until the solid volume fraction is found to drop below 0.01. The pellet radius at the end of each zone is found using equation (3.4), with average values for the melt volumetric flow rate and temperature used for the zone from the current inner loop iteration. The solid volume fraction at the end of the zone is found using the following equation, obtained by dividing equation (3.5) by itself for the zone entering and exiting streams:

$$F_{SI} = F_{SO} \left(\frac{r_{PI}}{r_{PO}} \right)^3 \quad (3.32)$$

At the end of the inner loop, a convergence test is performed. The convergence criteria are twofold: first the position of the start of melting (point PSM) must not have changed in the current iteration from the previous iteration, and if this is the case, the sum of the absolute values of the changes of the average melt pressures over the current iteration must be less than 1. If both of these conditions are met, the inner loop is converged, and the algorithm proceeds to the calculations of the outer loop.

3.4.3 Outer Loop

In the outer loop, for simulations of reactive extrusion of PP with peroxide-initiated reactive degradation, the profile of average weight-average molecular weight of the polymer in the extruder channels is computed, using the converged temperature and filling level profiles from the inner loop. Calculations begin at the start of the first zone downstream of the peroxide injection point, and continue to the die. It is assumed that the peroxide is added as a stream of pure liquid to the polymer melt at a location of partial-filling (and therefore atmospheric pressure). It is also

assumed that the peroxide remains segregated from the melt until the start of the first fully-filled zone downstream of the injection point, at which point it becomes uniformly mixed into the melt. At this point the tracking of the degradation reaction begins. Starting values for the peroxide concentration in the melt and the polymer MWD moments are found from the specified peroxide stream feed rate and the undegraded polymer properties respectively. In each calculation zone the average residence time is computed as the mass holdup (found using the degree-of-fill) divided by the mass throughput:

$$\bar{t}_R = \frac{fA_{Free}L}{\dot{m}}[\rho_S F_S + \rho(1 - F_S)] \quad (3.33)$$

The average peroxide concentration at the end of the zone is computed by an exponential decay equation using the average residence time and the decomposition rate constant expression of equation (3.30), employing the average melt temperature for the zone. The average values of the MWD moments at the end of the zone are found by solving the coupled moment ordinary differential equations of equation (3.27) by a Runge-Kutta method of order 4. The average weight-average molecular weight of the polymer is then found using equation (3.29).

Once the molecular weight profile has been computed, the outer loop is tested for convergence. The convergence criterion is that the sum of the absolute values of the changes in the weight-average molecular weights over the current outer loop iteration must be less than 1. If this condition is met, the outer loop is converged, and the profiles of all degrees of freedom in the extruder are output. If convergence has not been achieved, the program proceeds to the start of the inner loop and recalculates the pressure, filling level, melt temperature, and solid volume fraction profiles using the updated molecular weight profile.

3.5 Simulation Procedure and Results

In this section the predictive capabilities of the steady-state CSCO extrusion process model are examined for both a reactive and a non-reactive system, in the processing of a PP resin. For the non-reactive system, the extruder and screw geometries are presented, and the predicted degree of freedom profiles are analyzed for several sets of operating conditions. A sensitivity analysis of the predicted average residence times for this system versus several model parameters is also given, to determine the key parameters which must be known to the greatest precision, to have confidence in the average residence time predictions of the simulations. For the reactive system, a different screw configuration in the same extruder is considered, with the addition of one peroxide stream at a position towards the axial mid-point of the machine. The predicted DOF profiles for different levels of peroxide addition and different operating conditions are examined, and then the predicted extrudate weight-average molecular weights are compared to experimental values at single values of screw speed and throughput and several different peroxide levels.

3.5.1 Material Properties

The polymer considered in the simulations described in this section was Montell KF6100 polypropylene, a commercial isotactic PP provided in pellet form, which comes blended with 1 wt% Irganox 1010, an antioxidant used to retard oxidative degradation. Table 3.1 shows the material physical and thermodynamic parameter values used in the simulations. Several of the values were taken as generic PP property values.

The chemorheology of the material was described using data from Wang (1996), who

Table 3.1: Material Data for Simulations			
<i>Parameter</i>	<i>Symbol</i>	<i>Value</i>	<i>Source</i>
Melt density	ρ	750 kg/m ³	Tzoganakis et al (1988a)
Solid density	ρ_S	905 kg/m ³	Montell Polyolefins (1995)
Bulk solid density	ρ_{Bulk}	560 kg/m ³	Laboratory measurement
Pellet hydraulic diameter	D_P	2 mm	Laboratory estimate
Melt thermal conductivity	λ	0.185 W/(m °C)	Tzoganakis et al (1988a)
Melt specific heat capacity	c_P	2.428 kJ/(kg °C)	Tzoganakis et al (1988a)
Fusion temperature	T_M	160°C	Wang (1996)
Heat of fusion	ΔH_F	95.54 kJ/kg	Wang (1996)
Entering weight-average molecular weight	$\bar{M}_{W,In}$	279700 kg/kmol	Wang (1996)
Entering number-average molecular weight	$\bar{M}_{N,In}$	51800 kg/kmol	Wang (1996)

prepared peroxide-degraded samples of stabilized Montell KY6100 PP (similar to KF6100 PP) in a twin-screw extruder, and then carried out rheological and molecular characterization of the samples using a capillary rheometer and a gel permeation chromatograph. The flow curves of shear viscosity against shear rate for the samples are shown in Figure 3.10, along with the measured weight-average molecular weights. The curves depict the characteristic shear-thinning behaviour of polymer melts, with viscosity decreasing as the shear rate increases, and they also show the tremendous viscosities of the materials, in the hundreds of Pa s. The curves can also be seen to depict nearly linear relationships between viscosity and shear rate (on logarithmic axes) for the samples, indicating they comply with the power-law constitutive equation over the range of shear rates shown. The range of shear rates for the Figure, in the tens to hundreds of s^{-1} , is typical for conditions in polymer processing operations (Rauwendaal, 1986). The last thing the curves show is that as the weight-average molecular weight of the polymer decreases, its melt viscosity decreases, which is consistent with expectations.

The power-law parameters for both the virgin and degraded materials were determined by regressing the logarithm of the melt viscosity against the logarithm of the shear rate. The parameter values for the virgin PP are given in Table 3.2. Unfortunately the rheological data in Wang (1996) were only given for single temperatures (230°C for the virgin polymer and 210°C for the degraded samples) so from this data it was not possible to directly determine the temperature dependencies of the power-law parameters. For the virgin PP, the temperature dependence of the consistency index was estimated as being the same as that of unstabilized Montell KY6100 PP, again from Wang (1996). The power-law index was assumed to be independent of temperature.

For the degraded polymers, the calculated power-law index and power-law consistency

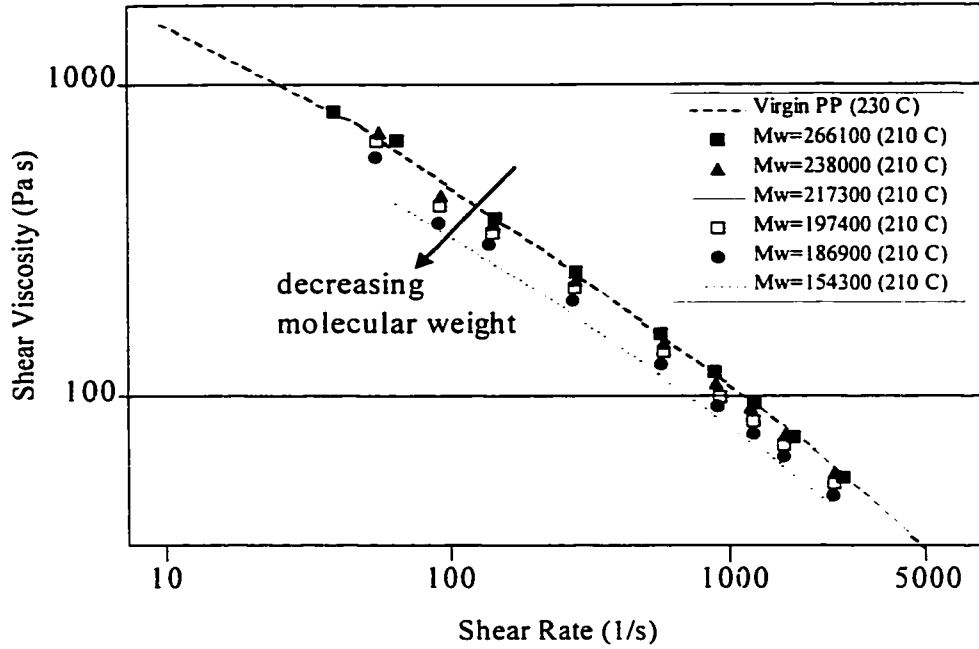


Figure 3.10: Flow Curves of Polypropylene Resins

<i>Parameter</i>	<i>Symbol</i>	<i>Value</i>
Power-Law Index	n	0.373
Temperature dependence of consistency index	β	$0.025^{\circ}\text{C}^{-1}$
Temperature-independent part of consistency index	K_{0T}	$2.49 \times 10^6 \text{ Pa s}^n$

index values are plotted against weight-average molecular weight in Figures 3.11 and 3.12 respectively. In Figure 3.11, the six power-law index data points do show some scatter, but there is an apparent trend towards higher values (indicating more Newtonian behaviour) as molecular weight decreases. The data were fit to a first degree polynomial regression model against the logarithm of molecular weight, yielding the following equation:

$$n = 1.006 - 0.0539(\ln \bar{M}_w) \quad (3.34)$$

The line this represents is shown in Figure 3.11. For the reactive extrusion simulations, it was assumed the power-law index of the PP was independent of temperature. In Figure 3.12, the power-law consistency indices decrease as molecular weight decreases. A first degree polynomial regression model was again used, this time to fit the logarithm of the consistency index to the logarithm of molecular weight, yielding this equation:

$$\ln K_{T=210} = -2.416 + 0.937 \ln \bar{M}_w \quad (3.35)$$

The line represented by this is shown in Figure 3.12. For the simulations it was assumed that the temperature dependence of the consistency index was constant at the value in Table 3.2, so the following equation was obtained from equation (3.35) for the temperature-independent part of the consistency index:

$$\ln K_{0T} = 2.834 + 0.937 \ln \bar{M}_w \quad (3.36)$$

3.5.2 Screw and Barrel Geometries

The assumed screw and barrel geometries for the simulations in this section were those of a 1.2 m long Leistritz LSM 30-34 self-wiping co-rotating twin-screw extruder, with 10 equal length barrel sections. The specified extruder geometric parameters are given in Table 3.3, along

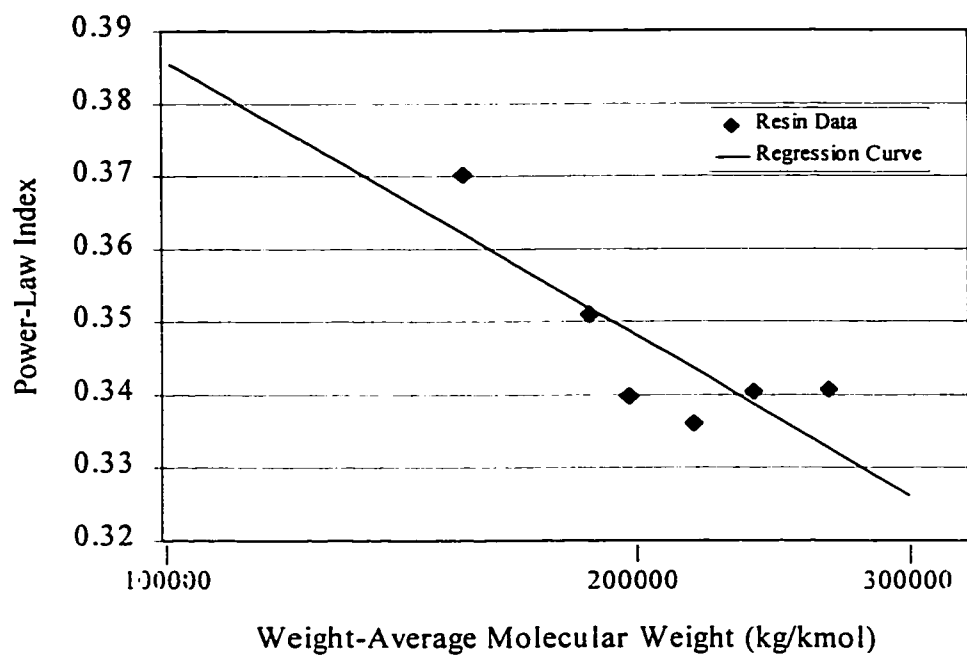


Figure 3.11: Power-Law Indices of Degraded Samples at 210°C

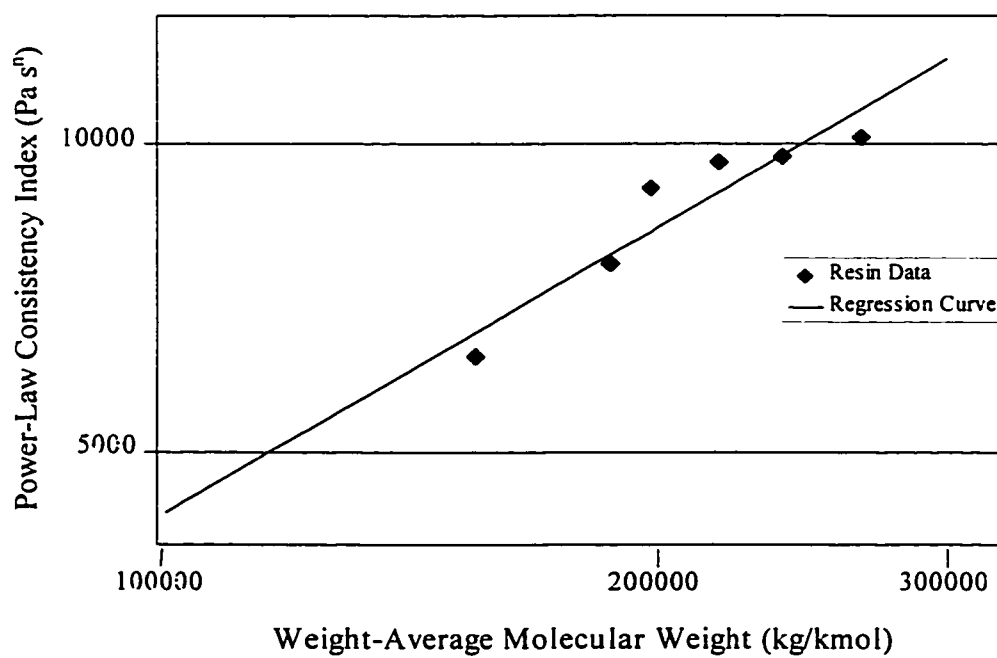


Figure 3.12: Power-Law Consistency Indices of Degraded Samples at 210°C

with several quantities of interest computed from the screw self-wiping profile. The screws were bilobal, with a relatively small diameter of 33.7 mm, typical for a laboratory scale machine. The total screw length equaled 35.6 screw diameters. The ratio of the screw centreline separation to the screw diameter for this system exceeded the limit of 0.85 of equation (3.7) for omission of curvature from the process model. The radial flight clearance for this system was fairly large relative to the average channel depth, and as such its contribution to the total channel depth was worth including. For larger diameter screws though, the radial flight clearance would likely be less significant in relative terms. The fractional intermeshing region channel shift was reasonably large for this system, but was still much below the 0.5 level at which the channel shift begins to have a dominant role in the pressurization behaviour of conveying screw elements, as indicated by Wang et al. (1989).

3.5.3 Simulations of Conventional Extrusion of Polypropylene

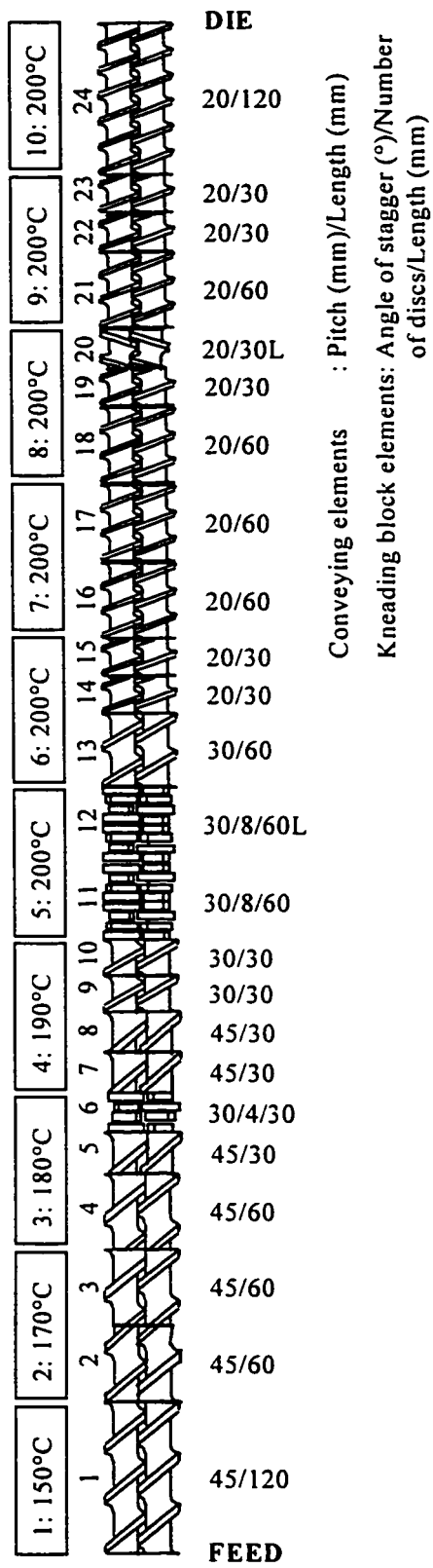
The non-reactive extrusion simulations utilized the screw configuration shown in Figure 3.13, as well as the rheological data for virgin KF6100 PP given in Table 3.2. The screw configuration is the same as that used in the residence time distribution measurement experiments described in Chapter 4. The configuration features 3 kneading block sections (one reverse staggered), a reverse conveying screw element upstream of the die, and conveying screw elements with pitches decreasing from feed to die. It is a fairly complicated design, which gives rise to several pressurization zones within the extruder. Also shown in Figure 3.13 are the barrel zone temperature setpoints, which increased quickly in the direction of flow to 200°C.

In Table 3.4 the element geometry parameters are given for a 20 mm pitch conveying screw

<i>Parameter or Quantity</i>	<i>Symbol</i>	<i>Value</i>
Total screw length		1200 mm
Number of barrel sections		10
Screw outer diameter	D_s	33.7 mm
Number of screw flights	i	2
Radial flight clearance	s_R	0.3 mm
Screw centreline separation	a	30.0 mm
Maximum channel depth	h_{Max}	3.7 mm
Criterion for omission of screw curvature	a/D_s	0.89
Average channel depth	\bar{h}	2.8 mm
Relative size of radial flight clearance	s_R/\bar{h}	0.11
Fractional intermeshing region channel shift	e_{Max}/b_{Max}	0.25
Extruder free cross-section area	A_{Free}	4.3 cm ²

<i>Parameter or Quantity</i>	<i>Symbol</i>	<i>Value for Conveying Element</i>	<i>Equivalent Value for Kneading Block Element</i>
Pitch	t	20 mm	90 mm
Criterion for applicability of equation (3.6)	t/D_s	0.59	2.67
Maximum channel width	b_{Max}	7.9 mm	27.5 mm
Maximum flight width	e_{Max}	2.0 mm	6.8 mm
Helix angle	ϕ_s	10.7°	40.4°
Channel aspect ratio	$b_{Max}/(\bar{h}+s_R)$	2.5	8.8
Flight clearance ratio	s_R/s_R	1	1.05

Figure 3.13: Screw Configuration for Conventional Extrusion Simulations



element from this system, as well as for one of the kneading block elements. The most significant values in the table are shown in shaded cells. The conveying screw element data are applicable to the elements in the region before the die, which are most likely to be fully-filled in any extrusion process. The equivalent screw pitch, maximum channel width, and maximum flight width for the kneading block element can be seen to be much larger than those for the conveying screw element. Unfortunately, the equivalent screw pitch for the kneading blocks was so large that it fell outside the range of applicability of the screw characteristic curve approximation equation (3.6), as indicated by the conditions in equation (3.7). The other concern was the low channel aspect ratio for the small pitch conveying screw element. For such an element, the applicability of the lubrication approximation which has traditionally been the basis for the modeling of the conveying capacity of screw elements is questionable. The use of small pitch elements in the extruder zone before the die is standard practice though, so this is a problem that should be dealt with in future modeling efforts.

The results for four simulation runs are presented here. The operating conditions for the runs are given in Table 3.5, along with several additional results of interest from the simulations. The runs represent a 2^2 factorial experiment on the model predictions of extruder behaviour over screw speed and throughput, at the levels of 100 and 200 rpm, and 3 and 10 kg/h. Experimental runs at the same operating conditions were performed on a laboratory extruder fitted with a 2 hole capillary die, from which the diehead pressures for the simulations were obtained. Details of these runs are given in Chapter 4. The first things to notice in Table 3.5 are the extreme values for the runs of the dimensionless melt volumetric flow rate in fully-filled forward conveying channels ($\pi_{\dot{V},Min}$ and $\pi_{\dot{V},Max}$). As can be seen, in 3 of the 4 runs, the minimum value of this quantity was

below the lower limit of 0.3 (for fluids with power-law indices below 0.5) for applicability of equation (3.6), as stated in equation (3.7). In all 3 cases this value arose in the long forward staggered kneading block section of the screws (element 11 in Figure 3.13), where the equivalent screw pitch has previously been shown to be too large for equation (3.6). The maximum values of the dimensionless volumetric flow rates were well within the prescribed bounds of equation (3.7) for all 4 runs.

Also given in Table 3.5 are values of the ratio of the channel melt volumetric flow rate in the last calculation zone of the screws to the value that would be assumed if leakage flows were neglected. For all 4 runs the ratio was significantly greater than 1, indicating the important (in some cases even dominant) contribution of leakage flows to channel melt flow rates. Comparing the numbers to each other, it is apparent that leakage flows were most significant (in relative terms) in runs at high screw speeds and low throughputs. Increasing screw speed increases leakage flows by increasing the melt pressure gradient in the channel direction.

Figure 3.14 shows the predicted degree-of-fill profiles for the simulation runs. All 4 runs show three regions of complete filling: the first in the region upstream of the reverse staggered kneading block, the second upstream of the reverse conveying screw element, and the third just upstream of the diehead. In the partially-filled regions, the filling levels were found to be lowest in the solids conveying region, and to increase towards the die as the screw pitches decrease. For the 4 runs, the start of the first fully-filled region (which is point PSM, the position from which the melting calculations are begun) was in the first or second screw element upstream of the long forward staggered kneading block element (element 9 or 10). In the Figure, the average filling level was clearly the highest for run 2, followed by run 4, run 1, and run 3. The fractional fully-filled

<i>Quantity or Parameter</i>	<i>Symbol</i>	<i>Run 1 Value</i>	<i>Run 2 Value</i>	<i>Run 3 Value</i>	<i>Run 4 Value</i>
Screw speed	n_0	100 rpm	100 rpm	200 rpm	200 rpm
Mass throughput	\dot{m}	3 kg/h	10 kg/h	3 kg/h	10 kg/h
Diehead pressure	P_{Die}	694 kPa	1256 kPa	569 kPa	1148 kPa
Iterations to convergence		20	16	14	17
Criterion for applicability of equation (3.6)	$\pi_{\dot{V},Min}$	0.19	0.32	0.16	0.22
Criterion for applicability of equation (3.6)	$\pi_{\dot{V},Max}$	0.45	0.73	0.39	0.53
Ratio of melt volumetric flow rate to value for no leakage flows at end of extruder	$\frac{\dot{V}_{Z,Melt}}{\dot{m}/(\rho k)}$	2.85	1.38	4.95	2.01
Fractional fully-filled length		0.198	0.333	0.179	0.221
Dimensionless position of start of melting	PSM	0.388	0.358	0.392	0.379
Initial solid volume fraction	F_{S0}	0.445	0.445	0.445	0.445
Melting length		87 mm	146 mm	94 mm	133 mm

lengths for the runs, shown in Table 3.5, also went in the same order. This indicates that increasing throughput had the effect of increasing filling, and increasing screw speed had the opposite effect. This is consistent with the experimental observations of Duley and Daigneault (1994).

Figure 3.15 shows the predicted profiles of cumulative average residence time for the simulation runs. The cumulative average residence time at a point is the aggregate mass holdup in regions upstream of that point divided by the mass throughput. The curves indicate the relative contributions of the different screw sections to the total average residence times of the polymer in the systems. The solids conveying zone can be seen to have made only a minor contribution, since transport by forced conveyance was assumed here, with the average residence time in each zone equal to the minimum residence time. In the melt conveying zone, each curve had a segmented shape, with the higher slope segments in regions of complete filling, and the lower slope segments in regions of partial-filling. The curves split into two pairs in the melt conveying zone based on throughput, with the curves for lower throughput at higher times. Within each pair, the curve for lowest screw speed was on top. Thus increasing throughput had the effect of lowering cumulative average residence times, and increasing screw speed had the same effect. The screw speed effect makes sense, since in Figure 3.14 the average filling level at a given throughput was lower for higher screw speed. The throughput effect was a bit more complicated, since both the numerator (the average filling level) and denominator of the average residence time in each calculation zone were a function of the throughput. The observation that increasing the throughput moved the curves to lower times indicates the effect on the denominator was proportionately greater.

Figure 3.16 shows the predicted average melt pressure profiles for the simulation runs. Three regions of pressures greater than atmospheric were found for each run, corresponding to the

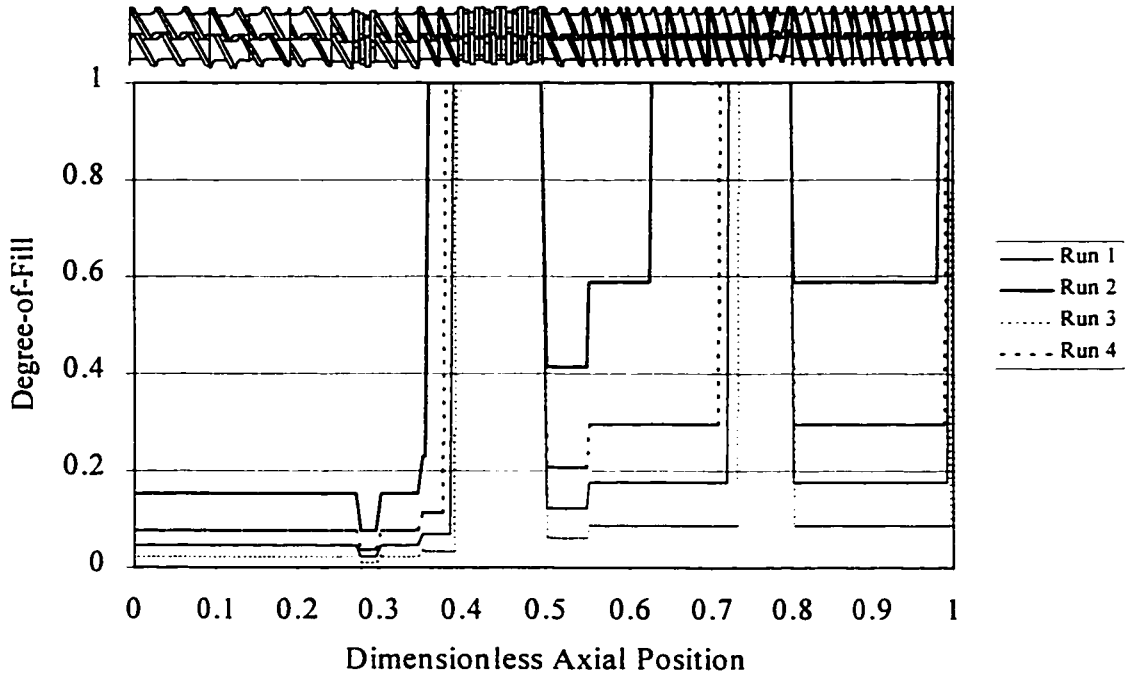


Figure 3.14: Degree-of-Fill Profiles for Conventional Extrusion Simulations

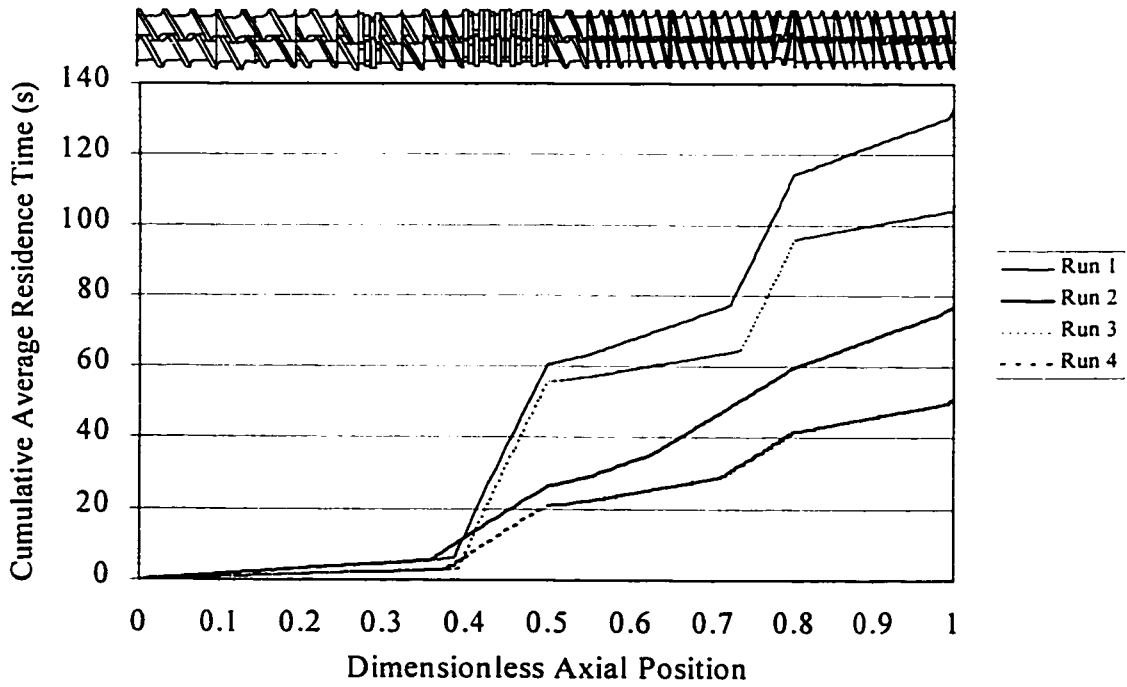


Figure 3.15: Cumulative Average Residence Time Profiles for Conventional Extrusion Simulations

three regions of complete filling for each run. The highest pressures for each run were found in the second pressurization zone upstream of the reverse conveying screw element; the pressures here and in the region of the kneading block far exceeded that at the diehead. For the first two pressurization zones, the melt pressure peaked at the upstream end of their respective reverse conveying elements, and then dropped off sharply and completely over the length of that element. In the profiles for the first pressurization zone, an additional cusp was seen where the slope decreased as the melt passed from the screw element to the kneading block, which has a lower pressurization capacity due to its much larger pitch and leakage flows. In the Figure, the peak melt pressures can be seen to be essentially determined by throughput only, with larger pressures following from higher throughputs. This just indicated that the reverse conveying elements functioned equivalently to internal dies, with larger pressure drops necessary to drive more material through. The screw speed only affected the filled screw length (or backup length) necessary to generate the pressure to overcome the flow restrictions of the reverse conveying elements.

A summary of the results of the solids melting calculations for the 4 simulation runs is given in Table 3.5. As stated previously, the position of the start of melting for 3 of the runs was found to lie in element 10, and for run 2 it was found to lie upstream of this, in element 9. The initial solid volume fraction for all runs was found to be the rather low value of 0.445, the value of which was dependent on the screw channel geometry at point PSM. The solid weight fraction this represented was 0.492. The melting lengths for the runs were found to be fairly short, with larger values for higher mass throughput, but little apparent effect of screw speed.

Figure 3.17 shows the predicted average melt temperature profiles for the simulation runs,

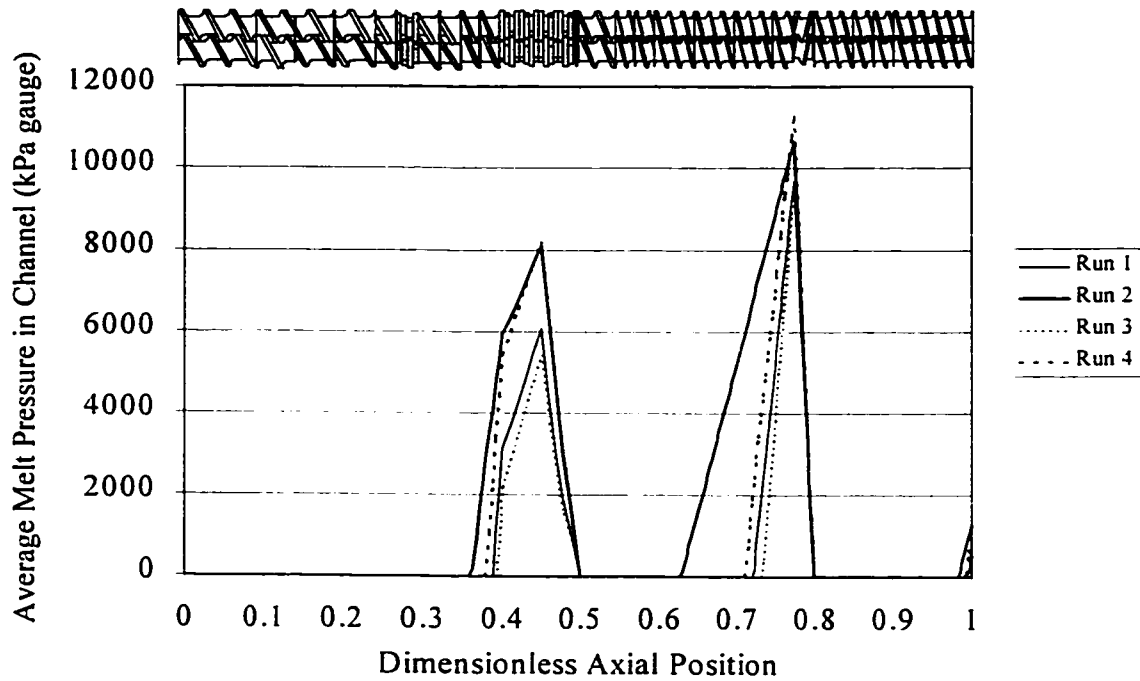


Figure 3.16: Average Melt Pressure Profiles for Conventional Extrusion Simulations

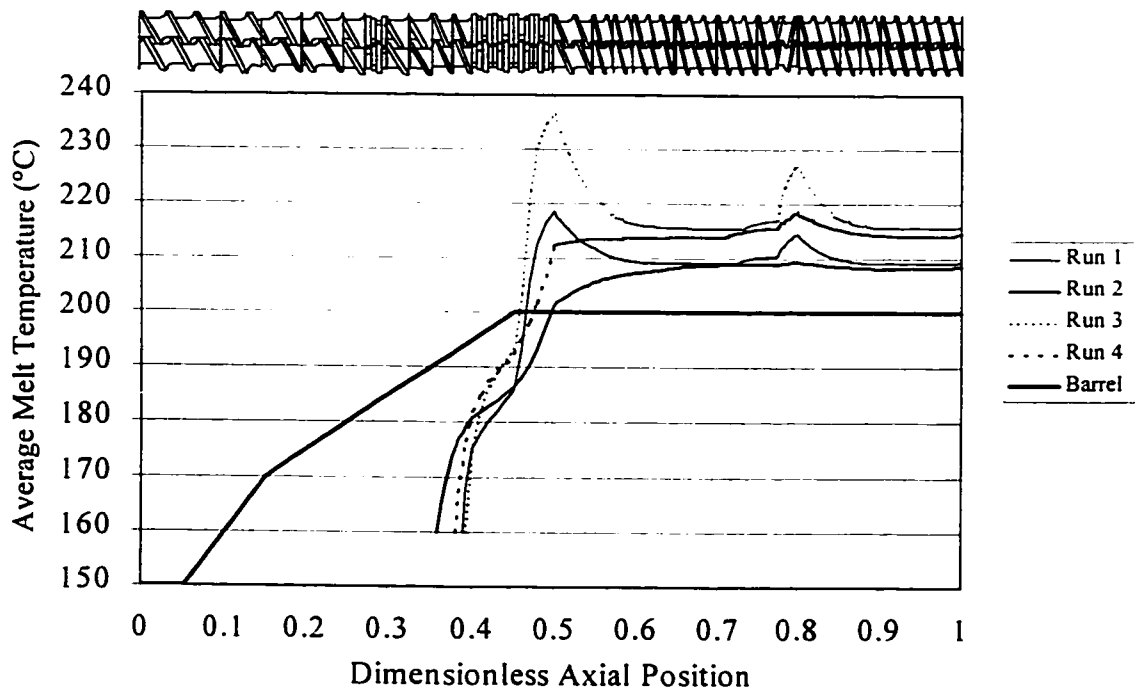


Figure 3.17: Average Melt Temperature Profiles for Conventional Extrusion Simulations

along with the specified profile of barrel temperature setpoints. The curves show several distinct regions of temperature development. As with the melt pressures, these regions followed the filling level profiles of Figure 3.14. In the two filled regions upstream of the reverse conveying elements, the melt temperatures grew rapidly until the end of each region was reached, and then decayed down to equilibrium values in the regions of partial-filling. These equilibrium temperatures were significantly higher than the barrel wall temperatures, and were reached on the basis of a balance between the rate of heat generation by viscous dissipation in the melt, and the rate of heat removal by conduction with the barrel surface. The lower temperature growth in the partially-filled regions can be attributed to the lower average residence time of the melt there. The curves can be seen to have split into two pairs as the end of the screws was approached, with the curves for the higher screw speed on top. This makes sense, since higher screw speeds mean higher average channel shear rates, leading to higher rates of heat generation by viscous dissipation. Within each pair, the curve for lower throughput was at higher temperatures. This again can be attributed to the higher average residence time of the material in the system at lower throughputs.

3.5.4 Sensitivity Analysis of Predicted Average Residence Times in Conventional Extrusion

An analysis of the sensitivity of the model predictions of polymer average residence time in the conventional extrusion system described in the previous subsection, to perturbations in material parameter values, radial flight clearance, and barrel temperature setpoint in the melt conveying zone of the extruder, is given here. Separate simulations were performed with each model parameter increased by 2%, and the percent change in the predicted average residence time

determined. The operating conditions for the simulations were 150 rpm and 6.5 kg/h (representing the mid-point of the operating region examined above), and an experimentally determined diehead pressure value of 1001 kPa. The predicted average residence time for this system using the nominal values of all model parameters was 72.8 s. The flight clearance was included in the sensitivity analysis since it is the one screw geometry parameter that may change with time, from mechanical wear of the screw elements. The barrel temperature setpoint in the melt conveying zone of the extruder was included to examine the impact of the model assumption of perfect temperature control on the barrel surface.

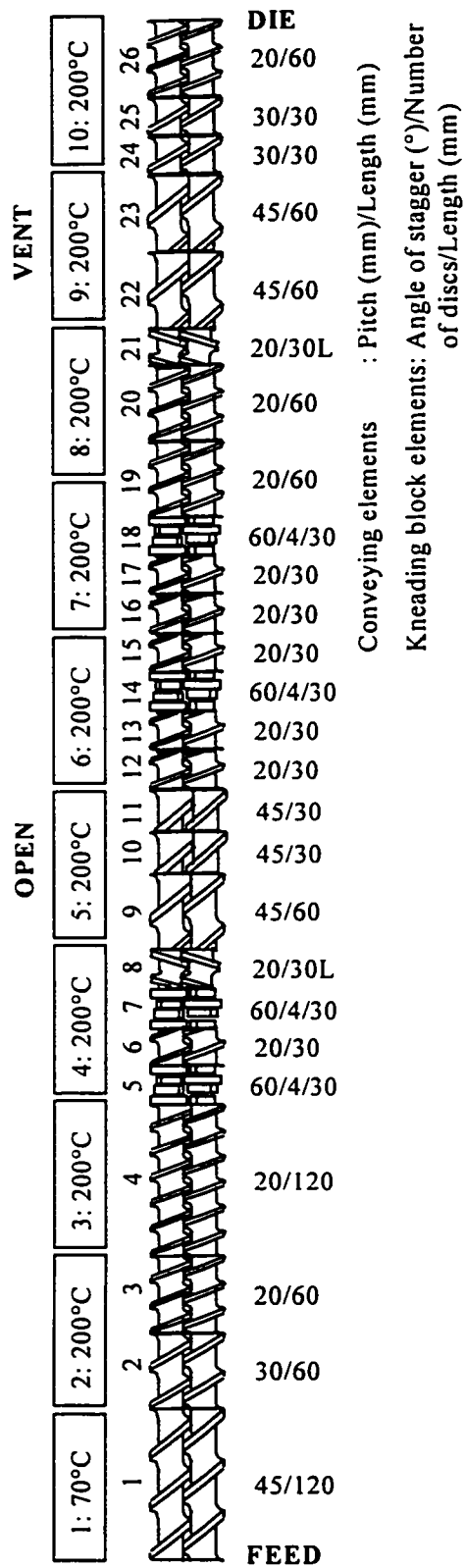
Table 3.6 shows the sensitivity analysis results. As can be seen, the model predictions of average residence time were relatively insensitive to perturbations in most of the parameters considered, specifically the solid polymer bulk density and pellet size, the melt thermodynamic data, the melt consistency index parameters, and the barrel temperatures in the melt conveying zone. The parameters to which the model predictions were most sensitive are the melt power-law index and density, and on the lower end, the polymer solid density and radial flight clearance. These then are the key parameters, which must be known to the highest level of precision to ensure reliability of average residence time predictions in the simulations.

3.5.5 Simulations of Peroxide-Initiated Controlled Degradation of Polypropylene - Part I

The reactive extrusion simulations utilized the screw configuration shown in Figure 3.18. The Figure also shows the barrel zone temperature setpoints for the runs, and that the fifth and ninth barrel sections were open to the atmosphere. This data came from Wang (1996), who carried out a series of experimental PP controlled degradation runs in a Leistritz 30-34 CSCO extruder,

Table 3.6: Sensitivity Analysis Results		
<i>Model Parameter</i>	<i>Perturbed Value</i>	<i>Percent Change in Predicted Average Residence Time</i>
Melt density	765 kg/m ³	0.47
Solid density	923.1 kg/m ³	0.14
Bulk solid density	571.2 kg/m ³	0.03
Pellet hydraulic diameter	2.04 mm	0.01
Melt thermal conductivity	0.189 W/(m °C)	-0.01
Melt specific heat capacity	2.477 kJ/(kg °C)	0.01
Fusion temperature	163.2 °C	0.04
Heat of fusion	97.45 kJ/kg	0.01
Power-law index	0.3805	-0.70
Temperature dependence of power-law consistency index	0.0255 °C ⁻¹	0.03
Temperature-independent part of power-law consistency index	2.54×10 ⁶ Pa s ⁿ	0.00
Radial flight clearance	0.306 mm	0.11
Barrel temperature setpoint in melt conveying zone	204 °C	-0.01

Figure 3.18: Screw Configuration for Reactive Extrusion Simulations



in which a stream of liquid Lupersol 101 was added to the polymer melt through the port in the fifth barrel section. Other machine specifications from Wang (1996) that were used in the simulations are a 2 hole capillary die, with each hole having a length of 12 mm and a diameter of 4 mm, and the use of a face plate on the end of the extruder. The screw configuration featured two reverse conveying screw elements, one upstream of each open barrel section to provide a melt seal, and also 4 short kneading block sections, two prior to the peroxide injection port to aid in melting of the solid polymer feed, and two downstream of the injection port to function in the dispersive mixing of the liquid peroxide into the molten polymer. The equivalent screw pitch for all the kneading block sections was 45 mm, for which t/D_s is 1.34, which is well within the specified limit given in equation (3.7) for applicability of equation (3.6). As well, the screw elements in the open barrel sections were all large pitch elements, with wide channels to give only partial-filling (and hence atmospheric pressure).

The simulations used the regression equations for the dependence of the power-law parameters of KF6100 PP on weight-average molecular weight given in equations (3.34) and (3.36), and the molecular weight values for the undegraded polymer in Table 3.1. Since the polymer contains a stabilizing agent and it was anticipated that melt temperatures would remain below the level at which thermal degradation becomes significant, the controlled degradation reaction kinetic model of equations (3.27) and (3.28) was considered applicable. Diehead pressures were computed using the tubular die characteristic equation for a power-law fluid (Rauwendaal, 1986):

$$\Delta P_{Die} = 2K \frac{L_{Die}}{R_{Die}} \left[\frac{(3n+1)\dot{m}}{2\pi\rho n R_{Die}^3} \right]^n \quad (3.37)$$

In the calculations the progress of the degradation reaction was tracked in the molten polymer right through the die. Hence the final computed polymer properties were true extrudate estimates. The value for the filled volume of the extruder face plate and die (minus the volume of the screw tips) that was used in the simulations is 50 cm^3 . The power-law parameters in equation (3.37) were computed using the temperature at the end of the screws, and the average PP weight-average molecular weight in the die/face plate combination.

For qualitative assessment of the predictive capabilities of the model, a total of 6 reactive extrusion simulation runs were performed, examining the effect of 3 different levels of peroxide addition on the model predictions of the extruder behaviour, at one screw speed and two throughputs. The operating conditions for the runs are given in Table 3.7, along with several additional results of interest from the simulations. The high level of peroxide addition was chosen to limit the extent of degradation of the polymer, so the regression formulas for the melt power-law parameters are not extrapolated too far outside the range of molecular weights for which they were determined. For all 6 runs the melting of the solid feed was computed as being completed prior to the injection point of the peroxide stream, and so was not affected by the reaction. Hence no details of the solids melting computations are given. Also, there were no problems with applicability of the screw characteristic curve approximation equation for any of the runs, as indicated by the extreme values of the dimensionless melt volumetric flow rate in fully-filled forward conveying channels, shown in Table 3.7. The effect of increasing the throughput on the predicted extruder behaviour was found to be the same as in the conventional extrusion simulations: to increase the average filling levels and decrease the average residence times.

Table 3.7 shows that for each level of throughput, as the peroxide stream feed rate was

Quantity or Parameter	Symbol	Run 1 Value	Run 2 Value	Run 3 Value	Run 4 Value	Run 5 Value	Run 6 Value
Screw speed (rpm)	n_0	100	100	100	100	100	100
Mass throughput (kg/h)	\dot{m}	2	2	2	8	8	8
Peroxide stream feed rate (wt% in melt)	$w_{I,In}$	0	0.02	0.06	0	0.02	0.06
Diehead pressure (kPa)	P_{Die}	637	548	439	1025	904	753
Outer loop iterations to convergence		1	5	6	1	5	6
Criterion for applicability of equation (3.6)	$\pi_{\dot{V},Min}$	0.30	0.30	0.30	0.45	0.45	0.45
Criterion for applicability of equation (3.6)	$\pi_{\dot{V},Max}$	0.42	0.42	0.42	0.65	0.65	0.65
Fractional fully-filled length		0.187	0.184	0.181	0.298	0.291	0.282
Dimensionless position of mixing of peroxide into melt		--	0.725	0.728	--	0.669	0.678
Relative extrudate weight-average molecular weight	$\frac{\bar{M}_{W,Out}}{\bar{M}_{W,In}}$	1	0.783	0.551	1	0.791	0.567
Relative peroxide level in extrudate	$\frac{w_{I,Out}}{w_{I,In}}$	--	3×10^{-4}	5×10^{-4}	--	0.049	0.062
Average residence time (s)	\bar{t}_R	241.4	239.5	237.6	103.4	102.5	101.4
Number of half-lives of peroxide in melt		--	11.9	11.0	--	4.4	4.0

increased, the extent of degradation of the polymer increased, as indicated by the extrudate weight-average molecular weights. At the higher peroxide addition level of 0.06 wt% (equal to 600 ppm), the molecular weight was predicted to be nearly halved. The number of half-lives that the peroxide was considered to be uniformly mixed into the melt (the reaction time) was reasonably high for all runs, and the consequence of this was that very little peroxide was computed as remaining undecomposed in the extrudate, which is desirable. There was a small increase in the relative extrudate peroxide level as the peroxide feed rate was increased, due to the slight reduction in the average residence time of the polymer in the extruder. The relative extrudate molecular weights are seen to be nearly equal for the same relative levels of peroxide addition. This was because the peroxide was essentially completely consumed in all the runs - the relative extrudate molecular weights for the higher throughput runs were only slightly larger since the peroxide was not quite consumed to the same level as in the lower throughput runs.

Figures 3.19, 3.20, and 3.21 show the predicted profiles of relative weight-average molecular weight, melt pressure, and melt temperature respectively, for the 6 simulation runs. In each Figure, only the profiles for the last half of the extruder are shown, as the peroxide was added to the polymer melt stream at the dimensionless axial position of 0.45, and so only influenced the extruder behaviour downstream of this point. Not shown then is the fully-filled zone prior to and including the first reverse conveying element, element 8 in Figure 3.18. Figure 3.20 shows that for each run there were two fully-filled zones downstream of the peroxide injection point, one prior to the second reverse conveying element in the screw configuration (element 21), and the other prior to the die. The beginning of the first fully-filled region in the Figure was the point at which the peroxide was considered to be uniformly mixed into the polymer melt by the simulation

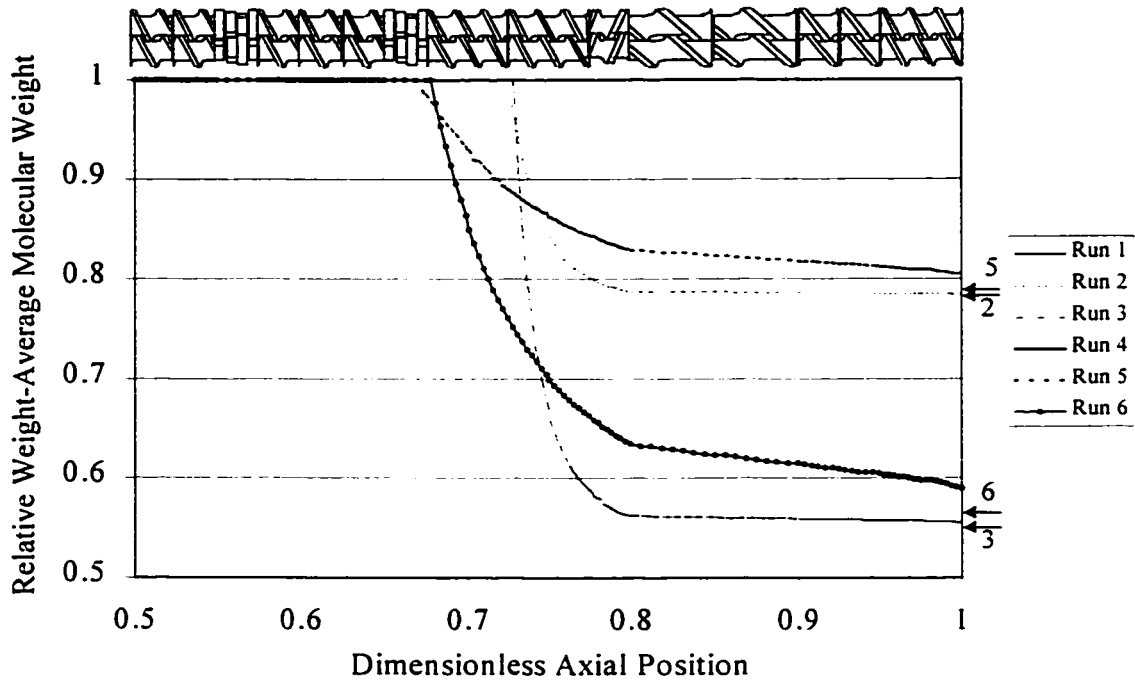


Figure 3.19: Relative Weight-Average Molecular Weight Profiles for Reactive Extrusion Simulations

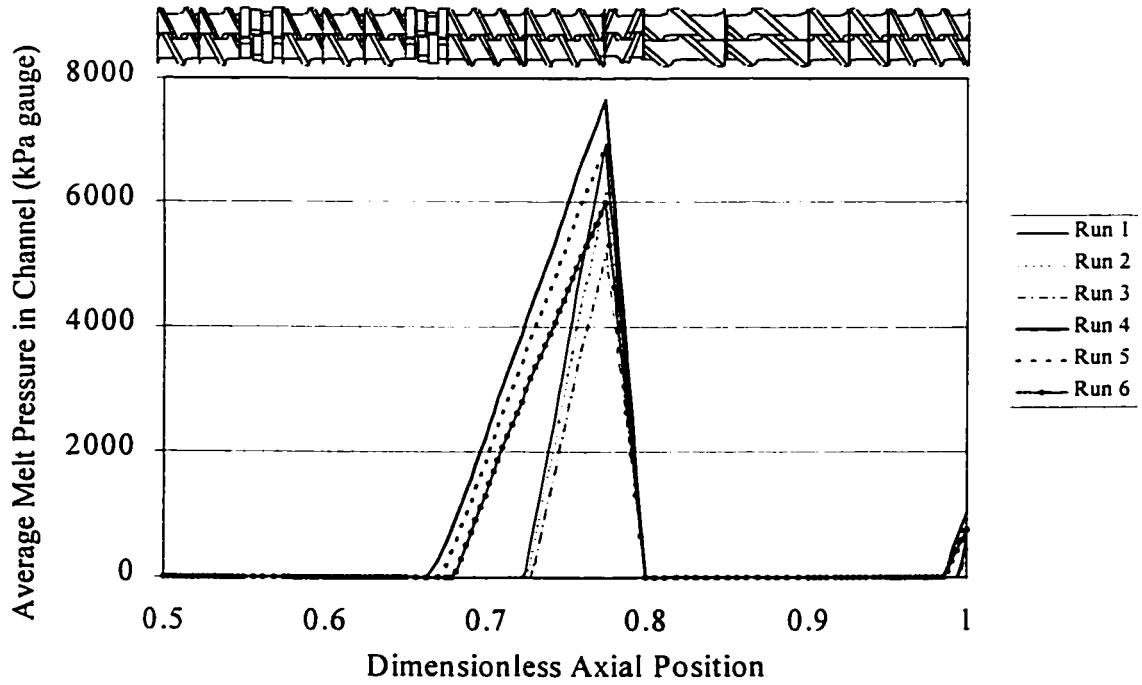


Figure 3.20: Average Melt Pressure Profiles for Reactive Extrusion Simulations

algorithm, so from this point onwards the progress of the peroxide-initiated controlled degradation reaction was computed. The dimensionless axial positions of this point for the 6 runs are given in Table 3.7. The point was found to occur distinctly further upstream for the high throughput runs, due to the accompanying higher filling levels.

Figure 3.19 shows that for the 4 runs in which peroxide was added to the system, the computed polymer molecular weights dropped off sharply from the points at which the reaction calculations were commenced. The sharp drop continued until the end of the first shown fully-filled region was reached, and then continued more gradually over the partially-filled zone that extended almost to the ends of the screws. The curves for the same relative level of peroxide addition approached each other as the end of the extruder was approached, with the curves for the higher throughput runs always on top because of the lower cumulative average residence times of the melt at each position. Arrows show the computed extrudate molecular weights for each reactive extrusion run. The drop in molecular weight in the die/face plate volume was higher for the high throughput runs, since the residual level of peroxide in the melt at the end of the screws was higher for these runs.

The melt pressure profiles in Figure 3.20 show that increased levels of peroxide addition were predicted to decrease pressure levels in the system. This same effect was seen in the computed diehead pressure values shown in Table 3.7. This can be attributed to the reduced melt viscosities caused by the reduction in weight-average molecular weight from the degradation reaction. The lower viscosities also caused reductions in the fractional fully-filled lengths and average residence times shown in the Table. The pressures at the same level of peroxide addition were also seen to be higher for the high throughput runs, which agrees with observations from the

conventional extrusion simulations. Also shown in Figure 3.20 are that the melt pressures were indeed zero beneath the vent of the ninth barrel section, and that the two kneading block sections downstream of the peroxide injection point were only partially-filled for the runs involving peroxide addition (for run 6 the second kneading block was fully-filled over less than half its length). Since the kneading block sections would not be properly able to dispersively mix the added peroxide into the melt unless they were fully-filled, this indicates that for reactive extrusion operation the screw configuration should be redesigned.

The melt temperature profiles in Figure 3.21 show that increased levels of peroxide addition were predicted to decrease temperature levels in the system. Again this was due to the reduced melt viscosities from the reaction, which led to reduced rates of heat generation by viscous dissipation in the melt. The temperatures at the same level of peroxide addition were also found to be higher for the low throughput runs, which again agrees with observations from the conventional extrusion simulations. As well, the differences at the end of the extruder between the profiles at the same peroxide level were found to be less at higher peroxide levels. Finally, Figure 3.21 shows that the computed melt temperatures did indeed remain well below the level at which thermal degradation of PP becomes significant, so the assumption that it could be neglected was valid.

3.5.6 Simulations of Peroxide-Initiated Controlled Degradation of Polypropylene - Part II

The predictive capabilities of the process model for PP controlled degradation reactive extrusion were assessed quantitatively by comparing predicted extrudate weight-average molecular weights to experimental values from Wang (1996), obtained at a screw speed of 60 rpm, a mass

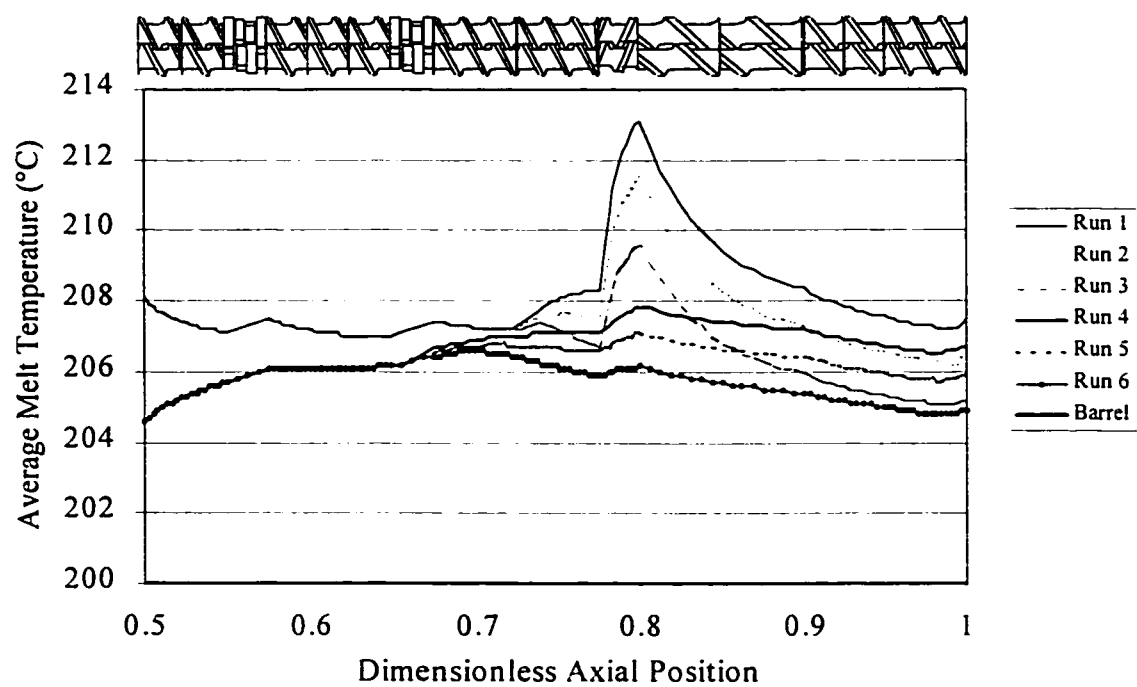


Figure 3.21: Average Melt Temperature Profiles for Reactive Extrusion Simulations

throughput of 1.4 kg/h, and 6 levels of peroxide addition ranging from 0.005 wt% (50 ppm) to 0.06 wt% (600 ppm). Table 3.8 shows a summary of the predicted extrudate molecular weights, along with some additional results of interest from the simulations. As can be seen in the Table, there were no problems in the simulations with using equation (3.6) out of its range of applicability. In all the simulation runs, the simulation algorithm could not converge to a single value of the position of the start of melting (point PSM), instead oscillating continuously between two values. This problem with the algorithm arises for simulations at low screw speeds and low throughputs. To deal with this, the degree-of-freedom profiles in the extruder were only computed downstream of the position of injection of the peroxide stream, at which point the polymer was assumed to be entirely molten, at 200°C and 0 kPa gauge.

Figure 3.22 compares graphically the experimental and predicted extrudate molecular weights. The agreement between the two was good at all levels of peroxide addition. The profile of measured molecular weights straddled the profile of predictions, and at the higher levels of peroxide addition the two profiles approached quite closely. These results were good, but unfortunately they were not as revealing as they could have been. Because of the low throughput used in the experimental runs, the average residence time of the polymer in the reaction zone was large, as indicated by the number of half-lives of the peroxide in the melt shown in the Table. This ensured that the peroxide was completely consumed in the degradation reaction, and so the extrudate molecular weight was independent of the extruder operating conditions and dependent only on the level of peroxide addition. Experimental runs with shorter average residence times in the reaction zone which lead to small but non-zero levels of peroxide in the extrudate would give better data for evaluation of the model predictions.

<i>Quantity or Parameter</i>	<i>Symbol</i>	<i>Run 1 Value</i>	<i>Run 2 Value</i>	<i>Run 3 Value</i>	<i>Run 4 Value</i>	<i>Run 5 Value</i>	<i>Run 6 Value</i>
Peroxide stream feed rate (wt% in melt)	$w_{I,In}$	0.005	0.010	0.015	0.02	0.04	0.06
Criterion for applicability of equation (3.6)	$\pi_{\dot{V},Min}$	0.43	0.43	0.43	0.43	0.43	0.43
Criterion for applicability of equation (3.6)	$\pi_{\dot{V},Max}$	0.43	0.43	0.43	0.43	0.43	0.43
Predicted extrudate weight-average molecular weight (kg/kmol)	$\bar{M}_{W,Out}$	261500	245600	231600	219000	180700	154100
Number of half-lives of peroxide in melt		15.4	15.2	15.1	14.9	14.3	13.9

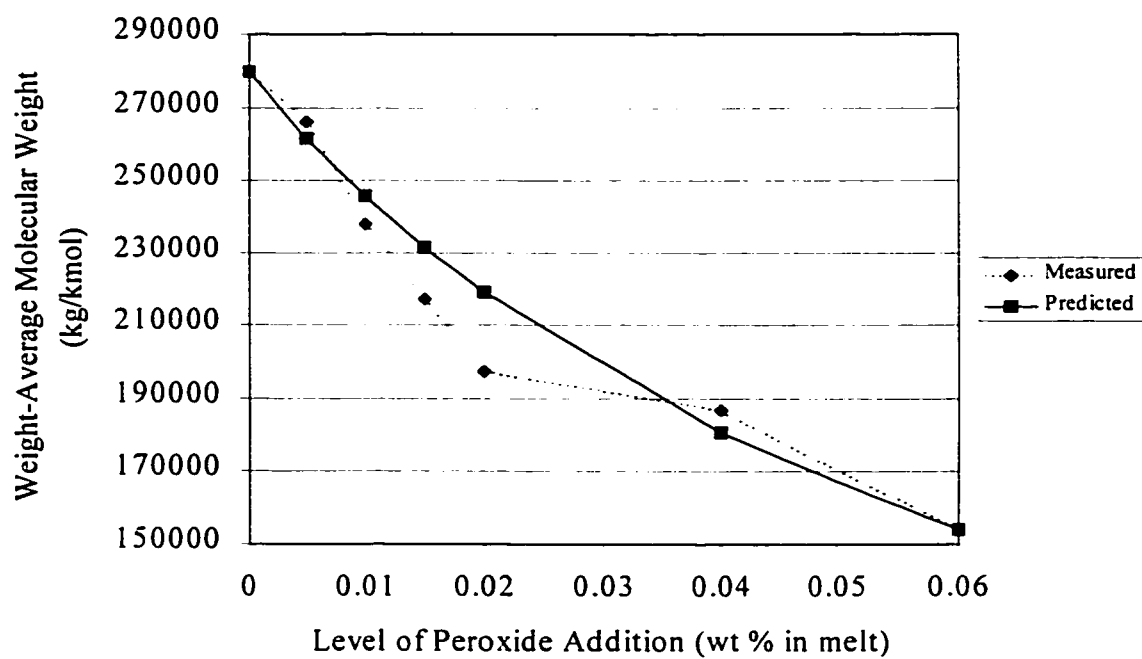


Figure 3.22: Experimental and Predicted Extrudate Molecular Weights

3.6 Discussion

In this section the simulation results of the previous section are discussed, following which the computational problems with the simulation algorithm are outlined. The section concludes with a discussion of the weaknesses of the composite process model for plasticating CSCO extrusion presented in this chapter, including suggestions for the solution of the most significant problems.

3.6.1 Simulation Predictions

Qualitatively, it can be said that the predicted process degree-of-freedom profiles for both the conventional and reactive extrusion simulations are acceptable. The profiles conformed to expectations and did not show any unexplainable features. The conventional extrusion simulation results showed that the effect of increasing mass throughput on the extruder operation was to raise melt pressure levels in fully-filled regions before flow restrictions, and thus raise filling levels; the effect of increasing screw speed was to reduce filling levels and raise melt temperatures. A problem was observed in several of the simulations with the dimensionless melt volumetric flow rate in a kneading block element being too low; the effect of this was the under-prediction of the pressurization capacity of this element in those simulations, and consequently an over-prediction of the fully-filled screw length in the region of the element (Potente et al., 1994). The sensitivity analysis results showed that predicted average residence times in conventional extrusion were most sensitive to perturbations in the parameter values for melt density and power-law index. The simulations of extrusion of PP with peroxide-initiated controlled degradation showed that the reaction was rapid at the prevailing conditions within the polymer melt in the extruder, to the extent that the extrudate weight-average molecular weight for all runs was essentially only a

function of the level of peroxide addition. Predicted extrudate molecular weights for 6 levels of peroxide addition at one screw speed and mass throughput were found to compare closely with measured molecular weights for the same conditions.

3.6.2 Simulation Algorithm Problems

In the performance of the simulation runs described in this chapter, two significant problems with the algorithm for the solution of the process model were encountered. The first was that at low screw speeds there was a threshold of mass throughput below which the algorithm would not be able to converge to a single value of the position of the start of melting, but would continuously oscillate between two values. The lower the screw speed was, the higher the throughput at which this threshold was reached. This is not too critical of a problem, but it limits the range of operating conditions at which simulations can be performed.

The second, more significant problem encountered in the simulations was that in every simulation but one, the leakage flow material balance of equation (3.9) gave negative values of the channel flow rate (i.e. the flow is towards the feed port of the extruder) in reverse conveying elements. The conditions for which this problem was greatest were those for which leakage flows were greatest (as shown in Table 3.5): low throughputs and high screw speeds. The temperature and solid volume fraction profile calculations cannot handle negative channel flow rates, so to deal with this problem the pressure changes in the reverse conveying elements were computed from equation (3.14) based on zero channel throughput, and the channel flow rates were computed based on the assumption of no leakage flows. In the one simulation run for which this was not an issue (run 2 of the conventional extrusion simulations), the same procedure was followed for the sake

of consistency. The effect of having to do this was that the computations overestimated the pressure drops over the reverse conveying elements, and consequently also overestimated the backup lengths upstream of them.

3.6.3 Process Model Weaknesses

The weaknesses of the models of the individual process phenomena that together comprise the composite process model of this chapter are assessed here, beginning with the models for solids conveying and melting. In the solids conveying zone of the extruder, the assumption that the average residence time of the material is simply equal to the minimum residence time due to forced conveyance is not entirely correct. It is known from visualization experiments using pellet form polymers that solid particles accumulate in the screw channels prior to the point at which the screw first becomes full of melt (Potente and Melisch, 1996). Thus, the true average residence time of the material in the solids conveying zone is greater than that for forced conveyance alone. The significance of this omission is fairly small though, since the contribution of the solids conveying region to the total average residence time estimates of the model is minor. Regarding the solids melting model, its primary weakness is that it does not provide any information on the progress of melting upstream of the position at which the screw channels become completely filled with melt. As shown in Table 3.5, for pellet form polymers the solid volume fraction at this point can be quite low, which begs the question of what went on prior to this position. Unfortunately, to date no such model has been formulated mathematically.

The melt conveying and pressurization model has a number of weaknesses, which have all been previously mentioned. The first is in the application of the screw characteristic curve

approximation equation to small pitch conveying screw elements for which the channel aspect ratio is relatively low. For such elements, the applicability of the lubrication approximation (i.e. the neglecting of the effect of the screw flights on the channel flow) is questionable. Based upon solution results of drag and pressure flows of Newtonian fluids in rectangular channels of different aspect ratios, an aspect ratio of at least 5 is necessary before the effect of the flights on the flow can be neglected (Middleman, 1977). This is a very significant problem, since small pitch screw elements are major contributors to pressurization in extruders, and as such it is important their pressurization capacity be properly represented. The effect of the use of this assumption is that the values of both the approximation equation coefficients ϕ_1 and ϕ_2 are overestimated for these elements. The influence of this on predictions of the pressurization capacities of these elements is difficult to say. One certain thing is that it leads to under-prediction of filling levels in partially-filled sections, due to an over-prediction of the drag flow capacities of the elements. The second major weakness of the model is that it does not reflect the true effect of the intermeshing region flow restriction in increasing the pressurization capacity of conveying screw elements. The result of this is melt pressures and backup lengths are over-predicted, though this is not overly significant for most systems, for which the fractional channel shift in the intermeshing region is small. Other problems with the model are that for reverse conveying elements it predicts negative channel flow rates at high screw speeds and low throughputs, and also that the range of applicability of equation (3.6) excludes very large (equivalent) pitch elements, such as kneading block elements with 30° angles-of-stagger.

All the above problems could be dealt with by reformulation of the screw characteristic curve approximation equations based on the melt conveying model of Huneault and Dumoulin

(1994). By modeling the flow in a screw element as drag and pressure flow in the channels superimposed on channel motion by forced conveyance, the true effect of the intermeshing region on pressurization would be reflected, and also for reverse conveying elements, since the drag and pressure flows in the channel are in the same direction, negative channel flow rates could never be computed. Also, by finite element method solution of the model equations, the true channel geometry could be used, allowing the pressurization capacities of channels over a wide range of aspect ratios to be properly determined, without the necessity of the use of the lubrication approximation.

The model with the greatest number of significant problems is the model for the melt temperature change in the extruder. The differential energy balance of equation (3.19) uses an estimate for the average channel shear rate based on drag flow only, which certainly is less than the true value for fully-filled channels. Hence the rates of viscous dissipation in these zones are under-predicted, leading to reduced melt temperature values. The energy balance also assumes that there is perfect temperature control on the barrel surface. This is not a good assumption, since heat transfer through the barrel is notoriously poor, especially for cooling (Todd, 1992). The true barrel surface temperatures will then be several degrees different than their setpoint values, with the greatest deviation likely in sections with fully-filled channels.

The greatest potential problem though with the model for melt temperature change is the omission of the contribution of leakage flows to temperature development in fully-filled screw channels. The simulations of this chapter have shown that most melt temperature growth takes place in fully-filled channels, and with the added influence of leakage flows this could be even more the case. The significance of this would be, of course, dependent on the magnitude of the

leakage flows in an extruder relative to the channel flow rates, which is likely to be smaller in large commercial extruders than in laboratory scale machines. The contribution of leakage flows could be significant due to the high shear rates and hence high rates of viscous dissipation in the radial flight clearances, which may result in the material emerging from the clearance at a much higher temperature than the bulk fluid in the channel. The effect of this omission could be the underestimation of temperature growth in fully-filled zones, with the accompanying over-prediction of melt pressures. As well, knowledge of the melt temperature in the flight clearance would permit more accurate determination of the melt power-law parameters there for equation (3.10), which could lead to larger computed values for the leakage flow rates. The one computational problem this approach would create is the feedback coupling of the temperature profiles in adjacent channels and flight clearances.

There are reasons to believe, however, that this omission is not a bad thing at all. Rauwendaal and Anderson (1994) performed a finite element simulation of non-isothermal flow of a non-Newtonian fluid in a two-dimensional region representing a cross-section of a SSE channel perpendicular to the flights, which included leakage flows. They predicted that the melt temperatures in the flight clearance would in fact remain quite close to that of the barrel surface, due to efficient heat transfer with the barrel wall across the very thin gap of the clearance. As well, Middleman (1977) specifically warns against the addition of this detail to the melt energy balance in extruder channels, saying that it may not be justified. He argues that the rheological response of a polymeric melt which rapidly passes into and out of the high-shear clearance region might be expected to show significant transient viscoelastic phenomena. It may be quite misleading to use a purely viscous fluid model to characterize the viscosity reduction due to the high shear rates in

the clearance region. As such, one should be wary of the temptation to produce more complicated (but not necessarily more realistic) models of flow in the flight clearance.

Lastly, the model for the peroxide-initiated controlled degradation of PP has two primary weaknesses, namely the assumptions in the solution algorithm that the added peroxide does not become mixed into the melt until the first fully-filled position downstream of the injection point, and also that it does not begin to decompose thermally until this point. The first assumption it was necessary to make since the kinetic model equations for computing the progress of the PP degradation reaction assume the free radical initiator is uniformly mixed into the polymer. The peroxide can only be added to the molten polymer at an axial position of partial-filling (and hence atmospheric pressure), and mixing in extruder channels is least efficient in partially-filled zones. Diffusion of the peroxide from the surface into the melt can also be considered negligible, due to diffusivities of even low molecular weight species in polymers being very small, of the order of 10^{-10} m²/s (Mark et al., 1993). Hence, it cannot be considered reasonable to assume that the peroxide is mixed into the melt prior to the first position of complete filling downstream of the injection point, at which point distributive mixing of the polymer from leakage flows and channel pressure backflows will begin. In well designed screws, this point will be in or just prior to a kneading block section, within which dispersive mixing from the chopping action of the kneading discs will rapidly mix the additive into the melt. This assumption does result in the largely surface degradation of the polymer that would occur in the partially-filled region near the injection point being missed, but this should not be too significant if the distance between the injection point and the first downstream point of complete filling is not too large. The second assumption was made simply for the sake of computational convenience. In reality the peroxide would begin to undergo

vigorous thermal degradation once it reached the prevailing temperatures in the extruder, even without mixing into the polymer melt. Published results from peroxide-initiated PP controlled degradation experiments in which the peroxide was only in contact with the polymer along a surface layer showed that the macrosegregation of the reactants resulted in a reduced initiation efficiency of the peroxide (Ryu et al., 1992). This was attributed by the authors to the loss of peroxide primary radicals by recombination to form stable products, as well as other side reactions. Thus, there certainly would be a loss of peroxide available for reaction with the polymer from the position of injection to the first downstream point of complete filling, but as long as this distance is not too great this problem should not be overly significant.

CHAPTER 4

RESPONSE SURFACE ANALYSIS OF EXPERIMENTAL AVERAGE RESIDENCE TIMES IN A CSCO EXTRUDER

4.1 Introduction

The average residence time of material in an extruder is one of the most important process variables in both conventional and reactive extrusion. Controlling the amount of time the material being processed is exposed to the high shear and temperature conditions of the extruder can be of critical importance in determining the quality of products made from mechanically and thermally sensitive materials, and in reactive extrusion applications the residence time of material in the system must be controlled so that sufficient time is allowed for the primary reactions to go to completion without allowing excessive times in which undesirable side reactions may take place. In normal practice, for an extruder with a particular geometry and screw configuration processing a given material, the average residence time of the material in the extruder is a function of the operating conditions, essentially the screw speed and throughput (the barrel temperature profile is normally not varied, and for a particular die the diehead pressure is dependent on the throughput). Because of the complicated behaviour of the extruder, empirical modeling is used to relate average residence times to screw speed and throughput. The standard experimental approach to this uses the one-factor-at-a-time strategy, in which RTD experiments are performed at several different levels of one operating condition, holding the other constant.

An alternative to this is response surface analysis, which uses optimal design theory concepts to obtain an empirical approximation to the true underlying process model. By comparison, response surface designs lead to better estimates of both linear and nonlinear effects

of variables, allow variable interaction to be detected, and give reliable estimates of the measurement error, with a modest experimental effort. In this chapter, the response surface technique is employed to determine an empirical relationship between experimentally determined average residence times (the response) and the operating conditions of screw speed and throughput (the factors), in conventional plasticating self-wiping co-rotating twin-screw extrusion of PP. A review of relevant literature on RTD studies in CSCO extruders is given, followed by the theory behind response surface analysis. The procedures followed in determining the polymer average residence times in the laboratory extruder are described, including data analysis techniques. The determined response surface is presented, and model diagnostics performed on the regression model. Average residence times predicted by simulation of the experimental runs using the composite process model solution algorithm of Chapter 3 are then presented and examined. The work in this chapter is described in Strutt et al. (1997).

4.2 Literature Review

The literature contains a number of experimental studies of RTD in CSCO extruders, employing various tracers and detection techniques. All come to the same conclusions regarding the effects of screw speed and throughput on average residence time, but occasionally they differ in their conclusions as to the effects of the operating conditions on the variance of the RTD. An early work was that of Rauwendaal (1981) who performed X-ray fluorescent tracer tests on a compounding screw with two kneading block elements, finding that high screw speed and high throughput each lead to shorter average residence times, and that decreasing throughput increases the variance of the RTD thus indicating better axial (distributive) mixing.

Potente and Ansahl (1990) considered the effect of different screw configurations on the RTD by looking at 4 different screws, 2 with reverse conveying screw elements after a kneading block section, and 2 simply with additional kneading blocks. Increasing screw speed was found to increase the variance of the RTDs, and the reverse conveying elements were found to increase average residence times. The authors also presented the results of fitting the measured RTDs to a statistical model.

Oberlehner et al. (1994) used an ultraviolet radiation absorbing tracer to determine local RTDs within individual conveying screw and kneading block elements, with the aim of forming a modular RTD of a complete screw. A major finding was that kneading blocks and reverse conveying screw elements each increase the RTD variance. Conventional RTD models (axial dispersion and tanks-in-series) were fit to the experimental data and gave good correspondence, save for the tail of the distribution which they failed to properly describe. An alternate RTD model was proposed based on a concept of residence time spectra, which did adequately represent this part of the distribution.

Puax and Ainsler (1994) used an in-line magnetic detection technique with iron powder as a tracer to measure the RTD of their extruder, finding as with other authors that the effects of increasing screw speed and throughput are to reduce average residence times, but also that increasing screw speed and throughput result in a decrease in the variance of the RTDs. The parameters for a tanks-in-series RTD model were determined from the data.

Kim and White (1994) described tracer tests using aluminum flakes on five different screw configurations with different combinations of reverse conveying screw and kneading block elements. The kneading blocks and reverse conveying elements were found to increase the average

residence times and the RTD variances. Increasing screw speed and throughput were also found to reduce average residence times and the variances of the RTDs.

Duley and Daigneault (1994) presented a comprehensive study of the effects of barrel temperature profile, screw speed, and throughput on the RTDs in 5 different screw configurations, using an on-line ultrasonic measurement technique. The barrel temperature was found to have little effect on the distribution, and screw speed and throughput were found to have the same effects as in previous studies. Filling level in the screws was also examined, and was found to increase with increasing throughput but decrease more quickly with increasing screw speed.

Chen et al. (1995) presented an on-line optical technique for RTD measurement using a laser light source and carbon black as a tracer. In their investigations of this measurement technique they found that increasing screw speed caused better mixing by increasing the variance of the RTD, while increasing the throughput had the opposite result.

Xie et al. (1997) described RTD experiments using an optical on-line measurement technique, involving two different sized CSCO extruders with three different screw configurations each, at several levels of screw speed and throughput. The authors demonstrated that for each of their runs the product of average residence time and screw speed (the dimensionless average residence time) increased in a nearly linear fashion with increasing values of the ratio of screw speed to throughput. Thus by linear regression they were able to obtain simple empirical relationships between average residence times in the screw configurations and the extruder operating conditions. As well, it was found that a screw configuration with two consecutive kneading block sections gave larger RTD variances than a configuration with the same two sections separated by a forward conveying screw element section.

4.3 Response Surface Analysis Theory

The key to the response surface analysis technique is the experimental design approach. In this work, a second-order central composite design is used, which allows any curvature of the response surface to be detected and modeled. The design consists of 12 experimental points over the domain of interest of the two independent variables, mass throughput and screw speed. The operating points consist of 4 center point replicates, 4 corner points (representing a 2^2 factorial experiment), and 4 axial starpoints (Box et al., 1978; Box and Draper, 1987). A second-degree polynomial regression model in terms of dimensionless independent variables is used to approximate the response surface:

$$(\bar{t}_R)_i = \beta_0 + \beta_1 x_{1i} + \beta_2 x_{2i} + \beta_{11} x_{1i}^2 + \beta_{22} x_{2i}^2 + \beta_{12} x_{1i} x_{2i} + \epsilon_i, \quad i=1, \dots, 12; \quad (4.1)$$

$$x_1 = \frac{n_0 - 150 \text{ rpm}}{50 \text{ rpm}}$$

$$x_2 = \frac{\dot{m} - 6.5 \text{ kg/h}}{3.5 \text{ kg/h}}$$

Here x_1 represents dimensionless screw speed, and x_2 represents dimensionless throughput. Figure 4.1 displays the relative positions of the operating points for the experiment. In matrix form this equation is:

$$\bar{t}_R = \underline{X} \underline{\beta} + \underline{\epsilon}; \quad \begin{aligned} E(\epsilon_i) &= 0 \\ \text{Var}(\epsilon_i) &= \sigma^2 = s_{Rep}^2 \end{aligned} \quad (4.2)$$

The average residence time error variance is estimated as the sample variance of the results for the 4 centre point replicate runs. The regression model parameter estimates are obtained by the standard least squares solution:

$$\hat{\underline{\beta}} = (\underline{X}' \underline{X})^{-1} \underline{X}' \bar{t}_R; \quad \text{Cov}(\hat{\underline{\beta}}) = s_{Rep}^2 (\underline{X}' \underline{X})^{-1} \quad (4.3)$$

95% confidence intervals for the parameters are then defined by:

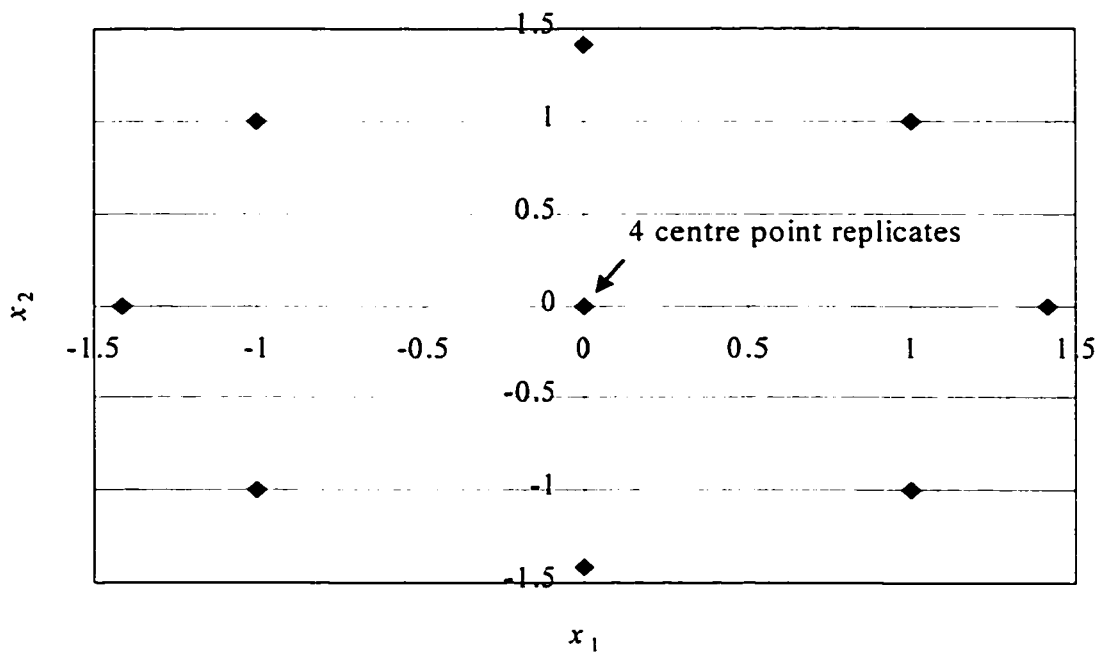


Figure 4.1: Second-Order Central Composite Design Operating Points

$$\hat{\beta}_j \pm t_{3,0.975} \sqrt{s_{Rep}^2 (X'X)^{-1} |_{j-1,j+1}}; \quad t_{3,0.975} = 3.182 \quad (4.4)$$

The number of degrees of freedom in the t -statistic is one less than the number of centre point replicates.

4.4 Procedures

4.4.1 Experimental Procedure

The extruder residence time distribution experiment was carried out on a Leistritz LSM 30-34 twin-screw extruder, equipped with a K-Tron LWFD5-200 loss-in-weight solids feeder, and fitted with a 2 hole capillary die, each hole having a length of 12 mm and a diameter of 4 mm, as well as a face plate on the end of the extruder. The extruder barrel sections have independent temperature control through electrical heating and water cooling. The screw geometry specifications and the screw and barrel configurations are the same as those used in Chapter 3 for the conventional extrusion simulations (shown in Table 3.3 and Figure 3.13). The open volume of the extruder face plate and die available for filling with molten polymer (minus the volume of the screw tips) was approximately 50 cm³. The profile of barrel temperature setpoints used in the experiments was the same as that for the conventional extrusion simulations, shown in Figure 3.13. The range of screw speeds was chosen to be centred around 100-200 rpm, and the range of mass throughputs around 3-10 kg/h. The upper limit on the range of mass throughputs was chosen so that at 100 rpm and this throughput the screw would not flood, and the lower limit was chosen so that the lowest throughput (for the axial starpoint in Figure 4.1 at the smallest value of x_2) would not be so small that the feeder could not handle it reliably. The complete set of operating

conditions for the 12 runs is given in Table 4.1. In the experiment, the runs were performed in random order.

The polymer used in the experiment was Montell KF6100 PP, a commercial isotactic PP provided in pellet form, which comes blended with 1 wt% Irganox 1010, an antioxidant used to retard oxidative degradation. The material used as a tracer was benzophenone, in crystalline form from BDH Laboratory Supplies. The molecular structure of benzophenone is shown in Figure 4.2. It was chosen as an infrared tracer - the carbonyl group in the molecule produces a sharp absorption peak in infrared wavelengths outside the absorption range of PP, even at low concentrations.

The procedure for each experimental run was as follows. The extruder was set to the appropriate screw speed and the feeder was started, and then 25-30 minutes were allowed to pass for the system to reach steady-state. The diehead pressure was then obtained, using a diehead pressure transducer connected to an Opto 22 data acquisition device, the output of which was sent to a personal computer via a serial data cable. A computer program sampled the serial data input every 2 seconds, and displayed the computed pressures on the computer monitor. The pressures of 15 consecutive samplings were averaged to obtain the diehead pressure values for each run, shown in Table 4.1. A measured mass of ground benzophenone crystals was then added to the feed throat of the extruder (constituting a pulse input) and a stop watch was started. In each case, the amount of tracer added was approximately equal to the mass of PP fed in one second for that run. This level was chosen as being of the order of magnitude of the smallest amount that could be added and still produce acceptably large absorbance peaks over the tail of the RTD.

For each run 10 extrudate samples were taken directly from the die, and allowed to solidify

Table 4.1: Extruder Average Residence Time Experiment Data

<i>Run</i>	<i>Screw Speed (rpm)</i>	x_1	<i>Mass Throughput (kg/h)</i>	x_2	<i>Diehead Pressure (kPa)</i>	<i>Experimental Average Residence Time (s)</i>	<i>Standard Deviation of RTD (s)</i>	<i>Dimensionless Variance of RTD</i>
1	100	-1	3	-1	694	166.1	31.1	0.035
2	200	1	3	-1	569	148.3	36.7	0.061
3	100	-1	10	1	1256	92.4	15.3	0.027
4	200	1	10	1	1148	65.9	23.1	0.123
5	150	0	6.5	0	1011	91.1	23.1	0.064
6	150	0	6.5	0	1016	94.2	24.9	0.070
7	150	0	6.5	0	974	97.9	25.2	0.066
8	79	-1.414	6.5	0	1045	135.8	25.1	0.034
9	221	1.414	6.5	0	961	95.7	23.9	0.062
10	150	0	1.55	-1.414	406	250.3	48.5	0.037
11	150	0	11.45	1.414	1262	73.6	16.2	0.048
12	150	0	6.5	0	1001	106.5	24.0	0.051

in air before being pelletized. The timing of the samples was based on an estimate of the average residence time for each run from a simulation run. The samples were taken at 15 s intervals immediately before and after this time, and 30 s intervals at larger times to capture the tail of the RTD. Thin films were prepared from the sample pellets in a hot press, which were then analyzed using a Nicolet 520 FTIR Spectrophotometer to a resolution of 2 cm^{-1} . Absorbance peak heights with two baseline points were taken from up to 3 locations on each film, at the carbonyl peak (corresponding to benzophenone) location of 1666 cm^{-1} and also the PP backbone peak of 809 cm^{-1} . The PP peak was used as an internal reference to compensate for the differences in sample thicknesses when comparing different spectra (Wang, 1996). The infrared transmittance spectrum for benzophenone is shown in Figure 4.2, and that for isotactic PP is shown in Figure 4.3 (Pouchert, 1981).

4.4.2 Data Analysis

Absorbance values obtained from FTIR spectrophotometry are related to the concentrations of absorbing species by means of the Beer-Lambert law (Miller and Stace, 1972):

$$A(\omega) = \log_{10} \frac{I_0}{I} = C \delta \epsilon(\omega) \quad (4.5)$$

In the case of polymers, the absorbing species is the structural unit. The measured absorbances at 1666 cm^{-1} were due to the presence of benzophenone only, and those at 809 cm^{-1} were due to the polymer only. Hence the ratio of the two absorbance values for each sample can be used to eliminate the effect of sample thickness:

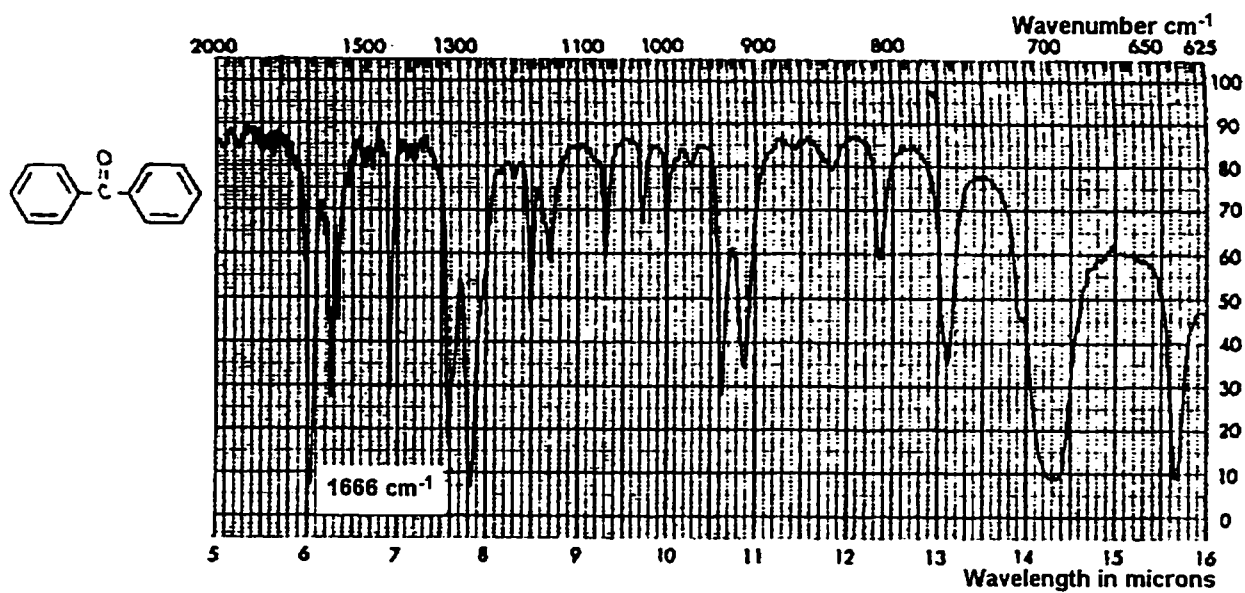


Figure 4.2: Benzophenone Infrared Transmittance Spectrum

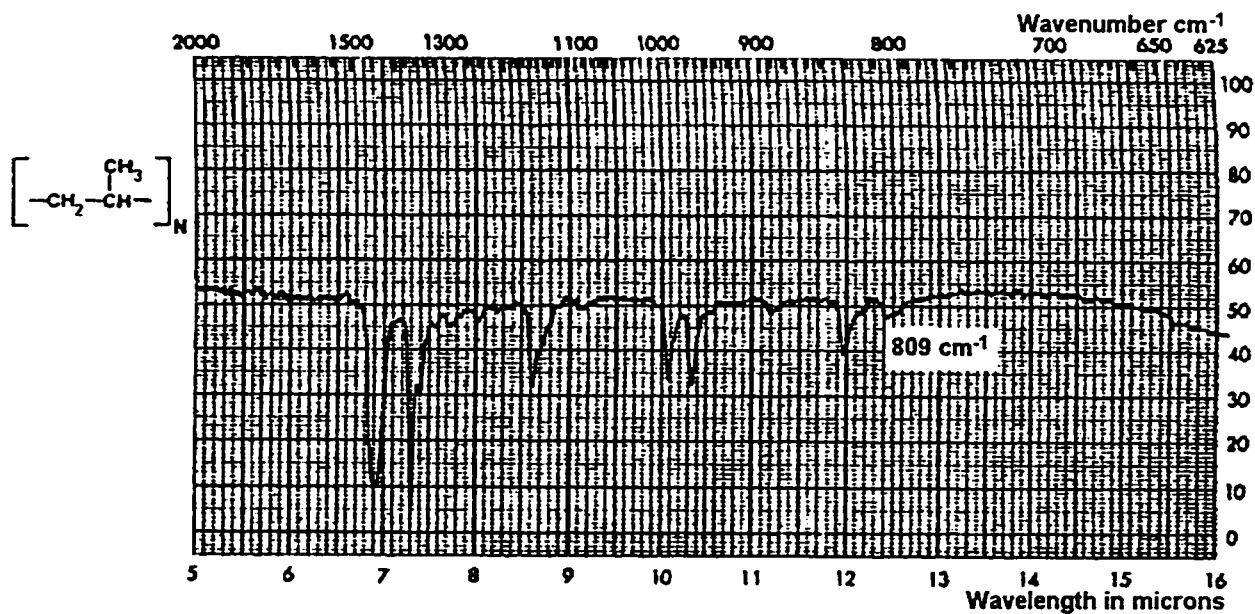


Figure 4.3: Isotactic PP Infrared Transmittance Spectrum

$$A_{Ratio} = \frac{A(1666cm^{-1})}{A(809cm^{-1})} = \frac{C_B \epsilon_B(1666cm^{-1})}{C_0 \epsilon_0(809cm^{-1})} = \frac{w_B \rho_{Blend} / M_B \epsilon_B(1666cm^{-1})}{w_{PP} \rho_{Blend} / m_0 \epsilon_0(809cm^{-1})} = k_C \frac{w_B}{1-w_B} \quad (4.6)$$

The above equation then relates the weight fraction of the tracer in each sample to the measured absorbances.

The value of the calibration constant k_C was determined by measuring the absorbances of samples of blends of known benzophenone weight fraction. Blends of low weight fractions of the tracer (1-5 wt%) were prepared in a single-screw extruder, and several extrudate samples from each run were pelletized, pressed into films, and analyzed with the Nicolet spectrophotometer. Figure 4.4 shows the average absorbance ratios for the reference samples plotted against the normalized tracer weight fractions. The calibration constant is equal to the slope of the regression line in the plot, which was 50.52.

With the benzophenone weight fraction in the extrudate at each sampling time determined by equation (4.6), the complete residence time distribution of the tracer was compiled for each run. The residence time distribution function is (Fogler, 1992):

$$E(t) = \frac{(\dot{m}/3600) w_B(t)}{\int_{t_{Min}}^{\infty} (\dot{m}/3600) w_B(t) dt} = \frac{\frac{A_{Ratio}(t)}{k_C + A_{Ratio}(t)}}{\int_{t_{Min}}^{\infty} \frac{A_{Ratio}(t)}{k_C + A_{Ratio}(t)} dt} \quad (4.7)$$

The value of this function is normalized by the total area beneath the curve of tracer mass flow rate in the extrudate, so that the fraction of the material fed to the extruder that spends an amount of time in the system between t_1 and t_2 is equal the area under the curve of $E(t)$ between those two times. The average residence time was then determined by numerical integration as the mean (or

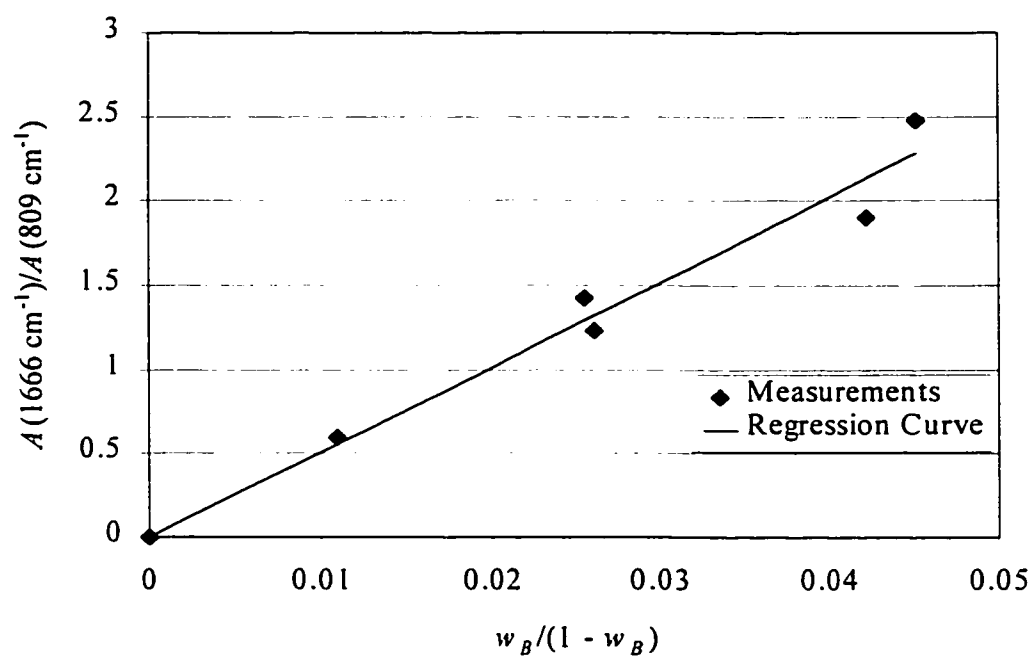


Figure 4.4: Benzophenone Absorbance Calibration Curve

first moment) of this function:

$$\bar{t}_R = \int_{t_{\min}}^{\infty} tE(t)dt \quad (4.8)$$

The variance of the RTD, which measures the spread of the distribution about the mean, was also computed numerically as the second moment of the RTD:

$$\sigma^2 = \int_{t_{\min}}^{\infty} E(t)(t-\bar{t}_R)^2 dt \quad (4.9)$$

4.4.3 Computer Simulation

As an additional means of quantitatively assessing the predictive capabilities of the CSCO extrusion process model presented in Chapter 3, the RTD runs were simulated and predictions of the average residence times of the polymer in the screws determined. The experimental diehead pressures shown in Table 4.1 were used in the simulations, along with the material data for virgin KF6100 PP given in Tables 3.1 and 3.2. The total predicted average residence time for each case was the sum of the contributions from the screws (as given by the simulation program) and that from the filled volume of the extruder face plate and die, which was computed by dividing the estimated filled volume of the face plate and die by the throughput for the run.

4.5 Results and Discussion

4.5.1 Experimental Average Residence Times

Table 4.1 shows the experimental average residence times for the 12 RTD runs. The times varied from a high of over 4 minutes to a low of just over 1 minute. To examine the degree of

success of the sampling and off-line analysis procedure used in this experiment in capturing the true RTD of the extruder, the aggregate extrudate tracer mass was computed for each run by numerical integration of the total area beneath the curve of extrudate tracer mass flow rate over the time span of the run. This quantity is the denominator of the residence time distribution function of equation (4.7). Table 4.2 shows the measured and computed tracer masses from the runs, and the percent error of the computed values. The Table shows that there were definite discrepancies between the computed and true masses, with the average absolute percent error for the runs being 19.1%. These errors can be attributed to the discretization of the profile of extrudate tracer weight fraction in each run due to the relatively small number of samples taken, as well as, to a lesser extent, error in the absorbance ratio calibration constant value and problems with nonuniformity of the sample films. One problem that was not encountered was violation of the assumption made in the determination of the absorbance ratio calibration constant that the tracer levels in the extrudate samples would not exceed 5 wt%; in fact the highest level observed in the experimental samples was 4.6 wt%, with the average level over all the analyzed samples being 0.9 wt%. Errors from the discretization of the tracer weight fraction profiles were further compounded by errors made in the timing of the samples, which resulted in the samples being maldistributed about the average residence time, and in some cases the tails of the profiles being missed due to the sampling beginning too late or ending too soon. For the runs with the latter problem, indicated by non-zero tracer levels in the first or last samples taken, it was arbitrarily assumed for the calculations that the tracer level in the extrudate was zero at a time 15 s before/after the first/last sample was taken. For two of the runs (runs 6 and 10) this was a significant source of error, and as shown in Table 4.2 led to under-computation of the tracer masses. For 9 of the remaining 10 runs, the tracer

Table 4.2: Actual and Computed Tracer Masses			
<i>Run</i>	<i>Actual Tracer Pulse Mass (g)</i>	<i>Computed Aggregate Tracer Mass in Extrudate (g)</i>	<i>Percent Error</i>
1	0.891	0.995	11.7
2	0.892	0.989	10.9
3	2.743	3.389	23.6
4	1.870	2.142	14.5
5	1.793	2.400	33.9
6	1.822	1.787	-1.9
7	1.840	2.216	20.4
8	1.823	2.715	48.9
9	1.890	1.468	-22.3
10	0.400	0.328	-18.0
11	3.051	3.654	19.8
12	1.820	1.886	3.6

masses were over-computed (all significantly so), which indicates that for these runs the widths of the peaks in the extrudate tracer weight fraction profiles were overestimated due to discretization effects. From these results it can be stated that the RTD measurement technique used in this experiment did not capture the true extruder RTD that closely, and as such the computed average residence times and RTD variances are not absolutely reliable. To deal with these problems, in future work an experimental technique should be used in which many more measurements of extrudate composition are taken in each run. The use of an on-line tracer detection technique, of which there are a number, would be the best way to accomplish this.

4.5.2 Variances of Experimental Residence Time Distributions

The experimental RTD standard deviations (square roots of the variances) and dimensionless variances for the 12 runs are given in Table 4.1. The variance of the RTD of a polymer in an extruder is a measure of the level of distributive (axial) mixing that the material undergoes as it passes through the system. Larger variances indicate more significant backmixing from leakage flows and channel pressure backflows in fully-filled conveying screw element and kneading block sections. The dimensionless variance (or coefficient of variation) is the variance divided by the square of the average residence time for a run. Its value is a relative measure of the broadness of the distribution. Comparison with the extreme values of zero for a plug flow reactor and 1 for an ideal stirred tank reactor gives insight into which system the extruder more closely approaches (Gendron et al, 1994).

Figures 4.5 and 4.6 show column plots of the standard deviations and dimensionless variances, respectively, of the experimental RTDs for the 9 operating points at which the runs were

performed. The values used in each Figure for the centre point column was the average value of the respective quantity for the 4 centre point replicates. Figure 4.5 shows a clear trend in the standard deviations towards larger values as mass throughput decreases, and also a (less clear) trend towards larger values as the screw speed increases. The observed throughput effect is in agreement with Rauwendaal (1981), and the observed screw speed effect is in agreement with Potente and Ansahl (1990) and Chen et al. (1995). Figure 4.6 shows that the dimensionless variances for all the runs were fairly small, with most less than 0.1. This indicates that the flow in the extruder much more closely approaches that of a plug flow reactor than an ideal stirred tank reactor, with distributive mixing being relatively minor and localized. There was a trend towards larger dimensionless variance values as the screw speed was increased, but no visible trend over the throughput axis.

4.5.3 Experimental Response Surface

The experimental average residence times for the 12 RTD runs given in Table 4.1 are used in equations (4.3) and (4.4), along with the sample variance of the average residence times of the centre point replicate runs of 44.3 s^2 , to generate 95% confidence intervals of the regression model parameter estimates:

$$\hat{\beta} = \begin{bmatrix} 97.4 \pm 10.6 \\ -12.6 \pm 7.5 \\ -50.7 \pm 7.5 \\ 4.0 \pm 8.4 \\ 27.1 \pm 8.4 \\ -2.2 \pm 10.6 \end{bmatrix} \quad (4.10)$$

It can be seen that all the parameter estimates were significant (their confidence intervals did not

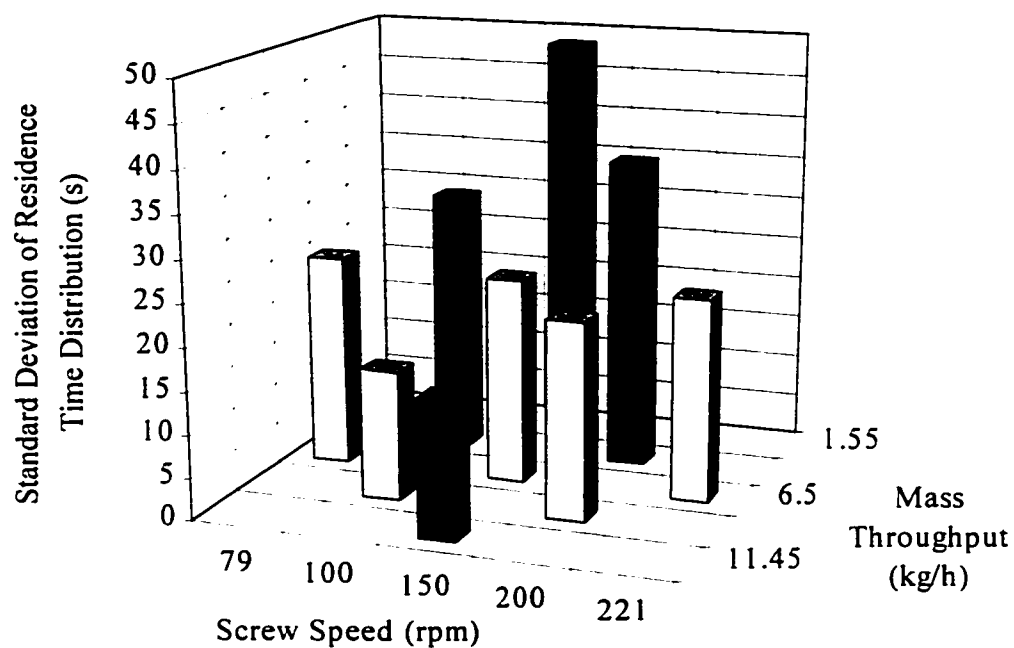


Figure 4.5: Standard Deviations of Experimental Residence Time Distributions

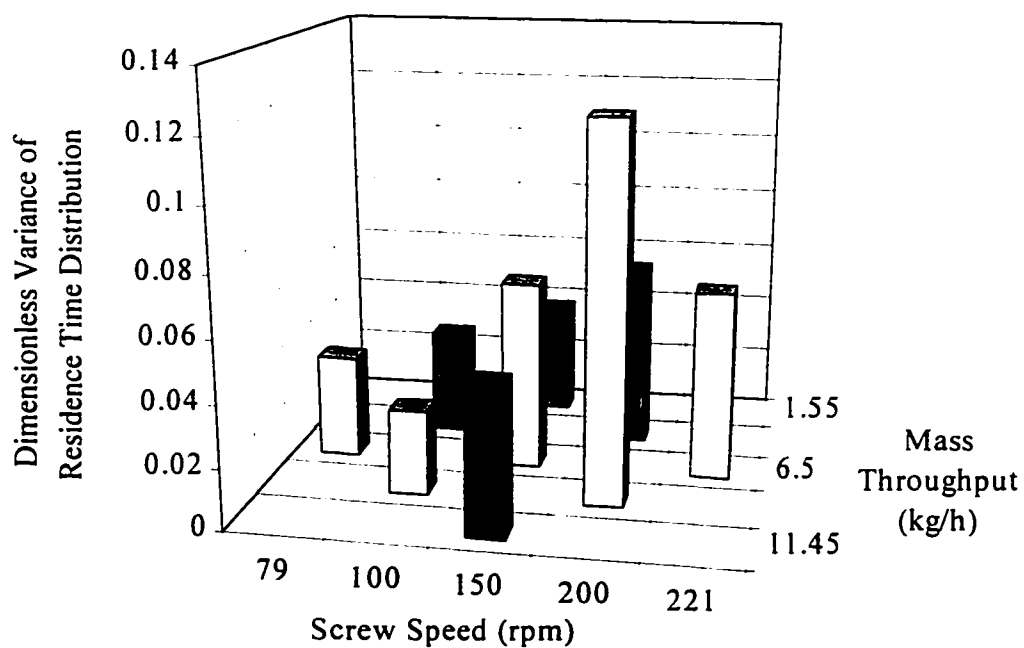


Figure 4.6: Dimensionless Variances of Experimental Residence Time Distributions

include zero) except for the two for the quadratic screw speed and interaction terms in the regression model. Reintroducing the dimensional independent variables, the equation for the experimental response surface was found to be:

$$\hat{t}_R = 322.8 - 0.25|n_0| - 43.2|\dot{m}| + 2.2|\dot{m}|^2 \quad (4.11)$$

Figure 4.7 shows a plot of equation (4.11), representing the experimental extruder average residence time response surface. Figure 4.8 shows a plot of contours of average residence time over the domain of consideration of the operating conditions. The two Figures show that the highest average residence times were observed for low throughputs and low screw speeds, and the lowest times for high throughputs and high screw speeds (the range of times is from around 190 s at 100 rpm and 3 kg/h to around 60s at 200 rpm and 10 kg/h). This quantitative model is consistent with the observations of other researchers, and also with our qualitative understanding of extruder operation: for high screw speeds the level of filling of the screws is lower and so the material spends less time in the extruder, and for high throughputs, material exits the extruder faster, again leading to a lower average residence time (Kim and White, 1994; Szydlowski and White, 1987). The shape of the surface in Figure 4.7 is concave up in the mass throughput axis. The increasing curvature as the mass throughput increases reflects the increased importance of the quadratic term in the regression model in this region. This same effect is observed in Figure 4.8 as increased spacing and curvature of the contours at higher throughput values. A mechanistic interpretation of this observation can be made, based on the two simultaneous effects that changing the throughput has on the extruder operation, which have competing effects on material average residence times in the system. Increasing throughput is known to increase the filling level in an

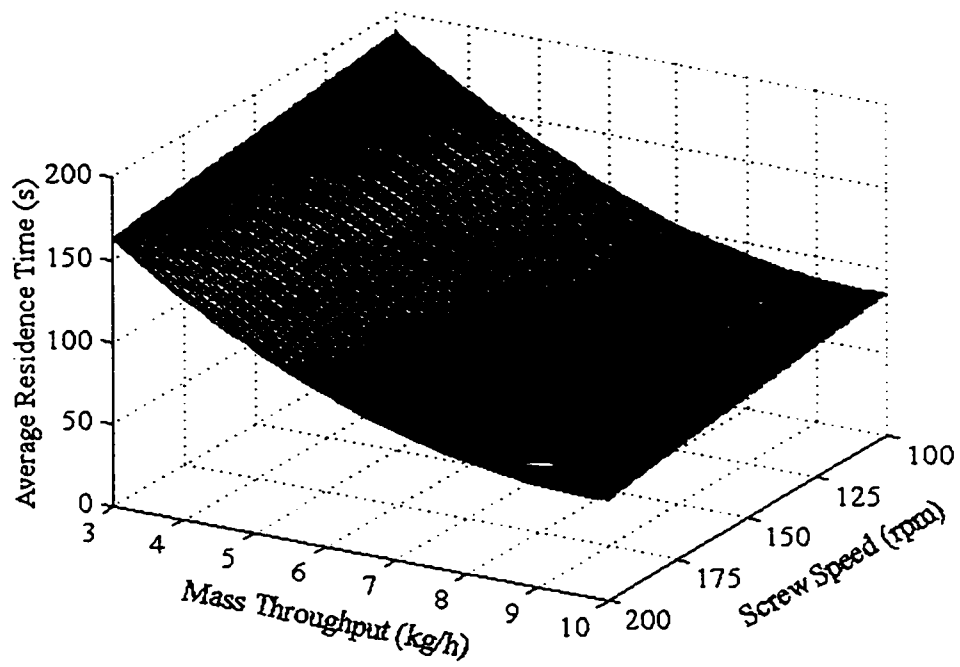


Figure 4.7: Experimental Extruder Average Residence Time Response Surface

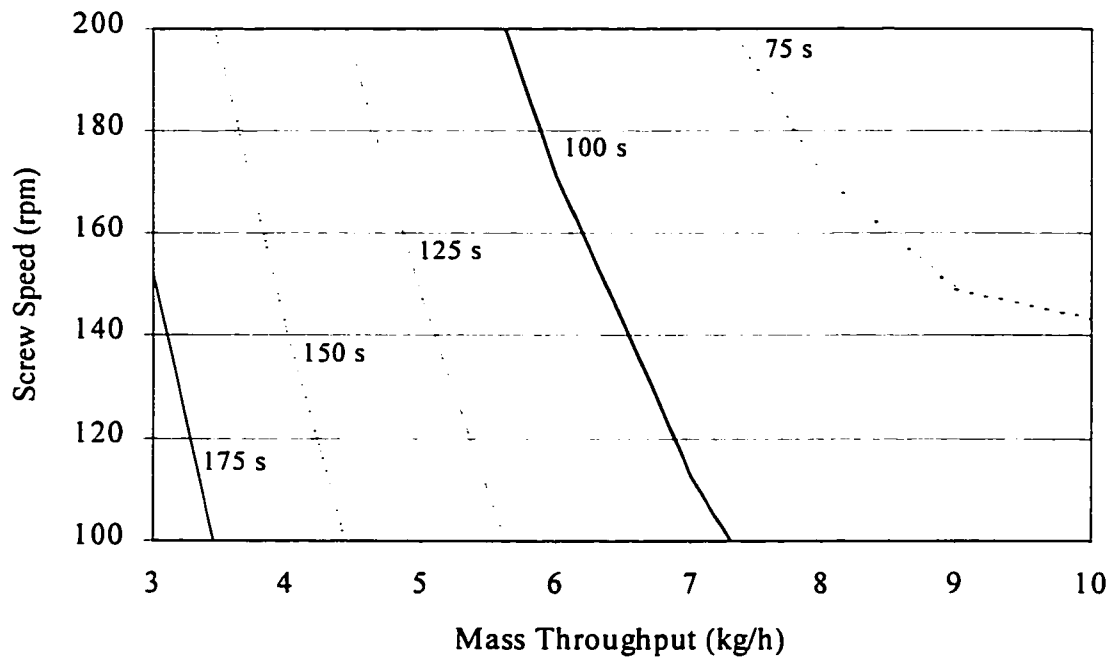


Figure 4.8: Experimental Extruder Average Residence Time Contours

extruder, which increases average residence times, while at the same time decreasing the times by removing material from the system more quickly. The increased curvature of the response surface suggests that for this system, as the throughput is increased the effect of increased filling levels in the extruder on average residence times becomes more significant.

4.5.4 Model Diagnostics

An important step in any empirical modeling effort is to check the validity of the model which has been fitted. This involves examining the analysis of variance table for the problem, as well as checking plots of the regression model residuals, which are the differences between the observations and the model predictions. Table 4.3 shows the analysis of variance table for this problem. The square of the multiple correlation coefficient, commonly known as R^2 , was found as the ratio of the regression and total sums of squares to be 0.959. The largest possible value of R^2 is 1, so this indicates that the regression model explained most of the variability in the experimentally determined extruder average residence times. Since the experimental design included replicate runs, an F test for lack of fit of the model can be performed. The test value of the F statistic as well as the critical value for the 99% significance level are:

$$F = \frac{MS(\text{Lack of fit})}{MS(\text{Replication})} = \frac{3092}{44.3} = 69.8; \quad F_{3,3,0.01} = 29.5 \quad (4.12)$$

Equation (4.12) shows that there was lack of fit of the regression model, at the 99% significance level.

Figure 4.9 shows a plot of the regression model residuals against the predicted average residence times. The magnitudes of the residuals are due to a combination of random error and lack of fit. For models in which lack of fit is not a problem, residual plots are examined to see whether

Table 4.3: Analysis of Variance Table			
<i>Source</i>	<i>Sum of Squares (SS)</i>	<i>Degrees of Freedom</i>	<i>Mean Square (MS)</i>
Regression	1.87×10^5	6	3.12×10^4
Residuals	9408	6	1567
Lack of fit	9275	3	3092
Pure error	133	3	44.3
Total	1.96×10^5	12	

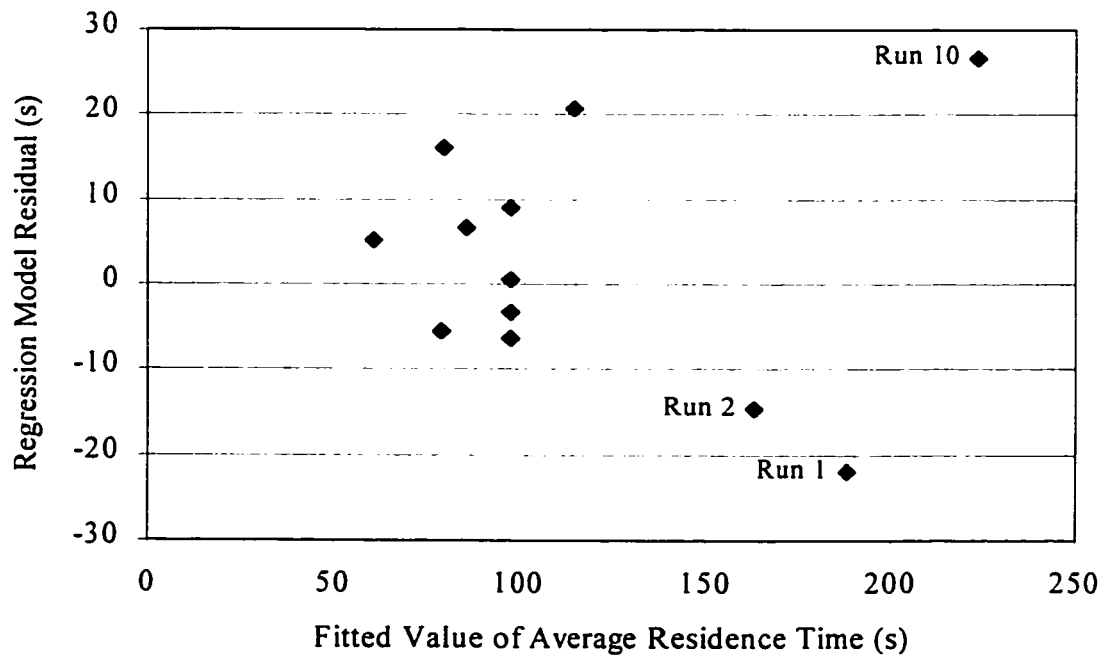


Figure 4.9: Regression Model Residual Plot

the assumptions regarding the distribution of the errors are valid (i.e. that the errors are normally distributed with mean of zero and constant variance). In this case though, the residual plot of Figure 4.9 indicates where the problem of lack of fit of the model was most acute. The Figure shows that this occurred at high average residence times, specifically for runs 1, 2, and 10, the runs for which throughput was the smallest. One possible explanation for this is that the variability of the experimental average residence times increased as the times themselves increased. This indicates that the regression model requires reformulation, to incorporate either a transformation of the observations or else a weighted regression approach.

4.5.5 Simulation Results and Response Surface

Table 4.4 shows the average residence times from the simulations of the 12 RTD runs. Runs 1 - 4 were the same as the conventional extrusion simulation runs described in Chapter 3. The problem of negative channel flow rates in reverse conveying elements was dealt with in the same way as in the simulations described in Chapter 3. Figure 4.10 shows a plot of the average residence times for the simulation runs against the experimentally determined average residence times. The Figure shows that the agreement between the two was very good over the full range of times, with the predicted times tending to be below the measured times at low values, and tending to be above the measured times at high values. The differences at high times can be at least partially explained by the fact that for the high average residence time runs, specifically runs 1 and 10, the throughput was low, and so the filling level was also low. Thus for these runs the problems in the calculations that lead to overestimation of filling levels had the greatest impact in inflating the average residence time predictions. These calculation problems are twofold: the computation

<i>Run</i>	<i>Average Residence Time from Simulation (s)</i>	<i>Criterion for Applicability of Equation (3.6) ($\pi_{\dot{V},Min}$)</i>	<i>Criterion for Applicability of Equation (3.6) ($\pi_{\dot{V},Max}$)</i>
1	178.2	0.19	0.45
2	150.6	0.16	0.39
3	90.7	0.32	0.73
4	64.1	0.22	0.53
5	93.6	0.21	0.51
6	93.6	0.21	0.51
7	93.6	0.21	0.51
8	124.2	0.29	0.66
9	82.5	0.19	0.45
10	272.7	0.15	0.38
11	68.2	0.27	0.64
12	93.6	0.21	0.51

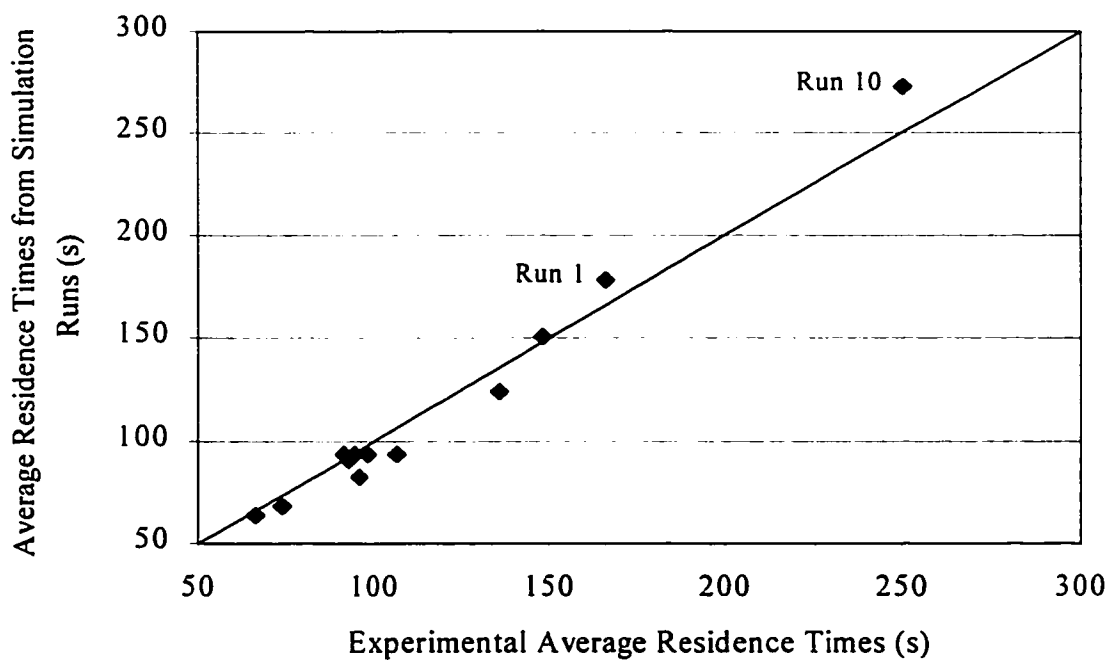


Figure 4.10: Comparative Average Residence Time Plot

of negative channel flow rates in reverse conveying elements, the correction for which causes the over-prediction of pressure drops over the elements and hence over-prediction of the backup lengths upstream of them; and the application of the screw characteristic curve approximation equation (equation (3.6)) to the long forward staggered kneading block section for which the dimensionless volumetric flow rate was out of range (as shown in Table 4.4), which results in under-prediction of the pressurization capacity of the element, and consequently an over-prediction of the fully-filled screw length in the region of the element.

The average residence times from the simulation runs were fitted to the 4 parameter regression model (the full model less the terms for which the parameter estimates were found to not be significant) used for the experimental average residence times. Reintroducing the dimensional independent variables, the equation for the response surface of predicted residence times was found to be:

$$\hat{t}_R = 362.1 - 0.28 |n_0| - 53.0 |\dot{m}| + 2.8 |\dot{m}|^2 \quad (4.13)$$

Figure 4.11 shows a plot of equation (4.13), representing the composite extrusion process model predicted average residence time response surface. Figure 4.12 shows a plot of contours of average residence time from the response surface. The two Figures are very similar in appearance to the corresponding plots for the experimental average residence times (Figures 4.7 and 4.8), which makes sense as it was previously shown that the measured and predicted times were in good agreement across the full range of times. The range of times that the response surface of Figure 4.11 covers is slightly larger than that for Figure 4.7: from around 200 s at 100 rpm and 3 kg/h to around 56s at 200 rpm and 10 kg/h. The larger range of average residence times is reflected in

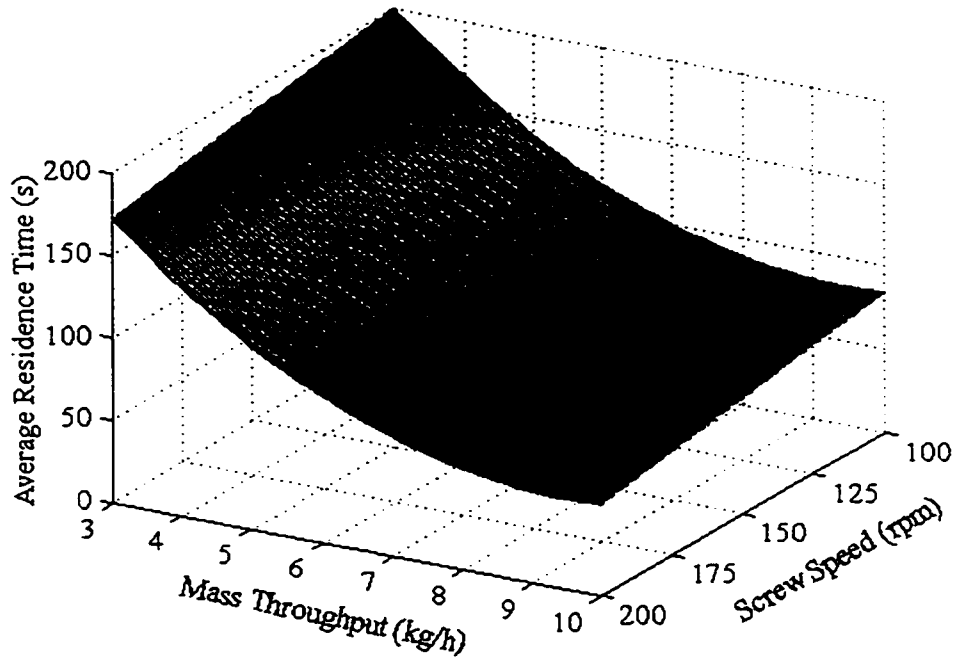


Figure 4.11: Extrusion Process Model Predicted Average Residence Time Response Surface

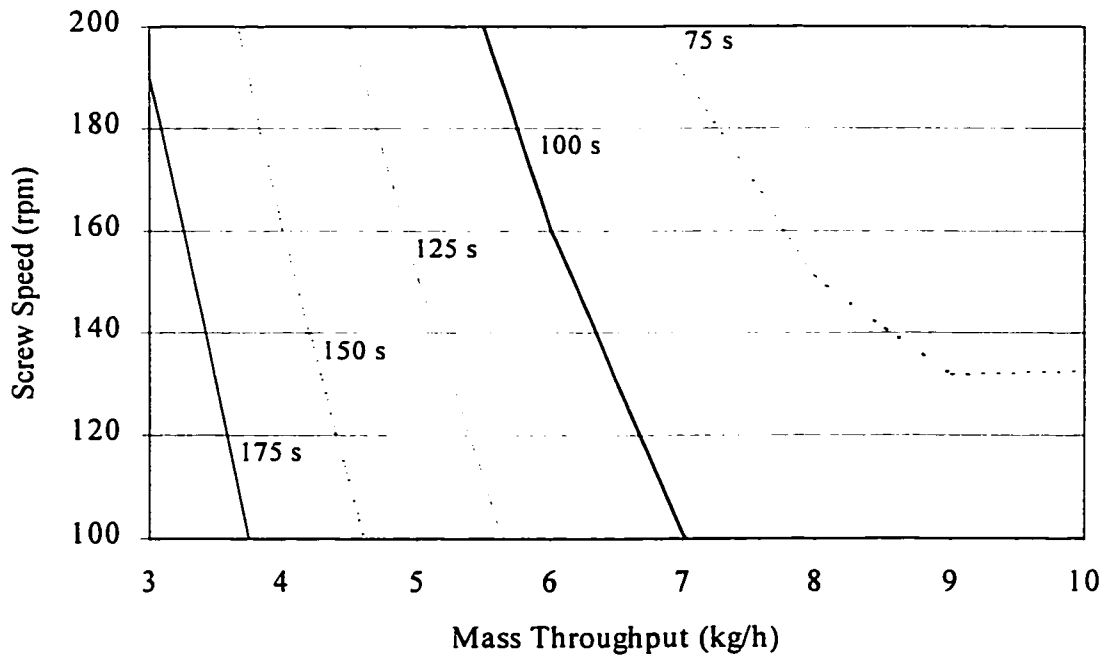


Figure 4.12: Extrusion Process Model Predicted Average Residence Time Contours

Figure 4.12 as a shift in the contours for the high times towards larger throughputs and a shift in the contours for low times towards smaller throughputs. The contours for 125 s were very nearly identical for both the experimental and simulation response surface equations.

CHAPTER 5

FINITE ELEMENT METHOD SIMULATION AND MIXING ANALYSIS OF POLYMER MELT FLOW IN A SINGLE-SCREW EXTRUDER CHANNEL

5.1 Introduction

In the previous chapters, a reduced-dimension macroscopic composite process model was used to simulate the steady-state behaviour of a complete modular CSCO extruder in conventional and reactive processing of PP. The effects of varying the extruder operating conditions, as well as the level of peroxide addition to the polymer melt, on the predicted profiles of average values of the process variables was studied. In the following chapters, simulations are described in which the same process parameters are varied (as well as others), but the effects of the changes are examined on the predictions of the flow of molten polymer at the microscopic scale, in the channel of a single-screw extruder in this chapter, and in the channel of a forward conveying screw element from a co-rotating twin-screw extruder in Chapter 6. Differential formulations of the process model equations for steady-state non-isothermal non-Newtonian flow of molten PP, including the peroxide-initiated controlled degradation reaction, are solved numerically using the finite element method (FEM) for a length of channel, yielding three-dimensional (3D) profiles of the field variables of velocity, melt temperature, melt pressure, and polymer molecular weight at the nodal points of the finite element meshes of the regions. In the simulations, the channel geometries, operating conditions, and peroxide levels and addition patterns are varied, and from the computed profiles of the field variables additional quantities of interest, giving more insight into the character of the flows, are calculated.

Principal among these additional calculated quantities are the area and flow mixing

efficiencies, which characterize the instantaneous conditions for mixing at a point in a flow field. Mixing is one of the most important functions of a screw extruder, since most polymer compounds are mixtures of one or more polymers with a variety of additives, and effective mixing is critical to the production of consistent, high quality extruded products. Mixing is defined as a process that reduces composition nonuniformity, by reducing concentration and temperature gradients in a flow. The basic mechanism of mixing is physical motion of the mixture components. Due to the extremely high viscosities of polymer melts, convection is the predominant mode of fluid motion in extruders, with even molecular diffusion being largely insignificant; the motion is a result of the shearing of the fluid in the screw channels. The mixing that arises from fluid convection is known as laminar mixing. This type of mixing belongs to the class called extensive mixing, which is described by the extent of deformation or strain to which fluid elements are exposed, without concern to the rate of application of strain or the magnitude of fluid stresses (Rauwendaal, 1991; Tadmor and Gogos, 1979). Theoretical analyses of laminar mixing generally are based on binary mixtures of immiscible fluids, for which the interfacial area density between the mixture components is a quantitative measure of the state of mixedness. Mixing efficiency measures indicate the conditions for growth of the infinitesimal area of a hypothetical interface separating the mixture components at a point in the flow. The instantaneous rate of change of the interfacial area depends on both the orientation of the interface and the mixing ability of the flow field. The area and flow efficiencies are respective measures of the approach to optimal of each of these things at the point in consideration.

The chapter begins with a review of the relevant literature on mixing analysis and finite element simulations of polymer melt flow in SSE screw channels, followed by an outline of the

conservation equations governing the fluid behaviour in the screw channel and the theory behind the mixing efficiency measures. The procedure for the FEM simulations is presented, and then results given for both conventional and reactive extrusion simulations of PP in two screw channel sections. Discussion of what the results indicate about the mixing natures of the flows is made, along with analysis of the predicted effects of the specified operating conditions and peroxide-initiated controlled degradation reaction on this nature. Finally, the reliability and accuracy of the simulation results are discussed, and ideas for future work presented. The work in this chapter is described in Strutt et al. (1998).

5.2 Literature Review

5.2.1 Finite Element Method Simulation of Melt Conveying in Single-Screw Extruders

Publications on finite element analyses of molten polymer flow in SSE channels have been appearing in the literature since at least the early 1970's. Recent increases in computing speed and memory capacity have allowed larger simulations to be performed, with more solution nodes and more realistic modeling of the flow system. An example is that of Spalding et al. (1993), who performed a finite element analysis of polymer melt flow in a three turn section of the metering zone of a SSE, using the commercial finite element code FIDAP. The true three-dimensional channel geometry was represented, including curvature and the radial flight clearance, and the flow was modeled as non-isothermal (with barrel and screw temperatures fixed) and non-Newtonian with the fluid having temperature-dependent viscosity. Predicted steady-state profiles of shear rate, velocity, melt temperature, and melt pressure were shown for a channel cross-section, for one simulation run at specified values of screw speed, mass throughput, and barrel and screw

temperatures. The computed down-channel pressure gradient was found to compare closely to an experimentally measured value for the same system.

Rauwendaal and Anderson (1994) took a different approach to finite element simulation of molten polymer flow in SSE channels, by making the assumption that the channel flow is fully-developed, and so only the two-dimensional region of the rectangular channel cross-section perpendicular to the screw flights must be meshed. This is known as 2.5D analysis. The flow was again modeled as non-isothermal (with the barrel temperature fixed and the screw surface insulated) and non-Newtonian, with temperature-dependent fluid viscosity and leakage flows included. The finite element equations were formulated and solved using a code written by the authors, and results were given as contour plots of velocity components and melt temperatures and pressures. Significant results were that the melt temperatures in the bulk of the channel were predicted to be considerably higher than those near the barrel wall, and also that the predicted temperatures in the flight clearance were lower than those in the channel, due to efficient heat transfer with the barrel surface. Increasing the flight clearance was predicted to worsen the problem of temperature non-uniformity across the channel, a result which was attributed to the resultant reduced circulation in the cross-section.

5.2.2 Theoretical Analysis of Laminar Mixing in Melt Conveying in Single-Screw Extruders

An early examination of mixing in SSE channels was that of Tadmor and Klein (1970), who based their analysis on velocity profiles derived for Newtonian isothermal viscous flow in a large aspect ratio channel (for which the lubrication approximation was made), with leakage flows

neglected. Classical laminar mixing theory shows that the growth of a randomly oriented interfacial area element in a fluid mixture subjected to large unidirectional shear is directly proportional to the total strain imposed, with the proportionality constant a function of the initial orientation of the element. As such, the authors stated that total strain can be used as a relative measure of mixing. The total strain that fluid elements undergo in a length of channel was computed on the basis of their starting depth in the channel, for several helix angles and pressure-to-drag flow ratio values. Smaller helix angles were found to increase the total strains, as well as increased back pressures (indicated by larger negative values of the pressure-to-back flow ratio). The authors went on to compute values of the weighted-average total strain, which is the sum of the total strains of the fluid elements across the channel cross-section, each weighted by the fraction of the flow rate experiencing it. The same trends against helix angle and pressure-to-drag flow ratio as for the total strain were observed.

Chella and Ottino (1985) took a more direct approach to analyzing laminar mixing in SSE channels, by simulating the growth along a length of channel of several hundred interfacial area elements distributed across the inlet plane. This is a better approach to mixing analysis than that used by the previous authors, as it does not rely on the indirect mixing measure of total strain. The authors again used a simplified model of the velocity profiles in the channel, which assumed Newtonian isothermal flow, and neglected leakage flows and flow in the channel depth direction. Profiles of flow-averaged relative growth values for the area elements against down-channel position were presented for a channel section of fixed length and cross-section aspect ratio, with helix angle and pressure-to-drag flow ratio varied. Qualitative agreement with the results of the previous authors was found, with extent of mixing being higher for small helix angles and larger

negative values of the pressure-to-drag flow ratio. The influence of the initial orientation of the area elements was also examined, and was found to have little effect on mixing. It was concluded that the mixing achieved in SSEs is generally poor, with the cross-channel flow being primarily responsible for the mixing that takes place. The flow in the extruder channel was characterized as exhibiting weak reorientation, with mixing efficiencies being partially restored in a periodic fashion due to flow recirculation at the screw flights. Since material interfaces in fluid mixtures subjected to large unidirectional strains become aligned with the direction of shearing, for which condition the rate of area growth is minimized, flow reorientation is necessary to maintain finite rates of area growth throughout the length of a mixer, either by randomizing the orientation of the area elements, or optimally by reorienting them normal to the direction of shearing (Tadmor and Gogos, 1979). Thus for the same total strain the extent of mixing in a SSE would be higher than in a mixer where no flow reorientation occurs (such as a helical annular mixer, consisting of two coaxial rotating cylinders), but less than in a mixer in which strong reorientation occurs (such as certain motionless mixers).

5.3 Theory

5.3.1 Model Equations

The flow of the molten polymer in the SSE channel is mathematically modeled by means of the conservation equations of mass, momentum, and energy, formulated for a steady-state, non-isothermal three-dimensional flow of an incompressible non-Newtonian fluid, with viscous dissipation and heat conduction included:

$$\begin{aligned}
\underline{\nabla} \cdot \underline{v} &= 0 \\
\underline{\nabla} \cdot \rho \underline{v} \underline{v} &= -\underline{\nabla} P - \underline{\nabla} \cdot \underline{\underline{\tau}} \\
\rho c_p (\underline{v} \cdot \underline{\nabla} T) &= \lambda \nabla^2 T - \underline{\underline{\tau}} : \underline{\nabla} \underline{v}
\end{aligned} \tag{5.1}$$

Implicit in the form of the energy balance equation are the assumptions that the melt thermodynamic properties are constant (i.e. not affected by changes in temperature or polymer molecular weight), and that the heat of reaction of the degradation process is negligible. Reactive processes are further described with species mass conservation equations (neglecting molecular diffusion) for the peroxide, as well as for the three moments of the polymer MWD:

$$\begin{aligned}
\underline{v} \cdot \underline{\nabla} I &= R_I = \frac{dI}{dt} \\
\underline{v} \cdot \underline{\nabla} Q_i &= R_i = \frac{dQ_i}{dt}; \quad i=0,1,2
\end{aligned} \tag{5.2}$$

The specific reaction rates in equation (5.2) follow from the kinetic model of equation (3.27), along with the closure method of equation (3.28). In all the simulations described in this chapter, the peroxide is taken as Lupersol 101, so the thermal decomposition rate constant expression of equation (3.30) is used, as well as the peroxide initiation efficiency value of 0.6. Worthy of note here is that the term for fluid inertia is included in the momentum conservation equation in equation (5.1), due to problems encountered in the simulations without it, specifically involving the computed peroxide species profiles.

The fluid is modeled as being purely viscous (i.e. elastic effects are neglected), with rheology described by a power-law model with temperature and weight-average molecular weight dependent parameters, and a viscosity plateau at low strain rates:

$$\underline{\underline{\tau}} = -\eta \underline{\underline{\dot{\gamma}}}; \quad \eta = \begin{cases} K(T, \bar{M}_w) \dot{\gamma}_0^{n(T, \bar{M}_w)-1}, & \dot{\gamma} < \dot{\gamma}_0 \\ K(T, \bar{M}_w) \dot{\gamma}^{n(T, \bar{M}_w)-1}, & \dot{\gamma} \geq \dot{\gamma}_0 \end{cases} \tag{5.3}$$

5.3.2 Mixing Efficiencies

Mixing analyses of the flow fields found in the simulations by numerical solution of the process model equations are performed on the basis of values of the area and flow mixing efficiencies across the flow domains. Although the modeling of each flow is performed with the implicit assumption that only one fluid is present, the simulation results can be assumed to be valid also for binary systems of immiscible fluids of similar densities and viscosities, with “passive” interfaces having negligible interfacial tension. Such mixtures are referred to as rheologically homogeneous, and have the property that flow and mixing within them are decoupled - i.e. the fluid mechanics of the mixture is unaffected by component distribution. Most fluid systems of practical interest do not behave this way, but analysis of the simpler idealization can provide valuable insight (Erwin, 1991). In a binary fluid system, mixing is associated with an increase in the interfacial area density; as such, mixing efficiency measures indicate the conditions for growth of an infinitesimal element of interfacial area at a point in the flow. This information gives insight into the mixing nature of the flow at the point, and also allows one to determine how this nature is influenced by changes in values of the model parameters.

The two mixing efficiency measures used in this chapter and the following are the area and flow efficiencies of Zerafati and Bigio (1994), which are appropriate for the analysis of three-dimensional flow fields. These measures together separate out the different factors that contribute to mixing, which for the growth of an interfacial area element at a point in a flow are the orientation of the element and the mixing ability of the flow field. Conceptually, the two mixing efficiencies together provide a basis for understanding the causes of inefficient mixing and also for finding ways to improve mixing. The following derivations are taken principally from Bigio

and Conner (1995).

The first measure, the area efficiency, indicates how closely the specified orientation of an interfacial area element at a point approaches the direction of maximum rate of growth. A small value of the area efficiency means the element is poorly oriented for growth; negative values are also possible, which indicate the element is actually oriented in such a way that it will shrink, not grow (a phenomenon known as demixing). The first step in deriving an expression for the area efficiency is to quantify the instantaneous rate of growth of the area element at the point in the flow. In Figure 5.1, the element is represented in its initial state as a plane at position \underline{X} bounded by the two differential vectors $d\underline{X}_1$ and $d\underline{X}_2$, with unit normal orientation \underline{N} (Ottino et al., 1981). The vectors are all defined relative to an arbitrarily oriented Cartesian coordinate system. After a material deformation, the plane is at the new position \underline{x} and is bounded by the deformed vectors $d\underline{x}_1$ and $d\underline{x}_2$, and has the unit normal orientation \underline{n} . For an incompressible fluid, the specific rate of stretching, α , of this plane is:

$$\alpha = \frac{dA_S/dt}{A_S} = -\underline{D}:\underline{n}\underline{n} = -\underline{n}\cdot\underline{D}\cdot\underline{n}; \quad A_S = \frac{|d\underline{a}|}{|d\underline{A}|} \quad (5.4)$$

$$\underline{D} = \frac{1}{2}[\underline{\nabla}\underline{v} + (\underline{\nabla}\underline{v})^T]$$

In the above equation, A_S is the relative area stretch, and \underline{D} is the rate-of-deformation tensor. A coordinate axis transformation is next applied to the equation to simplify expansion. Because the rate-of-deformation tensor is symmetric, its three eigenvectors are orthogonal unit vectors (Anton, 1981). If a coordinate axis rotation is applied, with the destination system of axes being the eigenvectors (also known as the principal directions), in the transformed coordinate system the rate-of-deformation tensor is diagonal, with elements equal to the three eigenvalues. The



Figure 5.1: Stretching of an Interfacial Area Element

transformation is carried out as follows:

$$\underline{\underline{D'}} = \underline{\underline{Q}}^{-1} \cdot \underline{\underline{D}} \cdot \underline{\underline{Q}} = \underline{\underline{Q}}^T \cdot \underline{\underline{D}} \cdot \underline{\underline{Q}} = \begin{bmatrix} \lambda_1 & 0 & 0 \\ 0 & \lambda_2 & 0 \\ 0 & 0 & \lambda_3 \end{bmatrix}; \quad \begin{array}{l} \underline{\underline{D}} \hat{n}_i = \lambda_i \hat{n}_i, \quad i=1,2,3 \\ \underline{\underline{Q}} = [\hat{n}_1 \ \hat{n}_2 \ \hat{n}_3] \end{array} \quad (5.5)$$

Note that the eigenvalues are ordered from largest to smallest (i.e. $\lambda_1 > \lambda_2 > \lambda_3$), and that the transformation matrix $\underline{\underline{Q}}$ is comprised of the three eigenvectors. In terms of the principal directions the specific rate of stretching becomes:

$$\alpha = -\underline{\underline{n'}} \cdot \underline{\underline{D'}} \cdot \underline{\underline{n'}}; \quad \underline{\underline{n'}} = \underline{\underline{Q}}^{-1} \cdot \underline{\underline{n}} = \underline{\underline{Q}}^T \cdot \underline{\underline{n}} \quad (5.6)$$

Expanding this yields:

$$\alpha = -\left[(n'_x)^2 \lambda_1 + (n'_y)^2 \lambda_2 + (n'_z)^2 \lambda_3 \right] \quad (5.7)$$

By the definition of the rate-of-deformation tensor, its diagonal elements are equal to the diagonal elements of the velocity gradient tensor, and hence its trace (or first scalar invariant) is equivalent to the equation of conservation of mass for an incompressible fluid. The consequence of this is that the eigenvalues of the rate-of-deformation tensor sum to zero:

$$I_D = \sum_{i=1}^3 D_{ii} = \nabla \cdot \underline{\underline{v}} = 0 = I_{D'} = \sum_{i=1}^3 D'_{ii} = \lambda_1 + \lambda_2 + \lambda_3 \quad (5.8)$$

Since λ_3 is the minimum eigenvalue, the above equation means that $\lambda_3 \leq 0$. Thus from equation (5.7), the maximum specific rate of stretching is achieved when the unit normal orientation vector of the interfacial area element is in the direction of the minimum eigenvalue, i.e. $\underline{\underline{n'}} = [0, 0, 1]^T$. At this orientation α is equal to $-\lambda_3$. The area efficiency is then defined as the specific rate of stretching normalized by this maximum value:

$$\eta_A = \frac{\alpha}{-\lambda_3} = (n_x')^2\beta + (n_y')^2\gamma + (n_z')^2; \quad \begin{aligned} \beta &= \lambda_1/\lambda_3 \\ \gamma &= \lambda_2/\lambda_3 \end{aligned} \quad (5.9)$$

The second mixing efficiency measure is the flow efficiency, which characterizes the mixing ability of the flow field at the point in consideration, in terms of its capability to create the potential for effective mixing. This is expressed quantitatively as the effectiveness of the flow field in converting the input mechanical energy into the magnitude of the minimum eigenvalue of the rate-of-deformation tensor, i.e. the maximum specific rate of stretching. The value of the flow efficiency at a point is independent of the orientation of any material interface at that point. The first step in deriving an expression for the flow efficiency is to write that the mechanical power input to the fluid per unit volume is converted either to kinetic energy or is dissipated because of the material viscosity:

$$P_{Input} = \frac{d}{dt} \left(\frac{1}{2} \rho v^2 \right) - \underline{\underline{\tau}} : \underline{\underline{D}} \quad (5.10)$$

Due to the extremely high viscosities of polymeric fluids, the latter term in the above equation dominates. Thus, for a power-law fluid the equation becomes:

$$P_{Input} = 2\eta \underline{\underline{D}} : \underline{\underline{D}} = 2K [2II_D]^{n-1} II_D = K [2II_D]^{n-1} = K |\underline{\underline{\dot{\gamma}}}|^{n-1}; \quad \begin{aligned} \underline{\underline{\tau}} &= -2\eta \underline{\underline{D}} = -\eta \underline{\underline{\dot{\gamma}}} \\ \eta &= K |\underline{\underline{\dot{\gamma}}}|^{n-1} \\ |\underline{\underline{\dot{\gamma}}}| &= \sqrt{\frac{1}{2} II_{\dot{\gamma}}} = \sqrt{2II_D} \end{aligned} \quad (5.11)$$

This equation indicates the relationship between the power input and the strain rate in the fluid. Next the second scalar invariant of the rate-of-deformation tensor (II_D), is expanded in terms of the eigenvalues of the tensor:

$$II_D = II_{D'} = \lambda_1^2 + \lambda_2^2 + \lambda_3^2 \quad (5.12)$$

Equation (5.12) is substituted into equation (5.11), and the result solved for the minimum eigenvalue:

$$\lambda_3 = -\frac{(P_{Input}/K)^{\frac{1}{n+1}}}{\sqrt{2}\sqrt{\beta^2+\gamma^2+1}} = -\frac{|\underline{\dot{\gamma}}|}{\sqrt{2}\sqrt{\beta^2+\gamma^2+1}} \quad (5.13)$$

Equation (5.13) states that the minimum eigenvalue is directly proportional to the strain rate (and hence the mechanical power input), and inversely proportional to the square root of the sum of the squares of the eigenvalue ratios. The flow efficiency is defined on the basis of this expression as:

$$\eta_F = -\frac{\lambda_3}{|\underline{\dot{\gamma}}|/\sqrt{2}} = [\beta^2+\gamma^2+1]^{-\frac{1}{2}} = [2(\beta^2+\beta+1)]^{-\frac{1}{2}} \quad (5.14)$$

The second eigenvalue ratio is eliminated using equation (5.8). Thus for different flow fields which give the same strain rate at a particular point in a flow, the highest flow efficiency at that point will belong to the flow field which has the largest magnitude minimum eigenvalue of its rate-of-deformation tensor, and hence the largest possible value of the specific rate of area stretch. The maximum value of the flow efficiency is $\sqrt{2/3}$ (0.816), which occurs for biaxial extension (or squeezing flow - the stretching of a sheet in two directions), for which $\beta=-0.5$. The minimum value is $\sqrt{1/6}$ (0.408), for uniaxial extension (the stretching of a material filament), for which $\beta=-2$. Another important class of 3D flows are those which are direct extensions of two-dimensional flows, for example simple shear flow between wide parallel plates and plane extension (the uniaxial stretching of a sheet with two sides constrained). For these flows $\beta=-1$, and so the flow efficiency is $\sqrt{2}/2$ (0.707).

Together, the area and flow mixing efficiencies separate out the factors that contribute to

effective mixing. If the input power to the fluid inefficiently creates small magnitude values of the minimum eigenvalue of the rate-of-deformation tensor, then little mixing will occur no matter how material interfaces are oriented. The same is true if a flow field capable of significant mixing is created efficiently, but the material interfaces are unfavorably oriented to the flow. Thus, the conditions for most effective mixing at a point in a flow are large values of both the area and flow mixing efficiencies.

5.4 Simulation Procedure

5.4.1 Model Parameter Values

The process model parameters for the simulations are the screw and channel geometry parameters, the polymer properties, and the assumed extruder operating conditions. The screw and channel geometry parameter values, given in Table 5.1, are for a laboratory-scale extruder with a single-flighted screw, and come principally from Tzoganakis et al. (1988a). The screw pitch is equal to the diameter, and the axial length is that for 4 screw turns. In the simulations, the channel geometry was varied by the use of two different pairs of values of channel depth and flight width. The second pair were chosen to give a much smaller channel aspect ratio than the first. The second flight width gives a channel width equal to that for a double-flighted screw having flights with the same width as the original single-flighted screw. Both channel depth values are relatively small, corresponding to the metering zone of the screw, just upstream of the die.

The polymer physical and thermodynamic property values, shown in Table 5.2, were also taken from Tzoganakis et al. (1988a). The PP melt chemorheology was represented with regression formulas for the power-law parameters against temperature and weight-average molecular weight,

Outer diameter	38.1 mm	
Pitch	38.1 mm	
Axial length	152.4 mm	
Channel depth	2 mm	3 mm
Flight width	6.35 mm	24.50 mm
Channel aspect ratio	15.0	3.9
Screw free cross-section area	185.7 mm ²	107.4 mm ²

Melt density	750 kg/m ³
Melt thermal conductivity	0.185 W/(m °C)
Melt specific heat capacity	2.428 kJ/(kg °C)
Entering weight-average molecular weight	330000 kg/kmol
Entering number-average molecular weight	43420 kg/kmol

which were determined using viscometric data obtained at three temperatures using 9 resins with different weight-average molecular weights (Tzoganakis, 1988). These data were chosen for use over those of Wang (1996), which were used in Chapter 3, since the range of weight-average molecular weights of the examined resins is larger, and the rheological characterization was performed at several different temperatures. The regression formulas are:

$$\ln K = -0.6294 \ln \bar{M}_w - 0.0243 T + 0.1364 (\ln \bar{M}_w)^2 \quad (5.15)$$

$$n = 1 - \frac{\chi \sin 2\theta + \sqrt{(\chi \sin 2\theta)^2 + 4(2 \sin^2 \theta - 1)(0.07 \sin \theta)^2}}{2(2 \sin^2 \theta - 1)}, \quad \begin{aligned} \theta &= \frac{\pi}{2} - \frac{1}{2} \tan^{-1} 0.00106 T \\ \chi &= \ln \bar{M}_w - \frac{0.0154 T - 1}{0.00106 T} \end{aligned} \quad (5.16)$$

Plots of the regression formulas over the ranges of temperature and weight-average molecular weight for which they were used in the extrusion simulations are shown in Figures 5.2 and 5.3, along with the original viscometric data. Figure 5.2 shows the predicted power-law consistency index decreasing with both decreasing molecular weight and increasing temperature. Figure 5.3 shows the predicted power-law index increasing with increasing temperature and also with decreasing molecular weight. The regression formula for the power-law index, given in equation (5.16), is a hyperbolic formula asymptotic to both the Newtonian value of 1 at low molecular weights, and to linear plots through the viscometric data at high molecular weights. The shapes of the curves were adjusted manually by modifying the parameter representing the distance between the foci of the hyperbola and the intersection point of the asymptotes, until the final value of 0.07 shown in equation (5.16) was chosen.

The operating condition values for the simulations are given in Table 5.3. The pressure-to-drag flow (PDF) ratio of a polymer flow in an extruder channel is defined as the ratio of the

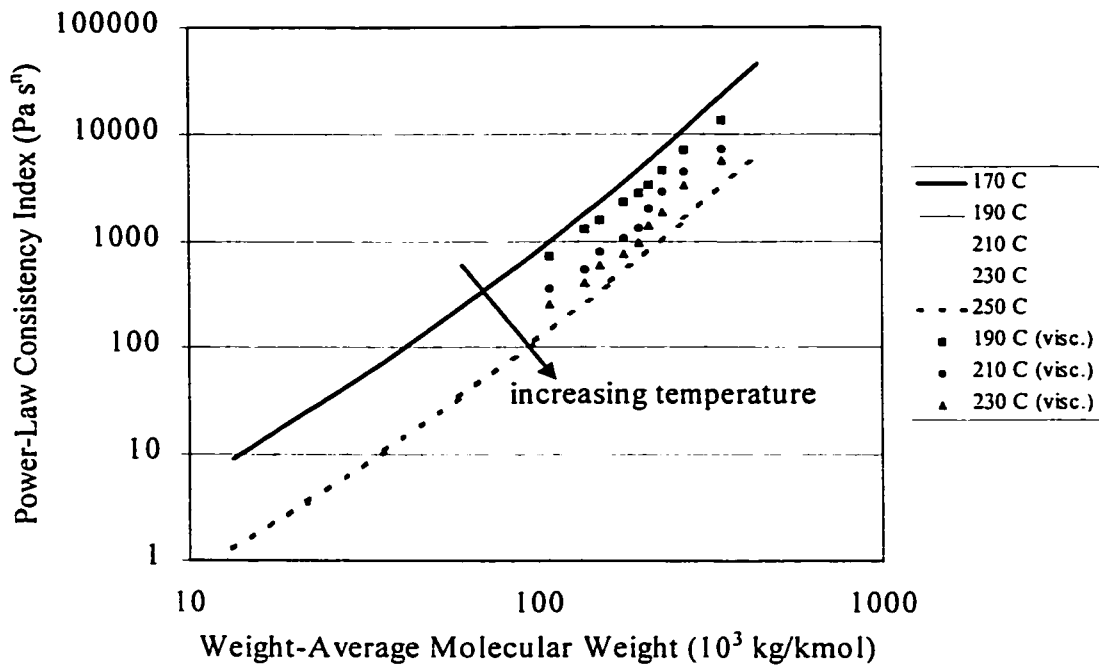


Figure 5.2: Power-Law Consistency Index Regression Formula Plot

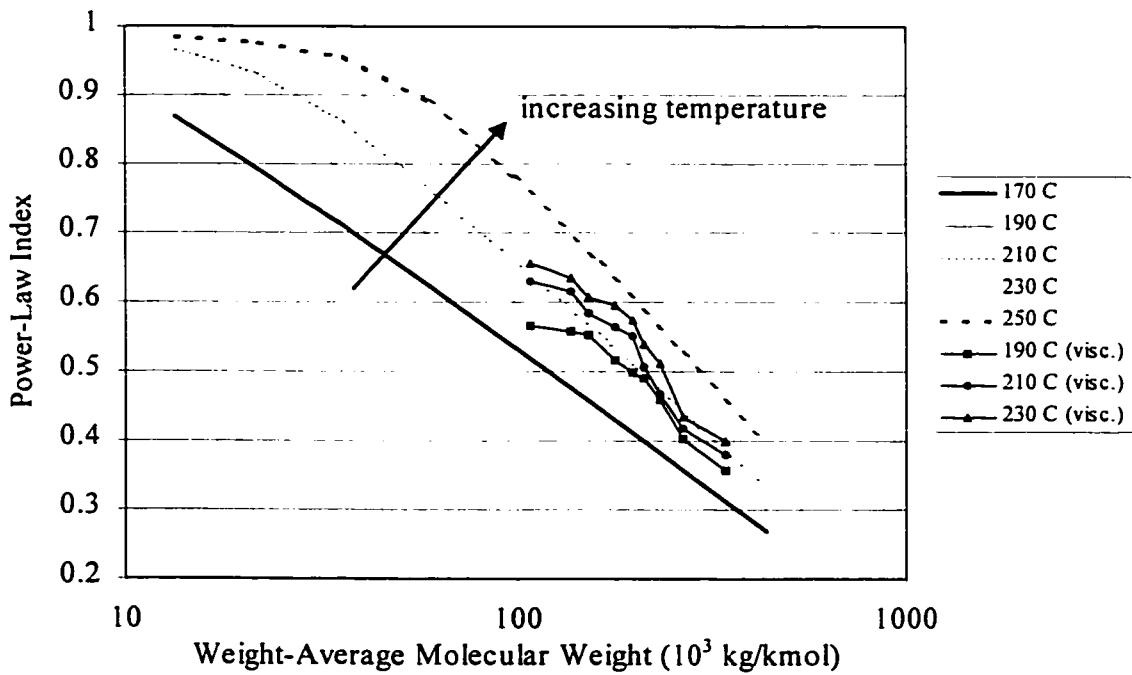


Figure 5.3: Power-Law Index Regression Formula Plot

pressure and drag flow terms in the screw characteristic equation for a Newtonian fluid:

$$\begin{aligned}
 Q_P/Q_D = r_D = \frac{H^2(-\Delta P/\Delta z)}{6\langle\eta\rangle v_{0z}}; \quad \langle\eta\rangle &= \frac{\eta_{In}\eta_{Out}}{\eta_{LM}} \\
 \eta_{LM} &= \frac{\eta_{Out} - \eta_{In}}{\ln(\eta_{Out}/\eta_{In})} \\
 \eta &= K(v_0/H)^{n-1} \\
 v_0 &= \frac{n_0}{60}\pi D_S
 \end{aligned} \tag{5.17}$$

The calculation uses an average value for the viscosity in the channel section, based on the inlet and outlet conditions, and using the nominal channel shear rate. The PDF ratio is also known as the throttle ratio, and in theory can vary in value from -1 to ∞ (Rauwendaal, 1986). A positive value of the PDF ratio corresponds to a flow in which the pressure is dropping in the direction of the screw channel, or in other words the pressure driven component of the flow is in the same direction as the drag component. The PDF ratio was chosen as an operating condition for the simulations since it provides a standard for comparison of flows of different screw speeds and viscosities (due to the effect of the degradation reaction) that is more meaningful than either mass throughput or pressure change alone. In particular, flows with the same PDF ratio have similar channel velocity profiles, and hence are of a similar laminar mixing character. In the simulations, the PDF ratio was varied between 0 (corresponding to pure drag flow) and 0.4 (giving a negative pressure gradient in the channel direction). Only non-negative PDF ratio values were used due to convergence problems encountered in simulations at values not much less than zero. The value for each run was specified indirectly by adjusting the mass throughput in the channel, as determined by the velocity profile on the inlet plane. The throughput could be varied independently of the screw speed since the channel section was examined in isolation; in a true SSE though the two

Inlet temperature	200°C	
Barrel wall temperature	220°C	
Screw speed	20 rpm	60 rpm
Pressure-to-drag flow ratio	0	0.4
Average inlet peroxide level	0 wt%	0.6 wt%

would not be independent, due to the coupling of the flow in the screw channel to that in the downstream die.

In the simulations, the screw speed and the peroxide level and addition pattern were also varied. The screw speed was either 20 or 60 rpm, and the average peroxide level in the melt at the inlet plane of the channel was either 0 wt%, or 0.6 wt% (6000 ppm). Hence both conventional and reactive extrusion simulations were performed. The high peroxide level was taken as the highest level considered in Tzoganakis (1988), and is ten times higher than the highest value considered in Chapter 3. In the reactive extrusion simulations, to address the problem that the distribution of peroxide in the melt stream entering the channel section which would be produced by an upstream injection port is unknown, three different inlet distribution patterns were considered, one uniform and two non-uniform. The non-uniform distributions were the barrel distribution, in which the peroxide was specified as entering only along the region of the inlet plane adjacent to the barrel wall, and the random distribution, for which local regions of higher peroxide weight fraction were specified randomly across the inlet plane. The barrel distribution is considered to be closest to that which would arise in a system with peroxide addition through an injection port across the barrel wall. The details on how these distributions were actually specified are given in the following subsection. Thus, in the simulations two different channel geometries were considered, along with two screw speeds, two levels of the PDF ratio, and four peroxide addition patterns. These lead to 32 possible different simulation runs.

5.4.2 Finite Element Method Details

The FEM simulations were carried out using version 7.62 of the commercial computational

fluid dynamics code FIDAP (developed by Fluent Inc. of Evanston, Illinois, USA), on an IBM Risc/6000 workstation with 128 Mb RAM. For each run a script file was written which included commands for the creation of the finite element mesh, commands for the specification of material properties and boundary conditions, and also simulation control commands which affected the derivation and solution of the finite element equations for the nodal unknowns. In the simulations, the three MWD moments were treated as independent chemical species, so that FIDAP could track the change in the polymer molecular structure as the free radical degradation reaction proceeded. Hence 9 degree of freedom profiles were computed by the software: melt temperature, melt pressure, three velocity components, peroxide weight fraction in the melt, and the three MWD moments.

The meshes for the two different channel geometries are each shown in an isometric view, a side view, and a cross-section view in a plane perpendicular to the screw axis, in Figures 5.4 and 5.5. The first geometry can be seen to have wide, shallow channels, and the second to have narrow, relatively deeper channels. The two meshes incorporate the true curvature of the screw channels, but do not include the radial clearance over the flights. The meshes are comprised of 4 boundary (two-dimensional) element groups along the outside, and one continuum (three-dimensional) element group within, representing the fluid. The boundary element groups are the inlet and outlet (each a lateral cross-section plane), the screw (which includes the inner curved surface of the mesh and the sides of the flights), and the barrel (the outer curved surface of the mesh). The reference coordinate system for each mesh is a Cartesian system, the origin of which is in the plane of the inlet, and for which the Z' axis coincides with the screw axis. The meshes include 60 layers of linear brick continuum elements, with 8 nodes each, located at the corners. This number was

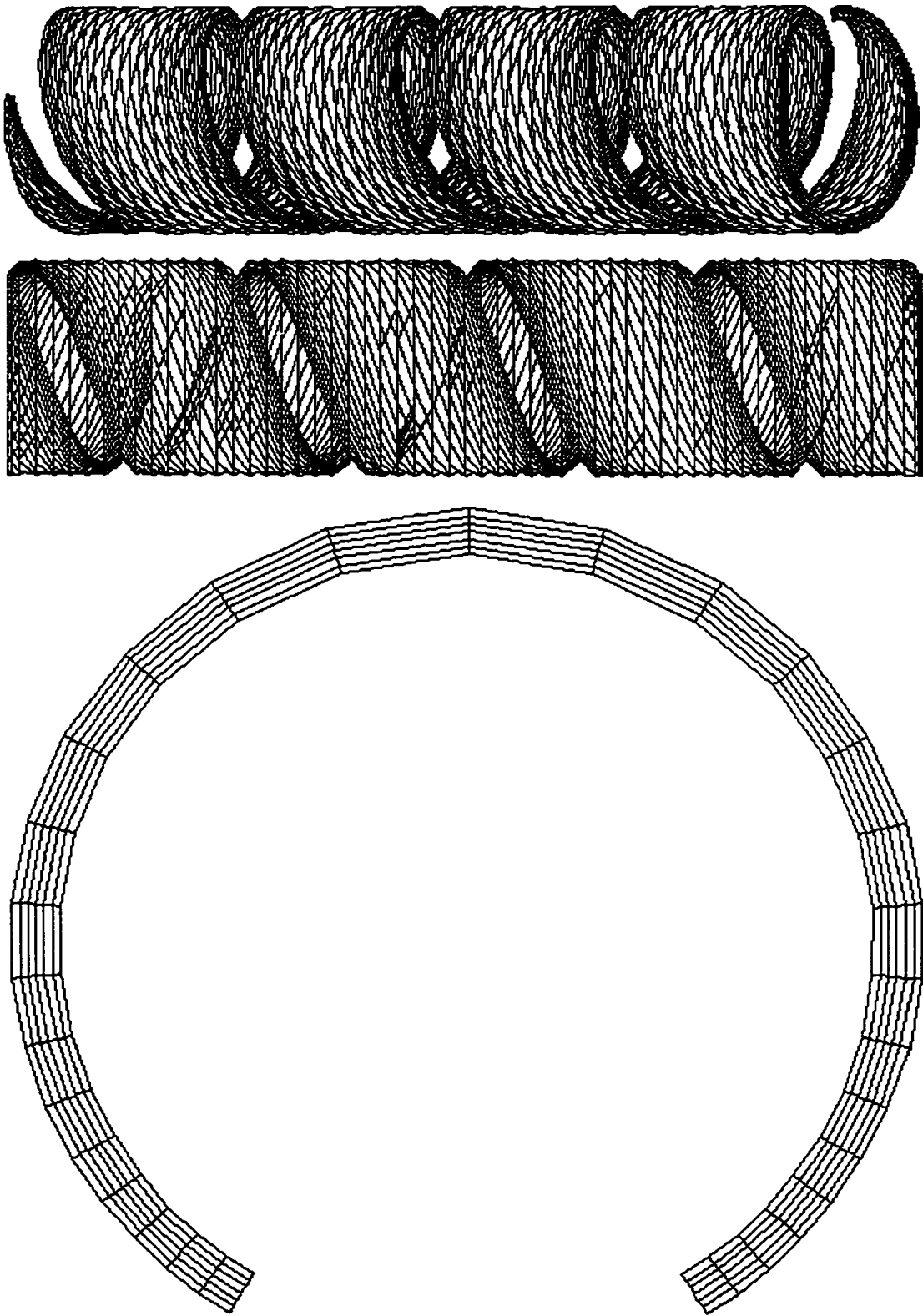


Figure 5.4: First Channel Geometry Finite Element Mesh

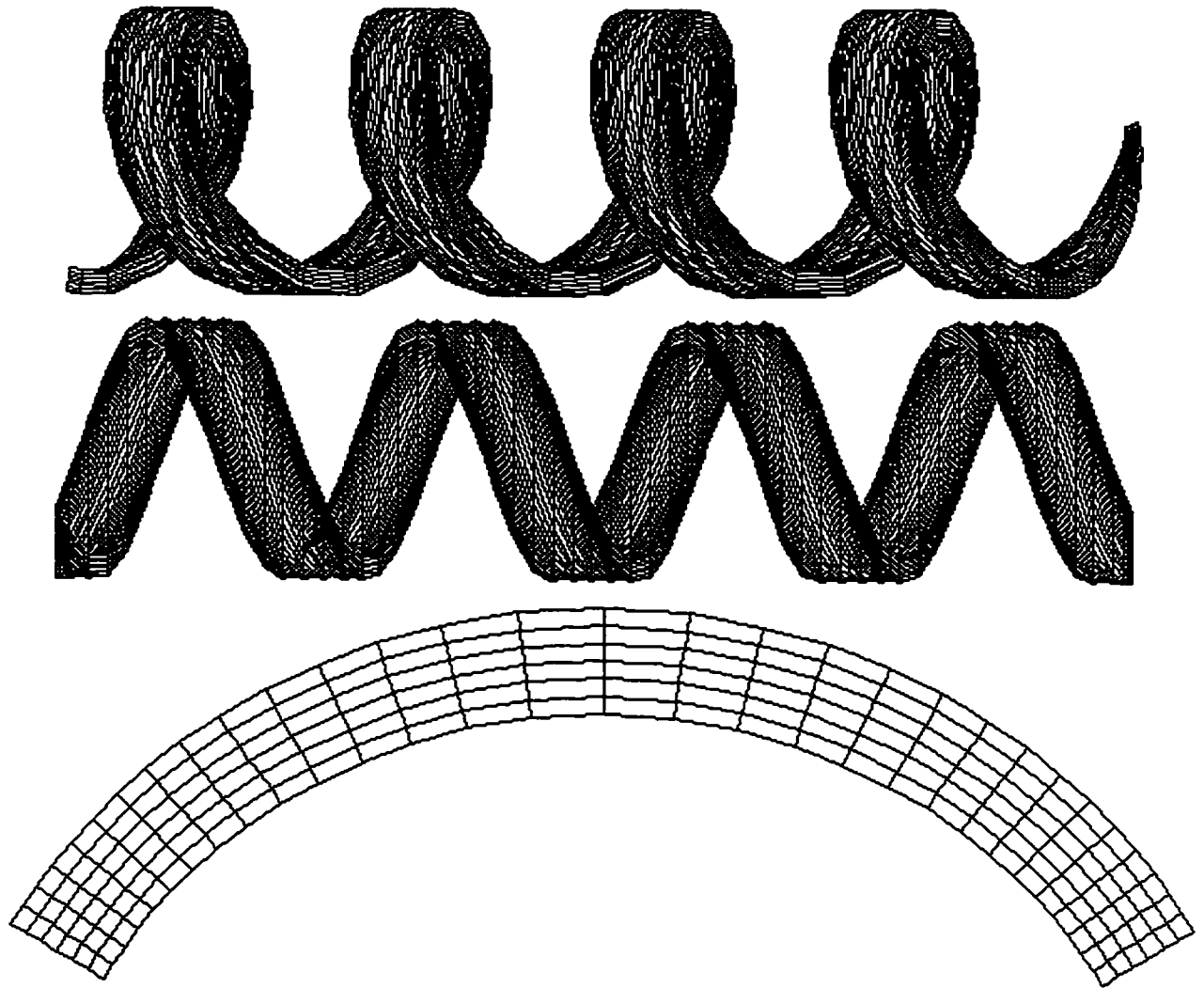


Figure 5.5: Second Channel Geometry Finite Element Mesh

determined by memory limitations, once the cross-section mesh had been fixed. The element axial lengths are uniform except for the first two layers after the inlet plane and the last four layers before the outlet plane, which are graded by a factor of 0.5 towards the respective planes. The mesh cross-sections contain 6 radial rows of 30 rectangular elements, graded slightly in the circumferential direction towards the sides of the screw flights. The total number of nodes in each mesh is 13237 (from the 61 cross-sections with 217 nodes each), and the number of elements is 15480 (comprised of 10800 continuum and 4680 boundary elements).

In the simulations, the melt density, thermal conductivity, and specific heat capacity were fixed at the constant values given in Table 5.2, and the viscosity was computed by a user-supplied subroutine. This is a Fortran subroutine supplied to FIDAP, which for each calculation point in the mesh finds the power-law parameter values from the regression equations (5.15) and (5.16), based on the temperature and weight-average molecular weight (determined from the MWD moment values) at the point, and then computes the viscosity from these values and the strain rate found from the velocity gradients at the point. The magnitude of the computed viscosity was bounded by using a lower limit of 10 s^{-1} for the strain rate. Using the inlet temperature in Table 5.3 and the entering weight-average molecular weight for the PP resin in Table 5.2, the maximum possible melt viscosity is then 2493 Pa s. The kinetic expression for the peroxide decomposition reaction was specified as a simple first-order polynomial in the peroxide weight fraction, and the expressions for the MWD moments were given in a user-supplied subroutine.

Boundary conditions for all the process degrees of freedom but pressure were specified on all the channel boundary surfaces, save the outlet. For each DOF, the boundary conditions were specified in the following order: inlet, barrel, screw. Hence the barrel conditions prevailed along

the outer edge of the inlet plane, and the screw conditions prevailed along the inner edges of the inlet plane and the contact lines between the tops of the screw flights and the barrel surface. Beginning with the velocities, the boundary conditions on the two solid boundaries (the barrel and screw surfaces) were specified on the basis of the no slip condition and the standard kinematic reversal assumption for the modeling of screw extruders, which has the screw being stationary and the barrel turning in the opposite direction to the true direction of screw rotation, at the same angular velocity. Hence there was a constant tangential velocity at every point on the barrel surface. This assumption can be justified due to the large screw diameter and small channel depth for each channel geometry, which result in the curvature effect on the melt velocity profile being negligible. On the inlet plane, the three velocity components at each node were computed by a user-supplied subroutine, based on the well known analytical solutions to the simplified forms of the momentum conservation equations for extruder channel flow (for steady-state fully-developed flow of a viscous Newtonian fluid in a large aspect ratio channel) (Middleman, 1977):

$$\begin{aligned} v_x(y) &= v_{0x} \frac{y}{H} \left(3 \frac{y}{H} - 2 \right) \\ v_z(y) &= v_{0z} \frac{y}{H} \left[1 + 3r_D \left(1 - \frac{y}{H} \right) \right] \end{aligned} \quad (5.18)$$

These profiles are for the channel cross-section perpendicular to the flights, and are written for a coordinate system embedded in the bottom of the channel. The effect of the flights on the flow is neglected, so v_y is taken as 0 everywhere. The cross-channel velocity (v_x) profile is derived to give a zero net flow rate, and has the feature that the sign of the velocity changes at two thirds the channel height, with drag flow above this level and pressure backflow below it. The down-channel velocity (v_z) profile is a function of the PDF ratio based on inlet conditions. The channel section

inlet plane is normal to the screw axis, not the flights, so the velocity profiles are modified by a coordinate axis rotation, and the channel curvature is represented by replacing the depth with the radius, yielding:

$$\begin{aligned}
 v_{x'}(r,\theta) &= -\frac{v_0 \sin\theta}{H^2}(r-0.5D_S+H)[H+3(0.5D_S-r)(r_D \cos^2\phi_S - \sin^2\phi_S)] \\
 v_{y'}(r,\theta) &= \frac{v_0 \cos\theta}{H^2}(r-0.5D_S+H)[H+3(0.5D_S-r)(r_D \cos^2\phi_S - \sin^2\phi_S)] \\
 v_{z'}(r,\theta) &= \frac{3v_0 \sin 2\phi_S}{2H^2}(r-0.5D_S+H)(0.5D_S-r)(r_D+1)
 \end{aligned} \tag{5.19}$$

Here the velocity component directions are the FIDAP global coordinate system directions, and the nodal point position is specified using the polar coordinates r and θ . Figure 5.6 shows plots of the velocity profiles predicted by equation (5.18) for several values of the PDF ratio, as well as the corresponding axial velocity profiles given by $v_{z'}$ in equation (5.19) (Tadmor and Gogos, 1979).

The temperature boundary conditions were straightforward, with the melt stream specified as entering the channel section at the uniform temperature given in Table 5.3, the barrel wall held at the constant temperature also given in Table 5.3, and the screw surface assumed insulated (i.e. a zero heat flux condition was applied). For the MWD moments, zero flux boundary conditions were specified on the screw and barrel surfaces, and a uniform profile for each was specified on the inlet plane, with the values computed from the molecular weights of the undegraded polymer. For the peroxide weight fraction, zero flux boundary conditions were also used for the screw and barrel surfaces, but on the inlet plane a user-supplied subroutine specified the nodal values based on the selected peroxide distribution. For the zero and uniform distributions, constant values of the peroxide weight fraction were used at every node. For the barrel distribution, the weight

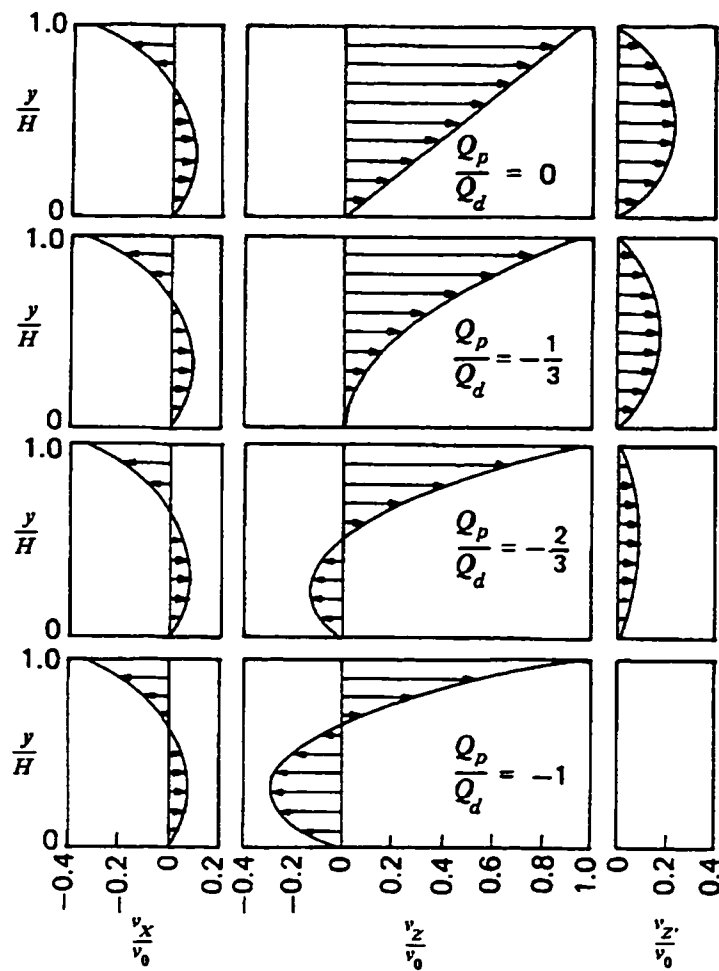


Figure 5.6: Inlet Velocity Profiles For Different Pressure-to-Drag Flow Ratios

Table 5.4: Maximum Inlet Peroxide Levels for Non-Uniform Distributions		
<i>Distribution Pattern</i>	<i>First Channel Geometry</i>	<i>Second Channel Geometry</i>
Barrel	4.04 wt%	3.98 wt%
Random	1.39 wt%	1.47 wt%

fraction was set at zero at every node except for the 62 nodes on the outer two rows of the mesh (next to the barrel wall), at which a constant, relatively high level was used. For the random distribution, the weight fraction was set at a high level at 100 of the 217 nodes on the inlet plane, and at zero on the remaining nodes. The choice of the 100 nodes was made in a pseudorandom manner, with the aid of a table of random numbers (Beyer, 1968). The high peroxide levels used for both channel geometries for the barrel and random distributions are shown as weight fractions in Table 5.4. The values were determined to give the same average inlet peroxide levels as the respective uniform distributions. The appearance of the two non-uniform peroxide addition patterns are shown for both channel geometries in Figures 5.7 and 5.8. In the plots, red represents the highest peroxide weight fraction and blue the lowest (zero), with yellow and green in between. The cross-sections in the plots are shown to roughly the same scale.

The last sections of the FIDAP script files contained the simulation control commands, which told the software the type of finite element analysis to perform, and which strategy to follow in solving the finite element equations for the nodal degree of freedom profiles. The first command used specified a mixed pressure formulation for the simulations (i.e. pressure is discretized and solved for as an unknown separate from the velocities), and selected a discontinuous pressure approximation. In this approach, the melt pressure was represented as piecewise constant throughout the mesh (discontinuous across element boundaries), with one pressure DOF created per continuum element, which was associated with the element centroid. For the velocity and temperature DOFs, FIDAP automatically used trilinear interpolation functions, which are continuous across element boundaries. Several additional commands were used to alter the way the problem was solved and hence aid convergence. First, an element-based dynamic relaxation

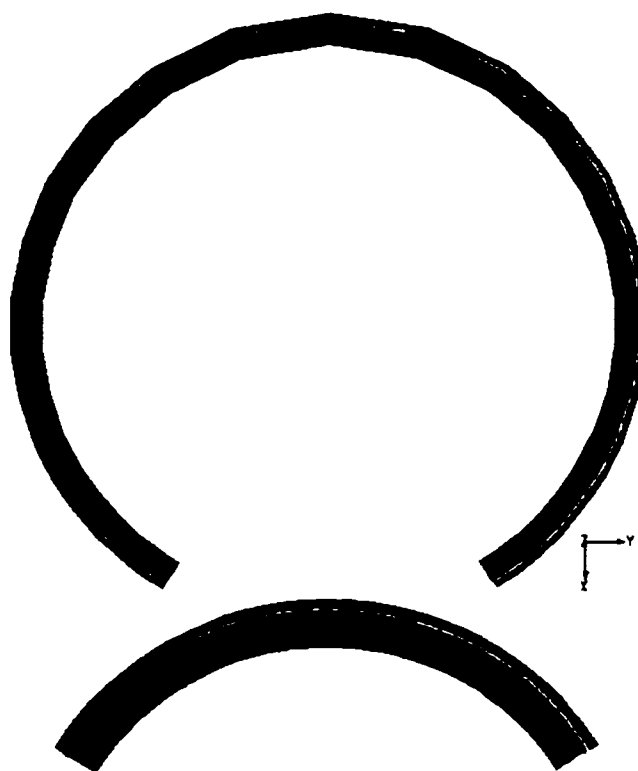


Figure 5.7: Barrel Peroxide Addition Patterns

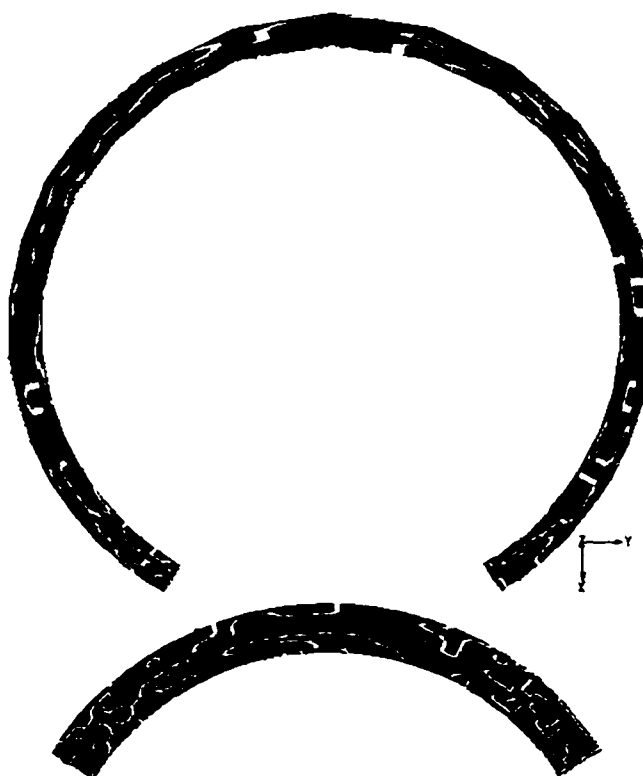


Figure 5.8: Random Peroxide Addition Patterns

scheme was used for finding new approximations for the nodal unknowns based on the approximations and residuals from the previous iteration of the solution procedure for the finite element equations. This can significantly reduce the number of iterations to convergence. For the reactive extrusion simulations, an additional dynamic viscosity relaxation scheme was used to stabilize the solution over the first 20 iterations. The use of this scheme was critical, since the great changes in fluid viscosity that take place over the channel length due to the degradation reaction make the problem very unstable otherwise. Also, a fixed streamline upwinding factor was used for the temperature DOF, to control numerical oscillations in the profiles, and in the formulation of the finite element equations the channel dimensions and velocities were scaled up by a factor of 1000 (from metres to millimetres). Lastly, a segregated solution algorithm for the finite element equations was used, by which the profiles of each DOF were solved for separately and sequentially in each iteration. The advantage of this approach is that it allows much larger problems to be solved than fully coupled algorithms, which solve for all DOF simultaneously in each iteration. The specified convergence criterion for the segregated algorithm was a maximum relative change of 0.001 of any nodal degree of freedom value between iterations.

5.4.3 Calculations and Iterative Procedure

Following convergence of each run, the complete nodal profiles of pressure, temperature, velocity components, species concentrations, and flow efficiencies were printed out to text files, along with the nodal coordinates in the global Cartesian coordinate system. The flow efficiencies were computed by FIDAP in a user-supplied subroutine which received the complete velocity gradient tensor at each node, and which found the three eigenvalues of the rate-of-deformation

tensor as the roots to its characteristic equation, derived from:

$$\det(\lambda \underline{I} - \underline{D}) = 0 \quad (5.20)$$

A C program processed the text files and sorted the profiles by mesh cross-section, and then another C program computed average values of the field variables along lateral cross-sections from the inlet plane to the outlet, using node pattern files which specified the node numbers of the corner nodes for each of the 180 two-dimensional elements in each lateral cross-section. Average melt pressures, weight-average molecular weights, and flow efficiencies were calculated by area average, which involved computing the area integral of the quantity over each 2D element, then dividing the total by the area of the cross-section. Average temperatures and peroxide weight fractions in the polymer melt were computed by flow average, which involved computing the area integral of the flux of the quantity (the quantity multiplied by the axial velocity) over each 2D element, then dividing the total by the volumetric flow rate across the cross-section. The numerical integrals in the computations were performed using a 4 point Gaussian quadrature technique.

As mentioned before, the PDF ratio for each simulation was obtained by adjusting the mass throughput in the channel, as determined by the velocity profile on the inlet plane. Thus an iterative procedure was used for each run, with an estimate made in each iteration for the throughput that would yield the target PDF ratio value, following which the simulation was performed, and the resulting PDF ratio computed based on the average inlet and outlet melt temperatures, pressures, and weight-average molecular weights. Once two results had been obtained at a particular screw speed, channel geometry, and peroxide distribution, a linear interpolation formula was used to make the throughput estimates. To accelerate the process, in each iteration run after the first, the converged steady-state field variable profiles from the previous iteration were taken as initial

guesses for the profiles for the new iteration. The convergence criterion for the procedure was that the computed PDF ratio be within 0.005 of the target value (i.e. between -0.005 and 0.005, or between 0.395 and 0.405).

5.5 Results and Discussion

5.5.1 First Channel Geometry - Degree of Freedom Profiles

Table 5.5 shows a summary of results of the 16 simulations performed on the large aspect ratio channel section, with the mesh shown in Figure 5.4. The mass throughputs were all in an intermediate range of values. The significant average melt pressure changes, for the runs at the high level of pressure-to-drag flow ratio, were negative, signifying pressure drops along the channel length, which are appropriate for a section of the metering zone of a SSE screw. The largest computed average pressure drop was 21.6 MPa (equal to 5.4 MPa per screw turn, or 43.0 MPa/m of helical channel length), for the conventional extrusion simulation at the high screw speed. The pressure changes were all small for the runs at the low level of PDF ratio, and indeed they should all have been exactly zero for pure drag flow. For the reactive extrusion simulations the average outlet peroxide conversions were generally quite high, indicating that the average residence times of the peroxide in the section were sufficient for high levels of consumption at the prevailing temperatures. The corresponding average outlet weight-average molecular weights were quite low, showing up to an order of magnitude reduction over the inlet value. The high level of peroxide added was thus predicted to cause significant degradation of the polymer.

First the values in Table 5.5 are compared between runs at different levels of the PDF ratio,

Table 5.5: First Channel Geometry Simulation Results							
Run	Screw Speed (rpm)	Inlet Peroxide Distribution	PDF Ratio Q_P/Q_D	Mass Throughput (kg/h)	Average Pressure Change (kPa)	Average Outlet Peroxide Conversion $\frac{w_{I,In} - w_{I,Out}}{w_{I,In}}$	Average Relative Outlet Molecular Weight $\frac{\bar{M}_{W,Out}}{\bar{M}_{W,In}}$
1	20	None	-0.001	2.59	38	--	1
2	20	None	0.400	5.15	-14028	--	1
3	20	Uniform	-0.001	2.53	3	0.978	0.108
4	20	Uniform	0.400	4.13	-884	0.900	0.115
5	20	Barrel	0.001	2.53	-2	0.979	0.112
6	20	Barrel	0.401	4.15	-1107	0.919	0.135
7	20	Random	0.003	2.53	-6	0.978	0.105
8	20	Random	0.399	4.13	-862	0.895	0.113
9	60	None	0.002	7.83	-96	--	1
10	60	None	0.400	15.34	-21642	--	1
11	60	Uniform	0.003	7.94	-21	0.706	0.138
12	60	Uniform	0.396	12.39	-3224	0.538	0.171
13	60	Barrel	0.001	8.04	-8	0.801	0.194
14	60	Barrel	0.397	12.88	-4998	0.712	0.254
15	60	Random	0.004	7.89	-22	0.699	0.134
16	60	Random	0.402	12.39	-3200	0.523	0.168

but the same screw speed and inlet peroxide distribution. In each pair of runs, the mass throughput was larger for the run at the high PDF ratio level, and consequently for the reactive extrusion simulations the average outlet peroxide conversions were lower and the average outlet weight-average molecular weights higher, because of smaller average residence times. Comparing between runs at the same screw speed but different inlet peroxide distributions, it can be seen that the mass throughputs and pressure drops for the conventional extrusion runs at the high PDF ratio were significantly larger than for the corresponding reactive extrusion runs, due to much larger average outlet viscosities following from higher molecular weights. The throughputs at the low PDF ratio were, in contrast, very similar for all inlet peroxide distributions.

For the reactive extrusion simulations, the results for corresponding runs were quite close to each other. This was particularly true for the uniform and random distributions, in contrast to the less uniform barrel distribution. The first distinction in the barrel distribution results was the higher predicted outlet peroxide conversions, which can be attributed to very sharp drops in peroxide levels just following the inlet plane, which were numerical artifacts in the simulations, which will be explained in detail later. Paradoxically, the barrel distribution runs also yielded higher average outlet weight-average molecular weights. These followed from the same problem of sudden drops in the peroxide levels after the inlet, which reduced the effective amounts of peroxide in the flows for degrading the polymer.

Finally, comparing results between runs at the different levels of screw speed, the throughputs for all runs and the pressure drops for the high PDF ratio runs were all higher at the high screw speed. Again this resulted in the reactive extrusion simulations at the high screw speed showing lower average outlet peroxide conversions and higher average outlet weight-average

molecular weights than those at the low screw speed, because of smaller average residence times. The lowest predicted conversions were for the uniform and random distributions at the high PDF ratio, at just over 0.5.

Computed profiles of average melt temperature, melt pressure, peroxide conversion, and relative weight-average molecular weight along lateral cross-sections in the mesh are shown in Figures 5.9, 5.10, 5.11, and 5.13, respectively. In the Figures results are shown principally for runs at the high screw speed, as the basic shapes of the curves were the same for both screw speeds. In the Figure legends, the fields in the series labels are the screw speed level, the inlet peroxide distribution, and the PDF ratio level, in that order. Thus the label “High/Uniform/Low” for a curve indicates that it is for run 11, at 60 rpm and a PDF ratio of 0, with the uniform inlet peroxide distribution. Figure 5.9 shows the average melt temperature profiles for three runs at 60 rpm and one at 20 rpm. The shown curves for high screw speed/no peroxide/low PDF ratio and high screw speed/uniform peroxide distribution/high PDF ratio were the extremes for the high screw speed runs - the other curves all fell between them. In each run the melt temperature rose quickly (in under 2 screw turns, or half the axial distance of the section) from the inlet value of 200°C to a plateau level slightly higher than the barrel temperature of 220°C, at which the rate of heat generation by viscous dissipation was exactly balanced by the rate of heat transfer to the barrel surface. The effect of the degradation reaction was to slow the temperature rise (seen as a reduction in the slopes of the curves early on), and to reduce the plateau temperatures, by reducing the melt viscosity through its molecular weight. The effects of increasing screw speed and increasing PDF ratio were similar, in that they both resulted in slower temperature rise (due to accompanying higher throughputs), and to higher plateau temperatures, though the screw speed effect on this was

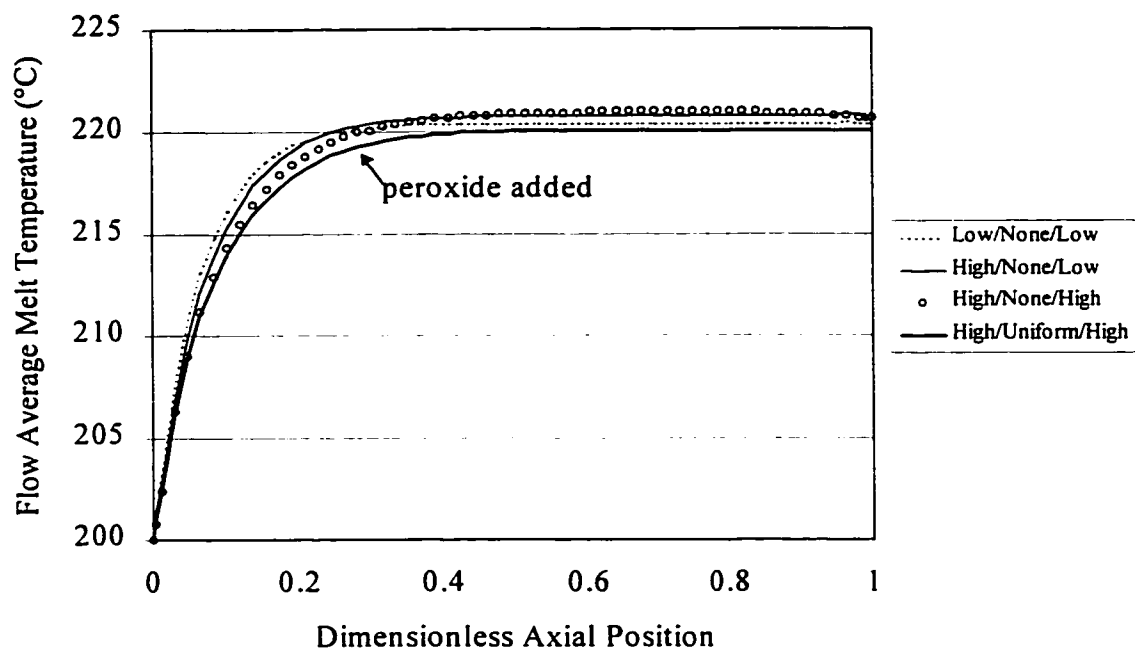


Figure 5.9: Average Temperatures for First Channel Geometry

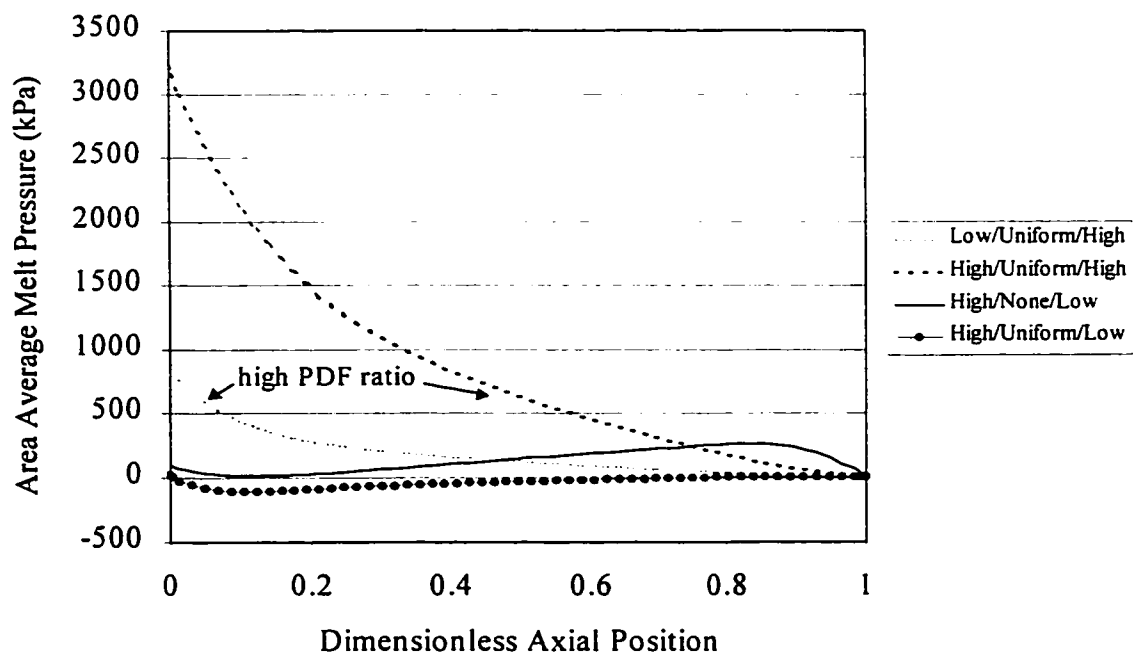


Figure 5.10: Average Pressures for First Channel Geometry

much more significant, due to its greater influence on rates of viscous dissipation.

Figure 5.10 shows the average melt pressure profiles for three runs at 60 rpm and one at 20 rpm. For the high PDF ratio, only the curves for the uniform peroxide distribution are shown, to keep the pressure scale small so details in the low PDF ratio curves can be seen. The curves show the melt pressures dropping smoothly from the inlet to around zero at the outlet, with gradual decreases in the slopes which can be attributed to reduced melt viscosities from the degradation reaction. The effect of increasing screw speed was to increase the pressure drops in the channel, and to elongate the regions over which the slope changes in the curves took place. For the runs at the low PDF ratio, the curves show that though the overall average pressure changes along the channel length may have been close to zero, that did not translate into the melt pressure being zero everywhere in the channel. Hence true drag flow behaviour was not attained in these runs. The curves show initial pressure drops in the channel after the inlet, followed by gradual pressure rises along most of the channel length, and then final pressure drops just before the outlet. The magnitude of these fluctuations was less in the low screw speed and reactive extrusion runs.

Figure 5.11 shows the average peroxide conversion profiles for six reactive extrusion simulation runs at 60 rpm and two at 20 rpm. The curves for the runs with the barrel peroxide distribution are shown as symbols only. The curves show smooth increases in the conversion levels (over most of the channel length), with those for the barrel distribution being the highest at each level of PDF ratio, followed by those for the uniform distribution, and closely below these the curves for the random distribution. The gap between the barrel and uniform/random distribution curves is also seen to decrease with axial position. The effects of decreasing screw speed and PDF ratio are both found to be to increase conversions, since both led to decreases in mass throughput

and hence increases in the average residence times of the material in the channel section. The plot for the low screw speed/low PDF ratio run (for which the outlet conversion was highest) shows very rapid degradation of the peroxide, with about half the peroxide consumed after one screw turn (at a dimensionless axial position of 0.25) and more than 80% after two screw turns.

In the profiles for the non-uniform peroxide distributions, a problem is encountered immediately following the inlet when the profiles dip into negative values, implying that the peroxide levels were increasing there, which of course is physically impossible. The barrel distribution run curves show an additional problem after this, with dramatic leaps in conversion seen immediately following the initial drop. This also occurred in the random distribution runs, but to a much lesser extent. These problems are a numerical artifact of the simulations, which occurred due to the extreme intensity of segregation of the peroxide on the inlet plane for the non-uniform distribution runs, between the nodes at which the peroxide was specified as existing and those at which it was specified as being absent. As the peroxide moved down the channel with the melt, the intensity of segregation began to diminish due to circulation in the channel, which spread the peroxide amongst a larger number of nodes than that on which it had been specified, on the inlet plane. This caused the observed original drop and leap in average peroxide conversions for each run. These fluctuations all took place very quickly, within the first 13% of the axial length of the first screw turn, or just over 3% of the total channel section length. These problems were greatest for the barrel distribution runs, for which the intensity of segregation and non-uniformity of the peroxide distribution were greatest. For the random distribution runs, the slight differences between their conversion profiles and those for the corresponding uniform distribution runs can be attributed to this cause.

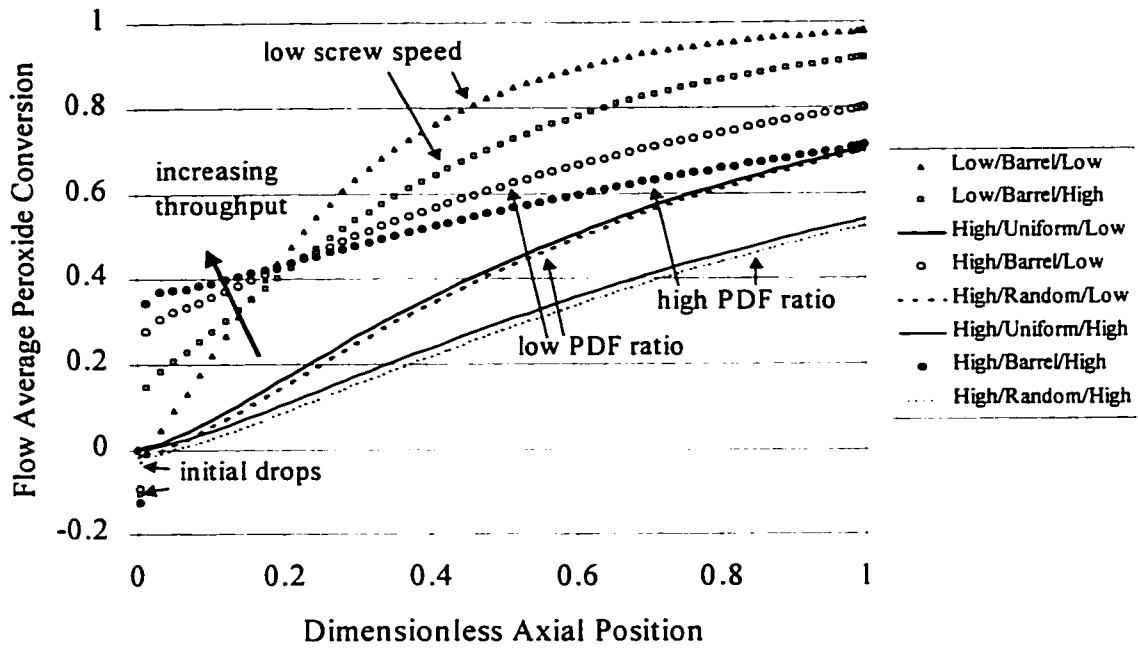


Figure 5.11: Average Peroxide Conversions for First Channel Geometry

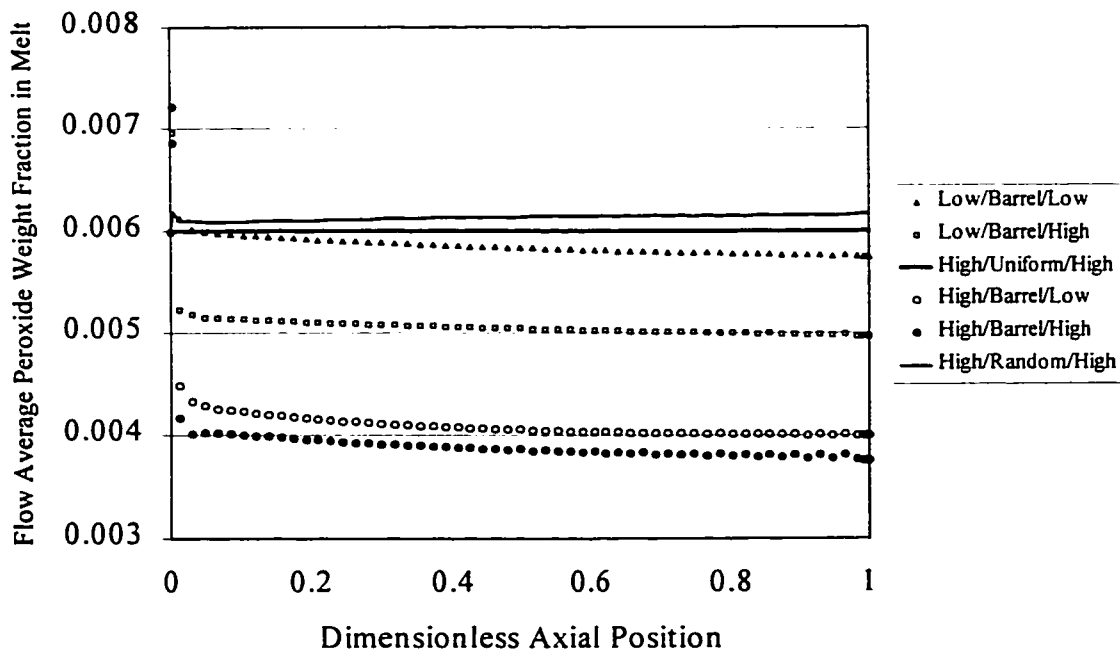


Figure 5.12: Average Peroxide Levels With No Peroxide Decomposition For First Channel Geometry

Figure 5.12 examines these numerical inconsistencies in more detail, showing plots of average peroxide weight fractions for the four barrel distribution runs, as well as for the uniform and random distribution runs at the high screw speed and high PDF ratio (i.e. high throughput), which were obtained by running the corresponding simulations with the peroxide thermal decomposition rate constant set to zero. Thus in the runs peroxide was present in the polymer melt, but did not react and did not affect the polymer MWD moments, and so the changes in the computed peroxide levels were due to numerical causes alone. The Figure shows that the peroxide levels in the uniform and random distribution runs remained close by the specified inlet value of 0.006 (0.6 wt%). For the barrel distribution runs though, there were clearly significant negative deviations from this value, following the initial jumps in peroxide level. The deviations were larger for runs at high throughputs, which is also reflected in Figure 5.11 with the jumps in peroxide conversion for the barrel distribution runs increasing in height with throughput. This numerical error resulted in considerable losses of peroxide for degradation of the polymer for the barrel distribution runs at higher throughputs.

Figure 5.13 shows the average relative weight-average molecular weight profiles for six reactive extrusion simulation runs at 60 rpm and one at 20 rpm. The curves show the molecular weights dropping smoothly from the initial value, and fall in the same order at each screw speed and PDF ratio level as the peroxide conversion curves, with those for the barrel distribution runs highest, followed by those for the uniform and random distributions nearly superimposed on each other. The observation that the barrel distribution run molecular weight profiles were highest, even though the apparent conversions for these runs were also highest, is a consequence of the above mentioned numerical problems which reduced the effective amount of peroxide available for the

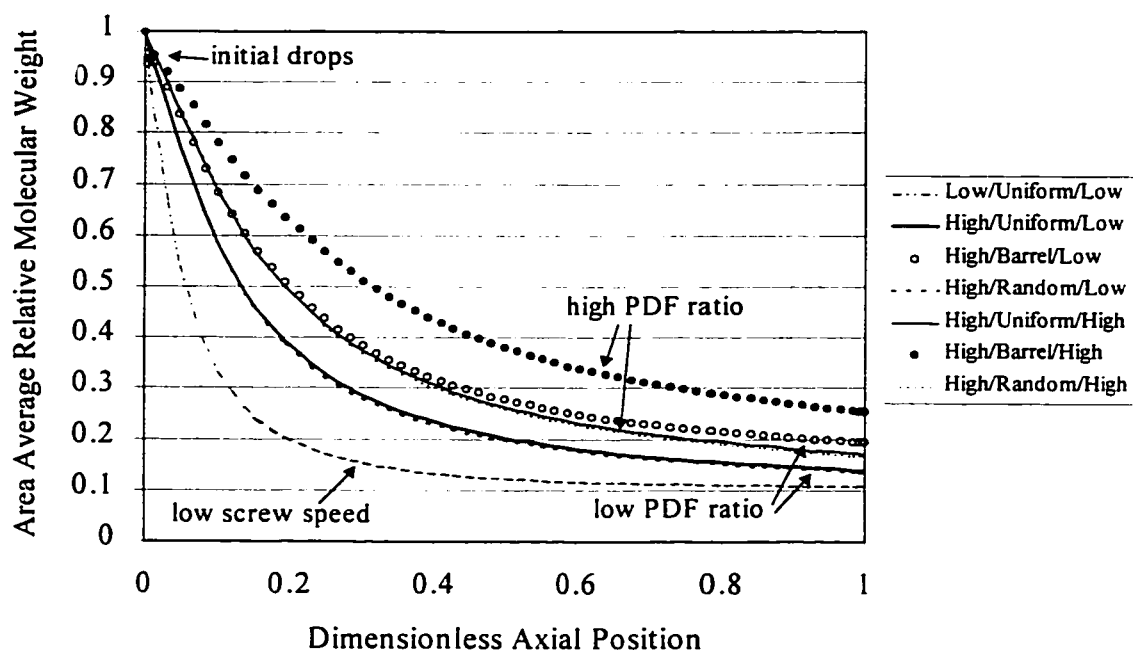


Figure 5.13: Average Relative Weight-Average Molecular Weights for First Channel Geometry

reaction. The previously observed effects of decreasing screw speed and PDF ratio in increasing peroxide conversions are echoed here in corresponding reductions in molecular weights under the same conditions. The plot for the low screw speed/low PDF ratio run illustrates how quickly the polymer molecular weight can change, with the molecular weight reduced to less than 20% of its initial value after only one screw turn.

To gain some insight into the variation of the degree of freedom values within the channel cross-sections, a series of plots is presented here for a cross-section through the mesh at right angles to the channel sides (i.e. to the screw flights) at a dimensionless axial position of 0.5, for run 12, at the high screw speed and high PDF ratio, and with the uniform inlet peroxide distribution. Figure 5.14 shows the velocity vectors at the nodes within the cross-section. The direction of the cross-channel component of the barrel velocity is left-to-right in the Figure. The plot clearly shows the characteristic extruder cross-section circulation pattern. Figure 5.15 shows the melt pressure distribution in the cross-section. The range of values the colours represent is 570 kPa (dark blue) to 710 kPa (dark red). The pressure clearly increased in the direction of drag flow in the cross-section, from the passive flight at the left to the active or pushing flight at the right, which conforms to expectations. This cross-channel pressure gradient was what drove the backflow in the bottom part of the channel, shown in Figure 5.14. The approximate cross-channel pressure gradient in this plane was 4.7 MPa/m. Figure 5.16 shows the distribution of velocity components normal to the cross-section (i.e. parallel to the flights). The range of the colours is from 0 mm/s to 119 mm/s, which is the tangential velocity of the barrel at 60 rpm. The top third of the channel is seen to be moving at high speeds close to that of the barrel surface, with the speed tapering off below this to zero on the screw and flight surfaces. Figure 5.17 shows the melt



Figure 5.14: Velocity Vectors in Cross-Section for First Channel Geometry

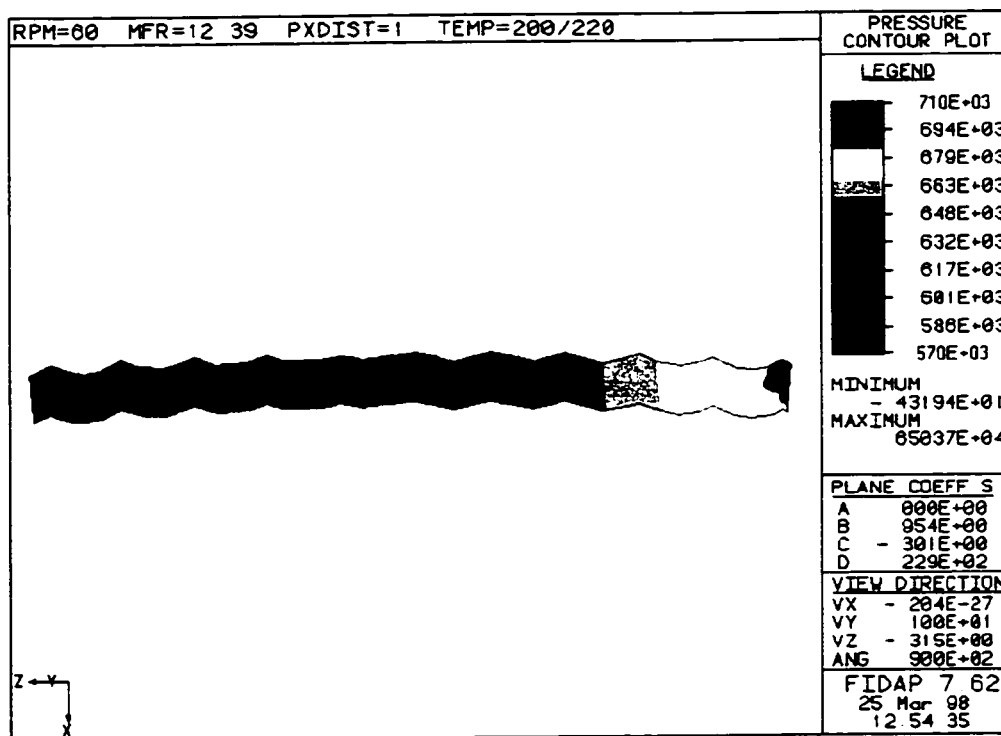


Figure 5.15: Pressures in Cross-Section for First Channel Geometry

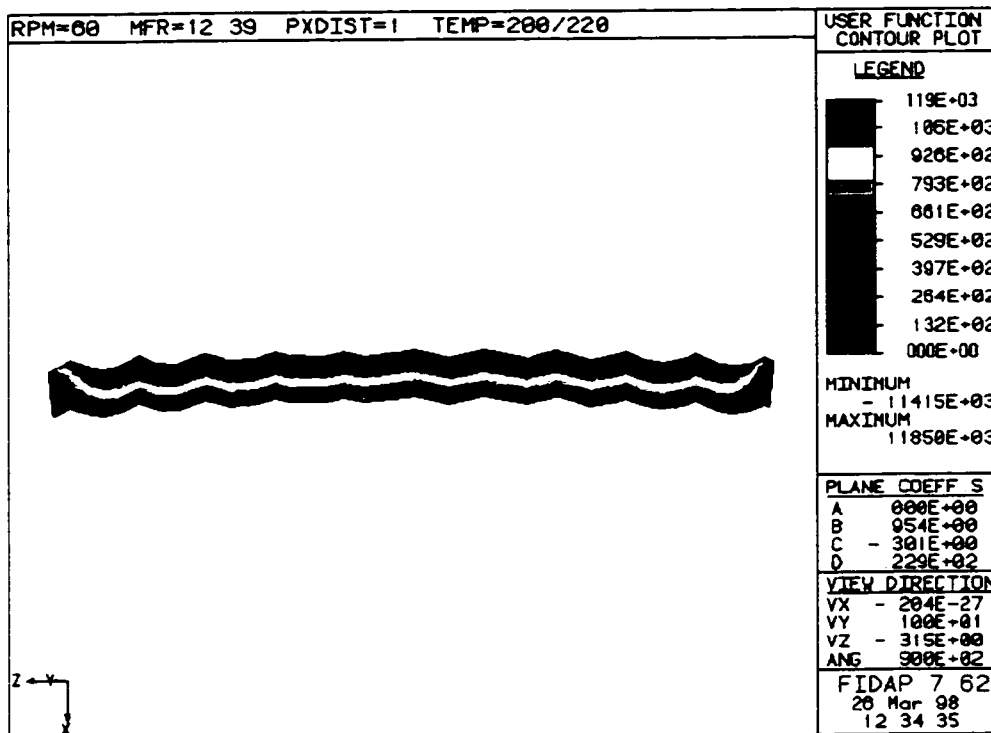


Figure 5.16: Normal Velocities in Cross-Section for First Channel Geometry

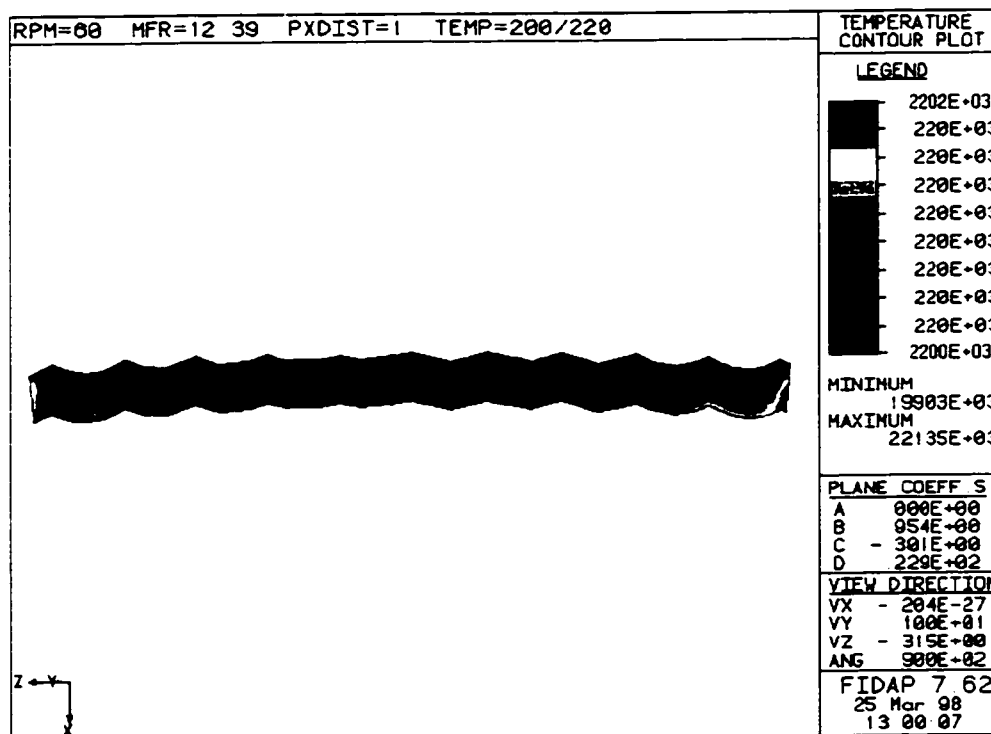


Figure 5.17: Temperatures in Cross-Section for First Channel Geometry

temperature distribution in the cross-section. The range of the colours is very small, only from 220.0°C to 220.2°C. Thus in spite of the appearance of the plot, there was little temperature variation across the channel. Figure 5.18 shows the distribution of peroxide weight fractions in the melt in the cross-section. The range of the colours is 0.0038 (0.38 wt%) to 0.0044 (0.44 wt%), again relatively small. The plot shows there was a slight cross-channel peroxide concentration gradient, with the level lowest at the passive flight and highest at the active flight. This can largely be attributed to the fact that the active flight in the Figure was axially closer to the inlet plane than the passive flight. Figure 5.19 shows the distribution of polymer relative weight-average molecular weights in the cross-section. The colour range is 0.23 to 0.29. Again a slight cross-channel gradient was observed, with the molecular weights lowest at the passive flight and highest at the active flight. The reason for this is the same as before, that the active flight was closer to the inlet.

Finally, Figure 5.20 (a) shows the pathlines for particles entering the mesh at three points on the inlet plane along a radial line, close to the active flight, again for run 12. The starting depths and residence times of the particles are given in Table 5.6. To give some perspective, the minimum residence time in the channel section for this run, based on a particle moving through the entire channel length at a speed equal to the down-channel component of the barrel tangential velocity, was 4.4 s. Thus all three particles were passing quickly through the system. The blue particle started on the inner part of the channel, the green particle in the middle, and the red particle on the outside part. Also shown in the Figure in part (b) is an expanded top-down view of the channel, displaying the radial and circumferential motion of the red particle. In part (a), the blue particle can be seen to have been migrating across the channel as it passed down the channel length, from the active flight to the passive flight (for the “front” part of the mesh closest to the viewer, the

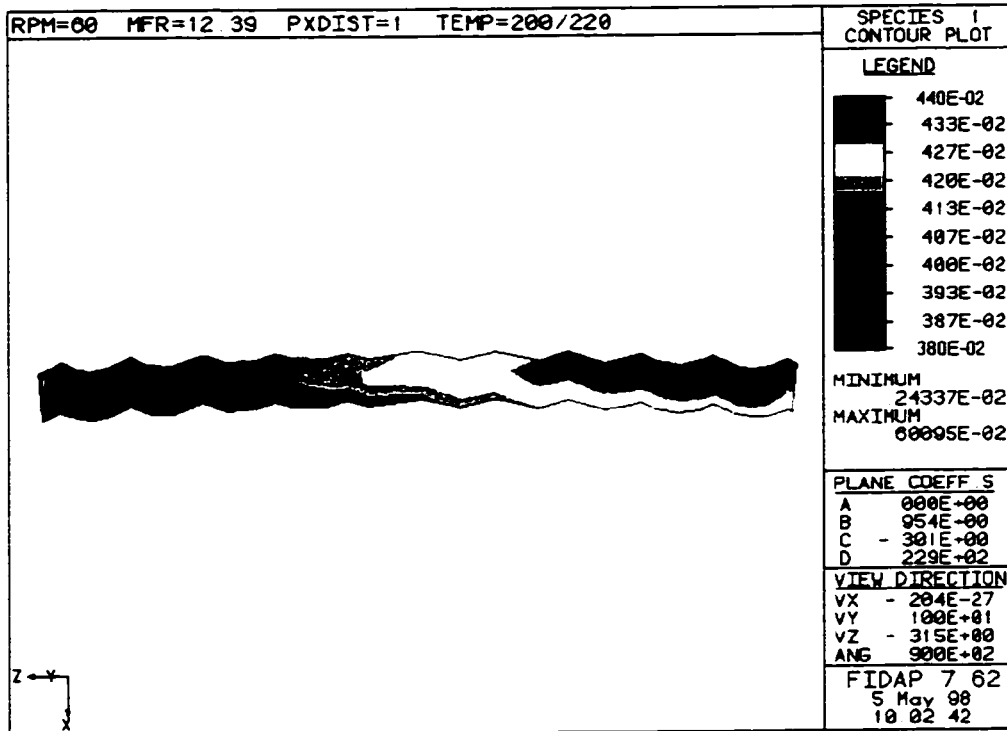


Figure 5.18: Peroxide Weight Fractions in Cross-Section for First Channel Geometry

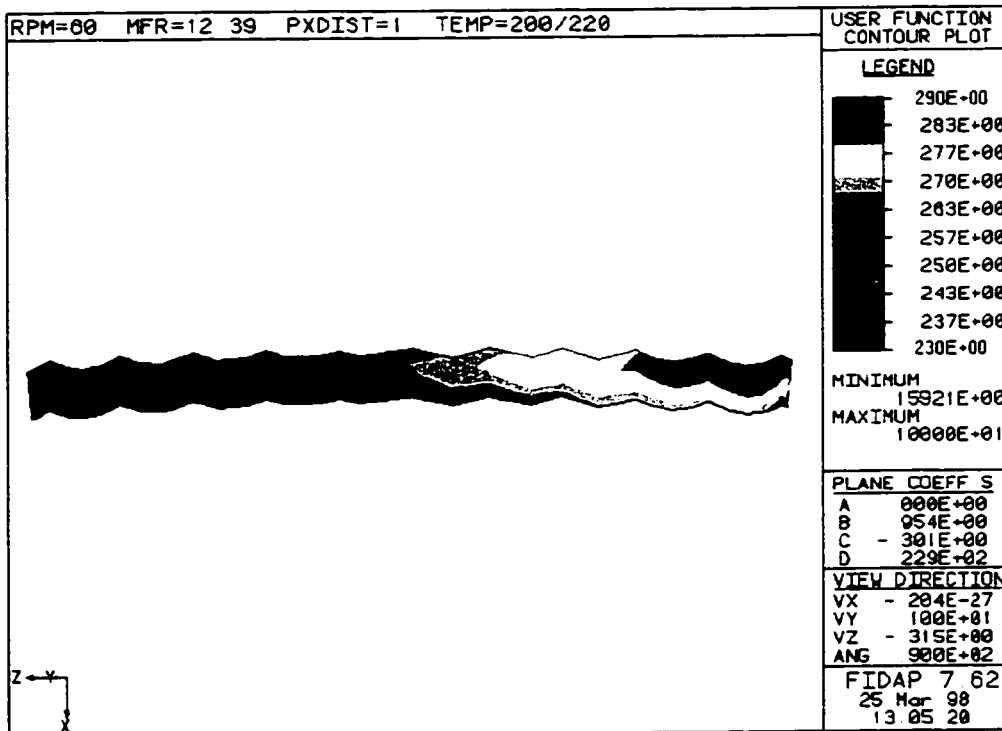


Figure 5.19: Relative Weight-Average Molecular Weights in Cross-Section for First Channel Geometry

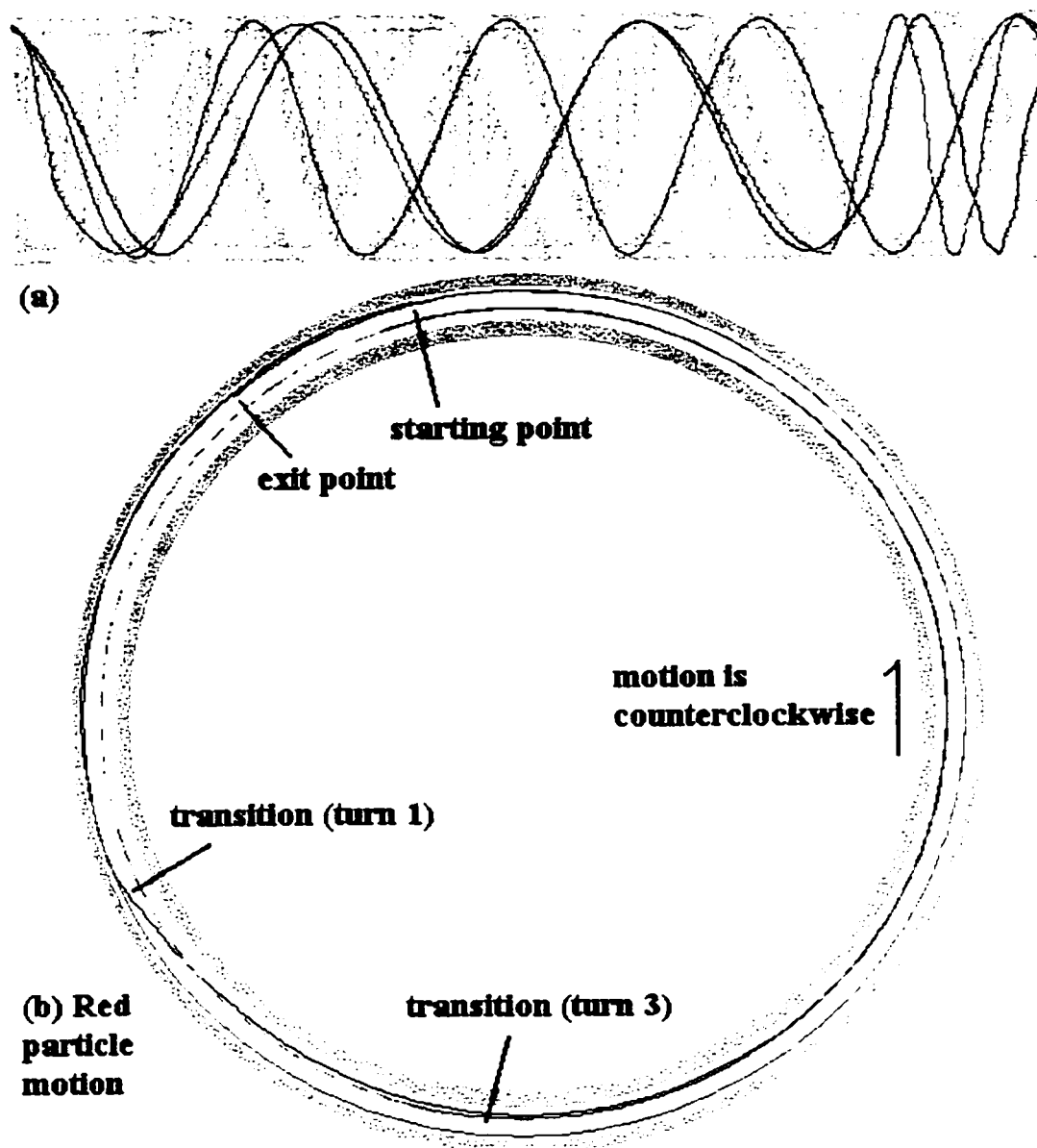


Figure 5.20: Particle Pathlines for First Channel Geometry

Table 5.6: Particle Pathline Data for First Channel Geometry		
<i>Particle</i>	<i>Entering Dimensionless Channel Depth</i>	<i>Residence Time (s)</i>
Blue	0.333	4.79
Green	0.5	4.95
Red	0.667	5.28

direction of the barrel tangential velocity is downwards, so the active flight is on the left and the passive flight on the right). This motion is consistent with the previously observed backflow in the inner part of the channel, and is the characteristic “helix within a helix” motion found in extruder channels. Once the particle reached the passive flight, after having moved through more than 3 turns of the channel, it circulated outwards to the outer part of the channel and began moving back across before reaching the outlet plane. The green particle, in contrast, made little cross-channel motion at all, remaining at essentially the same position and depth for its entire trip. This indicates that the division between the inner and outer parts of the channel for this geometry was at a dimensionless depth of approximately 0.5. The red particle was the most active of the three, passing along the outer part of the channel to the active flight in the first screw turn, then circulating into the inner part and moving back across the channel over the following 2 turns (actually passing the blue particle), before reaching the passive flight and circulating outwards prior to reaching the outlet. Part (b) of the Figure shows how the red particle moved radially as it circulated. The pathline shown here is colour coded for the axial position of the particle, with the line passing from blue through green, yellow, orange, and red as the particle moved from the inlet to the outlet of the channel. Clearly the particle only circulated at two channel depths, one as it passed along the outer part of the channel and one as it passed along the inner part. This observation is consistent with conventional understanding of fluid motion in extruder channels, wherein there are complementary positions in the upper and lower parts of the channels (viewed in a cross-section normal to the screw flights) between which particles circulate as they move downstream.

5.5.2 Second Channel Geometry - Degree of Freedom Profiles

Table 5.7 shows a summary of results of the 16 simulations performed on the small aspect ratio channel section, with the mesh shown in Figure 5.5. The largest computed average pressure drop for these runs was 12.2 MPa (equal to 3.1 MPa per screw turn or 24.3 MPa/m of helical channel length), for the conventional extrusion simulation at the high screw speed and high PDF ratio. For the reactive extrusion simulations the average outlet peroxide conversions were quite high, particularly for the low screw speed runs. The lowest predicted conversions were for the uniform and random distributions at the high PDF ratio, at just over 0.5. The corresponding average polymer weight-average molecular weights at the outlet were quite low, up to nearly an order of magnitude less than that of the undegraded material.

The observed relationships between the results in corresponding runs are the same as for the first channel geometry simulations. Of particular note is the observation again that the outlet conversions and molecular weights were higher for all four reactive extrusion runs with the barrel peroxide distribution than for the corresponding runs with the uniform and random distributions. Thus the numerical artifact encountered in the runs for the first channel geometry, which involved sudden drops in the peroxide levels after the inlet for the barrel distribution runs, was a problem in these runs as well. Comparing the results between corresponding runs for the two channel geometries, it can be seen that the mass throughputs were lower in the runs for the second channel geometry, due to the smaller cross-section area. The average pressure drops in the runs at the high PDF ratio were also smaller in the second set of runs, due to the larger channel depth which reduced the pressure drop necessary to reach a particular value of the PDF ratio, as shown in equation (5.17). Finally, the predicted outlet conversions and molecular weights for the reactive

Table 5.7: Second Channel Geometry Simulation Results

<i>Run</i>	<i>Screw Speed (rpm)</i>	<i>Inlet Peroxide Distribution</i>	<i>PDF Ratio</i> Q_P/Q_D	<i>Mass Throughput (kg/h)</i>	<i>Average Pressure Change (kPa)</i>	<i>Average Outlet Peroxide Conversion</i> $\frac{w_{I,In} - w_{I,Out}}{w_{I,In}}$	<i>Average Relative Outlet Molecular Weight</i> $\frac{\bar{M}_{W,Out}}{\bar{M}_{W,In}}$
17	20	None	-0.001	1.54	11	--	1
18	20	None	0.402	2.87	-7932	--	1
19	20	Uniform	-0.002	1.52	2	0.971	0.110
20	20	Uniform	0.397	2.18	-429	0.907	0.115
21	20	Barrel	0.000	1.51	0	0.973	0.116
22	20	Barrel	0.401	2.15	-531	0.924	0.133
23	20	Random	-0.002	1.53	2	0.968	0.105
24	20	Random	0.400	2.18	-407	0.902	0.111
25	60	None	0.003	4.65	-90	--	1
26	60	None	0.401	8.53	-12170	--	1
27	60	Uniform	-0.003	4.76	11	0.669	0.146
28	60	Uniform	0.403	6.86	-1704	0.523	0.176
29	60	Barrel	0.001	4.80	-4	0.745	0.183
30	60	Barrel	0.398	6.94	-2380	0.666	0.236
31	60	Random	-0.001	4.79	5	0.651	0.142
32	60	Random	0.400	6.86	-1646	0.504	0.172

extrusion simulations were similar for both sets of runs.

For the second channel geometry runs, the computed profiles of average melt temperature, pressure, peroxide conversion, and relative weight-average molecular weight along lateral cross-sections in the mesh show the same patterns as the corresponding plots for the first channel geometry runs, and so are not shown. To allow comparison of the severity of the numerical problems with the non-uniform peroxide distributions between the two sets of runs, Figure 5.21 shows plots of average peroxide weight fractions for the four barrel distribution runs, as well as for the uniform and random distribution runs at the high screw speed and high PDF ratio, which were obtained by running the corresponding simulations with the peroxide thermal decomposition rate constant set to zero. The Figure shows that the peroxide level increases slightly for the random distribution run, which is also observed in Figure 5.12, the corresponding Figure for the first channel geometry runs. Initial jumps in the peroxide level are also seen for the barrel distribution runs, followed by sharp drops to equilibrium levels below the specified inlet value of 0.006 (0.6 wt%). Again the magnitude of the negative deviation was proportional to the mass throughput in the run. The deviations in corresponding runs were smaller for the second set of runs, probably because the throughputs were also smaller. There was also a levelling off of the peroxide levels with axial distance in the barrel distribution runs for the second channel geometry which was not observed in those runs for the first channel geometry, for which the peroxide level continued to decrease slightly as the axial distance increased.

Figures 5.22 and 5.23 respectively show the velocities parallel and normal to a cross-section through the mesh at right angles to the channel sides at a dimensionless axial position of 0.5, for run 28, at the high screw speed and high PDF ratio, and with the uniform inlet peroxide

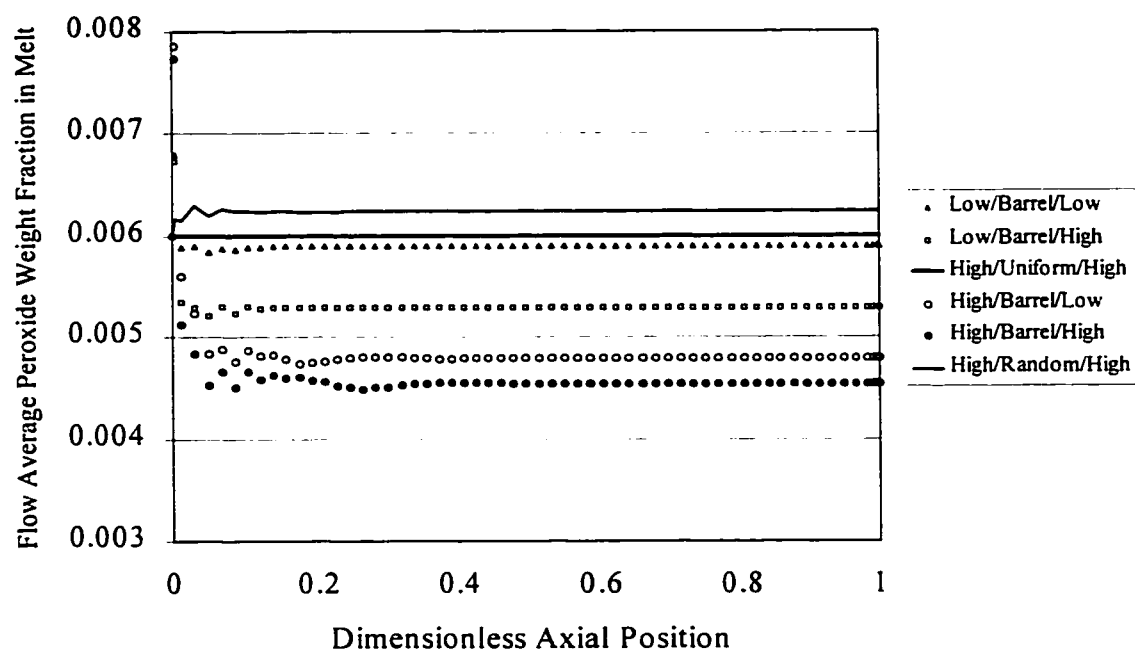


Figure 5.21: Average Peroxide Levels With No Peroxide Decomposition for Second Channel Geometry

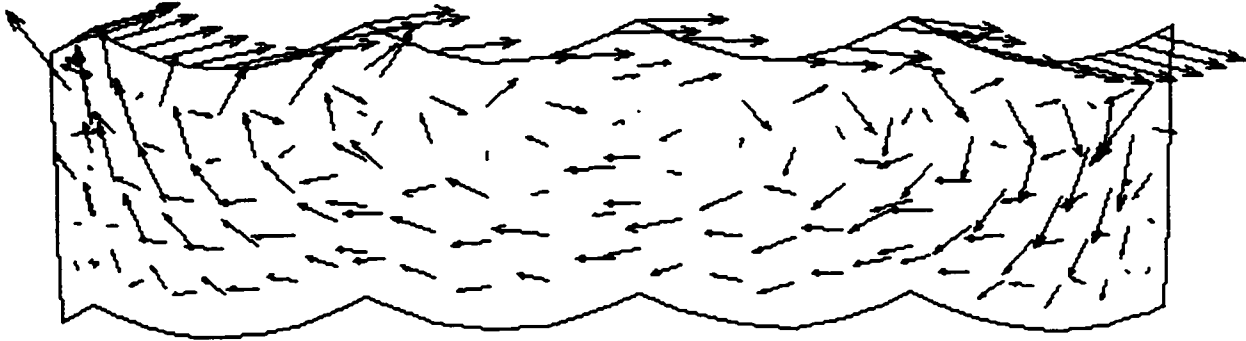


Figure 5.22: Velocity Vectors in Cross-Section for Second Channel Geometry

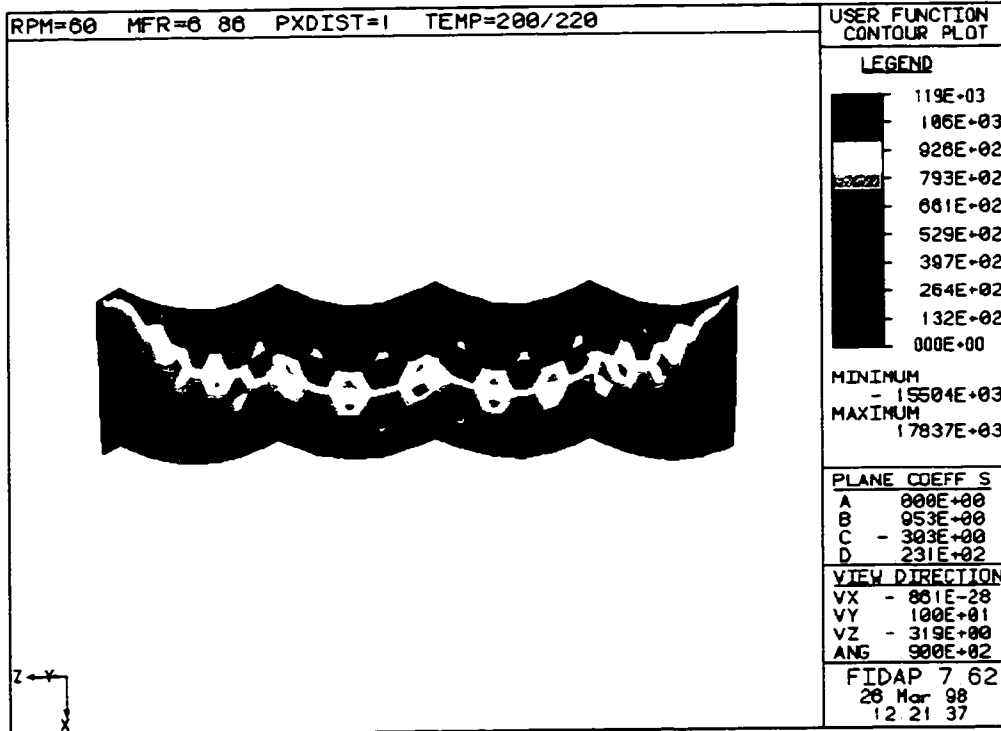


Figure 5.23: Normal Velocities in Cross-Section for Second Channel Geometry

distribution. Plots of melt pressure, temperature, peroxide weight fraction, and polymer relative weight-average molecular weights in the same cross-section show the same patterns as those previously presented for the corresponding run with the first channel geometry, and so are not shown. Figure 5.22 again displays the extruder cross-section circulation pattern. The range of the colours in Figure 5.23 is from 0 mm/s to 119 mm/s, the tangential velocity of the barrel at 60 rpm. The Figure again shows the top third to half of the channel moving at high speeds close to that of the barrel surface, with the speed tapering off below this to zero on the screw and flight surfaces. It should be noted that these Figures are not shown to the same scale as the corresponding ones for the first channel geometry, Figures 5.14 and 5.16.

Finally, Figure 5.24 shows the pathlines for particles entering the mesh at three points on the inlet plane along a radial line, close to the active flight, again for run 28. The relative cross-channel starting positions of these particles are the same as those for the particles in Figure 5.20. The starting depths and residence times of the particles are given in Table 5.8. The minimum residence time in this channel section is again 4.4 s. Thus two of the particles passed quickly through the system; the third was computed as becoming stuck on the screw flight and remaining there indefinitely. Again the blue particle starts on the inner part of the channel, the green particle in the middle, and the red particle on the outside part. The expanded top-down view of the channel shown here displays the radial and circumferential motion of the green particle, again with the colour of the line representing the axial position of the particle, from blue at the inlet to red at the outlet. In part (a), the blue particle shows a regular periodic motion as it passes down the channel length, in which it migrates along the inside part of the channel from the active flight to the passive flight, and then circulates outwards upon reaching the passive flight and rapidly moves back across

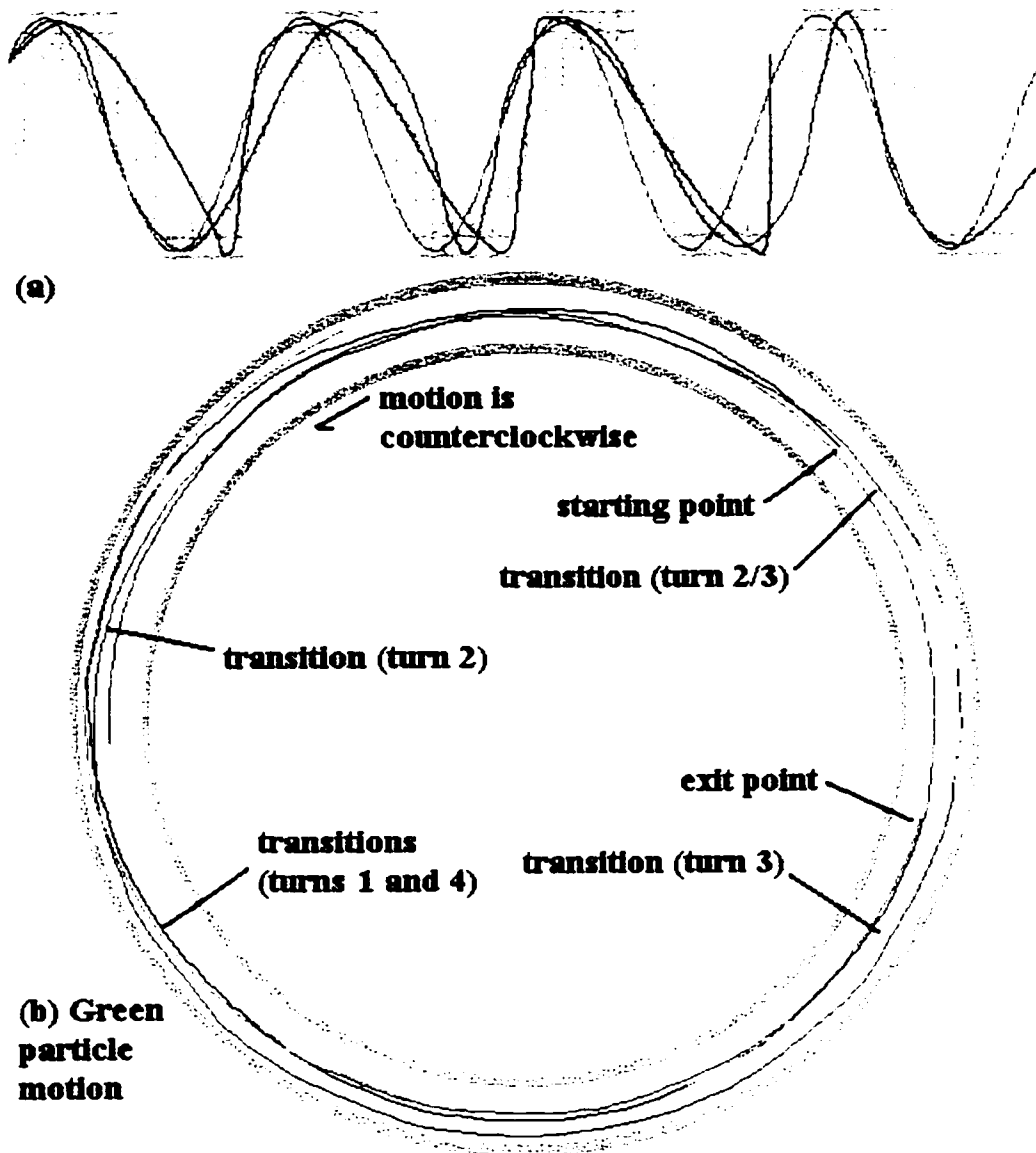


Figure 5.24: Particle Pathlines for Second Channel Geometry

Table 5.8: Particle Pathline Data for Second Channel Geometry		
<i>Particle</i>	<i>Entering Dimensionless Channel Depth</i>	<i>Residence Time (s)</i>
Blue	0.333	∞
Green	0.5	4.64
Red	0.667	4.79

the channel in a path nearly parallel to the barrel tangential velocity. At the end of the third time through this motion, near the end of the third screw turn, the particle seems to touch the active flight and is therefore not computed as moving any further, due to the no slip condition at the flight. The red particle shows essentially no cross-channel motion, and passes out of the system at the same position and depth that it entered. This indicates that the division between the inner and outer parts of the channel for this geometry was at a dimensionless depth of approximately 0.67. The green particle shows considerable cross-channel and radial motion, as seen in parts (a) and (b) of the Figure. The particle circulates between two depths no fewer than 6 times before passing out of the channel section.

5.5.3 Mixing Efficiency Analysis - Flow Efficiencies

The mixing analysis of the simulation run results is begun with examination of the predicted flow efficiencies, first in channel cross-sections, then as averages along the axial lengths of the channel sections. Figure 5.25 shows the flow efficiencies across a lateral cross-section at the midpoint of the channel for the high screw speed/uniform peroxide distribution/high PDF ratio run for both channel geometries, and Figure 5.26 shows the same for a cross-section perpendicular to the screw flights again across the channel axial midpoint. The arrows in the Figures indicate the direction of the barrel tangential velocity along the outsides of the cross-sections. The colour scales for all the plots are the same: from 0.47 (dark blue) to 0.813 (dark red). This covers nearly the entire range of possible values for the flow efficiency. The plots clearly show regions of high flow efficiency in the corners where the barrel surface meets the active flight, and corresponding (though smaller) regions of low flow efficiency in the opposite corners where the barrel surface

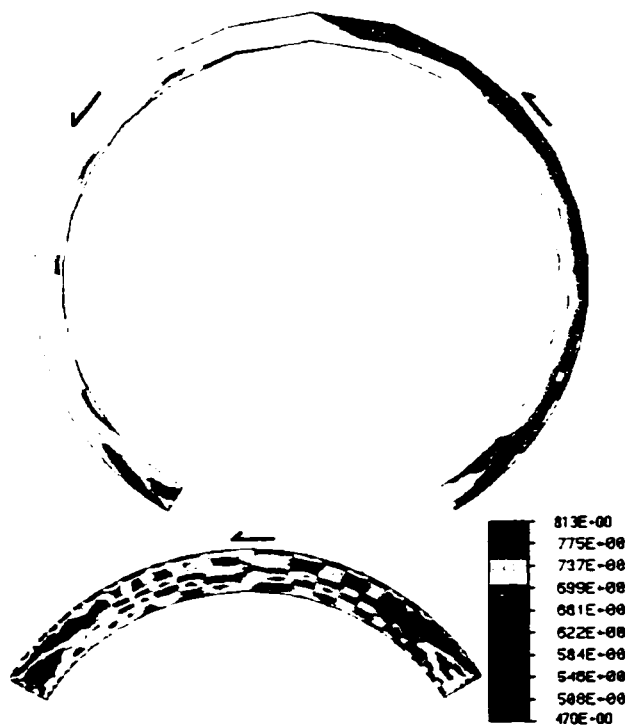


Figure 5.25: Flow Efficiencies in Cross-Sections Perpendicular to the Screw Axes

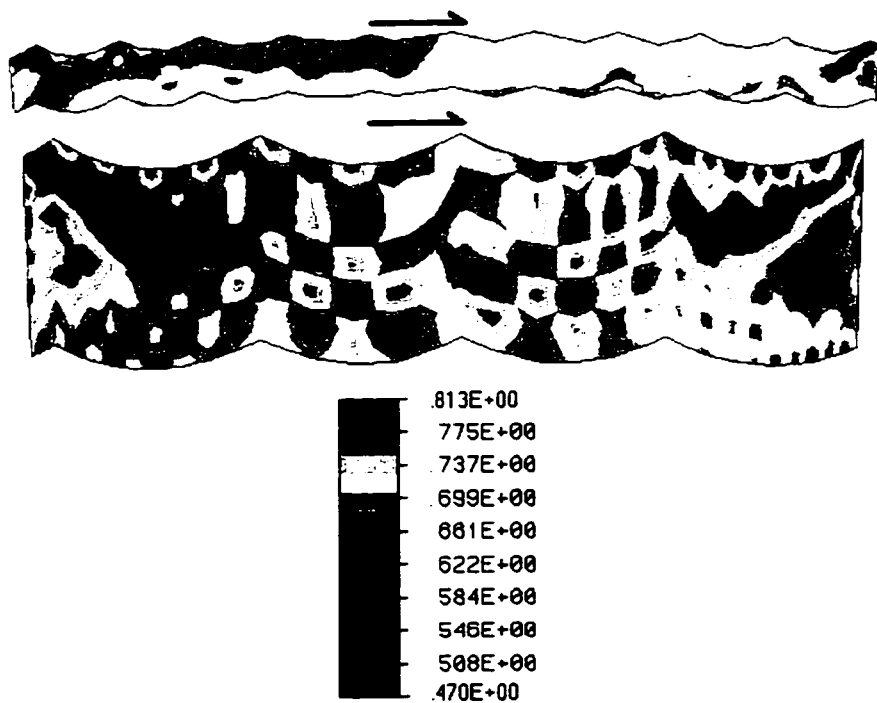


Figure 5.26: Flow Efficiencies in Cross-Sections Perpendicular to the Screw Flights

and passive flight meet. Beneath each of these regions, in the recirculation zones adjacent to the flights, there were complimentary regions of low and high flow efficiency, respectively. These observations indicate that at the top of the downward recirculation zone (next to the active flight) the fluid was computed as experiencing a squeezing flow as its cross-channel velocity component decreased, and that at the top of the upward recirculation zone (next to the passive flight) the fluid was computed as experiencing a uniaxial extension-type flow as its cross-channel velocity component increased again. In the bulk of the cross-sections though, the flow efficiencies were intermediate, in the region of 0.7, as indicated by yellow and green-yellow colours.

Next the computed area average flow efficiencies on lateral cross-sections along the channel lengths for both channel geometries are examined. Figure 5.27 shows the profiles for the no peroxide and uniform peroxide distribution runs at the low screw speed and low PDF ratio, in the large aspect ratio channel. The plot clearly shows that there was much less variation in the average flow efficiencies along the channel length than in the point values within channel cross-sections. Indeed the average flow efficiencies remained nearly constant along the channel, fluctuating only in the regions near the inlet and outlet; the profile plateaus were at values around 0.7065, which is very close to the value of 0.7071 for two-dimensional flows. The plateau value also indicates that the flow efficiencies in the bulks of the channel cross-sections were sufficiently low to overcome the effects of the relatively large high flow efficiency regions on the area averages. The Figure shows that there was no effect of the peroxide level on the flow efficiency profiles; there was also no effect of the peroxide distribution, though this is not shown since the profiles overlap so closely. This was also the case at the high screw speed and low PDF ratio. Figure 5.28 shows the profiles for the random distribution runs at the low PDF ratio, at both screw

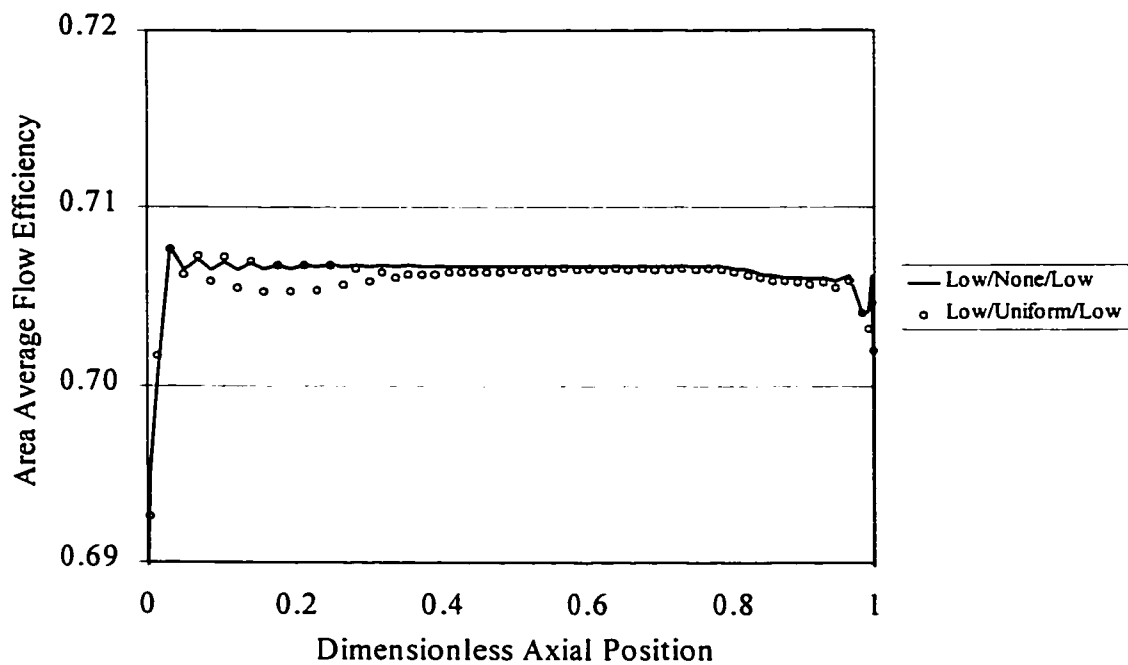


Figure 5.27: Average Flow Efficiencies for First Channel Geometry for Runs at Both Peroxide Levels

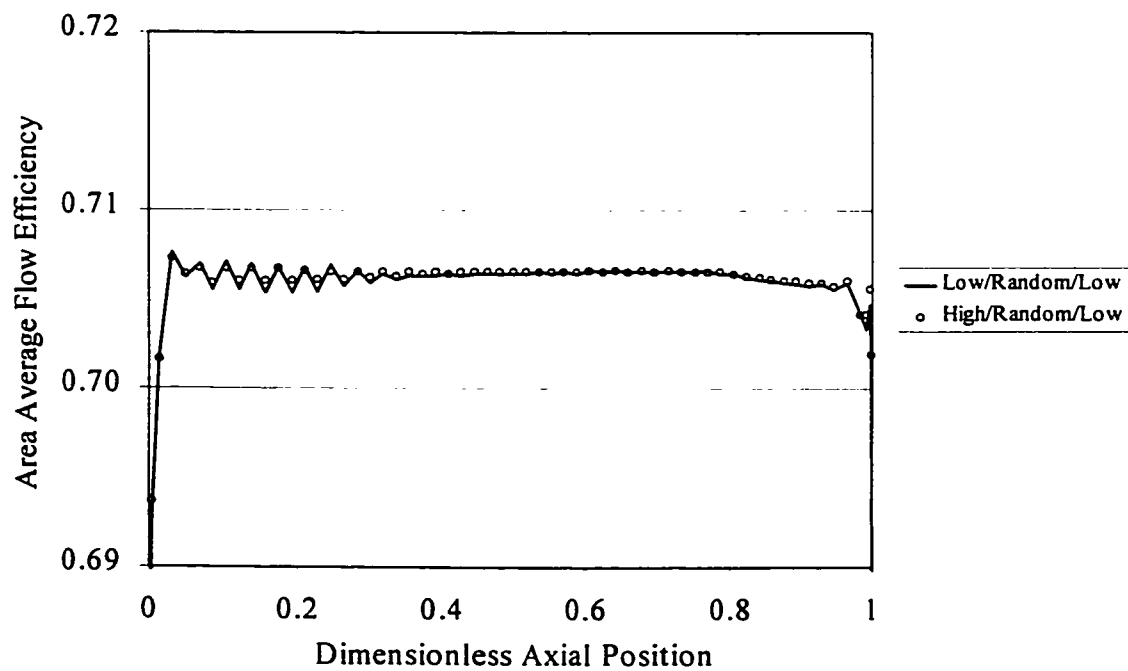


Figure 5.28: Average Flow Efficiencies for First Channel Geometry for Runs at Both Screw Speeds

speeds. The plot shows that there was no effect of the screw speed on the average flow efficiencies; this was true for all peroxide distributions and PDF ratio levels.

Figures 5.29 to 5.32 show the profiles for the runs at the high screw speed and all PDF ratio levels, for no peroxide, and the uniform, barrel, and random peroxide distributions respectively. The effects seen in these plots also appeared in those for the runs at the low screw speed, which are not shown. For the systems with no peroxide and the uniform peroxide distribution, one additional run each was performed at a very high throughput giving a PDF ratio of 1. The results data for these runs are given in Table 5.9 (in which they are referred to as runs 33 and 34), and the flow efficiency profiles are shown in Figures 5.29 and 5.30 respectively. Figures 5.29 and 5.31 show that for the runs with no peroxide and with the barrel peroxide distribution, there was an effect of the PDF ratio on the average flow efficiencies - at higher PDF ratios, the plateau values were less. The effect though was fairly small, with the drop being only about 0.001 in going from the runs at the low PDF ratio to those at the high PDF ratio. The inlet and outlet fluctuations are also seen to increase in magnitude with increased PDF ratio. The plateau level is seen to decrease further in Figure 5.29 as the PDF ratio is increased to 1, dropping another 0.0025 to 0.7030. Figures 5.30 and 5.32, in contrast, show almost no effect of PDF ratio on the average flow efficiency plateau levels for the uniform and random peroxide distribution runs. The curve in Figure 5.30 for the uniform distribution run at a PDF ratio of 1 also showed no significant change in the plateau level. The reason for the differences in the predictions of the effect of the PDF ratio on the average flow efficiency between the different inlet peroxide distributions is unknown. It would at first appear to indicate that significant degradation of the polymer nullifies the effect of increasing the PDF ratio. However, the fact that the effect was observed for the barrel distribution

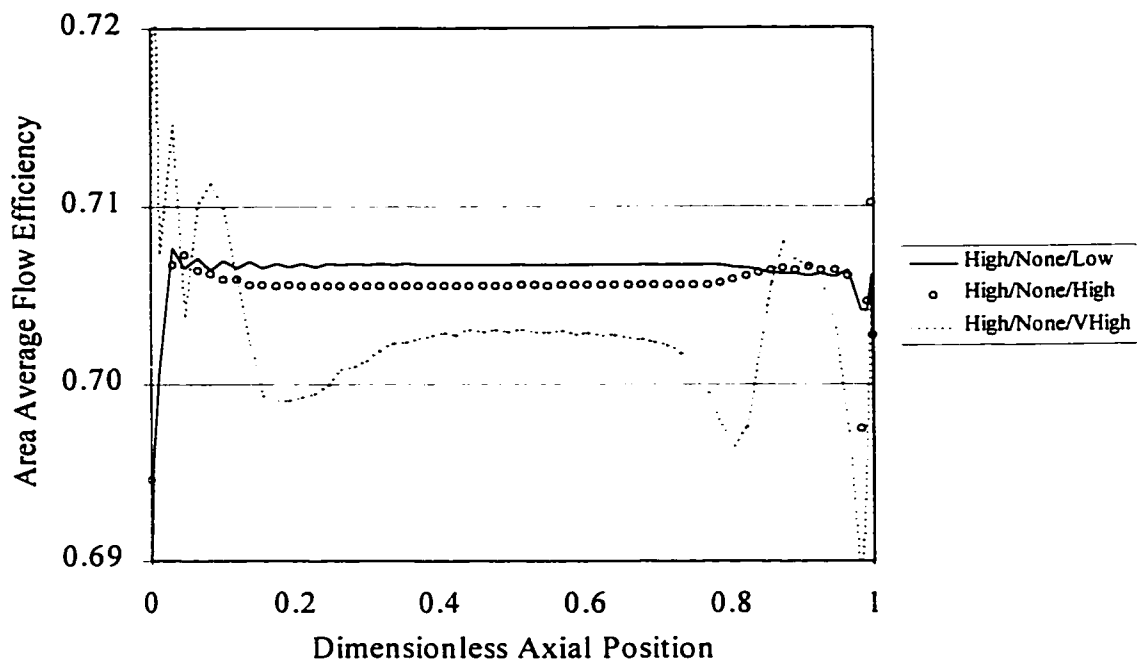


Figure 5.29: Average Flow Efficiencies for First Channel Geometry for Runs With No Peroxide

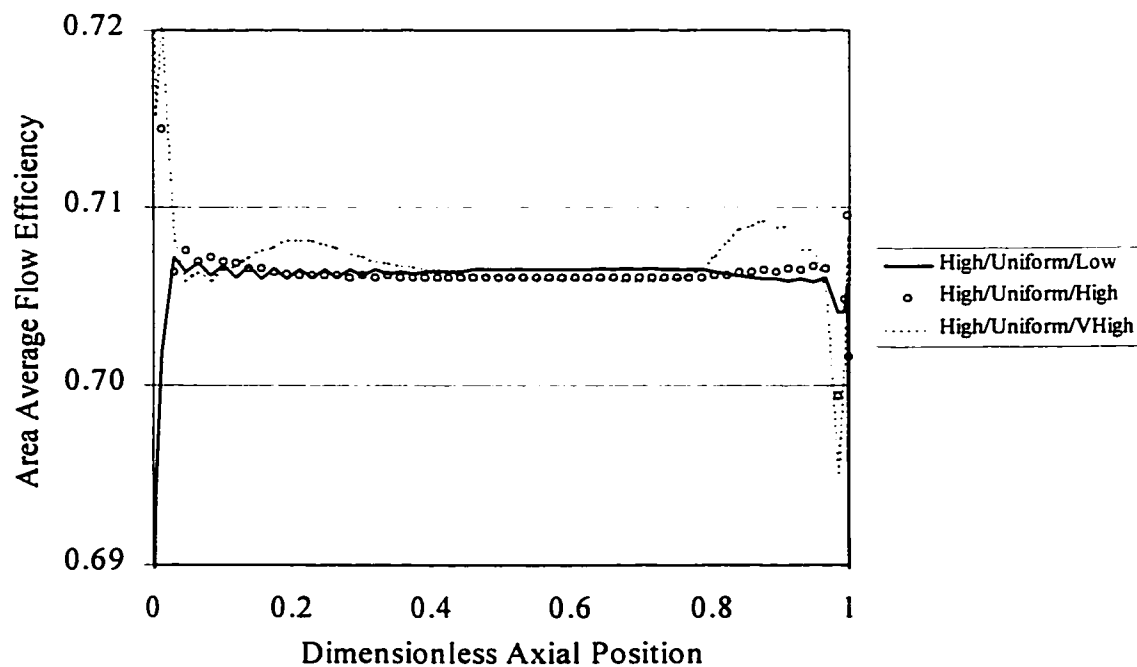


Figure 5.30: Average Flow Efficiencies for First Channel Geometry for Runs With Uniform Peroxide Distribution

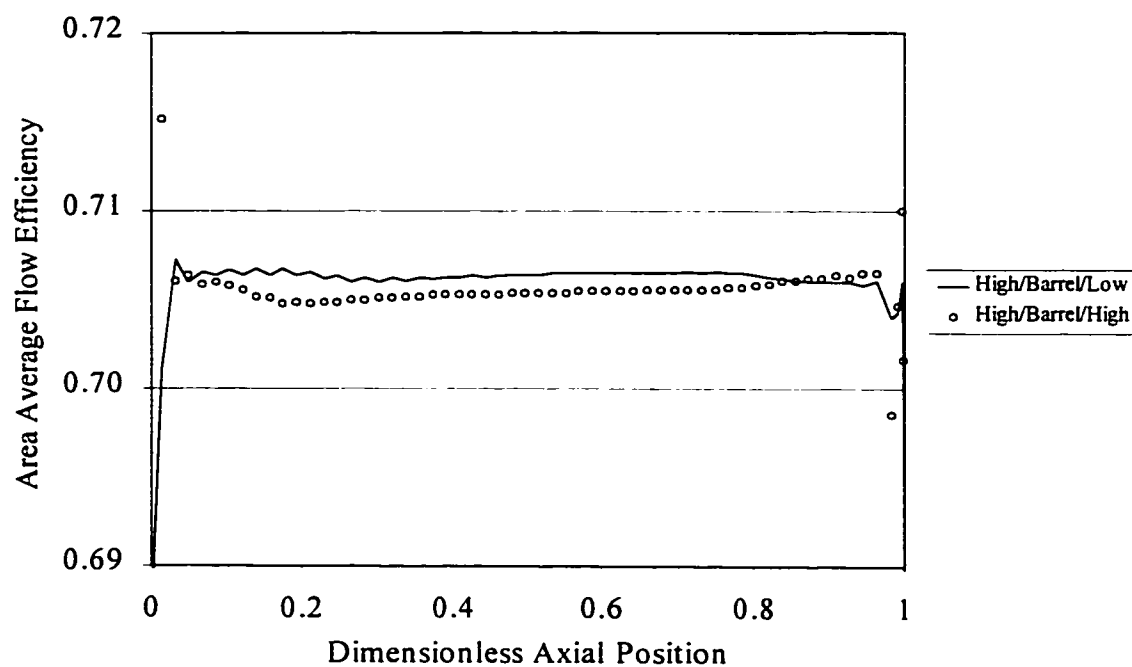


Figure 5.31: Average Flow Efficiencies for First Channel Geometry for Runs With Barrel Peroxide Distribution

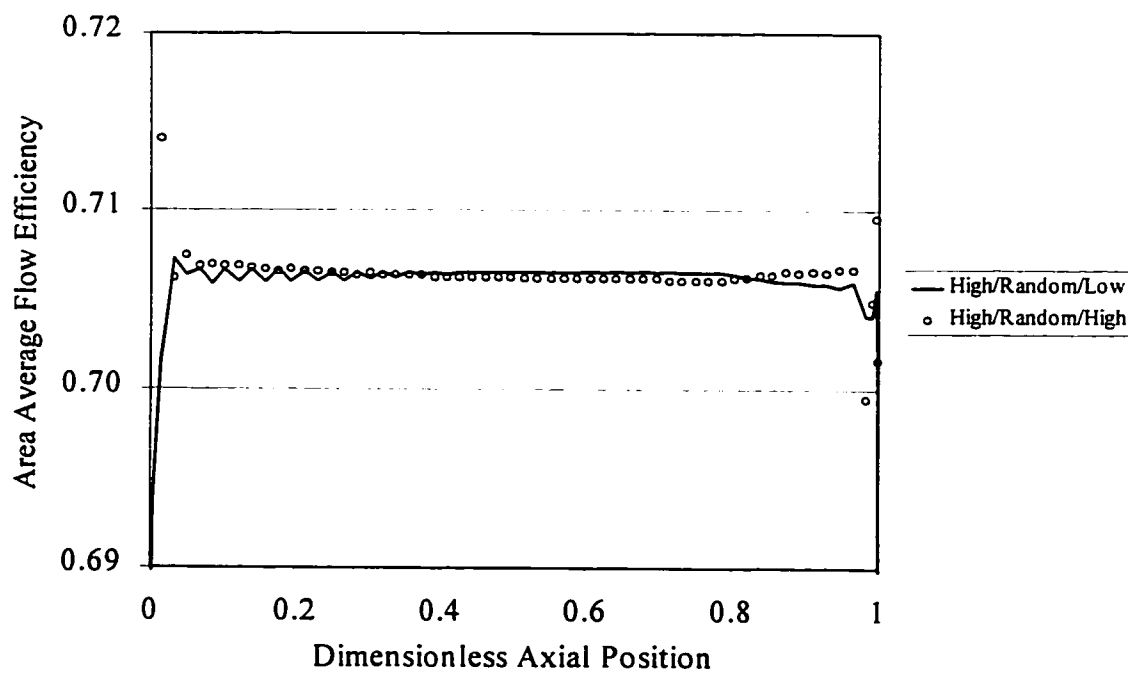


Figure 5.32: Average Flow Efficiencies for First Channel Geometry for Runs With Random Peroxide Distribution

Table 5.9: Simulation Results for Additional Runs							
<i>Run</i>	<i>Screw Speed (rpm)</i>	<i>Inlet Peroxide Distribution</i>	<i>PDF Ratio Q_P/Q_D</i>	<i>Mass Throughput (kg/h)</i>	<i>Average Pressure Change (kPa)</i>	<i>Average Outlet Peroxide Conversion $\frac{w_{I,In} - w_{I,Out}}{w_{I,In}}$</i>	<i>Average Relative Outlet Molecular Weight $\frac{\bar{M}_{W,Out}}{\bar{M}_{W,In}}$</i>
33	60	None	0.996	44.35	-53837	--	1
34	60	Uniform	0.998	21.49	-10906	0.364	0.223
35	60	None	0.997	22.04	-30242	--	1
36	60	Uniform	0.998	10.90	-5688	0.366	0.227

run at the low screw speed, for which the average outlet relative molecular weight was 0.135, and not for the uniform distribution run at the high screw speed and very high level of the PDF ratio, for which the outlet relative molecular weight was 0.223, contradicts this.

The profiles of area average flow efficiencies computed on lateral cross-sections along the channel lengths for the second channel geometry are now examined. Figure 5.33 shows the profiles for the no peroxide and uniform peroxide distribution runs at the low screw speed and low PDF ratio. Again the average flow efficiencies are found to remain close to plateau values along most of the channel length, with fluctuations in the inlet and outlet regions. The inlet fluctuations were more significant than in the simulations for the first channel geometry, especially for the reactive flow runs. The plateau levels were clearly lower for these simulations than before, at around 0.698. This is somewhat surprising, since in Figure 5.25 the high flow efficiency areas of the channel lateral cross-section seem to be larger relative to the size of the cross-section for the small aspect ratio channel than for the large aspect ratio channel. The Figure also shows that there was a slight effect of the peroxide level on the flow efficiency plateaus, with the addition of peroxide causing the plateau level to drop by about 0.0005. This effect was also seen in the barrel and random distribution runs, which are not shown since they overlap so closely, and at the high screw speed and both high and low PDF ratios. Figure 5.34 shows the profiles for the random distribution runs at the low PDF ratio, at both screw speeds. The plot shows that again there was no effect of the screw speed on the average flow efficiencies; this was true for all peroxide distributions and PDF ratio levels.

Figures 5.35 to 5.38 show the profiles for the runs at the high screw speed and all PDF ratio levels, for no peroxide, and the uniform, barrel, and random peroxide distributions respectively.

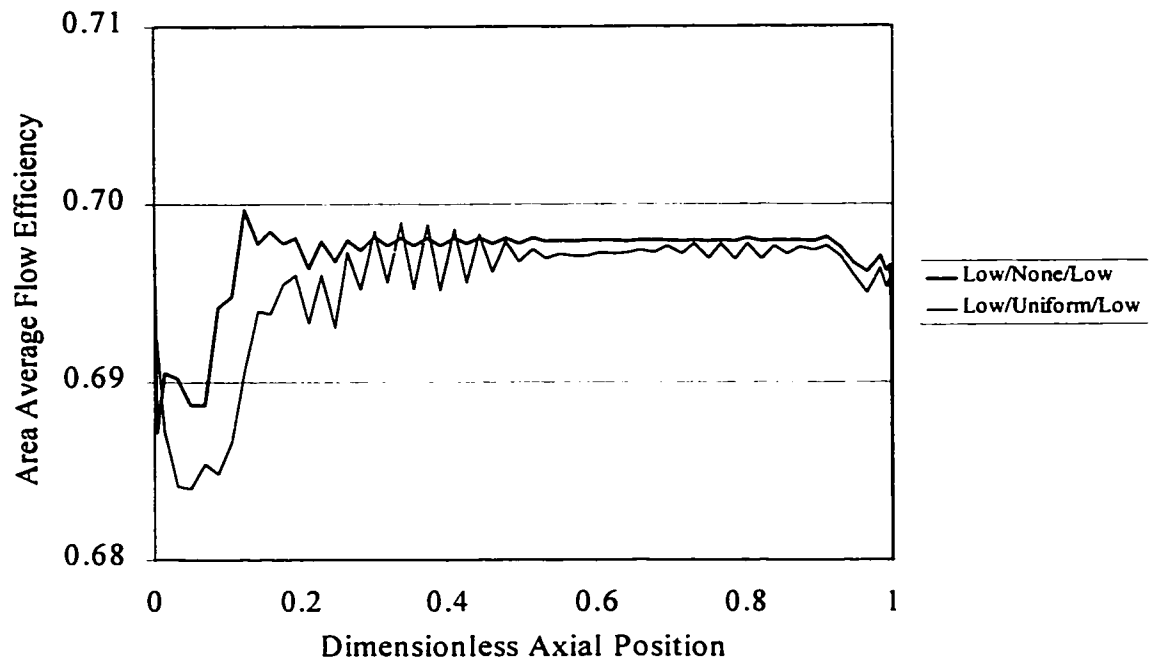


Figure 5.33: Average Flow Efficiencies for Second Channel Geometry for Runs at Both Peroxide Levels

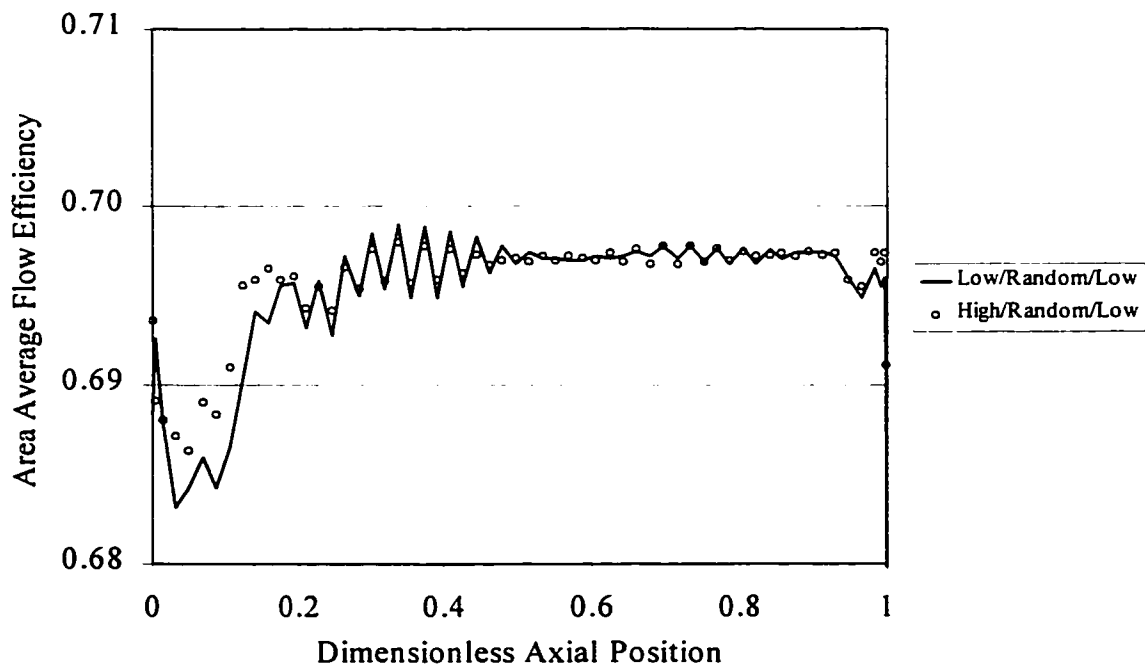


Figure 5.34: Average Flow Efficiencies for Second Channel Geometry for Runs at Both Screw Speeds

The effects seen in these plots again also appear in those for the runs at the low screw speed, which are not shown. For the systems with no peroxide and the uniform peroxide distribution, again an additional run for each was performed at a very high throughput giving a PDF ratio of 1. The results data for these runs appear in Table 5.9 as those for runs 35 and 36, and the flow efficiency profiles are shown in Figures 5.35 and 5.36 respectively. The Figures indicate some different trends than those seen in the same plots for the first channel geometry runs. Again there was a predicted effect of the PDF ratio on the average flow efficiencies, but here it is a positive one: at higher PDF ratios, the plateau values were greater. The magnitude of the effect was also larger, with the increase being about 0.003 in going from the runs at the low PDF ratio to those at the high PDF ratio. The effect was also seen in the runs for all four peroxide distributions, in contrast to the first channel geometry runs, where it was only seen in the no peroxide and barrel peroxide distribution runs. The effect is found to continue as the PDF ratio is increased further to 1, with the plateau level for the no peroxide runs increased by about 0.002 to 0.703 in Figure 5.35, while the level for the uniform distribution runs in Figure 5.36 increases only slightly, and even then only after nearly the full length of the channel section.

What the flow efficiency results for all 36 runs indicate is that the mixing abilities of both reactive and nonreactive polymer melt flows in SSE channels are, on average, very similar to those of two-dimensional flows, for the ranges of model parameters used in the simulations. The flows in the large aspect ratio channel were predicted to be slightly more efficient than those in the small aspect ratio channel, at converting the input fluid power at each point into the magnitude of the minimum eigenvalue of the rate-of-deformation tensor, or in other words the maximum specific rate of area stretch. The screw speed was predicted to have no effect on the mixing abilities of the

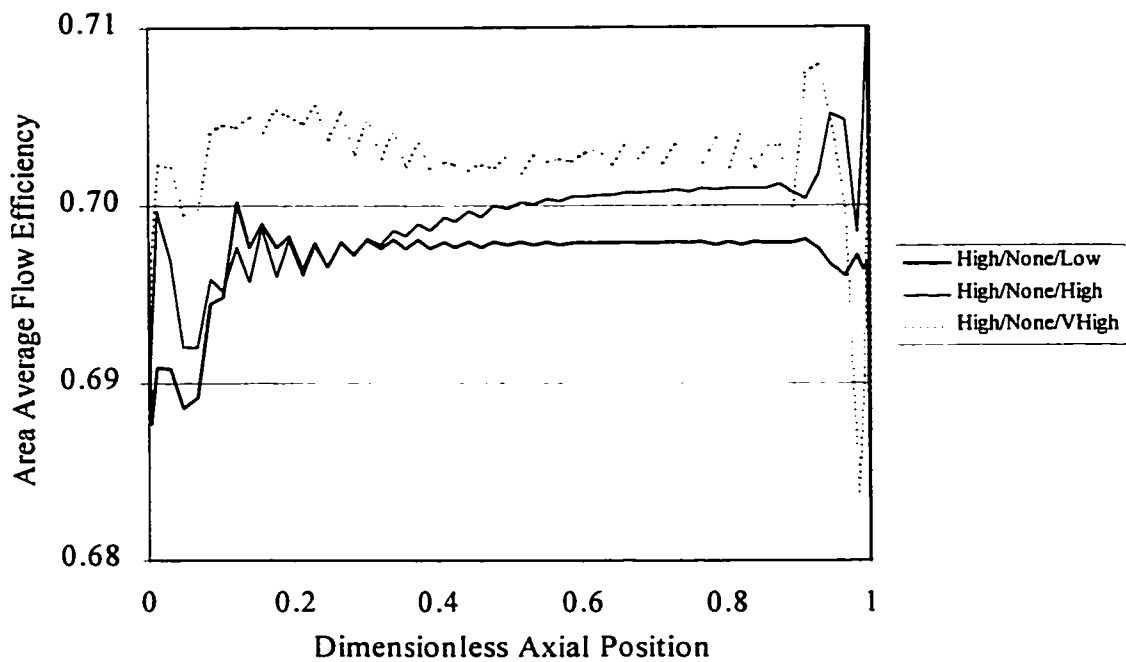


Figure 5.35: Average Flow Efficiencies for Second Channel Geometry for Runs With No Peroxide

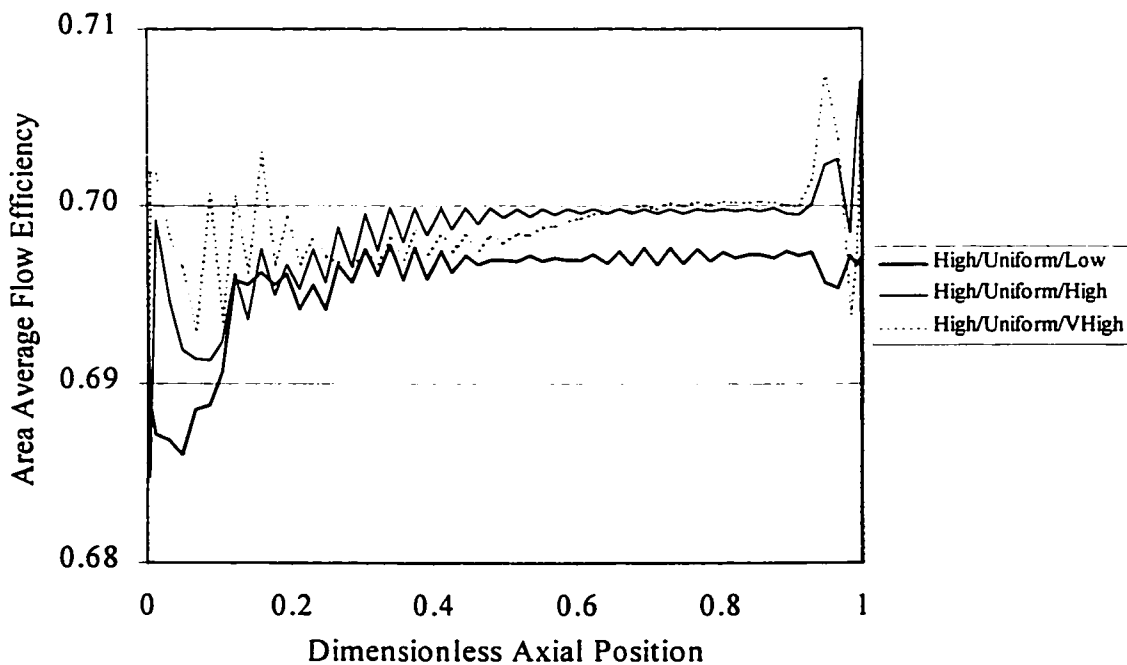


Figure 5.36: Average Flow Efficiencies for Second Channel Geometry for Runs With Uniform Peroxide Distribution

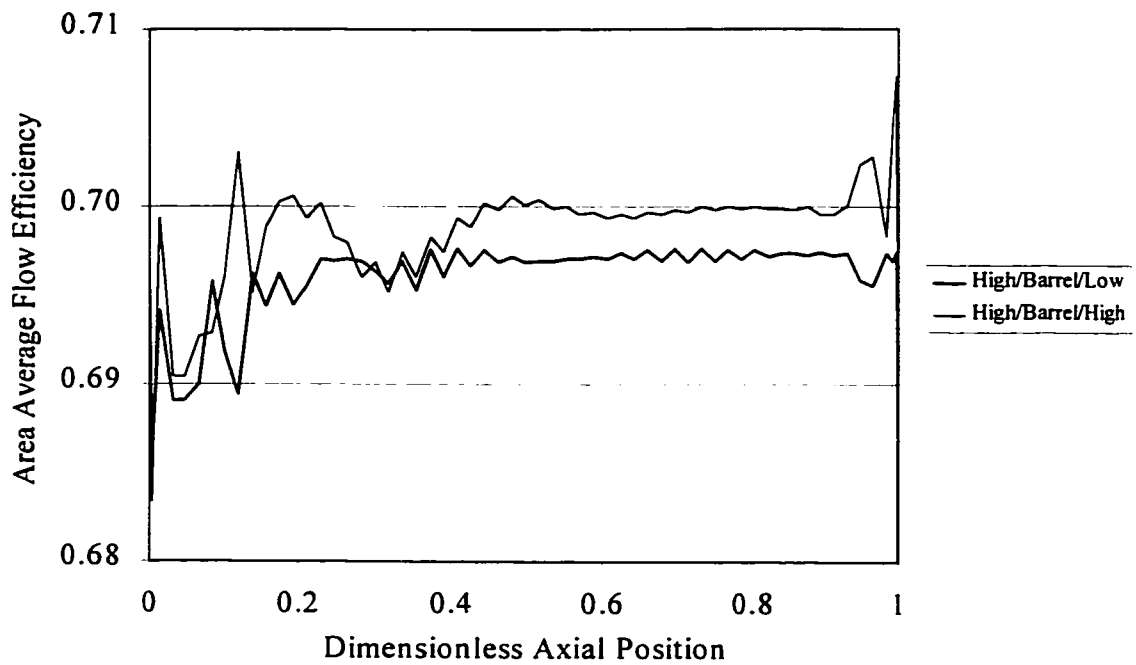


Figure 5.37: Average Flow Efficiencies for Second Channel Geometry for Runs With Barrel Peroxide Distribution

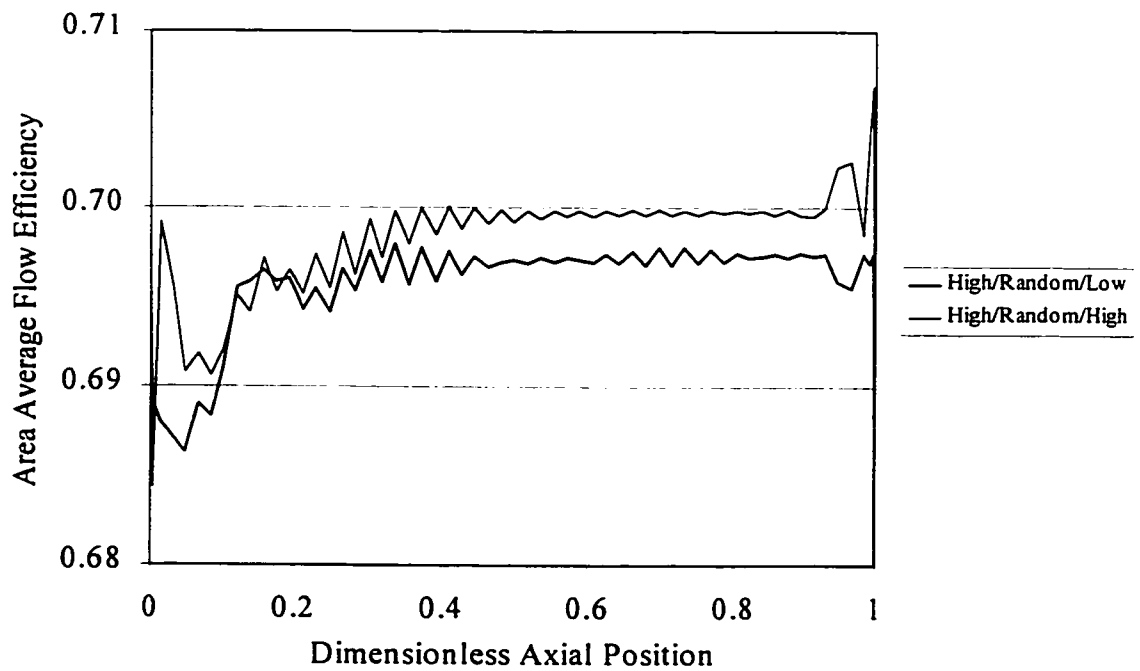


Figure 5.38: Average Flow Efficiencies for Second Channel Geometry for Runs With Random Peroxide Distribution

flow fields, and the peroxide level and addition pattern were predicted to have, at most, only slight effects. The principal influence on the mixing abilities of the flows was pressure-to-drag flow ratio. The extruder channel flow can be viewed as a cross-channel cavity flow in a long rectangular channel (a two-dimensional flow for which the flow efficiency is equal to 0.7071 everywhere), upon which is superimposed a combined drag and pressure flow in the longitudinal direction. The longitudinal flow is a consequence of the relative motion of the screw and barrel surfaces in the extruder; its makeup is indicated by the value of the PDF ratio. The effect of the longitudinal flow has been shown here to be to lower the average flow efficiencies in the channels, and thereby on average to add a small component of uniaxial extension to the channel flows. The drag flow effect alone was found in the results for the runs at the PDF ratio value of zero - it was predicted to be slight in the large aspect ratio channel, but reasonably large in the small aspect ratio channel. The effect of the pressure flow on top of the drag flow on the mixing abilities of the flows was found in the results at the PDF ratio values greater than zero. In the large aspect ratio channel the effect was predicted to be in the same direction as that of the drag flow (i.e. towards smaller flow efficiencies), whereas in the small aspect ratio channel it was predicted to be in the opposite direction, and again of larger magnitude than in the first channel geometry. The greater sensitivity of the flow efficiencies in the small aspect ratio channel to the down-channel drag and pressure flows is reasonable, since the size of the large areas of high and low flow efficiency in the recirculation zones adjacent to the screw flights are influenced by these flows, and these areas are of greater relative size in the lateral cross-sections of the small aspect ratio channel than in those of the large aspect ratio channel.

5.5.4 Mixing Efficiency Analysis - Area Efficiencies

The other element of mixing analysis of the channel flows is the area efficiencies of interfacial area elements along pathlines through the mesh. Area elements are specified with initial orientations and positions on the inlet plane, and then are tracked as they move through the system, with the area efficiency at each position being computed from the orientation vector of the element and the eigenvalues of the rate-of-deformation tensor. The element is actually represented by three points in the fluid (i.e. two infinitesimal line segments sharing one end point), and the orientation vector is found as the cross product of the vectors between the points. As the element moves in its flattened helical path, in which it translates in the down-channel direction while circulating in the cross-channel direction, it will reorient itself and alternately pass through regions of high and low area efficiency, indicating high and low (or even negative) actual rates of area growth relative to the optimum, the value of which is determined at each point by the flow efficiency. Unfortunately, to compute the area efficiencies of elements along pathlines requires the ability to calculate and output quantities at the points of the lines, a feature which FIDAP does not make available to its users. As such, no area efficiency results could be obtained for the simulations. The other possible option was to plot the predicted growths of the area elements alone. The problem with such results though, is that they confound the influences of both the area and flow efficiencies on the predicted element growths, and as such do not give any additional insight into the mixing nature of the flows. In other words, the results would only indicate how much growth an interfacial area element would undergo, and would not indicate how much of that growth was due to the orientation of the element relative to the flow field and how much to the mixing ability of the flow itself. For these reasons then, no elemental area growths are shown either.

5.5.5 Discussion

Qualitatively, it can be said that the predicted average degree-of-freedom profiles for the finite element simulations look good. The shapes of the profiles are largely smooth, and the predicted effects of the model parameters on the profiles conformed to expectations. As with all simulations, questions regarding the reliability and accuracy of the results must be dealt with. The issue of reliability principally has to do with whether or not the obtained results represent the true solution to the model equations in the system geometry. For finite element simulations this is the issue of the mesh independence of the solutions - have a sufficient number of elements been used in the mesh, so that any further addition will not result in significant changes to the degree of freedom profiles? Unfortunately the workstation used in this work did not have sufficient memory to allow this to really be tested for this system, since the original mesh was designed to be as large as would be allowed. The mesh independence of the simulation results could also be tested by performing simulations using a mesh of significantly reduced density, but this was not considered a viable option due to the original mesh being itself only of low to intermediate density. Based on the qualitative goodness of the results though, it is believed that reliability is not a problem here.

The issue of accuracy has to do with whether or not the simulation results can be taken as representative of the behaviour of the true system modeled. There are no experimental results for direct comparison with the predictions, so this must be inferred. First, regarding the fluid chemorheology, the temperature range in the simulations was well within that of the viscometric data from which the power-law parameter regression equations (5.15) and (5.16) were determined, but the same was not true for the weight-average molecular weights - the regression equations were used at molecular weights well below those of the resins from which the data were obtained. This

is particularly an issue for the power-law index, for which the location of the bends in the curves shown in Figure 5.3 are completely unknown. Thus in the reactive extrusion simulation runs, there is a question as to the accuracy of the degree of freedom profiles in the last part of the channel section, within which the computed molecular weights were lowest. To deal with this issue, the regression equations should be reformulated based on viscometric data from resins covering a larger range of molecular weights. Second, the use of the kinematic reversal assumption to represent the screw and barrel velocities can be considered to not significantly affect the accuracy of the results, even though it is not strictly correct. This is because the channels in the two geometries are shallow relative to the screw diameter, and so the use of this set of boundary conditions does not appreciably change the velocity gradients (and hence the flow efficiencies) in the flow. Overall then, there are minor concerns as to the accuracy of the results for the reactive extrusion runs.

There are additional concerns as to the applicability of the results to true extrusion systems, in which viscoelasticity of the melt and leakage flows over the screw flights exist, neither of which were included in the current model. Since the degradation reaction also affects the polymer elasticity, if the elasticity does change the flow efficiencies, then the conclusion that the reaction has no effect on the mixing abilities of the channel flows would have to be changed. FIDAP does have the capacity to simulate viscoelastic flows, so this should be pursued. Also, as was shown in Chapter 3, leakage flows can significantly affect the channel flow rates, and possibly also the temperature profiles. Hence they may have considerable influence over the area and flow mixing efficiencies in the channels. The addition of leakage flows to the model should thus also be pursued.

Finally, other suggestions for future work to improve the model and results are made here. To deal with the problems in the non-uniform peroxide distribution runs of the average peroxide levels changing just after the inlet, inlet levels that make the equilibrium peroxide levels within the mesh equal to 0.6 wt% in the melt should be used, rather than values which make the level equal to 0.6 wt% on the inlet plane only. These levels would have to be determined by trial-and-error for each run. Alternatively, the way the barrel and random distributions are specified could be changed, to smooth them out somewhat so that the peroxide levels at all nodes on the inlet plane are above zero, but the same overall patterns are preserved. By reducing the intensity of segregation of the peroxide between the nodes across the inlet, the problem of the average peroxide levels changing as the peroxide spreads across the channel cross-sections as the melt moves down the channel, could be remedied somewhat. Next, the problems encountered with convergence of runs at very low mass throughputs, giving negative PDF ratio values, should be tackled, perhaps through further refinement of the finite element mesh. Interfacial area elements in such systems would likely undergo more growth than in runs at higher throughputs, due to the higher average residence times of the fluid in the channel section, so it would be interesting to see if the mixing natures of the flows would be changed as well. Lastly, a program to compute area efficiencies along pathlines in the channels should be developed, which would track the position and orientation of each interfacial area element throughout the mesh based on the computed velocity field for a simulation, and at each point find the eigenvalues of the rate-of-deformation tensor. Such a program was used by Zerafati and Bigio (1994) to compute area efficiencies along pathlines in a wavy-walled channel. Once such a program was developed, the effect of the extruder operating conditions, inlet peroxide level and distribution, and channel geometry on the area efficiencies

could be studied. As well, the results of Chella and Ottino (1985), who predicted periodic restoration of mixing efficiencies along pathlines in single-screw extruder channels, could be updated for non-isothermal non-Newtonian reactive polymer flows.

CHAPTER 6

**FINITE ELEMENT METHOD SIMULATION AND MIXING ANALYSIS OF
POLYMER MELT FLOW IN A CSCO EXTRUDER CONVEYING SCREW
ELEMENT CHANNEL**

6.1 Introduction

In self-wiping co-rotating twin-screw extruders, most of the mixing experienced by a polymeric fluid takes place as it passes through kneading block sections of the screws. Laminar mixing in fully-filled conveying screw elements can also be important though, as the fluid can spend a considerable portion of its residence time in the extruder in filled lengths upstream of flow restrictions, such as kneading block elements, reverse conveying screw elements, and the die. In this chapter finite element simulations of steady-state non-isothermal three-dimensional reactive PP flows are described, in the channel of a forward conveying screw element from a CSCO extruder, with the operating conditions, peroxide level and addition pattern, and channel geometry varied. The chapter begins with a review of the relevant literature on finite element studies of fluid flows in CSCO extruder screw elements, followed by a description of the procedure for the simulations. Results are given for both conventional and reactive extrusion simulations, and then discussion of what the results indicate about the mixing natures of the flows is made, along with analysis of the predicted effects of the specified operating conditions and peroxide-initiated controlled degradation reaction on this nature. Finally, the reliability and accuracy of the simulation results are discussed, and ideas for future work presented. The work in this chapter borrows heavily from that for the finite element simulations of polymer melt flow in SSE channels described in Chapter 5, and so in the chapter sections where overlap takes place, the reader is

referred to the appropriate sections of Chapter 5.

6.2 Literature Review

Early works on finite element simulations of viscous flows in fully-filled CSCO extruder conveying screw elements focused on solving the momentum conservation equations in the two-dimensional domain of the channel cross-section perpendicular to the screw flights, and hence ignored the complication of the intermeshing region. Examples are Denson and Hwang (1980), who simulated Newtonian isothermal flow by numerical solution of the equation of motion for down-channel flow, and Lai-Fook et al. (1989), who simulated isothermal flow of a power-law fluid, with solution of the 2D profiles of the three velocity components and pressure. More recently, Potente and Flecke (1997) used this so-called two-and-a-half dimensional (2.5D) modeling approach to obtain predictions of particle pathlines within the screw channels, for the isothermal flow of a power-law fluid at different channel flow rates. By computing particle residence times from the pathlines, they were able to reproduce experimentally determined minimum residence times in a CSCO extruder.

Gotsis and Kalyon (1989) extended the use of the 2.5D technique by applying it to the intermeshing region. The meshed domain in the intermeshing region was the curved region representing the intersection of the channel with a plane through the channel centre parallel to the screw flights; the channel was assumed to be of a large aspect ratio and so the effect of the flights was neglected. Simulations of non-isothermal flows of a generalized Newtonian fluid with temperature-dependent viscosity were performed for the channel regions both inside and outside of the intermeshing region, and predictions obtained of the shapes of interfaces separating two

different coloured fluids with specified initial arrangements in the channels, after a certain amount of deformation had taken place. The predicted shapes were found to correspond closely with those determined by experiment for the same systems. The authors also showed plots of computed fluid stresses and velocity vectors in the fluid chambers around a pair of kneading discs, which were represented by a fully 3D mesh, which was updated as the discs turned.

Sastrohartono et al. (1995) updated the work of the previous authors by again separately modeling and simulating the flows both inside and outside the intermeshing region of the channel, but now the simulation results were coupled to one another to represent the flow in a complete channel. Non-isothermal flow of a non-Newtonian fluid was simulated in the translation region of the channel (outside of the intermeshing region) by means of a finite difference numerical technique, and within the intermeshing region the flow was simulated on the 2D domain by a finite element technique. Profiles of the process degrees of freedom were determined in the intermeshing region domain, and predicted pressure and temperature profiles along a channel length of 32.5 screw turns were obtained by carrying the flow computations through a large number of consecutive translation and intermeshing regions of a screw channel.

Huneault and Dumoulin (1994) took a step forward from the 2.5D approach to FEM simulations of flows in conveying screw elements, by performing fully three-dimensional simulations of isothermal flows of Newtonian and power-law fluids in curved screw channels with channel reorientations representing those in the intermeshing regions of true screw elements, and with channel shifts of either zero or half the channel width. The flow reorientation was found to not have a significant effect on pressure growth, but the large channel shift examined was found to greatly increase the pressurization capacity of the channel.

Goffart et al. (1996) also simulated the flows inside and outside the intermeshing region separately and coupled the results to one another to represent the flow in a complete channel. However, in their work the finite element meshes for both regions were fully three-dimensional and curved, with the mesh for the intermeshing region including the channel shift and reorientation at its centre. The flows in the two regions were modeled as isothermal and Newtonian, and leakage flows were neglected. Predicted average pressure changes, velocity profiles, and average shear and elongation rates were reported for the two different mesh sections, for different values of throughput, screw speed, helix angle, and fluid viscosity.

In the simulation of viscous flows in CSCO extruder kneading block elements, due to the complications of the time-dependent flow boundaries created by the continuous motion of the kneading discs and the complex geometries of the flow chambers due to the staggering of the kneading discs, very few numerical studies exist. The only finite element studies of note are those by Manas-Zloczower and co-workers, who deal with the problem of the moving flow boundaries by performing simulations in a number of sequential geometries representing a complete revolution of the kneading discs. Yang and Manas-Zloczower (1992) demonstrated this approach in simulating the steady-state isothermal 3D flow of a power-law fluid in a complete kneading block element with 5 bilobal kneading disc pairs, at several angles of stagger. The operating conditions for the simulations were screw speed and average pressure drop over the flow domain. Profiles of velocities and melt pressures were presented for cross-sections at different positions, as were average values in the fluid of shear stresses and a mixing parameter quantifying elongational flow components in the system. The average values of this parameter were found to be similar to that for simple shear flow. No significant effect of screw speed was found on the

parameter values, but slight effects of stagger angle and pressure drop were observed. Cheng and Manas-Zloczower (1997) updated these results for a kneading block element with trilobal discs. Similar effects of the operating conditions on the average values of the mixing parameter were found. The average values were slightly larger than those previously found for the bilobal discs, indicating an increase in the elongational flow components in the system.

An experimental work of interest is Maier et al. (1994), who studied the conversion levels in a co-rotating TSE of maleic anhydride terminal functional groups on ethylene-propylene rubber chains, reacted with oligomers bearing amine and alcohol functional groups at their own chain ends. The objective was to relate the measured conversion levels to mixing taking place in the screw channels. Trials were performed at two screw speeds and several throughput levels, and at different levels of addition of each oligomeric species. For the amidification reactive process, it was found that mixing was more efficient at lower screw speeds. For the esterification process (involving the oligomeric alcohol), the conversion results indicated non-homogeneous mixing of the additive into the melt stream.

6.3 Theory

The polymer flow in the fully-filled CSCO extruder forward conveying screw element is mathematically modeled in the same way as in the single-screw extruder channel section in Chapter 5, i.e. as a steady-state, non-isothermal 3D flow of an incompressible non-Newtonian fluid, with power-law fluid rheology and temperature and weight-average molecular weight dependent power-law parameters. The conservation equations (5.1) and (5.2) are used, along with the fluid constitutive equation (5.3).

6.4 Simulation Procedure

6.4.1 Model Parameter Values

The process model parameters for the simulations are the screw and element geometry parameters, the polymer properties, and the assumed extruder operating conditions. The screw and element geometry parameter values for the two considered channel geometries are given in Table 6.1. The channel geometry was varied in the simulations by the use of two different pairs of values of centreline separation and channel pitch. The first pair are for a small pitch forward conveying screw element in a Leistritz 30-34 laboratory-scale twin-screw extruder with bilobal screws, the same system studied in Chapters 3 and 4. Such an element has narrow channels and as such is useful for building up melt pressure in filled regions before flow restrictions in an extruder. Several such elements were placed upstream of the die in the screw configuration (shown in Figure 3.13) used in the RTD experiments described in Chapter 4. The second pair of values were chosen to give a larger channel aspect ratio than the first, but with a pitch still small enough that the assumption of complete filling of the element would not be unreasonable for normal CSCO extruder operation.

The polymer physical and thermodynamic property values were the same as those used in the SSE channel flow FEM simulations, shown in Table 5.2. The PP melt power-law parameter regression equations (5.15) and (5.16) were also used again. The operating condition values for the simulations are given in Table 6.2. Constant temperatures were used again for the channel inlet and barrel temperatures, but higher values for each were used than in the SSE simulations, since the average residence times of the polymer in the TSE element channel were less, and so higher temperatures were needed to achieve similarly high peroxide conversion levels in all reactive

<i>Parameter or Quantity</i>	<i>Symbol</i>	<i>Value</i>	
Screw outer diameter	D_s	33.7 mm	
Number of screw flights	i	2	
Screw centreline separation	a	30.0 mm	32.0 mm
Maximum channel depth	h_{Max}	3.7 mm	1.7 mm
Average channel depth	\bar{h}	2.8 mm	1.4 mm
Fractional intermeshing region channel shift	e_{Max}/b_{Max}	0.25	0.42
Pitch	t	20 mm	30 mm
Maximum channel width	b_{Max}	7.9 mm	10.1 mm
Maximum flight width	e_{Max}	2.0 mm	4.3 mm
Helix angle	ϕ_s	10.7°	15.8°
Channel aspect ratio	b_{Max}/\bar{h}	2.8	7.4

Inlet temperature	220°C	
Barrel wall temperature	240°C	
Screw speed	100 rpm	250 rpm
Pressure-to-drag flow ratio	0	-0.25
Average inlet peroxide level	0 wt%	0.6 wt%

extrusion simulation runs. The screw speed was varied between 100 and 250 rpm, which are typical for CSCO extruder operation, and again are higher than in SSEs. The pressure-to-drag flow ratio was varied between 0 (corresponding to pure drag flow) and -0.25 (giving a positive pressure gradient in the channel direction). The negative PDF ratio value gave rising pressures along the channel length in the simulations, which is the normal operating state for fully-filled forward conveying screw elements. Again the value for each run was specified indirectly by adjusting the mass throughput in the channel, as determined by the velocity profile on the inlet plane. In the simulations, the peroxide level and addition pattern were also varied. The same average peroxide levels in the melt at the inlet plane of the channel (0 or 0.6 wt%) were used as in the SSE channel flow simulations, as well as the same inlet distribution patterns (uniform, barrel, and random). The details on how these distributions were actually specified are given in the following subsection.

6.4.2 Finite Element Method Details

The FEM simulations were carried out, as before, using version 7.62 of the commercial computational fluid dynamics code FIDAP. Again 9 degree of freedom profiles were computed by the software: melt temperature, melt pressure, three velocity components, peroxide concentration in the melt, and the three MWD moments. Leakage flows were also not considered. In creating the finite element mesh, it was necessary to take the approach of only meshing one of the three independent flow channels in the screw element. The mesh could not be created on the basis of the cross-section perpendicular to the extruder axis as was done with the SSE channel section in Chapter 5, due to the change in shape of the fluid chambers as they cross the intermeshing region of the screws. Figure 6.1 shows the complete channel mesh for the first

channel geometry in an isometric view and a top view; the top view also shows the direction of the global coordinate system for that view. The Figure shows that the true curvature in the direction of the channel helix is represented, and also that the mesh is extended through 2 complete “figure-eight” turns of the channel, in which material twice passes back and forth between the two screws. Figure 6.2 shows the 2D symmetric mesh on the inlet plane to the channel section (which is perpendicular to the screw flights), and also the mesh in the cross-section at the centre of the first intermeshing region of the channel (which is parallel to the global $Y'Z'$ plane). The first mesh in Figure 6.2 also shows the direction of the local coordinate system for the cross-section, which has its origin at the top centre of the region. The Figure shows that the true self-wiping channel cross-section geometry for bilobal screws is represented, but that the true curvature of the top of the channel (representing the intersection with the barrel surface) is not represented. As well, the presence of the flight clearance above the channel was neglected.

As Figure 6.2 makes clear, the channel mesh was created differently in the translation and intermeshing regions. In the translation region, the cross-sections were all created to the same size and shape as the inlet plane (which is located at the centre of what would be the true channel translation region). In the first translation region section, denoted by **A** in Figures 6.1 and 6.2, the cross-sections were staggered slightly in the circumferential direction towards the inlet. In the following translation regions, the cross-sections were uniformly spaced in the circumferential direction. In the intermeshing region, all the cross-sections up to that at the centre of the region (denoted by **C** in Figures 6.1 and 6.2) were again created to the same size and shape as the inlet plane, in orientations perpendicular to the screw flights at their respective positions. The cross-sections were staggered in the circumferential direction towards the centre of the region. As

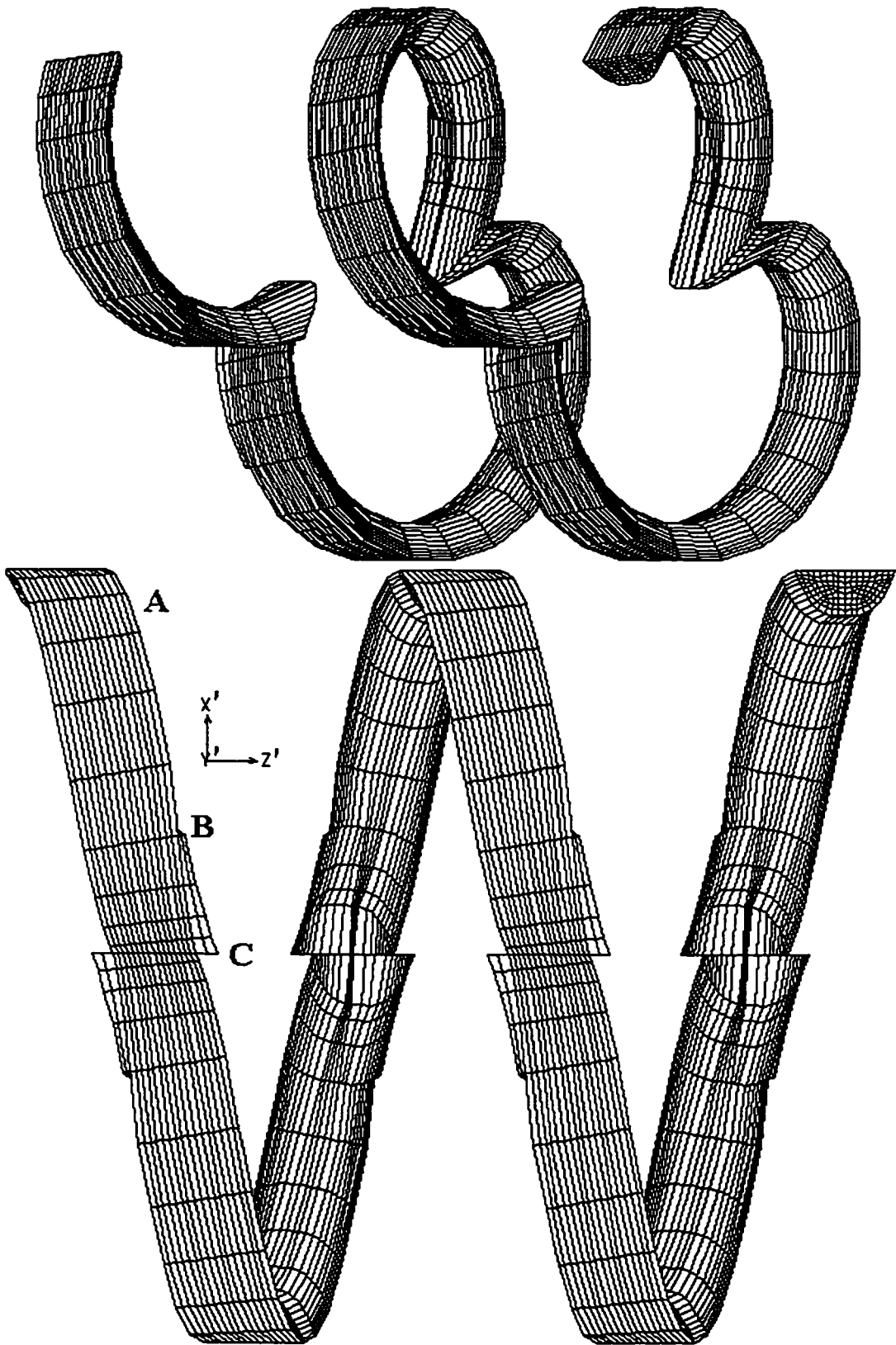


Figure 6.1: First Channel Geometry Finite Element Mesh

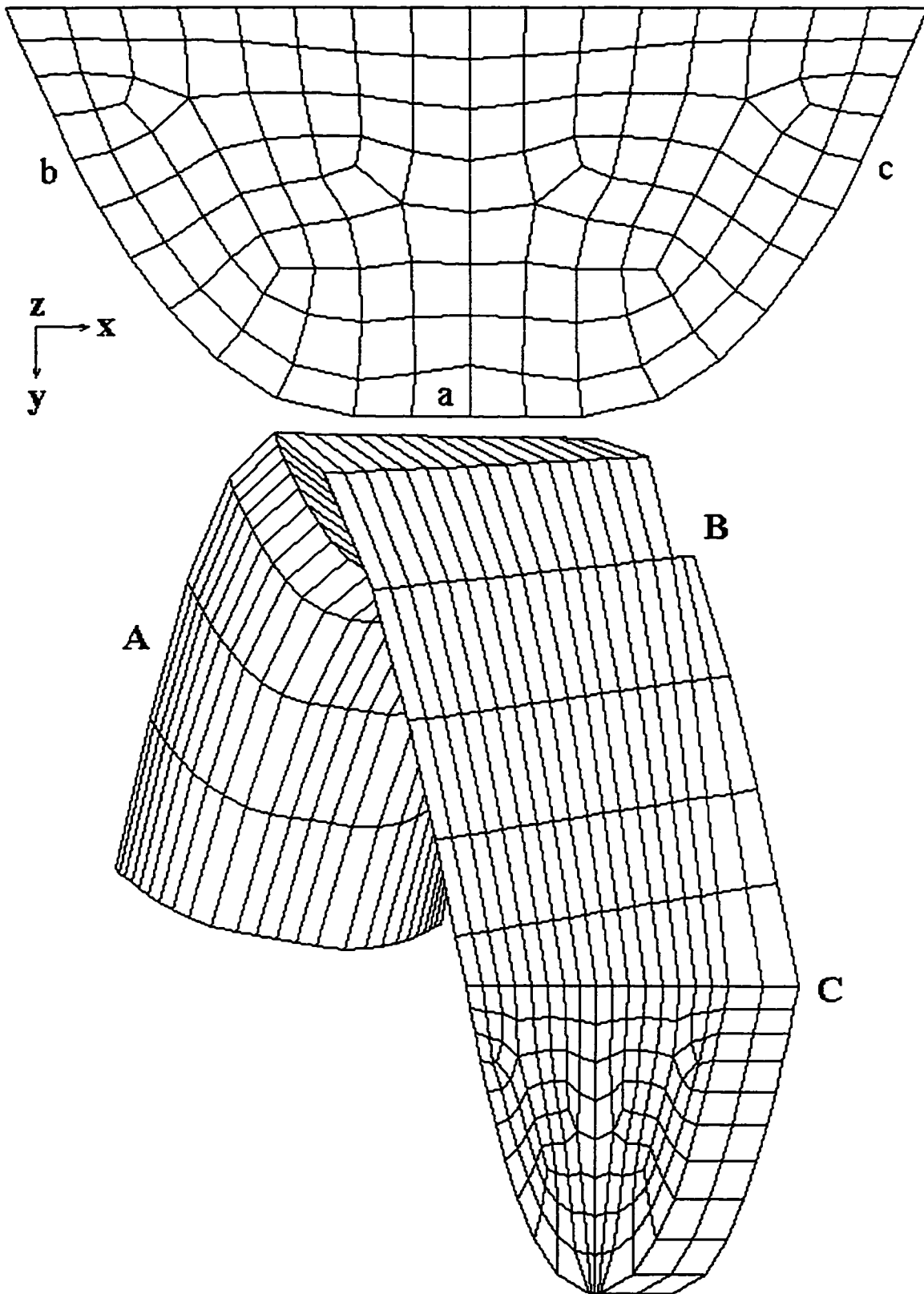


Figure 6.2: First Channel Geometry Cross-Section Meshes

mentioned above, the cross-section at the centre of the intermeshing region was parallel to the global $Y'Z'$ plane (for connecting the differently oriented cross-sections of the two screws). This cutting plane orientation led to increased channel depth and cross-section area at this position.

The meshing in the intermeshing region cross-sections was approached differently than in the translation region. A basic consideration in meshing a channel for fluid flow in FIDAP is that the same mesh must be able to be “projected” through from the inlet to the outlet of the channel. This creates a difficulty in the centre of the intermeshing region though, at which a shift in the channel occurs due to the presence of a flight of the second screw in the channel of the first. To deal with this, in the intermeshing region cross-sections the mesh was split into two sections, the first being a core section with the same mesh as the inlet plane, but with the flat channel bottom (denoted by **a** in Figure 6.2) connecting the sides of the screw flights (denoted by **b** and **c**) made narrower, and the second being a side section with a mapped mesh filling out the remainder of the area of the cross-section. As the centre of the intermeshing region was approached, the core section was contracted and the side section expanded; it was the core section which “carried” the inlet mesh through the intermeshing region. At the centre of the region, ideally the flat channel bottom should have been reduced to zero width; however this would have changed the core section mesh so could not be considered. Instead, the channel bottom was reduced in width by 85%, which allowed the core section mesh to be preserved while still representing nearly all the true channel shift. The extreme contraction of the elements in the bottom of the cross-section mesh can be seen in the mesh at position **C** in Figure 6.2. Also at the centre of the intermeshing region, the side section ended abruptly, showing that it represents the part of the channel which is blocked by the opposing flight of the other screw. Position **B** in Figures 6.1 and 6.2 is the start of the side section

in the channel. The elements in this section should have been extended to the start of the intermeshing region, but this would have necessitated the mixing of continuum element types (wedge and brick), so was not considered. By using a reasonably large number of cross-sections in the intermeshing region, the volume of channel which was omitted by this approach was kept fairly small.

An isometric view of the full channel mesh for the second channel geometry is shown in Figure 6.3, along with a view of the mesh on the inlet plane. The channels for this geometry are wider and shallower than those for the first geometry, with a more prominent flat channel bottom. As in Chapter 5, the meshes for both geometries were comprised of 4 boundary (2D) element groups along the outside, and one continuum (3D) element group within, representing the fluid. The boundary element groups were again the inlet and outlet planes, the screw (which included the inner surfaces of the mesh and the end faces of the intermeshing region side sections), and the barrel (the outer curved surface of the mesh). As well, linear brick continuum elements with 8 nodes each were used again.

Table 6.3 shows a number of different data values for the finite element meshes used in the simulations. The first thing to notice is that two different meshes were used for the runs with the first channel geometry. The difference between the two is that for the 100 rpm runs, 10 cross-sections were used in each full translation and intermeshing region section, and for the 250 rpm runs, 12 cross-sections were used in each respective section. Consequently the number of cross-sections, nodes, and elements in the 250 rpm runs were higher than those for the 100 rpm runs. For the runs with the second channel geometry, only one mesh was used since runs were only performed at one screw speed (100 rpm), which will be discussed later. The Table also shows the

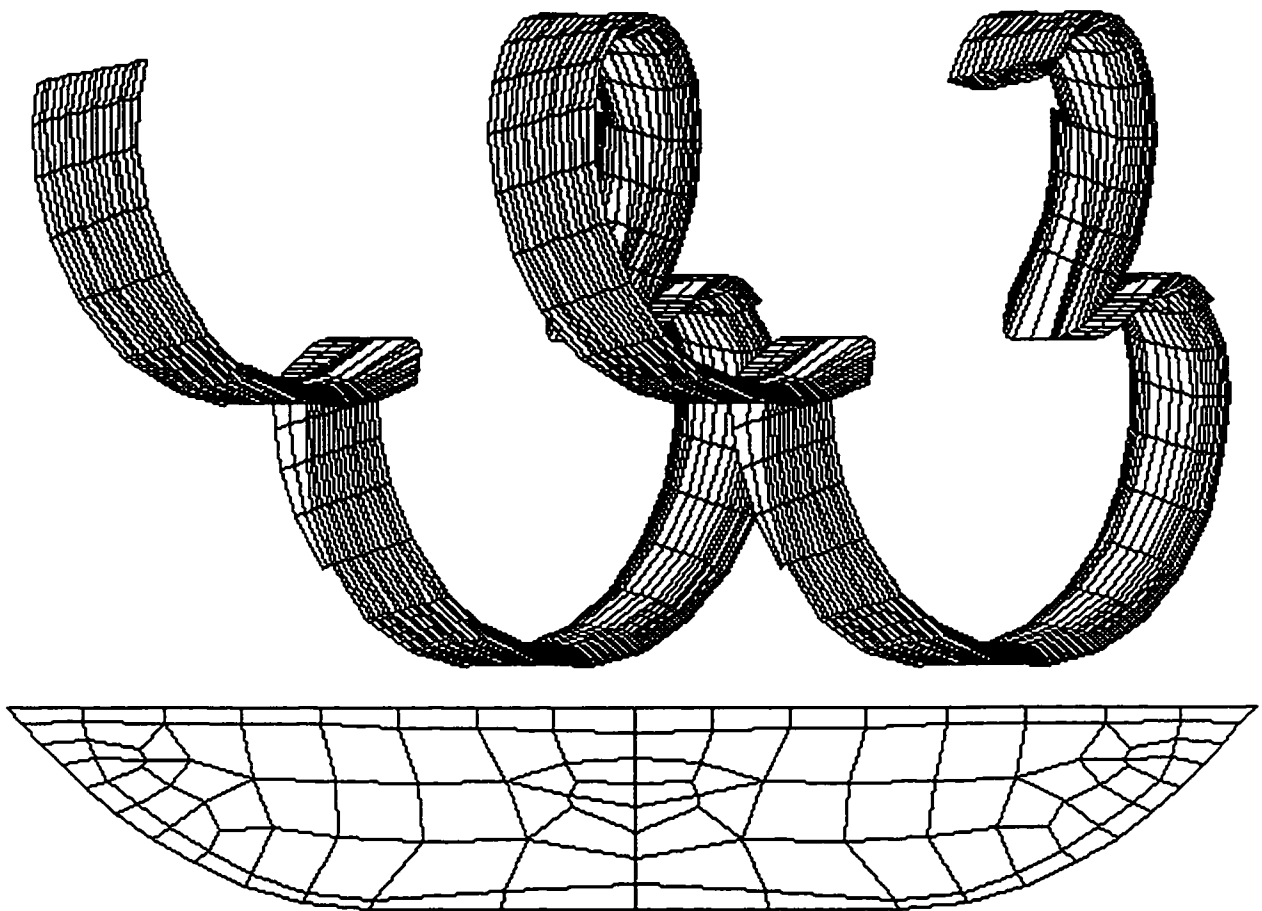


Figure 6.3: Second Channel Geometry Finite Element Mesh

Table 6.3: Finite Element Mesh Data			
<i>Quantity</i>	<i>First Channel Geometry, 100 rpm</i>	<i>First Channel Geometry, 250 rpm</i>	<i>Second Channel Geometry</i>
Cross-sections	81	97	81
Nodes	12625	15121	10519
Continuum elements	10560	12704	8480
Boundary elements	3896	4568	3844
Nodes in translation region cross-section	145	145	119
Two-dimensional elements in translation region cross- section	124	124	98
Axial length	61.2 mm	61.2 mm	92.7 mm
Cross-section area in translation region	22.0 mm ²	22.0 mm ²	13.9 mm ²
Cross-section area at centre of intermeshing region	49.1 mm ²	49.1 mm ²	46.2 mm ²
Percent area decrease for flow in section B	9.0	7.5	12.2

axial lengths of each mesh, measured from the top centre point of the inlet plane to the corresponding point on the outlet plane. For a true CSCO extruder conveying screw element, the channel length would be 3 times the screw pitch, or 60 and 90 mm for the first and second geometries respectively. The discrepancy for each was due to the channel shift at the centre of the intermeshing region being less than the true value. The Table also shows that the cross-section area at the centre of the intermeshing region was much larger than that of a channel cross-section perpendicular to the screw flights, and that the drops in the cross-section areas open for flow in the first section of the intermeshing regions for each mesh were in the vicinity of 10%. This decrease was smaller for the first channel geometry mesh for the 250 rpm runs, which had more cross-sections than the mesh for the 100 rpm runs.

In the simulations, the melt density, thermal conductivity, and specific heat capacity were fixed at the same values used in the SSE channel flow simulations (given in Table 5.2), and the viscosity was computed by the same user-supplied subroutine as before. A lower limit of 10 s^{-1} was again used for the strain rate, which gives a maximum possible melt viscosity of 1533 Pa s . As well, the same kinetic expressions for the 4 species reactions were used as in Chapter 5. Boundary conditions for all the process degrees of freedom but pressure were again specified on all the channel boundary surfaces, save the outlet, in the same order of inlet, barrel, and screw. In the boundary condition specifications, the end faces of the blocked side sections in the intermeshing region were treated as part of the screw surface. The velocity boundary conditions on the two solid boundaries (the barrel and screw surfaces) were again specified on the basis of the no slip condition and the kinematic reversal assumption, which was applicable again due to the shallow channels relative to the screw diameter for each channel geometry. Even though it is physically

impossible for the barrel wall (with the figure-eight shaped cross-section profile) to turn, this is a convenient assumption for modeling purposes.

As mentioned above, the tops of the channel cross-sections were represented as straight lines (rather than slightly curved ones); this necessitated the use of a special velocity boundary condition on the nodes of the barrel surface, to ensure that the tangential velocity was constant across the surface:

$$\left. \begin{aligned} v_{X'} &= -\frac{y'v_0}{\sqrt{(x')^2+(y')^2}} \\ v_{Y'} &= \frac{x'v_0}{\sqrt{(x')^2+(y')^2}} \end{aligned} \right\} v_{X'}^2 + v_{Y'}^2 = v_0^2 \quad (6.1)$$

These velocity components are relative to the global coordinate system for the channel. Essentially each velocity component was multiplied by the ratio of the true barrel radius to the radial distance from the point to its respective screw axis. An additional complication arose along the top of the cross-section at the centre of the intermeshing region. This line represents the cusp of the figure-eight barrel profile along which the two screw chambers intersect, and as such there are two different possible barrel tangential velocities at each point along the line. The vector sum of these velocities is in a direction parallel to the global X' axis (and perpendicular to the cross-section). At first it would seem that this is the velocity that should be specified along this line, but in practise since the velocity has a significant component normal to the barrel surface sections on either side of the centre of the intermeshing region, it leads to the computation of large swings in the channel flow rates in that region. A large outward flow rate is computed across the last upstream barrel section before the centre of the intermeshing region, followed by an equally large

inward flow rate across the first downstream barrel section. Table 6.4 shows this for the three channel meshes used in the simulations. One major consequence of such fluctuations is that negative (i.e. upstream) flow rates are computed across the cross-sections at the centre of the intermeshing region in runs at small specified channel flow rates. As such, the actual velocity boundary condition used on the barrel surface at the centre of the intermeshing region was that of zero velocities at each point.

Table 6.4 also shows the other computed mass flow rates across the barrel surface sections in the upstream halves of the intermeshing region for each mesh. The values for each section are functions of the screw speed and mesh shape only. In the unlisted sections, the computed flow rates were zero. The last section before the centre of the intermeshing region was the fifth for both the 100 rpm runs with the first channel geometry and the runs with the second channel geometry, and was the sixth for the 250 rpm runs with the first channel geometry. In parentheses in this column is the barrel velocity boundary condition used at the centre of the intermeshing region. The values also represent how much the computed channel flow rates changed between the cross-sections connected by each barrel surface section. Hence, the flow rate was computed as being smallest across the cross-section at the centre of the intermeshing region. Because each flow rate fluctuation was balanced by an equal and opposite change at the corresponding position on the other side of the intermeshing region, the channel flow rate at the end of the section was the same as the entering value. The flow rates across the first two barrel surface sections were due to the channel contraction and the sudden appearance of the side section, which left some nodal velocities unbalanced along the first three channel cross-sections in the intermeshing region. The fluctuations were relatively small though, and even counterbalanced each other to an extent. The

Table 6.4: Mass Flow Rates Across Barrel Surface Sections in First Half of Intermeshing Region			
<i>Barrel Surface Section</i>	<i>First Channel Geometry, 100 rpm</i>	<i>First Channel Geometry, 250 rpm</i>	<i>Second Channel Geometry</i>
First	0.04 kg/h (out)	0.06 kg/h (out)	0.06 kg/h (out)
Second	0.10 kg/h (in)	0.18 kg/h (in)	0.22 kg/h (in)
Last (Zero velocity)	0.21 kg/h (out)	0.38 kg/h (out)	0.58 kg/h (out)
Last (Vector sum velocity)	2.29 kg/h (out)	4.67 kg/h (out)	2.79 kg/h (out)

flow rates across the last barrel section before the centre of the intermeshing region were more significant though, especially for the runs with the second channel geometry. They again were due to the use of zero velocities at the nodes along the top of the cross-section at the centre of the intermeshing region, which left the tangential velocities along the top of the upstream cross-section entirely unbalanced. Finally, the corresponding flow rates for the second channel geometry were larger than those for the 100 rpm runs with the first channel geometry, in spite of the fact that the runs were all done at the same screw speed, owing to the wider channel cross-sections and hence greater barrel section surface areas.

On the inlet plane, the three velocity components at each node were computed by a user-supplied subroutine, based on down-channel and cross-channel profiles derived from the extruder channel lubrication flow profiles given in equation (5.18). The profiles in their original form are written for velocity components relative to the local coordinate system for the inlet plane, so after modification by coordinate axis rotations the velocity profiles relative to the global coordinate system were found to be:

$$\begin{aligned} v_{x'} &= 0 \\ v_{y'} &= v_0 \left(1 - \frac{y}{h(x)} \right) \left[1 - 3 \frac{y}{h(x)} (\sin^2 \phi_S - r_D \cos^2 \phi_S) \right] \\ v_{z'} &= \frac{3}{2} v_0 \sin 2\phi_S \frac{y}{h(x)} \left(1 - \frac{y}{h(x)} \right) (r_D + 1) \end{aligned} \quad (6.2)$$

The local nodal coordinates x and y are used in the equations, and the channel depth is computed as a function of the cross-channel position of the node. Figure 6.4 shows vector plots of the specified velocities on the inlet plane for two different conditions. In the first plot (on the left) the PDF ratio is zero, so the velocities are all directed inwards across the inlet plane, with nearly a linear variation in magnitude from top to bottom. In the second plot, the PDF ratio is -0.25, and

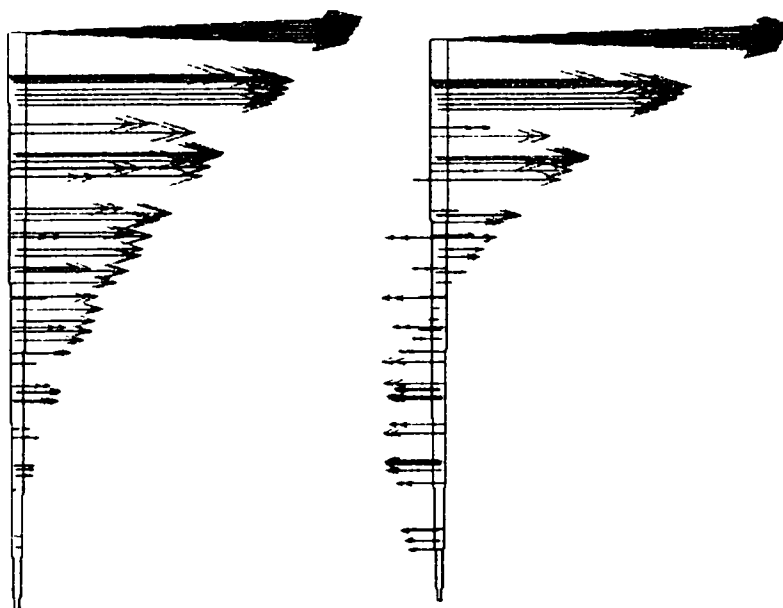


Figure 6.4: Vector Plots of Velocities on Inlet Plane

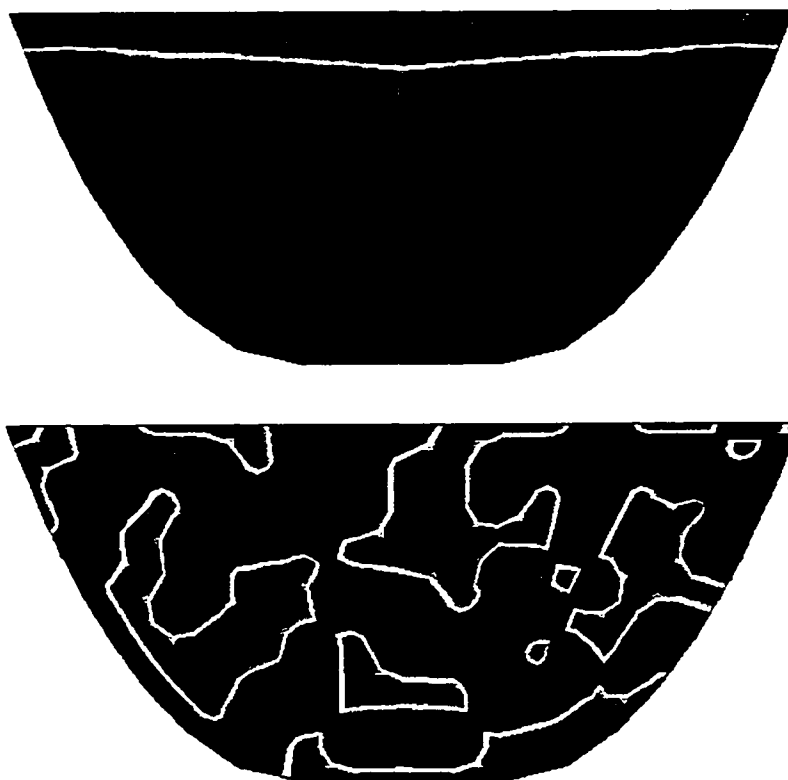


Figure 6.5: Barrel and Random Peroxide Addition Patterns

consequently outward directed velocities appear on the inlet plane towards the bottom of the cross-section.

For the temperature and species degrees of freedom, the same boundary conditions were used as in the SSE channel flow simulations, with the inlet and barrel temperatures specified as being constant and the screw insulated, and zero flux conditions for the peroxide and the MWD moments used on the screw and barrel surfaces. On the inlet plane, constant values of the MWD moments were specified, and for the peroxide species a user-supplied subroutine was again used to specify the nodal values of the weight fraction in the melt based on the selected peroxide distribution. For the barrel distribution, the peroxide level was set at a non-zero value at the 34 nodes along the top of the inlet cross-section, and for the random distribution, the level was made non-zero at 72 nodes again chosen in a pseudorandom manner, with the aid of a table of random numbers. The levels used for each run were again determined to give the same flow average inlet peroxide level as the uniform distribution. Unlike the SSE channel flow simulations, the actual peroxide levels for the non-uniform distribution runs were different for each run, due to the significant variation in the shape of the inlet velocity profile with changing values of r_D , the PDF ratio based on inlet conditions. These values are tabulated in the following section of this chapter. The appearance of the barrel and random peroxide addition patterns are shown for the first channel geometry in Figure 6.5. In each plot, red again represents the highest peroxide concentration and blue the lowest (zero), with yellow and green in between.

Finally, the simulation control commands for the simulations described in this chapter were the same as those used for the SSE channel flow simulations in Chapter 5. The one difference was in the runs to the PDF ratio value of -0.25, for which a higher streamline upwinding factor was

used for the temperature DOF, and also for which upwinding was introduced for the peroxide and MWD moment species, to aid convergence.

6.4.3 Calculations and Iterative Procedure

The treatment of the data from the converged simulation runs was again closely patterned after that used for the data from the SSE channel flow simulations. The complete profiles of the nodal DOFs were printed out to text files, along with the global nodal coordinates and computed values of the flow efficiency, which were processed by a C program and sorted by node number into lists for each cross-section in the meshes. Another C program took the sorted data and computed average values of the field variables on the cross-sections, using node pattern files which specify the corner node numbers of the two-dimensional elements in each cross-section. Average melt pressures, weight-average molecular weights, and flow efficiencies were calculated by area average, and average temperatures and peroxide weight fractions were computed by flow average, both again using a 4 point Gaussian quadrature technique for the numerical integrals. A similar iterative procedure to before was also used in reaching the target value of the PDF ratio for each simulation by adjusting the mass throughput in the channel. The one significant difference was for the non-uniform peroxide distribution runs, for which an additional program was needed, which recomputed the nodal peroxide level necessary to achieve the desired flow average peroxide level on the inlet plane, for each new value of the channel flow rate in the iterative process.

6.5 Results and Discussion

6.5.1 First Channel Geometry - Degree of Freedom Profiles

Table 6.5 shows a summary of results of the 16 simulations performed for the first geometry channel section. The channel flow rates ranged from around 1 kg/h to around 10 kg/h, which for a complete conveying screw element with bilobal screws and three independent channel flows would give extruder throughputs of 3 kg/h to 30 kg/h, which is within range for a laboratory-scale CSCO extruder. For the high screw speed runs, the flow rates were all more than an order of magnitude larger than the fluctuation that occurred at the centre of the intermeshing region, as shown in Table 6.4. However, for the low screw speed runs this wasn't the case, with the runs at the negative pressure-to-drag flow ratio all being less than 8 times the corresponding flow rate fluctuation level, and for the reactive extrusion runs only about 5 times the value. For runs 4 and 8, the uniform and random distribution runs at the low screw speed and negative PDF ratio, the Table shows that the PDF ratio values did not quite reach the target value of -0.25. This was the result of a problem encountered with the PDF ratio values no longer continuing to diminish with decreasing channel flow rates below 1 kg/h. Rather than decrease the flow rates further for these runs and correspondingly increase the relative magnitudes of the channel flow rate fluctuations, it was decided to stop the runs at around 1 kg/h.

The Table shows significant pressure growths were predicted for the negative PDF ratio runs, up to 7.6 MPa for the conventional extrusion simulation at the high screw speed (equal to 3.8 MPa per figure-eight turn of the channel, or 23.5 MPa/m of helical channel length). As with the SSE channel flow simulations, the pressure changes were small for the zero PDF ratio runs, and should all have been exactly zero for pure drag flow. For the reactive extrusion simulations the

Run	Screw Speed (rpm)	Inlet Peroxide Distribution	PDF Ratio Q_P/Q_D	Mass Flow Rate (kg/h)	Maximum Nodal Peroxide Level on Inlet (wt %)	Average Pressure Change (kPa)	Average Outlet Peroxide Conversion $\frac{w_{I,In} - w_{I,Out}}{w_{I,In}}$	Average Relative Outlet Molecular Weight $\frac{\bar{M}_{W,Out}}{\bar{M}_{W,In}}$
1	100	None	-0.003	3.33	--	53	--	1
2	100	None	-0.251	1.59	--	5061	--	1
3	100	Uniform	0.001	4.03	0.6	-2	0.911	0.121
4	100	Uniform	-0.244	1.03	0.6	532	1.000	0.121
5	100	Barrel	0.003	3.90	1.44	-7	0.936	0.148
6	100	Barrel	-0.247	1.02	0.44	803	1.000	0.168
7	100	Random	-0.001	4.03	1.32	2	0.907	0.117
8	100	Random	-0.238	1.01	1.76	493	1.000	0.116
9	250	None	-0.002	8.46	--	66	--	1
10	250	None	-0.252	4.05	--	7624	--	1
11	250	Uniform	0.003	9.82	0.6	-17	0.640	0.161
12	250	Uniform	-0.250	4.47	0.6	1208	0.930	0.125
13	250	Barrel	0.000	9.65	1.43	-1	0.711	0.183
14	250	Barrel	-0.250	4.55	0.75	1271	0.923	0.131
15	250	Random	0.003	9.82	1.32	-20	0.629	0.156
16	250	Random	-0.253	4.60	1.46	1196	0.910	0.123
17	100	None	0.000	2.40	--	18	--	1

average outlet peroxide conversions were quite high, with the runs at the low screw speed and negative PDF ratio (and the lowest mass flow rates) showing essentially complete consumption of the entering peroxide within the channel section. This again indicates that the average residence times of the peroxide in the section were sufficient for high levels of consumption at the prevailing temperatures. The corresponding average outlet weight-average molecular weights were again low, showing up to nearly an order of magnitude reduction over the inlet value.

Comparing the values in Table 6.5 first between runs at the same screw speed and inlet peroxide distribution but different levels of the PDF ratio, it can be seen that in each pair of runs the mass flow rates were larger for the run at the zero PDF ratio level, about two times larger for the high screw speed runs but up to nearly four times larger for the reactive extrusion runs at the low screw speed. Consequently for the REX simulations the average outlet peroxide conversions for the zero PDF ratio runs were lower and the average outlet weight-average molecular weights higher, because of smaller average residence times. There was one exception to this, namely run 6 with the barrel distribution and the low screw speed, which will be discussed in more detail later. The maximum nodal inlet peroxide levels necessary to give flow average peroxide levels of 0.6 wt% on the inlet plane followed different patterns between runs at the different PDF ratio levels, for the two non-uniform peroxide distributions. For the barrel distribution runs, the maximum inlet level for the negative PDF ratio runs was less than that for the zero PDF ratio runs, since more of the down-channel flow across the inlet plane passed through the boundary elements adjacent to the barrel surface, on the nodes of which the peroxide level was specified. The opposite trend was observed for the random distribution runs, for which the maximum inlet peroxide level was larger for the negative PDF ratio runs. This indicates that more nodes were specified with a non-zero

peroxide level in the bottom part of the channel than the top for these runs, which in Figure 6.5 can be seen to have been the case.

Comparing between runs at the same screw speed and PDF ratio but different inlet peroxide distributions, it can first be seen that the predicted pressure increases for the conventional extrusion runs at the negative PDF ratio were significantly larger than for the corresponding REX runs, due to much larger average outlet viscosities following from higher molecular weights. The mass flow rates for the conventional extrusion runs were also smaller than those for the corresponding reactive extrusion runs, except in the case of the runs at the low screw speed and negative PDF ratio. The results for corresponding REX runs were quite close to each other in each case. As found in the SSE channel flow simulations in Chapter 5, the results were generally closest between the uniform and random distribution runs. As before, for the barrel distribution runs both the outlet peroxide conversions and polymer relative molecular weights were higher than those for the uniform distribution runs, indicating the numerical artifact observed in the previous chapter which reduced the effective amounts of peroxide in the flows for degrading the polymer, has recurred. Because of the higher molecular weights in these runs, the predicted average pressure changes for the negative PDF ratio runs were also higher, and the mass flow rates intermediate between the values for the no peroxide and uniform peroxide distribution runs (run 14 was an exception to this last point). For the random distribution runs, both the outlet conversions and molecular weights were less than those for the corresponding uniform distribution runs, which indicates that the numerical artifact affected these runs as well, though as with the SSE channel flow simulations the magnitude of the effect was fairly small. Lastly, the maximum nodal inlet peroxide levels were all greater for the non-uniform distribution runs than that for the uniform distribution runs, with the

one exception of run 6.

Finally, comparing results between runs at the different levels of screw speed, the throughputs for all runs and the pressure increases for the negative PDF ratio runs were all higher at the high screw speed. Again this resulted in the reactive extrusion simulations at the high screw speed showing lower average outlet peroxide conversions and higher average outlet weight-average molecular weights than those at the low screw speed, because of smaller average residence times. The lowest predicted conversions were for the uniform and random distributions at the zero PDF ratio, at around 0.62.

Computed profiles of average melt temperature, melt pressure, peroxide conversion, and relative weight-average molecular weight along cross-sections in the channel mesh for the first geometry channel section are shown in Figures 6.6, 6.7, 6.8, and 6.10, respectively. In the Figures results are again shown principally for runs at the high screw speed, as the basic shapes of the curves were the same for both screw speeds. The same conventions are used in the series labels in the Figure legends as were used in Chapter 5, namely that the fields in the labels are the screw speed level, the inlet peroxide distribution, and the PDF ratio level, in that order. For the PDF ratio field, “Low” designates the PDF ratio of zero, and “VLow” designates the ratio of -0.25. In each Figure there is an additional data series shown as filled squares, which appears as four sets of three squares along a straight line. Each set of squares represents the positions of the start, middle, and end of each of the four intermeshing region sections of the channel.

Figure 6.6 shows the predicted average melt temperature profiles for three runs at 250 rpm and one at 100 rpm. Again the shown curves for high screw speed/no peroxide/very low PDF ratio and high screw speed/uniform peroxide distribution/low PDF ratio were the extremes for the high

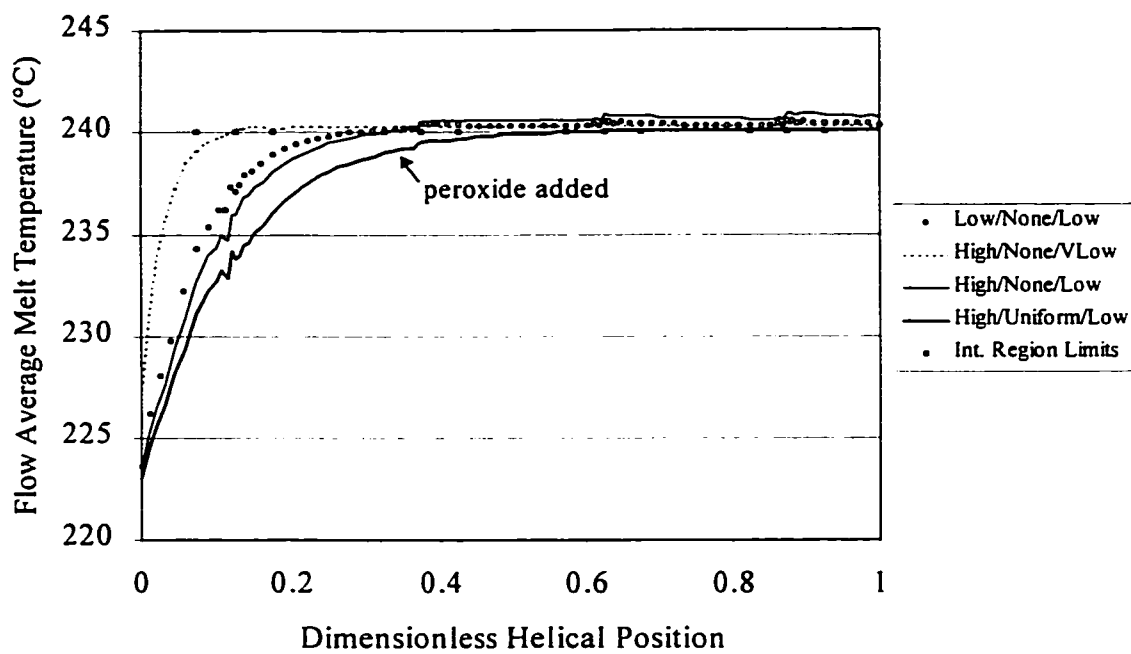


Figure 6.6: Average Temperatures for First Channel Geometry

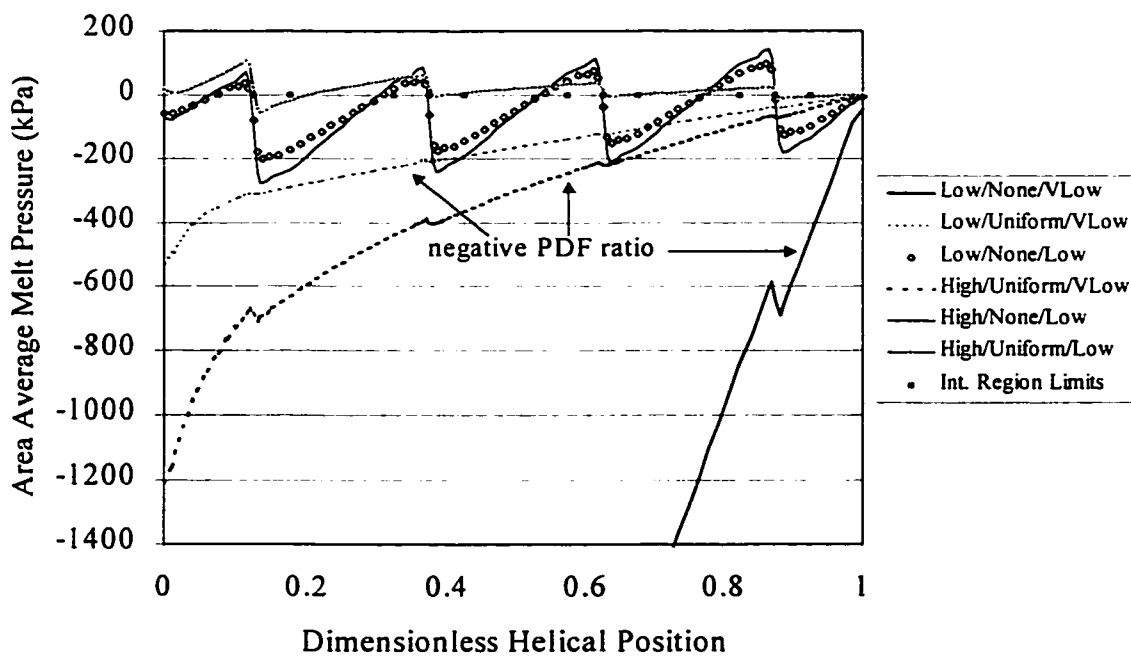


Figure 6.7: Average Pressures for First Channel Geometry

screw speed runs - the other curves all fell between them. Similar trends are found here as in the melt temperature profiles for the SSE channel flow simulations. Again in each run the melt temperature rose quickly (in under one figure-eight turn, or half the helical distance of the channel) from the inlet value near 220°C to a plateau level slightly higher than the barrel temperature of 240°C, at which the rate of heat generation by viscous dissipation was exactly balanced by the rate of heat transfer to the barrel surface. The effect of the degradation reaction was again to slow the temperature rise, and to reduce the plateau temperatures by reducing the melt viscosity through its molecular weight. The effects of decreasing screw speed and decreasing PDF ratio were similar, in that they both led to faster temperature rise (due to accompanying lower throughputs), and also to reduction of the plateau temperatures. The PDF ratio effect on the temperature growth was much more dramatic than that of the screw speed though. Different from the SSE simulation results was that the average temperature on the inlet plane for each run was higher than the setpoint of 220°C, due to the barrel temperature prevailing along the top of plane, adjacent to which a significant fraction of the channel flow rate passed. The effect of this increased as the PDF ratio decreased, as shown in the Figure with the inlet temperature increasing from around 223°C for the runs at the zero PDF ratio to about 227°C for the run at the negative PDF ratio. As well, though the curves are mostly smooth, some small oscillations are seen in those for the zero PDF ratio runs at the positions of the intermeshing region centres of the channel sections.

Figure 6.7 shows the predicted average melt pressure profiles for three runs at 250 rpm and three at 100 rpm. Only the tail end of the profile for the low screw speed/no peroxide/very low PDF ratio run is shown to keep the pressure scale small so details in the zero PDF ratio curves can be seen. There were two distinct patterns exhibited by the profiles, the distinction being made

on the basis of the PDF ratio level. For the zero PDF ratio runs, the profiles are of a saw-tooth form, with the pressures building over each translation region section of the channel as well as over the adjacent sections of the intermeshing regions, and then dropping suddenly at the centre of each intermeshing region as the melt passes through the restricted channel there. The magnitudes of these pressure drops were less in the low screw speed and reactive extrusion runs. The curves show that again true drag flow behaviour was not attained in these runs, as the melt pressures were not zero everywhere in the channel, even though the overall average pressure changes along the channel length were close to zero. For the negative PDF ratio runs, the melt pressure profiles show the pressures rising quite smoothly from the inlet to around zero at the outlet, with gradual decreases in the slopes for the reactive extrusion simulations which can be attributed to reduced melt viscosities from the degradation reaction. The effect of increasing screw speed was to increase the pressure growth in the channel, and to elongate the regions over which the slope changes in the curves took place. These curves also show small saw-tooth pressure drops at the centres of the intermeshing regions, which again were largest for the conventional extrusion runs, and diminished in size for the REX runs in the channel direction as the melt viscosity fell due to the controlled degradation reaction.

Figure 6.8 shows the predicted average peroxide conversion profiles for four reactive extrusion simulation runs at 250 rpm and one at 100 rpm. The curves show that the conversion increases were steady along the channel lengths for the runs with the higher channel flow rates, while for the runs with the low flow rates (at the low screw speed and negative PDF ratio) the conversions climbed very rapidly, until the peroxide was computed as having essentially disappeared from the melt at about the half-way point of the channel. For each combination of

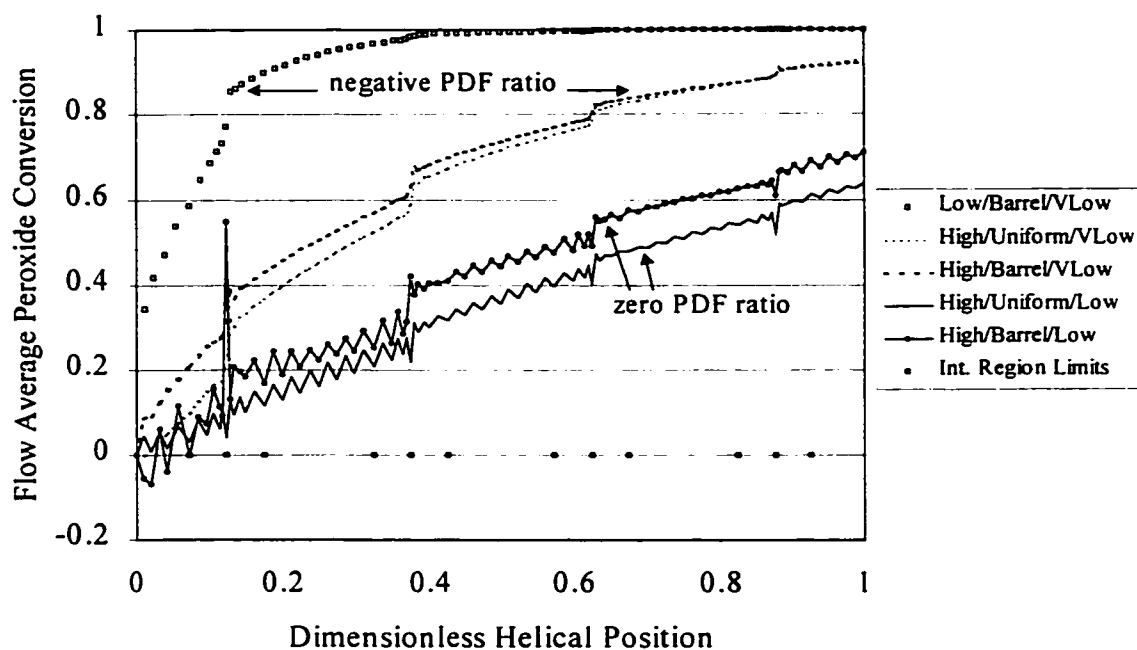


Figure 6.8: Average Peroxide Conversions for First Channel Geometry

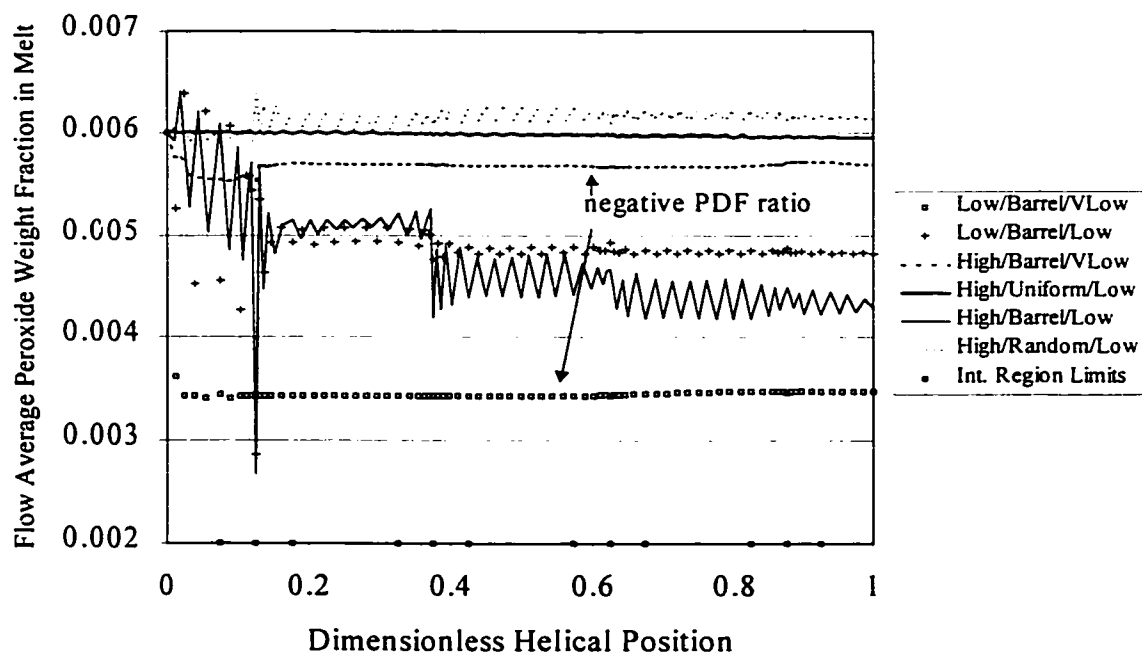


Figure 6.9: Average Peroxide Levels With No Peroxide Decomposition For First Channel Geometry

screw speed and PDF ratio, the conversion profile for the barrel distribution run was highest, followed by that for the uniform distribution run, and then closely below this the curve for the random distribution run. The shapes of the profiles at the two PDF ratio levels are again quite different from each other. For the negative PDF ratio runs the profiles are quite smooth, while those for the zero PDF ratio runs are very jagged, showing steady oscillations that decreased in amplitude along the channel length as the peroxide level in the melt diminished. These oscillations were particularly significant for the barrel distribution runs in the part of the channel upstream of and including the centre of the first intermeshing region, even causing negative conversions to be computed at several positions. Both sets of profiles do, however, share the feature of small jumps in the conversion levels at the centres of the intermeshing regions of the channel, which decreased in height in the channel direction. These jumps represent the influence of the blocked ends of the channel side sections in the intermeshing regions, which were predicted to create slow flow regions of increased fluid residence time within which the peroxide levels of the entering melt decreased considerably.

Figure 6.9 shows plots of average peroxide weight fractions for the four barrel distribution runs, as well as for the uniform and random distribution runs at the high screw speed and zero PDF ratio. These data were obtained by running the corresponding simulations with the peroxide thermal decomposition rate constant set to zero, and so the changes in the computed peroxide levels were due to numerical causes alone. Thus the trends in these curves allow one to see which of the patterns in the peroxide conversions observed in Figure 6.8 and Table 6.5 are numerical artifacts. First, the Figure shows that the peroxide levels in the uniform and random distribution runs remained close by the specified inlet value of 0.006 (0.6 wt%). These curves show that the

jumps in the peroxide conversion profiles found at the centres of the intermeshing regions were due to genuine physicochemical, and not numerical, phenomena. As well, the curve for the random distribution run shows a small increase in the average peroxide level in the channel following the centre of the first intermeshing region. This is evidence of the same numerical artifact in the computations for these runs that was encountered in the non-uniform distribution SSE channel flow simulations, caused by the extreme intensity of segregation of the peroxide on the inlet plane between the nodes at which it was specified as existing, and those at which it was specified as being absent. This spontaneous increase in the channel peroxide levels accounts for the lower outlet conversions and molecular weights for the random distribution runs versus the uniform distribution runs, seen in Table 6.5.

Second, Figure 6.9 shows that for the barrel distribution runs, there were clearly significant negative deviations from the specified inlet peroxide level. These deviations varied in extent, from less than 10% at the high screw speed and negative PDF ratio, to around 20% - 25% for the runs at the zero PDF ratio level, and up to over 40% at the low screw speed and negative PDF ratio. These again are evidence of the numerical artifact in the calculations associated with the computation of the spreading of the initially highly segregated peroxide distribution. These numerical errors resulted in sizeable losses of peroxide for degradation of the polymer for the barrel distribution runs, and were the cause of the higher outlet conversions and molecular weights for the barrel distribution runs versus the uniform distribution runs, seen in Table 6.5. However, unlike for the non-uniform peroxide distribution SSE channel flow simulations, the drops in the peroxide levels in the channels were not preceded by initial jumps. The numerical artifact also was aggravated by the centres of the intermeshing regions, to an extent that was a function of the

uniformity of the peroxide levels in the channel. This was not an issue for the two negative PDF ratio runs, since due to their low channel flow rates their peroxide levels had each stabilized prior to the centre of the first intermeshing region. For the corresponding zero PDF ratio runs it was significant though, particularly for the high screw speed run with the highest flow rate of the group. The nonuniformity of the channel peroxide levels for these runs was shown by the oscillations in the profiles, which diminished in the flow direction after stabilizing following large drops in the peroxide levels at the centre of the first intermeshing region. Across the first two intermeshing regions for the low screw speed run, and the first three for the high screw speed run, there were further drops in the peroxide levels, which indicates that for these runs the extra heights of the conversion level jumps seen at the centres of the intermeshing regions of the channel (as shown in Figure 6.8), above those for the corresponding uniform distribution runs, had a numerical source. Finally, the magnitudes of the negative deviations at least partly followed the pattern seen for the barrel distribution SSE channel flow simulations, of increasing at higher channel flow rates. The deviation for the negative PDF ratio run at the high screw speed was less than that for the zero PDF ratio run at the same screw speed, as was that for the zero PDF ratio run at the low screw speed. The significant exception was for the negative PDF ratio run at the low screw speed (run 6 in Table 6.5), which showed by far the greatest deviation despite having the lowest channel flow rate. Why the deviation for this run was so much greater than that for the high screw speed run at the same PDF ratio is unclear. The drop in peroxide level for this run was more than double that for the low screw speed run at the zero PDF ratio (run 5), which was the cause of the previously mentioned inconsistency in Table 6.5 of the outlet relative molecular weight for run 6 being greater than that of run 5, despite its much lower channel flow rate.

Figure 6.10 shows the predicted average relative weight-average molecular weight profiles for five reactive extrusion simulation runs at 250 rpm and one at 100 rpm. The curves show the molecular weights for each run dropping rapidly for the first half of the channel length, down to between 15% and 25% of the initial value, and then largely remaining stable after this. The curves fell in order of channel flow rate, with the molecular weights being highest at each position for the run with the highest flow rate (and hence smallest reaction time). At each combination of screw speed and PDF ratio, the profiles again fell in the same order as the peroxide conversion curves, with those for the barrel distribution runs highest, followed by those for the uniform and random distributions nearly superimposed on each other. This ordering of the profiles was again a consequence of the numerical artifact in the simulations, which reduced the effective amount of peroxide available for the degradation reaction in the barrel distribution runs. Oscillations in the curves are also again seen to appear, particularly for the zero PDF ratio runs, which had the highest relative channel flow rates for their respective screw speeds. The oscillations diminished in the channel direction as the peroxide levels in the melt decreased. The fluctuations were particularly a problem for the two barrel distribution runs at the zero PDF ratio, where in the same position in the first half of the channel the polymer molecular weight actually increased in each run over a short length of channel, which of course is physically impossible. Finally, the curves showed sharp drops across the centres of the channel intermeshing regions, which correspond to the previously observed jumps in peroxide conversion at the same locations. These again were due to the blocked ends of the channel side sections in the intermeshing regions increasing the residence time of part of the fluid in their vicinity, within which the polymer molecular weight decreased beyond that of the surrounding material due to the greater reaction time there for the degradation process.

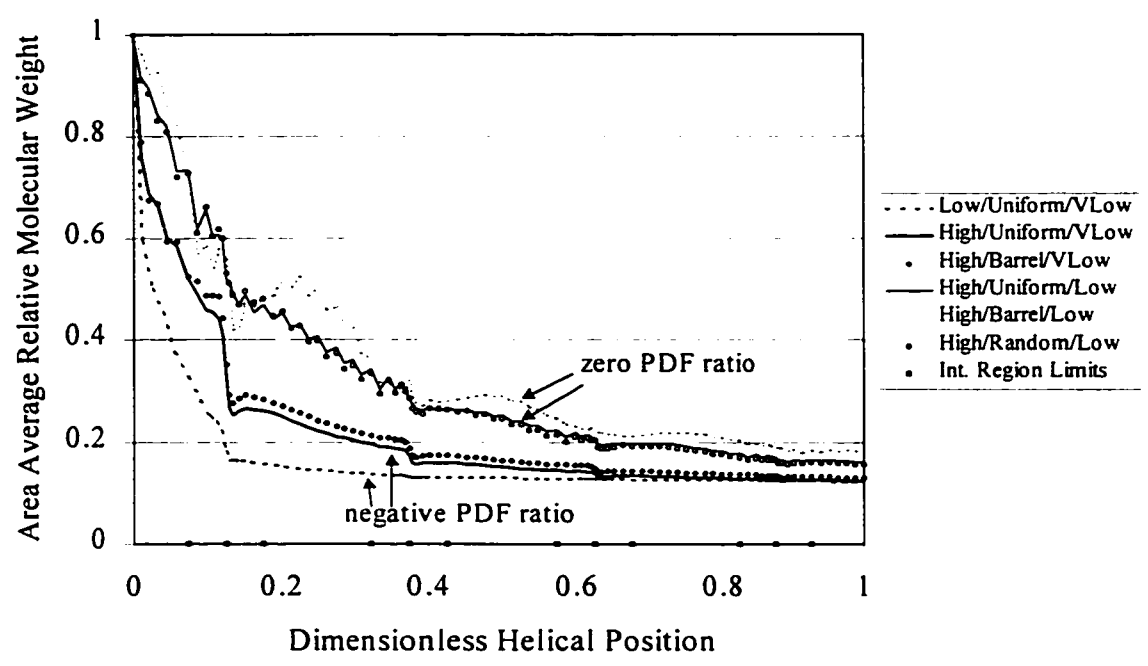


Figure 6.10: Average Relative Weight-Average Molecular Weights for First Channel Geometry

To gain some insight into the variation of the predicted degree of freedom values within the channel cross-sections, a series of plots is presented here for a cross-section through the mesh at right angles to the channel sides (i.e. to the screw flights) at the midpoint of the channel, for run 11, at the high screw speed and zero PDF ratio, and with the uniform inlet peroxide distribution. The cross-section shown is at the centre of the translation region, one figure-eight turn of the channel downstream from the inlet. Figure 6.11 shows the velocity vectors at the nodes within the cross-section. The direction of the cross-channel component of the barrel velocity is left-to-right in the Figure. The plot clearly shows the characteristic extruder cross-section circulation pattern, with a stagnation point along the centreline of the channel at a dimensionless depth of about one-third. Figure 6.12 shows the melt pressure distribution in the cross-section. The range of values the colours represent is -21.1 kPa (dark blue) to 61.8 kPa (dark red). The plot shows that there was little pressure variation across most of the cross-section, with a region of low pressure arising in the corner region at the left where the passive flight meets the barrel wall, and a corresponding region of high pressure in the opposite corner where the active flight meets the barrel wall. Figure 6.13 shows the distribution of velocity components normal to the cross-section (i.e. parallel to the flights). The range of the colours is from 0 mm/s to 433 mm/s, which is just below the tangential velocity of the barrel at 250 rpm. The normal velocities show a nearly linear variation between the maximum value on the barrel surface and the minimum value on the channel bottom and the sides of the flights. This makes sense, as the run was for a PDF ratio of zero, representing pure drag flow, and a linear velocity profile is characteristic of drag flow between adjacent solid surfaces. For contrast, Figure 6.14 shows the normal velocity components across the same cross-section, for run 12, at the high screw speed and negative PDF ratio, and with the uniform peroxide distribution.

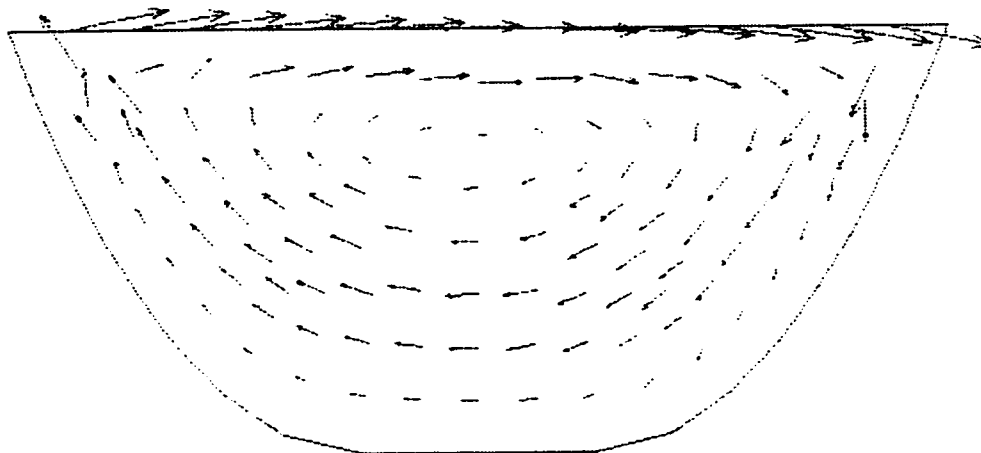


Figure 6.11: Velocity Vectors in Cross-Section for First Channel Geometry

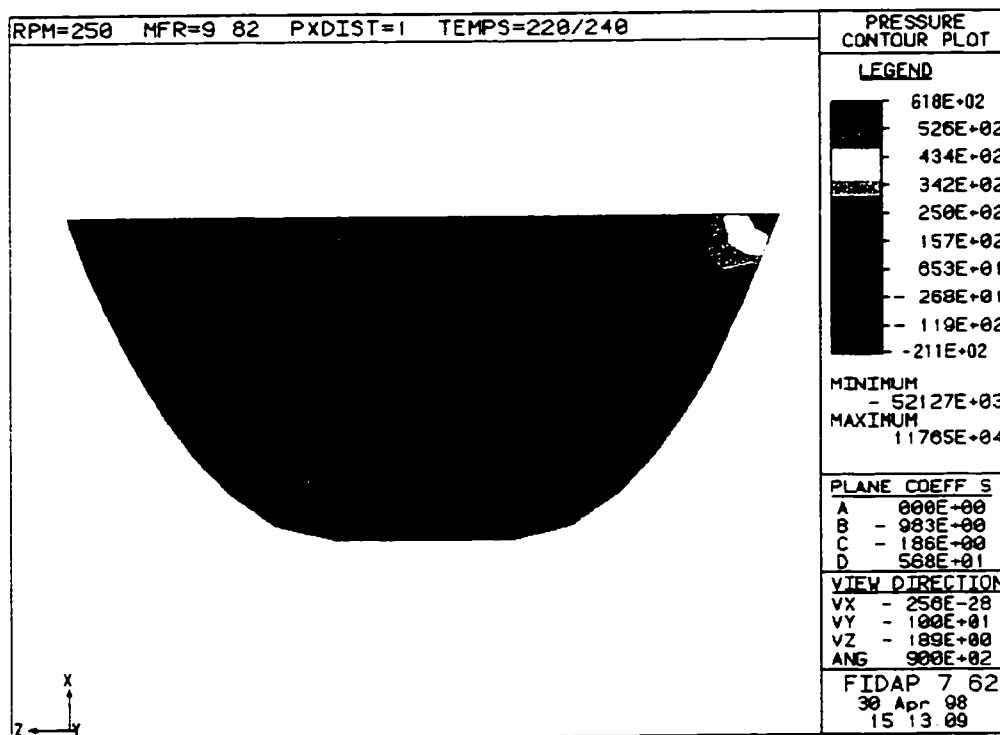


Figure 6.12: Pressures in Cross-Section for First Channel Geometry

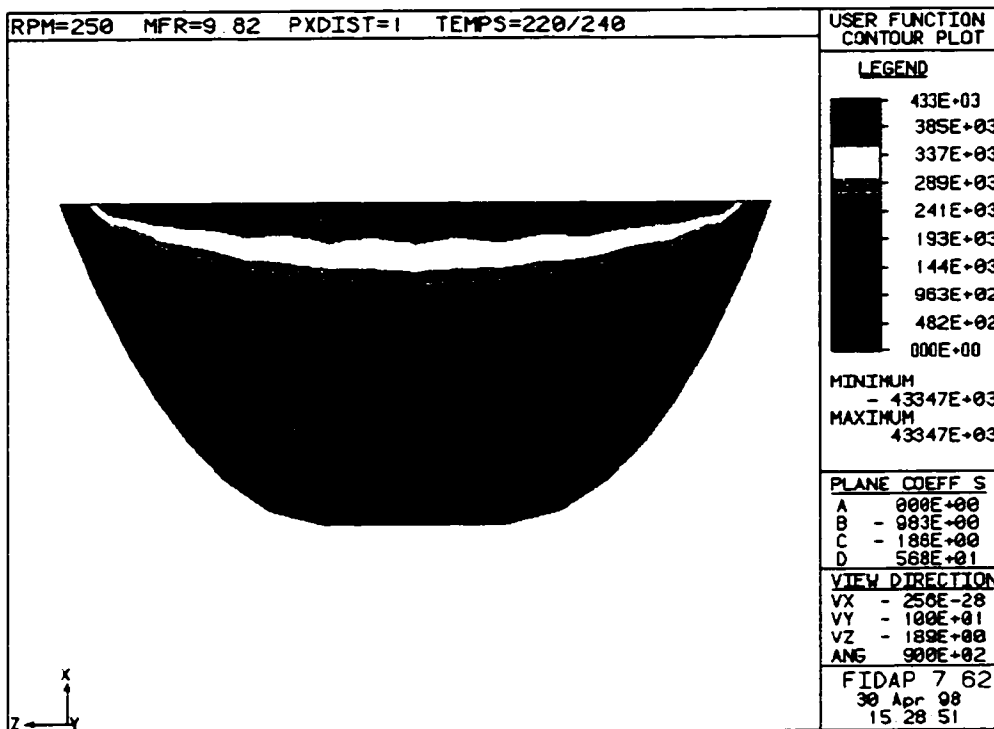


Figure 6.13: Normal Velocities in Cross-Section for First Channel Geometry, $Q_p/Q_d=0$

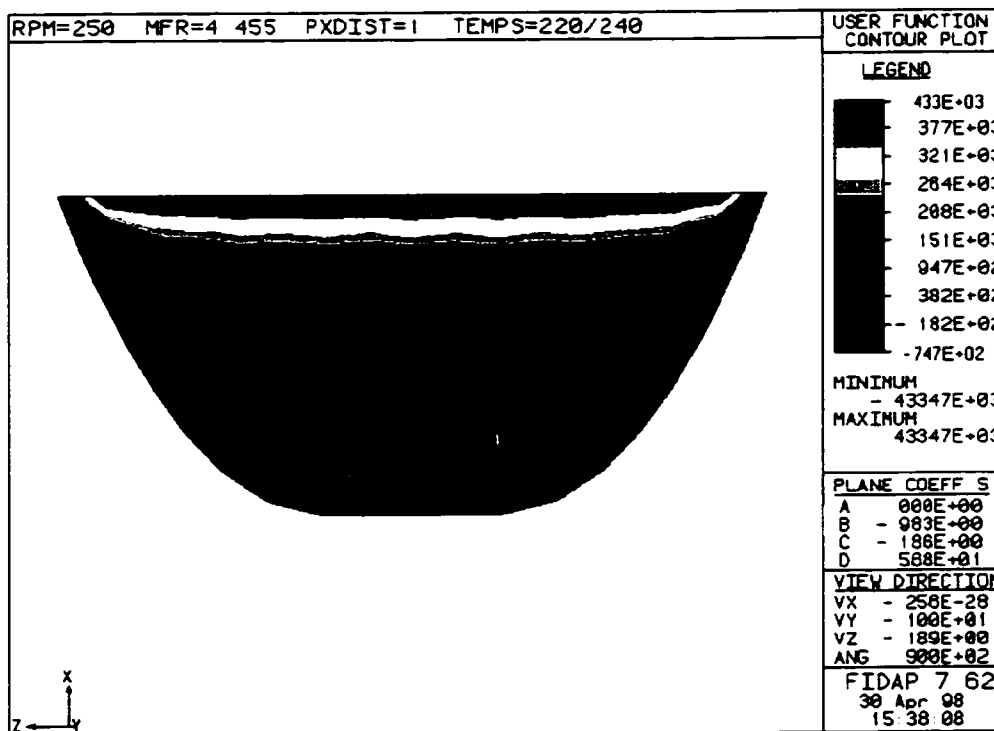


Figure 6.14: Normal Velocities in Cross-Section for First Channel Geometry, $Q_p/Q_d=-0.25$

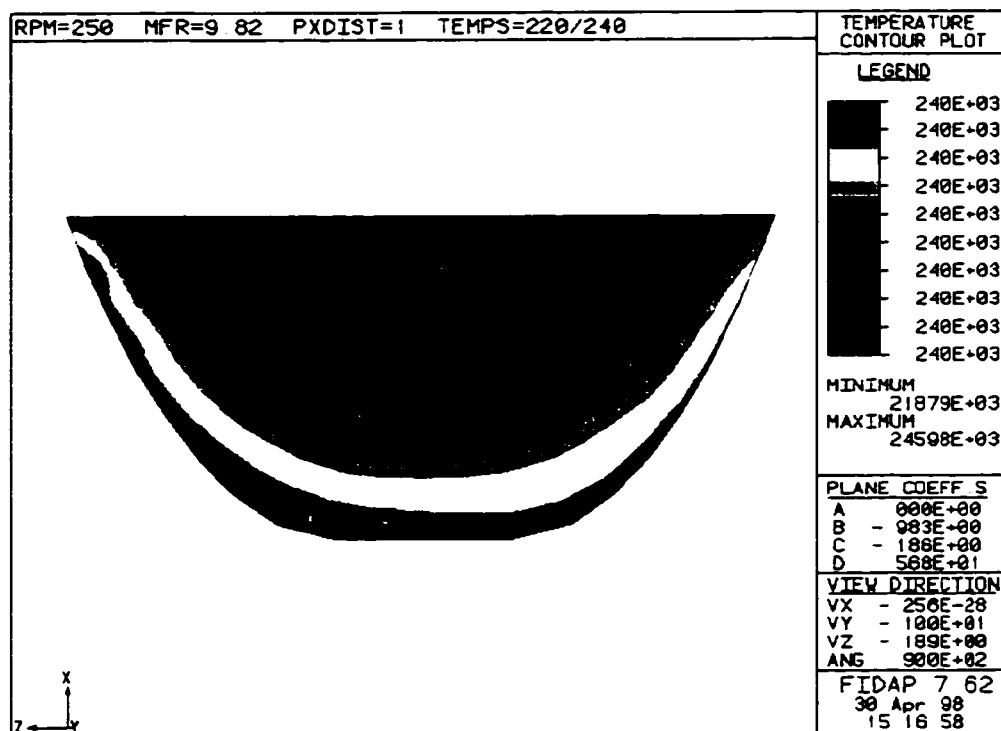


Figure 6.15: Temperatures in Cross-Section for First Channel Geometry

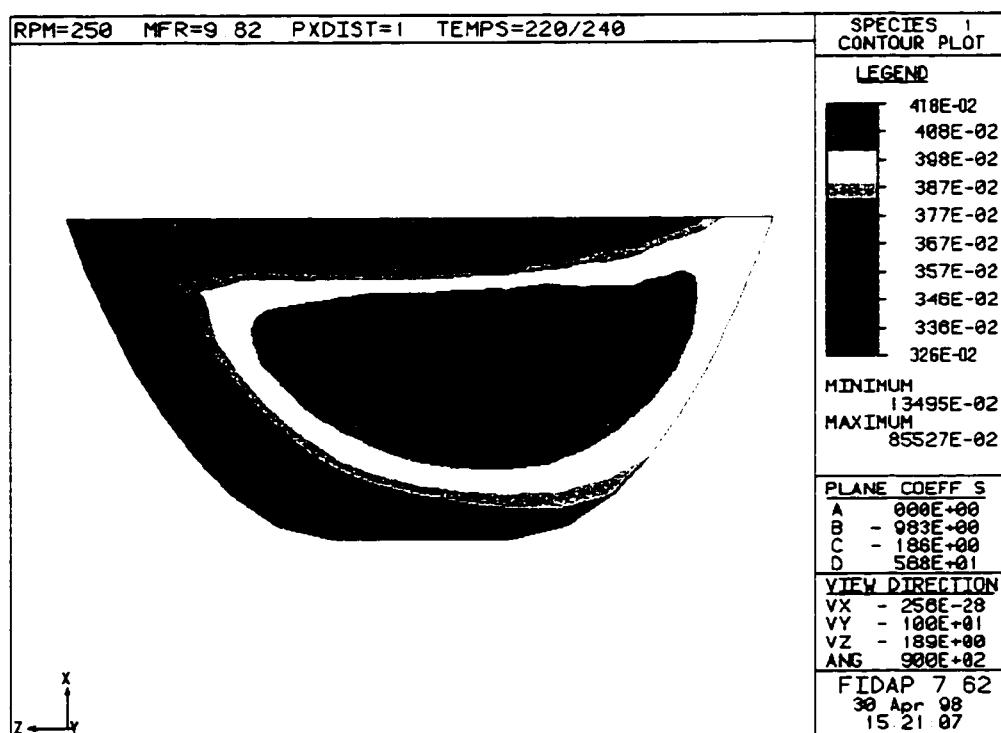


Figure 6.16: Peroxiside Weight Fractions in Cross-Section for First Channel Geometry

The range of the colours here is from -75 mm/s to 433 mm/s. The plot clearly shows a sizeable backflow region with negative normal velocities in the bottom half of the channel. This also makes sense, as in the run a significant rise in melt pressure occurred along the channel length, and a pressure backflow would be expected to be superimposed upon the standard linear drag flow velocity profile, producing negative normal velocities in the bottom of the channel, as shown in Figure 5.6. Figure 6.15 shows the melt temperature distribution in the cross-section, again for run 11. The range of the colours is small, only from 239.6°C to 240.5°C. Thus the temperature variation in the channel was small, though slightly lower temperatures appeared in the centre of the channel, away from the walls. Figure 6.16 shows the distribution of peroxide weight fractions in the melt in the cross-section. The range of the colours is 0.0032 (0.32 wt%) to 0.0042 (0.42 wt%), again relatively small. The plot shows that the peroxide levels were highest in the middle of the channel, away from the walls. Figure 6.17 shows the distribution of polymer relative weight-average molecular weights in the cross-section. The colour range is 0.20 to 0.28. The appearance of Figure 6.17 is essentially identical to that of Figure 6.16, showing that the highest molecular weights were found in the centre of the channel, away from the walls. The patterns in Figures 6.15, 6.16, and 6.17 are all due to the fact that the residence times of fluid elements are smallest in the channel centres, and so at any channel cross-section the conditions there are going to be closest to those at the inlet, namely low temperatures, high peroxide levels, and high molecular weights.

Finally, Figure 6.18 (a) shows the pathlines for two particles entering the mesh along the centreline of the inlet plane, again for run 11, at the high screw speed and zero PDF ratio, and with the uniform inlet peroxide distribution. The starting depths and residence times of the particles are given in Table 6.6. The minimum residence time in the channel section for this run was 0.84 s, and

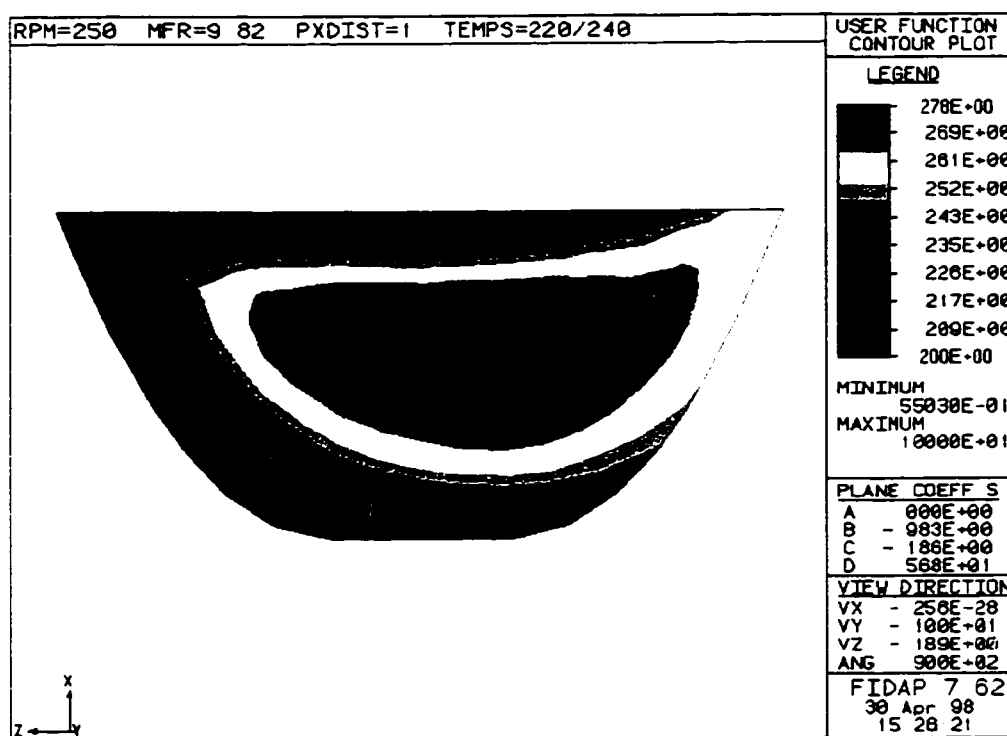


Figure 6.17: Relative Weight-Average Molecular Weights in Cross-Section for First Channel Geometry

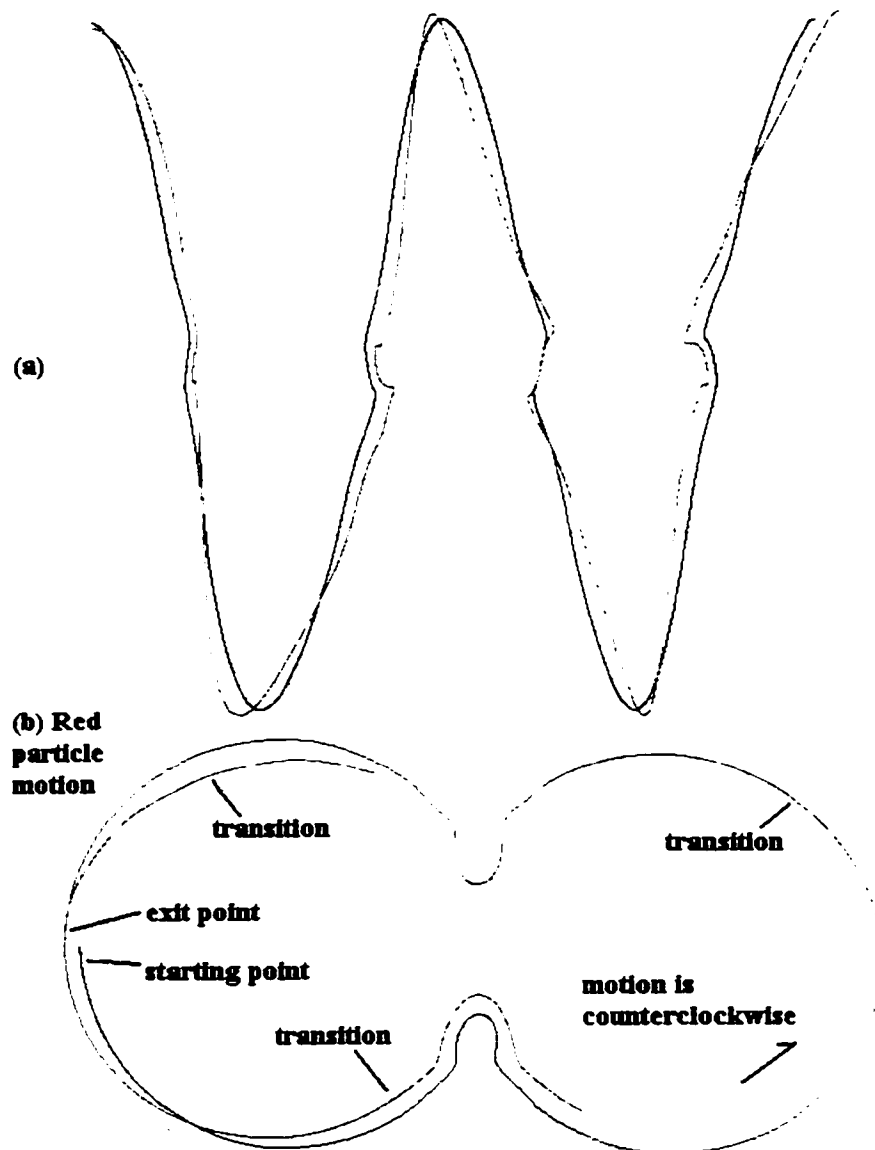


Figure 6.18: Particle Pathlines for First Channel Geometry

Table 6.6: Particle Pathline Data for First Channel Geometry		
<i>Particle</i>	<i>Entering Dimensionless Channel Depth</i>	<i>Residence Time (s)</i>
Blue	0.375	1.55
Red	0.5	1.76

the average residence time about 2.3 s, so the particles were passing fairly quickly through the system. Also shown in the Figure in part (b) is an expanded top-down view of the channel, displaying the radial and circumferential motion of the red particle. In part (a), the red particle can be seen to have been migrating back and forth across the channel as it passed down the channel length, between the active and passive flights. Again this is the characteristic “helix within a helix” motion found in extruder channels. The blue particle, in contrast, made little cross-channel motion at all, remaining at essentially the same position and depth for its entire trip. This makes sense, as the position of the particle in the channel was very close to the stagnation point for cross-channel motion seen in Figure 6.11. Both particles also showed definite sideways shifts in their paths as they passed through the centres of the intermeshing regions of the channel section. Part (b) of the Figure shows how the red particle moved radially as it circulated. The pathline shown here is again colour coded for the axial position of the particle, with the line passing from blue through green, yellow, orange, and red as the particle moved from the inlet to the outlet of the channel. The particle again circulated between two channel depths, one close to the barrel wall as it moved from the passive flight to the active flight, and the other at about two thirds the channel depth as it moved back to the passive flight. It was also predicted to follow a distinctive “U” shaped path as it moved through the centres of the channel intermeshing regions, following the cusp of the barrel surface there.

6.5.2 Second Channel Geometry - Degree of Freedom Profiles

As mentioned previously, simulations were performed using the second channel geometry at only one screw speed (100 rpm); this was due to the simulations consistently crashing at 250

rpm. As well, at the low screw speed none of the reactive extrusion simulations were found to converge. These problems indicate that the mesh for this geometry, shown in Figure 6.3, requires some significant refinements. As such only one primary simulation was performed for the second geometry channel section, for the low screw speed and the zero PDF ratio, with no peroxide. The results for this run are shown in Table 6.5 as that for run 17. The channel flow rate for this run was less than that at the corresponding conditions for the first channel geometry, which makes sense as the channel cross-section area for the second geometry is less than that for the first. No runs to negative PDF ratios were attempted for this system, due to the very significant relative sizes of the flow rate fluctuations at the intermeshing regions centres, as shown in Table 6.4. As such, since only one run was performed for this system, no degree-of-freedom profiles or particle pathlines will be shown.

6.5.3 Mixing Efficiency Analysis - Flow Efficiencies

The mixing analysis of the simulation run results is performed by examination of the predicted flow efficiencies, first in a channel cross-section, then as averages along the lengths of the channel sections. As with the SSE channel flow simulations, due to software limitations, area efficiencies along interfacial area element pathlines could not be obtained for the simulations, and so only flow efficiency results are shown here. Figure 6.19 shows the predicted flow efficiencies across a cross-section through the mesh at right angles to the channel sides at the midpoint of the first geometry channel, for run 11, at the high screw speed and zero PDF ratio, and with the uniform inlet peroxide distribution. Figure 6.20 shows the same plot for run 12, at the negative PDF ratio. The direction of the cross-channel component of the barrel velocity is again left-to-right

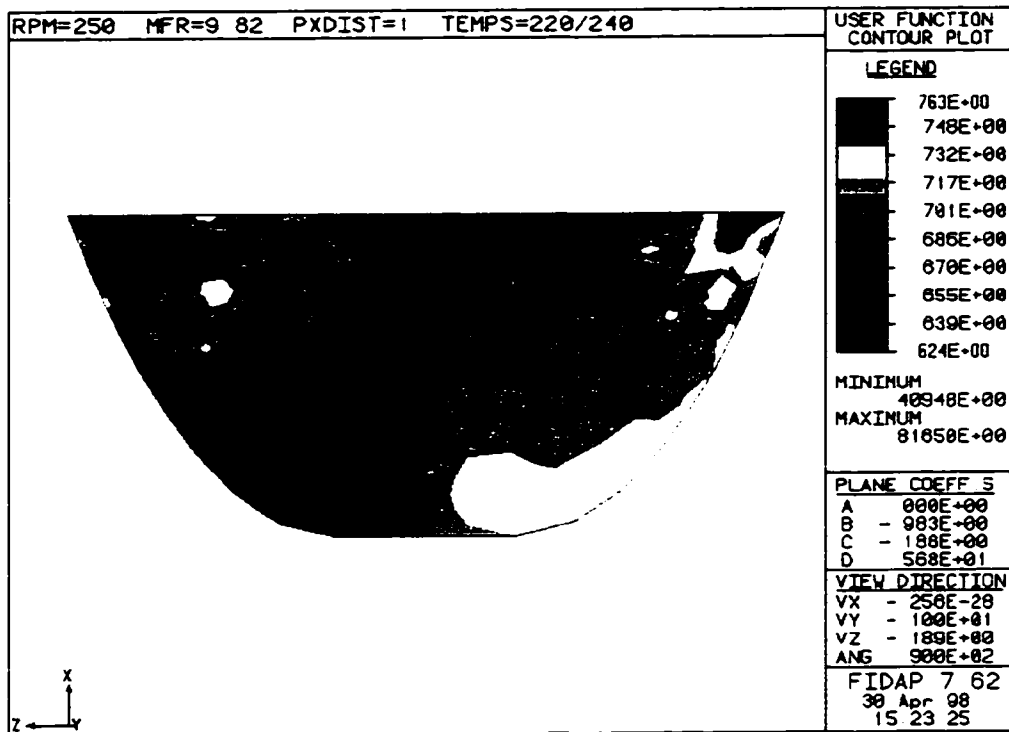


Figure 6.19: Flow Efficiencies in Cross-Section for First Channel Geometry, $Q_p/Q_d=0$

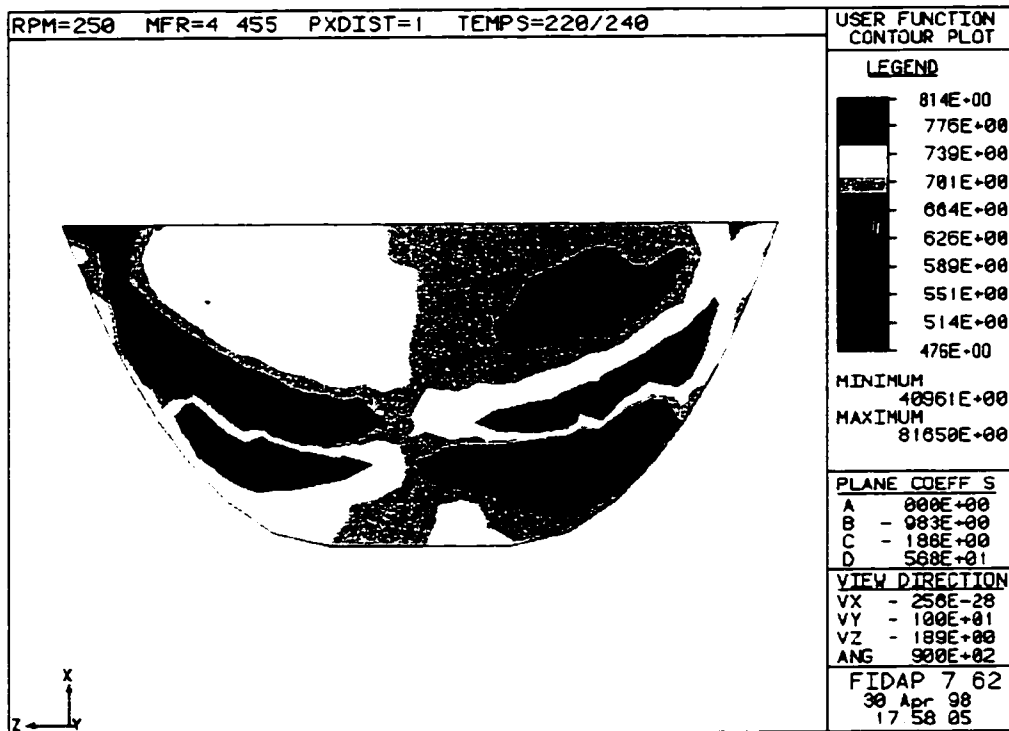


Figure 6.20: Flow Efficiencies in Cross-Section for First Channel Geometry, $Q_p/Q_d=-0.25$

in both Figures. The colour scale for Figure 6.19 is fairly small, from 0.624 (dark blue) to 0.763 (dark red). The Figure shows that the flow efficiencies across nearly the entire channel were close to 0.7, the value for two-dimensional flows, as indicated by the yellow and green colours. A region of comparatively high flow efficiency is seen in the corner where the barrel surface meets the active flight, and a corresponding region of lower flow efficiency is seen in the opposite corner where the barrel surface and passive flight meet. These observations are consistent with those for the SSE channel cross-sections, indicating that at the top of the downward recirculation zone (next to the active flight) the fluid was computed as experiencing a squeezing flow as its cross-channel velocity component decreased, and that at the top of the upward recirculation zone (next to the passive flight) the fluid was computed as experiencing a uniaxial extension-type flow as its cross-channel velocity component increased again.

In Figure 6.20, the colour scale is much larger than that for Figure 6.19, going from 0.476 to 0.814, which covers nearly the entire range of possible values for the flow efficiency. Again the flow efficiencies across most of the channel are found to be close to 0.7, as indicated by the yellow and green-yellow colours. As well, in the corners where the screw flights meet the barrel surface, corresponding regions of relatively low and high flow efficiencies are again seen. A significant difference from Figure 6.19 was the prominent regions of high and low flow efficiencies found adjacent to the flights, close to the position in the cross-section at which the normal velocities change sign, as seen in Figure 6.14. On each flight there appeared a large region of high flow efficiency vertically adjacent to a smaller region of very low flow efficiency, with the high flow efficiency region on top beside the active flight, and on the bottom beside the passive flight. The positions of these regions in the cross-section suggest that they are associated with changes in the

computed normal velocities of the fluid as it circulates, as opposed to the extreme flow efficiency regions in the corners of the cross-section, which are associated with changes in the cross-channel velocities of the fluid.

Next the computed area average flow efficiencies on cross-sections along the channel lengths for both channel geometries are examined. Figure 6.21 shows the profiles for the barrel and random peroxide distribution runs at the high screw speed and zero PDF ratio, in the first geometry channel. The Figure first shows that the average flow efficiencies were not nearly as steady as in the SSE channel flow simulations, with significant fluctuations in the levels appearing in the intermeshing regions of the channel, and smaller amplitude oscillations in the translation region sections. The oscillations in the intermeshing regions were quite regular, showing the same pattern in each region after the first. The oscillations in the translation regions decreased in amplitude in the down-channel direction between consecutive regions, as the peroxide levels in the melt diminished. Second, the Figure shows that the average flow efficiency values were all close by 0.7071, the value for two-dimensional flows (the level of which is indicated by the intermeshing region limit markers in the Figure). The values in the translation regions were only slightly below this level, while towards the centres of the intermeshing regions the baseline levels of the oscillations were more definitely below it, at around 0.700. This can be interpreted as representing the effect of the reduction in the channel width at the centres of the intermeshing regions due to the presence of the flight of the second screw in the channel of the first, which adds a small component of uniaxial extension to the flow, and thereby causes a drop in the average flow efficiencies. Third, the Figure shows that there was little effect of the peroxide distribution on the profiles; this was the case for both screw speeds and both PDF ratios, for all peroxide distributions,

including that of no peroxide. Figure 6.22 shows the profiles for the uniform distribution runs at the negative PDF ratio, at both screw speeds. The Figure shows that again there was little effect of the screw speed on the average flow efficiencies; this was true for all peroxide distributions and both PDF ratio levels.

Figure 6.23 shows the predicted average flow efficiency profiles for the runs at the high screw speed and no peroxide, at both PDF ratios. Clearly an effect is seen here, with the translation region flow efficiencies for the negative PDF ratio run being definitely lower than those for the zero PDF ratio run, at a value of close to 0.700. This same effect was seen between corresponding runs with all peroxide distributions and at both screw speeds. The oscillations in the intermeshing regions were also of a somewhat different pattern for the negative PDF ratio run, though in a similar range of values to those for the zero PDF ratio run. To examine the effect of PDF ratios greater than zero on the flow efficiencies, an additional run was performed for this system at the high screw speed with no peroxide, at the PDF ratio value of 0.25. The results data for this run are given in Table 6.7 as those for run 18. For this run a significant pressure drop was computed in the channel direction. Figure 6.24 shows the flow efficiency profiles for this run and that for the same screw speed and peroxide distribution, at the zero PDF ratio. The Figure shows that slight reductions (around 0.0015) were predicted for the values in the the translation regions of the channel. As well, in the intermeshing regions of the channel, the pattern of the flow efficiency oscillations was not altered, but the amplitudes did change somewhat.

Finally, the predicted flow efficiency profiles for the second geometry channel are shown in Figure 6.25. A second run was also performed for this system at the high PDF ratio value of 0.25, for which the results are given in Table 6.7 as those for run 19. The Figure shows that there

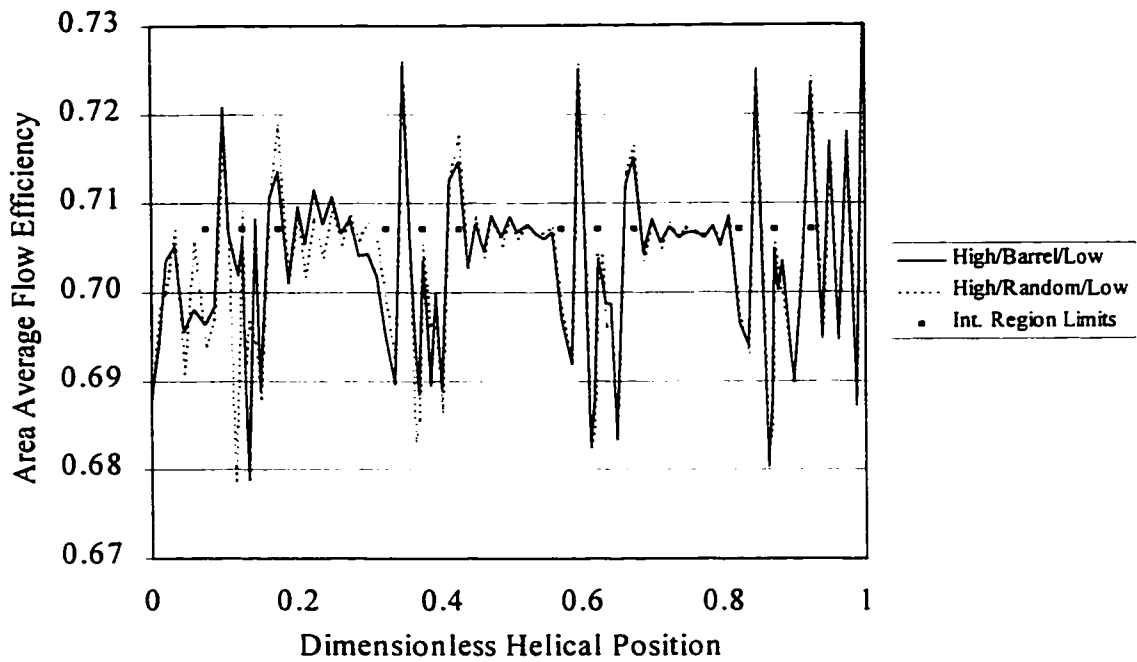


Figure 6.21: Average Flow Efficiencies for First Channel Geometry for Runs with Different Peroxide Distributions

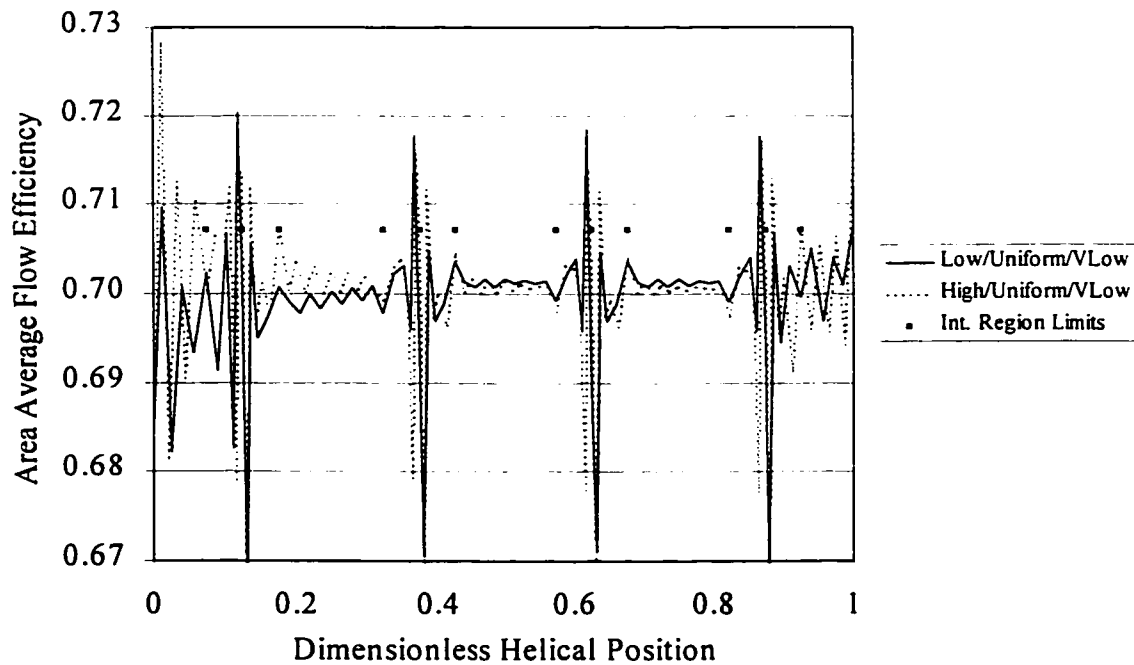


Figure 6.22: Average Flow Efficiencies for First Channel Geometry for Runs at Both Screw Speeds

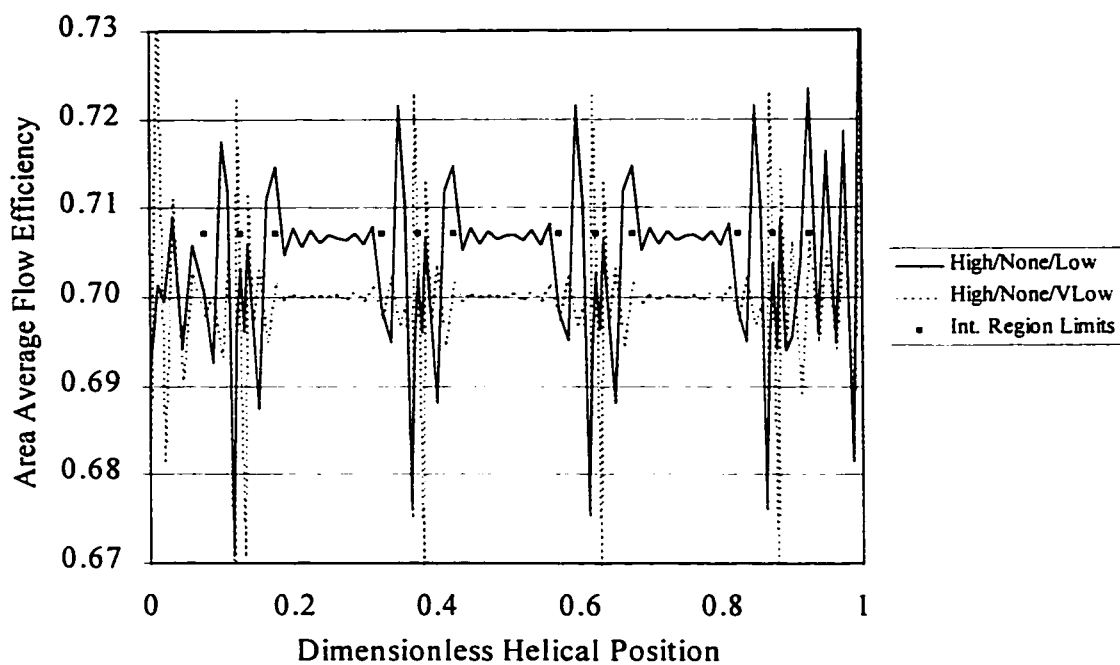


Figure 6.23: Average Flow Efficiencies for First Channel Geometry for Runs With No Peroxide - 1

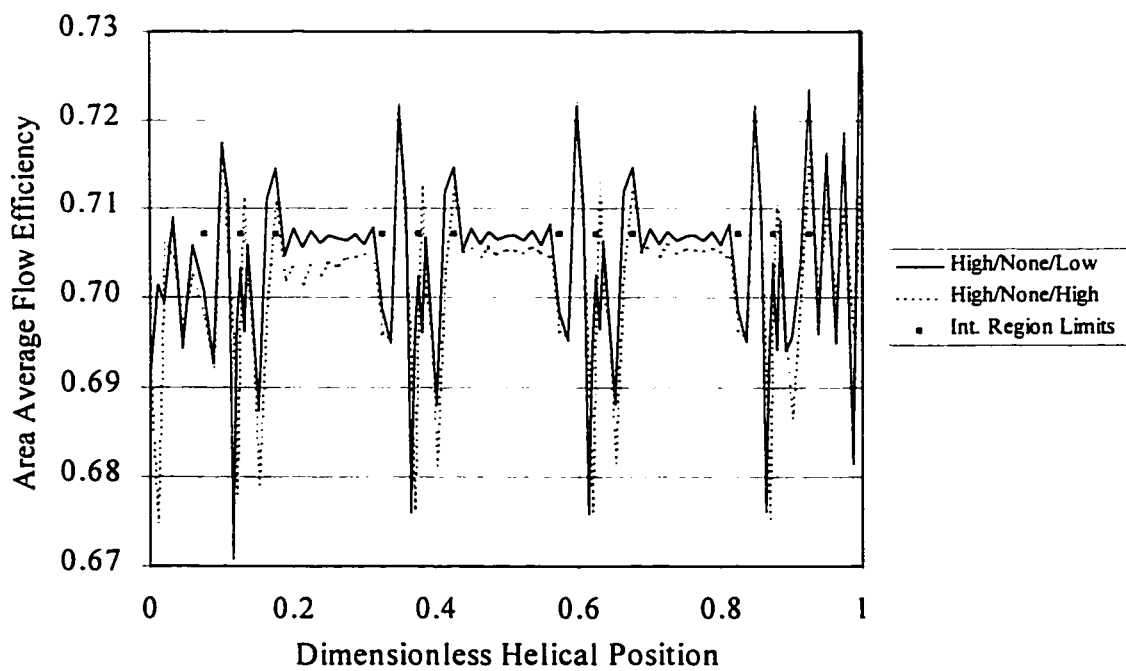


Figure 6.24: Average Flow Efficiencies for First Channel Geometry for Runs With No Peroxide - 2

Table 6.7: Simulation Results for Additional Runs							
Run	Screw Speed (rpm)	Inlet Peroxide Distribution	PDF Ratio Q_P/Q_D	Mass Flow Rate (kg/h)	Average Pressure Change (kPa)	Average Outlet Peroxide Conversion $\frac{w_{I,In} - w_{I,Out}}{w_{I,In}}$	Average Relative Outlet Molecular Weight $\frac{\bar{M}_{W,Out}}{\bar{M}_{W,In}}$
18	250	None	0.249	14.69	-7761	--	1
19	100	None	0.251	4.09	-15534	--	1

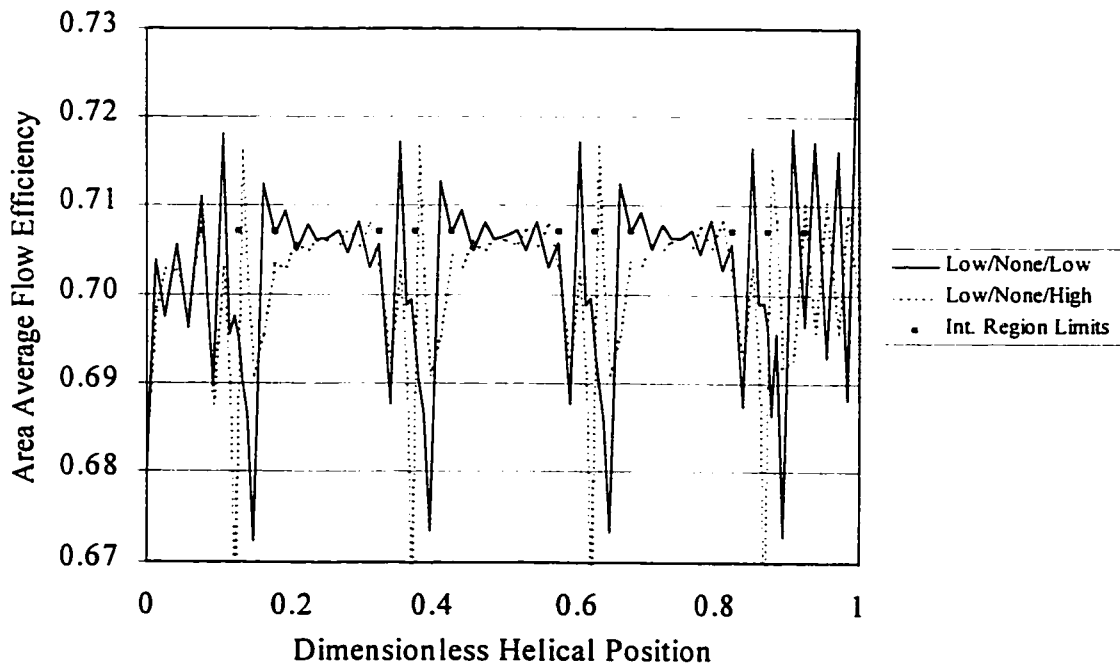


Figure 6.25: Average Flow Efficiencies for Second Channel Geometry

was no predicted effect of either the changed geometry or increased PDF ratio levels on the flow efficiencies in the translation regions of the channel. However, there was a slight apparent reduction in the baseline level of the fluctuations in the intermeshing regions of the channel, to about 0.695. This can be attributed to the greater relative channel contraction at the centre of the intermeshing region for this geometry, which added a larger component of uniaxial extension to the flow than found in the first geometry channel, thereby causing a larger drop in the average flow efficiencies. These results must be considered tentative though, since the previously mentioned convergence problems for runs with this geometry indicate that the mesh employed here was inadequate, and with an altered mesh changes in the flow efficiency trends for this system with the simulation parameters are a strong possibility.

What the flow efficiency results for the 19 runs indicate is that the mixing abilities of both reactive and nonreactive polymer melt flows in fully-filled CSCO extruder forward conveying screw element channels are, on average, very similar to those of two-dimensional flows, for the ranges of model parameters used in the simulations. The flows in the translation region channel sections were predicted to be slightly more efficient than those in the intermeshing region sections, at converting the input fluid power at each point into the magnitude of the minimum eigenvalue of the rate-of-deformation tensor, or in other words the maximum specific rate of area stretch. This difference was greater in the second geometry channel, with the larger aspect ratio and shallower channels, due to the greater relative channel shift in the intermeshing region. Hence the effect of the presence of the intermeshing region in the channel is to slightly reduce the overall mixing ability of the channel flow. However, this does not necessarily mean that actual rates of mixing in CSCO extruder screw element channels are reduced by the presence of the intermeshing region,

as to make such a determination requires consideration of the effect of the intermeshing region on the orientations of interfacial area elements relative to their respective directions for maximum growth, as indicated by the values of the area efficiency along pathlines through the intermeshing region, which were not determined here.

In contrast to screw speed and peroxide level and addition pattern, the pressure-to-drag flow ratio was predicted to have an effect on the mixing abilities of the flow fields (at least for the translation regions in the first geometry channel), with both positive and negative PDF ratio values having influences of a similar character, but that for the negative PDF ratios being of a greater magnitude. The channel flow in the translation region can be viewed as a cross-channel cavity flow in a channel with the self-wiping cross-section profile (a two-dimensional flow for which the flow efficiency is equal to 0.7071 everywhere), upon which is superimposed a combined drag and pressure flow in the longitudinal direction. The effect of the longitudinal flow has been shown here to be to lower the average flow efficiencies in the channels, and thereby on average to add a small component of uniaxial extension to the channel flows. The drag flow effect alone was found to be slight in the results for the runs at the zero PDF ratio. The effect of the pressure flow on top of the drag flow on the mixing abilities of the flows was found in the results at the non-zero PDF ratios. It was observed that the effects on the flow efficiencies of pressure flows both with and opposed to the underlying drag flows were in the same direction, towards smaller values. Hence the largest average flow efficiencies that can be achieved in polymer melt flows in CSCO extruder conveying screw element channels are for drag flow alone.

As mentioned in Chapter 2, the flow in CSCO extruder conveying screw element channels is similar to that in SSE channels, since both have open channels in the direction of flow and

transport material by mechanisms of drag and pressure flow. As such it is insightful to compare the predictions of the mixing abilities of the flows in the different systems to one another, under the different parameter ranges examined in this and the previous chapter. The mixing abilities of the flows in the two systems clearly are very similar to each other. Both have similar values of the average flow efficiencies throughout, with the same predicted dependence on screw speed and peroxide distribution (i.e. none). The comparison is especially good between the translation region flow in the first TSE geometry channel and that in the first geometry SSE channel section. The two flows have equivalent flow efficiency values in the zero PDF ratio runs, which are similarly affected by increases in the PDF ratio above zero. This is actually somewhat surprising, due to the considerable difference in the aspect ratios of the two channels. Significant differences with the twin-screw extruder channel are, as just mentioned, that the (translation region) flow efficiencies are unaffected by channel aspect ratio, and that the flow efficiencies are lower in the intermeshing region than in the rest of the channel.

6.5.4 Discussion

Qualitatively, it can be said that the predicted average degree-of-freedom profiles for the finite element simulations generally look good. The shapes of the profiles are largely smooth, and the predicted effects of the model parameters on the profiles conformed to expectations. The exceptions to this were in the conversion and molecular weight profiles for the barrel distribution REX simulations, which showed some considerable fluctuations, as well as the effects of a numerical artifact in the computations. Also, fluctuations in the flow efficiency profiles for all runs were a problem, and these had the unfortunate effect of partly obscuring the trends of the values

in the intermeshing regions of the channel. These problems have a direct impact on the matter of the reliability (i.e. the mesh independence) of the simulation results. They strongly suggest that the finite element meshes used in this chapter were too coarse, that more cross-sections were needed, as well as more nodes within each cross-section. Again, this could not be tested since the meshes used in the simulations were as large as the workstation used for the work could handle.

The matter of the accuracy of the simulation results, that is whether or not the results can be taken as representative of the behaviour of the true system modeled, is dealt with now. The accuracy of the results must again be inferred, due to the lack of experimental results for direct comparison with the predictions. Some experimental measurements of point velocities in CSCO conveying screw element channels do exist (Karwe et al., 1995), but the conditions for which they were determined were sufficiently different from those used in this chapter (30 rpm screw speed and Newtonian fluid rheology at the comparatively low viscosity of 75 Pa s) as to make their usefulness here questionable. First, regarding the fluid chemorheology, the temperatures in the simulations did extend up to 10°C above that of the viscometric data from which the power-law parameter regression equations (5.15) and (5.16) were determined, and as in the SSE channel flow simulations the weight-average molecular weights did extend to values well below those of the resins from which the data were obtained. Thus in the reactive extrusion simulation runs in particular, there is a question as to the accuracy of the degree of freedom profiles in the last part of the channel section, within which the computed molecular weights were lowest and the melt temperatures highest. As before, to deal with this issue, the regression equations should be reformulated based on viscometric data from resins covering a larger range of molecular weights, collected over a larger range of temperatures.

The second concern about the accuracy of the results follows from the use of the kinematic reversal assumption to represent the screw and barrel velocities. The use of this set of boundary conditions does not appreciably change the velocity gradients (and hence the flow efficiencies) in the flows, since the channels in the two geometries are shallow relative to the screw diameter. However, it does create the problem of the influence of the intermeshing region channel shift on the pressure development in the channel being improperly represented, as stated by Huneault and Dumoulin (1994). As well, it creates the perhaps even greater problem of the self-wiping nature of the channel being lost in the simulations, with the barrel moving instead of the screws. This was seen in the simulations as partially stagnant regions being created at the blocked ends of the side sections in the intermeshing regions. In reality the screw surfaces at the end of these sections are not stationary, so such flow regions do not arise. This was particularly a problem for the REX simulations at the negative PDF ratio, for which significant degradation of both the peroxide and the polymer were predicted to occur at the intermeshing region centres. Hence these two problems certainly affect the accuracy of the form of the pressure profiles in the intermeshing region, as well as those for the peroxide conversions and molecular weights in the REX simulations. To deal with these problems, the use of more realistic velocity boundary conditions in the simulations should be pursued.

There are additional concerns as to the applicability of the results to true extrusion systems, in which viscoelasticity of the melt and leakage flows over the screw flights exist, neither of which were included in the current model. Since the degradation reaction also affects the polymer elasticity, if the elasticity does change the flow efficiencies, then the conclusion that the reaction has no effect on the mixing abilities of the channel flows would have to be changed. This is more

of an issue with these simulations than in those for the SSE channel flows, due to the elongational flow of the polymer in the intermeshing region resulting from the channel shift, which would definitely be influenced by the addition of elasticity to the fluid rheological model. Also, as was shown in Chapter 3, leakage flows can significantly affect the channel flow rates, and possibly also the temperature profiles. Hence they may have considerable influence over the area and flow mixing efficiencies in the channels. The addition of leakage flows to the model should thus also be pursued. A final concern is that the temperature range considered in these simulations was high enough that in a true extrusion system thermal degradation of the polymer might begin to become a problem. Hence the omission of this reaction from the kinetic model of the degradation process would lead to under-estimation of the molecular weight changes in the polymer. This would likely be a minor problem though, but would further undermine the accuracy of the REX simulation predictions.

Finally, other suggestions for future work to improve the model and results are made here. To deal with the problem in the barrel peroxide distribution runs of the average peroxide levels dropping spontaneously after the inlet, the form of the distribution on the inlet plane should be modified so that it is smoother, i.e. the intensity of segregation of the peroxide between the nodes across the inlet is reduced. As well, the definition of the adiabatic average viscosity in equation (5.17) should be changed, to more accurately reflect the true average thermophysical state of the polymer melt in the channel sections. As seen in Figure 6.10, in the reactive extrusion simulations, the average molecular weight and hence the viscosity of the polymer changed very rapidly, and so along the bulk of the channel length the state of the polymer was much closer to its outlet state than its inlet state. Simply basing the value of the adiabatic average viscosity on the inlet and outlet

conditions caused the computed values for these simulations to be much larger than what they should have been, which in turn made the magnitudes of the PDF ratios for these runs much smaller than their true values. To deal with this, the average viscosity used in the computation of the PDF ratio should be based on average values of the melt temperature and molecular weight which cover the complete channel length.

Also, as mentioned above, further refinements of the finite element meshes should be pursued, for the second geometry channel to deal with the severe conversion problems encountered, and for the first channel geometry to improve the reliability of the simulation results by reducing the fluctuations in the predicted conversion and flow efficiency profiles. The problem of the choice of the barrel velocity boundary condition at the centre of the intermeshing region could also be dealt with by a sharp increase in the number of mesh cross-sections there. If the spacing between the cross-sections right at the centre of the intermeshing region was small enough, the proper vector sum velocity boundary condition could be used along the top of the cross-section at the centre of the region, without causing such significant fluctuations in the channel flow rates as were predicted for the meshes used in this chapter. Lastly, as with the SSE channel flow simulations, a program to compute area efficiencies along pathlines in the channels should be developed, which would track the position and orientation of each interfacial area element throughout the mesh based on the computed velocity field for a simulation, and at each point find the eigenvalues of the rate-of-deformation tensor. Once such a program was developed, the effect of the extruder operating conditions, inlet peroxide level and distribution, and channel geometry on the area efficiencies could be studied. As well, the conclusion of Bigio and Stry (1990) that conveying elements in co-rotating TSEs demonstrate little tendency to reorient material elements

in their channels, could be examined. Such a program would be more difficult to write for this system, however, than for the SSE channel section system, due to the much less regular (and changing) cross-section mesh along the flow path, and also the more complicated channel geometry.

CHAPTER 7

CONCLUSIONS AND RECOMMENDATIONS

7.1 Conclusions

This work brought together extruder flow simulations, peroxide-initiated reactive degradation of polypropylene, and mixing efficiency analysis of flows. Steady-state reactive extrusion process models, incorporating the controlled degradation reaction, were presented (which were extensions to existing non-reactive models), in both a differential model formulation and a reduced dimension macroscopic formulation for self-wiping co-rotating twin-screw extruder systems. The differential formulation was solved for a single-screw extruder system, and both formulations were solved for CSCO extruder systems. Simulation results for both reactive and non-reactive PP flows were obtained, to examine the effects of the reaction and other processing parameters on the model predictions of the extruders' behaviour, as well as on the mixing ability of the flows within their channels, as characterized by the flow efficiency.

The extended macroscopic composite process model for CSCO extrusion was presented in Chapter 3. Additional extensions to the model were presented, beyond those for the chemical reaction, for the presence of unmelted solids in the extruder channels, the contribution of the radial clearance to the channel depth, and the effect of solids melting on temperature growth in the polymer melt. The degree of freedom profiles from both the conventional and reactive extrusion simulations conformed to expectations, and predicted PP extrudate molecular weights for runs at 6 levels of peroxide addition at one screw speed and mass throughput level were found to compare closely with measured molecular weights for the same conditions. As well, it was observed that under some conditions the channel flow rates in fully-filled sections can be very significantly

increased by leakage flows over the screw flights. A sensitivity analysis revealed that the model predictions of average residence times in conventional extrusion are most sensitive to perturbations in the parameter values for melt density and power-law index. Problems were encountered in the simulations as the channel flow rates in reverse conveying elements were computed as negative, due to excessive leakage flows.

In Chapter 4, experimental average residence times were presented from a laboratory scale CSCO extruder, which were obtained by tracer pulse RTD experiments using an experimental design based on response surface analysis theory, with screw speed and mass throughput as independent variables. It was concluded that the experimental average residence times were not overly reliable, due to the computed tracer masses being different than the true values. A response surface for the average residence times was generated on the basis of a second-order regression model, and showed that the times were highest for low screw speeds and low throughputs, which conformed to expectations. However, the regression model was found to show significant lack of fit, particularly at high average residence times. Simulations were performed for the same conditions as the experiments, and the predicted average residence times were found to agree well with the experimental values.

The differential process model formulation for steady-state non-isothermal non-Newtonian reactive flow of molten PP was presented in Chapter 5. The model was solved for a 4 turn length of a shallow single-screw extruder channel, using the finite element method, with the channel geometry, extruder operating conditions, and the level and pattern of peroxide addition all varied. Profiles of average degrees of freedom along the channel axis were examined, along with nodal values within a cross-section perpendicular to the screw flights. The average DOF profiles were

seen to look good, and the predicted effects of the model parameters on the profiles conformed to expectations. Very significant degradation of the polymer was predicted in the reactive extrusion simulations. Problems were encountered though, in the form of spontaneous changes in the melt peroxide levels in the runs with non-uniform peroxide distributions. Significant variations in the flow efficiency were seen within the channel cross-sections, from which it was concluded that the fluid experiences a squeezing flow at the channel corner where the barrel surface meets the active flight, and a uniaxial extension-type flow at the opposite channel corner. On the basis of profiles of average flow efficiencies along the channels, it was concluded that the mixing ability of SSE channel flows is very similar to that of two-dimensional flows. No significant effect of either screw speed or peroxide distribution were found on the flow efficiencies. However, both pressure-to-drag flow ratio and the channel aspect ratio were found to have a significant influences. Finally, it was concluded that the simulation results could be considered reliable, but there were some concerns as to their accuracy, due to the omission of leakage flows and also the significant predicted degradation of the PP in the REX runs.

The differential process model was solved using the finite element method for a two “figure-eight” turn length of the channel of a fully-filled CSCO extruder forward conveying screw element in Chapter 6. The extruder operating conditions, the level and pattern of peroxide addition, and the channel geometry were again varied. Again the predicted effects of the model parameters on the process average DOF profiles conformed to expectations, and the profiles were mostly seen to look good. Some problems were apparent, however, in the profiles for the higher throughput runs, especially for the runs with the barrel peroxide distribution. As well, the problems with spontaneous changes in the melt peroxide levels in the runs with non-uniform peroxide

distributions were encountered again. The flow efficiency values in the channel cross-section were seen to vary more widely in the runs at the negative PDF ratio than in the runs at the zero PDF ratio. It was concluded that this was due to alternate squeezing and elongation of the fluid as its normal component of velocity changes during circulation. The average flow efficiency profiles along the channels revealed that the mixing ability of CSCO conveying screw element channel flows is again very similar to that of two-dimensional flows, with the effect of the intermeshing region being to slightly reduce the flow efficiencies. No significant effect of either screw speed or peroxide distribution were found on the flow efficiencies. However, pressure-to-drag flow ratio was found to have a significant influence on the flow efficiencies in the translation region of the channels, and the magnitude of the channel shift in the intermeshing region was found to influence the values in that region. Finally, there were some concerns as to the reliability of the simulation results due to fluctuations in the DOF profiles, and also concerns about the accuracy of the results, due to the omission of leakage flows and the use of velocity boundary conditions which caused the loss of the true self-wiping nature of the channel.

The principal original contributions of this work are thus:

- a macroscopic composite twin-screw extrusion process model was formulated, which was demonstrated to be able to accurately predict polymer average residence times in CSCO extruders
- by solving a differential process model for steady-state reactive extrusion in channel lengths from both a SSE and a fully-filled conveying screw element from a co-rotating TSE, it was demonstrated that the channel flows in both systems have components of biaxial and uniaxial extension, but on average the flows have mixing abilities very similar to those of

two-dimensional flows

Since two different approaches were taken to extrusion modeling and simulation in this work, a brief comment on the usefulness of each is appropriate. The macroscopic TSE model would be useful for extrusion process design, i.e. the evaluation of the suitability of a particular screw configuration for the processing of a given material at particular operating conditions. It has the advantage that it gives information on the performance of the extruder as a whole, as well as on the performance of the individual screw elements in the system. It is not capable, however, of giving insight into the nature of the channel flows at the point level. The differential model, in contrast, can give such information. When solved using the FEM, the differential model is useful in high detail analysis of flows, for computation of flow-characterizing parameters, such as the flow efficiency, throughout the system, and also for the study of the performance of novel screw element designs in different applications. The differential model cannot, however, be used for extrusion process design, because of the massive computational resources such an employment would require.

7.2 Recommendations

The principal recommendations for future work are:

1. The screw characteristic curve approximation equations used in the macroscopic CSCO extruder process model should be reformulated, based on the results of finite element solutions of polymer melt flows in channels with the true self-wiping geometry, covering a large range of channel aspect ratios, and using the screw and barrel velocity boundary conditions of Huneault and Dumoulin (1994). Such equations would reflect the true effect

of the channel intermeshing regions on melt pressurization, and would also remove the possibility of negative channel flow rates being computed in reverse conveying elements.

2. Finite element simulation runs should be pursued for the SSE channel system, to negative values of the PDF ratio, in order to find the effect of these conditions on the average flow efficiencies in the channel.
3. The addition of leakage flows to the SSE channel flow simulations should be pursued.
4. The CSCO extruder channel mesh should be further refined, to increase the number of cross-sections in each channel region, to reduce fluctuations in the computed DOF profiles and thereby improve the reliability of the simulation results.
5. In both the single- and twin-screw channel systems, the barrel inlet peroxide distribution should be changed, to reduce the intensity of segregation of the peroxide on the inlet plane, and in that way reduce the numerical problems with these runs which cause sizeable losses of peroxide for degradation of the polymer.
6. Programs should be written to compute the area efficiencies of interfacial area elements along pathlines in both the single- and twin-screw extruder channel systems.

REFERENCES

Agassant, J.-F., P. Avenas, J.-P. Sergent, and P.J. Carreau, 1991, Polymer Processing: Principles and Modeling, Hanser, Munich.

Anton, H., Elementary Linear Algebra, 3rd ed., Wiley (1981).

Bawiskar, S., and J.L. White, 1995, "Solids Conveying and Melting in a Starve Fed Self-Wiping Co-rotating Twin-Screw Extruder", *Intern. Polym. Proc.*, 10, #2, pp. 105-110.

Beyer, W.H. (ed.), 1968, CRC Handbook of Tables for Probability and Statistics, 2nd ed., CRC Press, Boca Raton.

Bigio, D., and J.H. Conner, 1995, "Principal Directions as a Basis for the Evaluation of Mixing", *Polym. Eng. Sci.*, 35, #19, pp. 1527-1534.

Bigio, D., and W. Stry, 1990, "Measures of Mixing in Laminar Flow", *Polym. Eng. Sci.*, 30, #3, pp. 153-161.

Booy, M.L., 1978, "Geometry of Fully Wiped Twin-Screw Equipment", *Polym. Eng. Sci.*, 18, #12, pp. 973-984.

Box, G. and N. Draper, 1987, Empirical Model-Building and Response Surfaces, Wiley, New York.

Box, G., W.G. Hunter, and J.S. Hunter, 1978, Statistics for Experimenters, Wiley, New York.

Chella, R., and J.M. Ottino, 1985, "Fluid Mechanics of Mixing in a Single-Screw Extruder", *Ind. Eng. Chem. Fundam.*, 24, pp. 170-180.

Chen, T., W.I. Patterson, and J.M. Dealy, 1995, "On-Line Measurement of Residence Time Distribution in a Twin-Screw Extruder", *Intern. Polym. Proc.*, 10, #1, pp. 3-9.

Chen, Z., and J.L. White, 1994, "Simulation of Non-isothermal Flow in Twin-Screw Extrusion", *Intern. Polym. Proc.*, 9, #4, pp. 310-318.

Cheng, C.Y., 1995, "Effects of Polypropylene Crystallinity on Extrusion", *SPE ANTEC Tech. Papers*, 53, pp. 98-106.

Cheng, H., and I. Manas-Zloczower, 1997, "Study of Mixing Efficiency in Kneading Discs of Co-Rotating Twin-Screw Extruders", *Polym. Eng. Sci.*, 37, #6, pp. 1082-1090.

Denson, C.D., and B.K. Hwang Jr., 1980, "The Influence of the Axial Pressure Gradient on Flow Rate for Newtonian Liquids in a Self-Wiping, Co-Rotating Twin-Screw Extruder", *Polym. Eng. Sci.*, 20, #14, pp. 965-971.

Dreiblatt, A., and K. Eise, 1991, "Intermeshing Corotating Twin-Screw Extruders", chapter in Mixing in Polymer Processing, Rauwendaal, C.J. (ed.), Dekker, New York.

Duley, G. and L. Daigneault, 1994, "Residence Time Distribution in a Leistritz 34 mm Intermeshing Co-Rotating Twin-Screw Extruder", research report issued to the National Research Council of Canada, Boucherville QC.

Erwin, L., 1991, "Principles of Laminar Fluid/Fluid Mixing", chapter in Mixing in Polymer Processing, Rauwendaal, C.J. (ed.), Dekker, New York.

Fogler, H.S., 1992, Elements of Chemical Reaction Engineering, 2nd ed., Prentice Hall, New Jersey.

Fritz, H.G., and B. Stohrer, 1986, "Polymer Compounding Process for Controlled Peroxide-Degradation of PP", *Intern. Polym. Proc.*, 1, #1, pp. 31-41.

Gendron, R., L.E. Daigneault, J. Tatibouet, and M.M. Dumoulin, 1994, "Residence Time Distribution in Extruders Determined by In-line Ultrasonic Measurements", *SPE ANTEC Tech. Papers*, 52, pp. 167-171.

Goffart, D., D.J. Van Der Wal, E.M. Klomp, H.W. Hoogstraten, L.P.B.M. Janssen, L. Breyse, and Y. Trolez, 1996, "Three-Dimensional Flow Modeling of a Self-Wiping Corotating Twin-Screw Extruder. Part I: The Transporting Section", *Polym. Eng. Sci.*, 36, #7, pp. 901-911.

Gotsis, A.D., and D.M. Kalyon, 1989, "Simulation of Mixing in Co-Rotating Twin Screw Extruders", *SPE ANTEC Tech. Papers*, 47, pp. 44-48.

Hulburt, H.M., and S. Katz, 1964, "Some Problems in Particle Technology: A Statistical Mechanical Formulation", *Chem. Eng. Sci.*, 19, pp. 555-574.

Huneault, M.A. and M.M. Dumoulin, 1994, "3D Finite-Element Analysis of the Flow in the Intermeshing Region of Co-Rotating Twin Screw Extruders", *SPE ANTEC Tech. Papers*, 52, pp. 327-331.

Karwe, M.V., Y. Jaluria, and V. Sernas, 1995, "Flow in the Channels of a Co-Rotating Twin-Screw Extruder: Modeling and Experiments", *Compounding 95 Proc.*, Philadelphia, USA.

Kim, B., 1996, "Studies of Thermal/Peroxide Induced Degradation and Maleation of Polypropylene in a Modular Intermeshing Twin Screw Extruder", PhD dissertation, University of

Akron, Ohio, USA.

Kim, B. and J.L. White, 1997, "Simulation of Thermal Degradation, Peroxide Induced Degradation, and Maleation of Polypropylene in a Modular Co-Rotating Twin Screw Extruder", *Polym. Eng. Sci.*, 37, #3, pp. 576-589.

Kim, P.J., and J.L. White, 1994, "Flow Visualization and Residence Time Distributions in a Modular Co-rotating Twin-Screw Extruder", *Intern. Polym. Proc.*, 9, #2, pp. 108-118.

Krell, M.J., A. Brandolin, and E.M. Valles, 1994, "Controlled Rheology Polypropylenes: An Improved Model with Experimental Validation for the Single Screw Extruder Process", *Polym. Reac. Eng.*, 2, #4, pp. 389-408.

Lai-Fook, R.A., A. Senouci, A.C. Smith, and D.P. Isherwood, 1989, "Pumping Characteristics of Self-Wiping Twin-Screw Extruders - A Theoretical and Experimental Study on Bipolymer Extrusion", *Polym. Eng. Sci.*, 29, #7, pp. 433-440.

Maier, C., M. Lambla, and D. Bigio, 1994, "Non-Homogeneous Mixing Rates and Conversion", *SPE ANTEC Tech. Papers*, 52, pp. 123-126.

Mark, J.E., A. Eisenberg, W.W. Graessley, L. Mandelkern, E.T. Samulski, J.L. Koenig, and G.D. Wignall, 1993, Physical Properties of Polymers, 2nd ed., American Chemical Society, Washington.

Michaeli, W. and A. Grefenstein, 1996, "An Analytical Model of the Conveying Behaviour of Closely Intermeshing Co-rotating Twin Screw Extruders", *Intern. Polym. Proc.*, 11, #2, pp. 121-128.

Michaeli, W., A. Grefenstein, and U. Berghaus, 1995, "Twin- Screw Extruders for Reactive Extrusion", *Polym. Eng. Sci.*, 35, #19, pp. 1485-1504.

Middleman, S., 1977, Fundamentals of Polymer Processing, McGraw-Hill, New York.

Miller, R.G.J. and B.C. Stace (eds.), 1972, Laboratory Methods in Infrared Spectroscopy, 2nd ed., Heyden and Son, New York.

Montell Polyolefins, 1995, KF6100 Product Data Sheet.

Oberlehner, J., P. Cassagnau, and A. Michel, 1994, "Local Residence Time Distribution in a Twin-Screw Extruder", *Chem. Eng. Sci.*, 49, #23, pp. 3897-3907.

Ottino, J.M., W.E. Ranz, and C.W. Macosko, 1981, "A Framework for Description of Mechanical Mixing of Fluids", *AIChE J.*, 27, #4, pp. 565-577.

Potente, H., and J. Ansahl, 1990, "Residence Time Characteristics of Tightly Intermeshing Co-Rotating Twin-Screw Extruders", *Kunststoffe German Plastics*, 80, #8, pp. 29-32, 926-932.

Potente, H., J. Ansahl, and B. Klarholz, 1994, "Design of Tightly Intermeshing Co-Rotating Twin-Screw Extruders", *Intern. Polym. Proc.*, 9, #1, pp. 11-25.

Potente, H., J. Ansahl, and R. Wittemeier, 1990, "Throughput Characteristics of Tightly Intermeshing Co-rotating Twin-Screw Extruders", *Intern. Polym. Proc.*, 5, #3, pp. 208-216.

Potente, H., and J. Flecke, 1997, "Analysis and Modeling of the Residence Time Distribution in Intermeshing Co-Rotating Twin Screw Extruders Based on Finite Element Simulations", *SPE ANTEC Tech. Papers*, 55, pp. 110-114.

Potente, H., and U. Melisch, 1996, "Theoretical and Experimental Investigations of the Melting of Pellets in Co-rotating Twin-Screw Extruders", *Intern. Polym. Proc.*, 11, #2, pp. 101-108.

Potente, H., U. Melisch, and K.P. Palluch, 1996, "A Physico-Mathematical Model for Solids Conveying in Co-Rotating Twin Screw Extruders", *Intern. Polym. Proc.*, 11, #1, pp. 29-41.

Pouchert, C.J., 1981, The Aldrich Library of Infrared Spectra, 3rd ed., Aldrich Chemical Company, Milwaukee.

Puaux, J.P., and A. Ainsler, 1994, "Residence Time Distribution of a Twin-Screw Extruder", *SPE ANTEC Tech. Papers*, 52, pp. 1500-1503.

Rauwendaal, C.J., 1981, "Analysis and Experimental Evaluation of Twin-Screw Extruders", *Polym. Eng. Sci.*, 21, #16, pp. 1092-1100.

Rauwendaal, C.J., 1986, Polymer Extrusion, Hanser, New York.

Rauwendaal, C.J., 1991, "Mixing in Single-Screw Extruders", chapter in Mixing in Polymer Processing, Rauwendaal, C.J. (ed.), Dekker, New York.

Rauwendaal, C. and J. Anderson, 1994, "FEA of Flow in Single Screw Extruders", *SPE ANTEC Tech. Papers*, 52, pp. 298-303.

Ryu, S.H., C.G. Gogos, and M. Xanthos, 1992, "Parameters Affecting Process Efficiency of Peroxide-Initiated Controlled Degradation of Polypropylene", *Adv. Polym. Tech.*, 11, #2, pp. 121-131.

Sakai, T., N. Hashimoto, and N. Kobayashi, 1987, "Experimental Comparison Between Counter-Rotation and Co-Rotation on the Twin Screw Extrusion Performance", *SPE ANTEC Tech.*

Papers, 45, pp. 146-151.

Sastrohartono, T., Y. Jaluria, and M.V. Karwe, 1995, "Numerical Simulation of Fluid Flow and Heat Transfer in Twin-Screw Extruders for Non-Newtonian Materials", *Polym. Eng. Sci.*, 35, #15, pp. 1213-1221.

Spalding, M.A., J. Dooley, K.S. Hyun, and S.R. Strand, 1993, "Three Dimensional Analysis of the Metering Section of a Single-Screw Extruder", *SPE ANTEC Tech. Papers*, 51, pp. 1533-1541.

Strutt, D., C. Tzoganakis, and T. Duever, 1997, "Response Surface Analysis of Average Residence Times in a Co-Rotating Twin Screw Extruder", *SPE ANTEC Tech. Papers*, 55, pp. 146-150.

Strutt, D., C. Tzoganakis, and T. Duever, 1998, "Mixing Analysis of a Reactive Extrusion Process in a Single-Screw Extruder", *SPE ANTEC Tech. Papers*, 56, pp. 227-231.

Szydowski, W. and J.L. White, 1987, "An Improved Theory of Metering in an Intermeshing Corotating Twin-Screw Extruder", *Adv. Polym. Tech.*, 7, #2, pp. 177-183.

Szydowski, W., R. Brzoskowski, and J.L. White, 1987, "Modeling Flow in an Intermeshing Co-Rotating Twin-Screw Extruder: Flow in Kneading Discs", *Intern. Polym. Proc.*, 1, #4, pp. 207-214.

Tadmor, Z., E. Broyer, and C. Gutfinger, 1974, "Flow Analysis Network (FAN) - A Method for Solving Flow Problems in Polymer Processing", *Polym. Eng. Sci.*, 14, #9, pp. 660-665.

Tadmor, Z. and C.G. Gogos, 1979, Principles of Polymer Processing, Wiley, New York.

Tadmor, Z., and I. Klein, 1970, Engineering Principles of Plasticating Extrusion, Van Nostrand, New York.

Todd, D.B., 1992, "Consider Reactive Extrusion", *Chem. Eng. Prog.*, 88, #8, pp. 72-74.

Tzoganakis, C., 1988, "Peroxide Degradation of Polypropylene During Reactive Extrusion", PhD dissertation, McMaster University, Hamilton, Ontario, Canada.

Tzoganakis, C., 1989, "Reactive Extrusion of Polymers: A Review", *Adv. Polym. Tech.*, 9, #4, pp. 321-330.

Tzoganakis, C., J. Vlachopoulos, and A.E. Hamielec, 1988a, "Modeling of the Peroxide Degradation of Polypropylene", *Intern. Polym. Proc.*, 3, #3, pp. 141-150.

Tzoganakis, C., J. Vlachopoulos, and A.E. Hamielec, 1988b, "Production of Controlled-Rheology Polypropylene Resins by Peroxide Promoted Degradation During Extrusion", *Polym. Eng. Sci.*, 28, #3, pp. 170-180.

Uhland, E. and W. Wiedmann, 1994, "Perspectives in Application of Screw Reactors in Plastics Processing", *Macromol. Symp.*, 83, pp. 59-75.

Wang, X.C., 1996, "Branching of Polypropylene Through Reactive Extrusion", PhD dissertation, University of Waterloo, Ontario, Canada.

Wang, Y., and J.L. White, 1989, "Non-Newtonian Flow Modeling in the Screw Regions of an Intermeshing Corotating Twin-Screw Extruder", *J. Non-Newtonian Fluid Mech.*, 32, pp. 19-38.

Wang, Y., J.L. White, and W. Szydlowski, 1989, "Flow in a Modular Intermeshing Co-Rotating Twin-Screw Extruder", *Intern. Polym. Proc.*, 4, #4, pp. 262-269.

White, J.L., 1990, Twin Screw Extrusion, Hanser, New York.

White, J.L., S. Montes, and J.K. Kim, 1990, "Experimental Study and Practical Engineering Analysis of Flow Mechanisms and Starvation in a Modular Intermeshing Corotating Twin-Screw Extruder", *Kautschuk und Gummi Kunststoffe*, 43, #1, pp. 20-25.

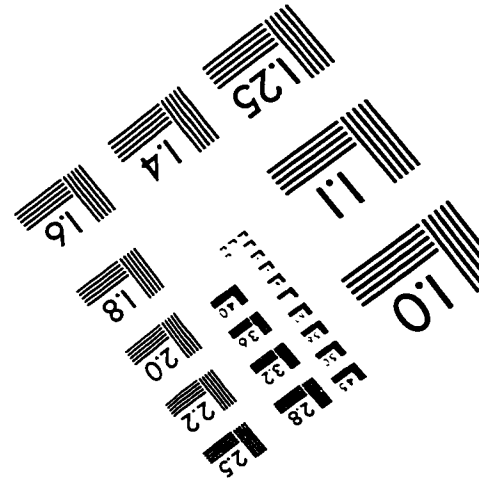
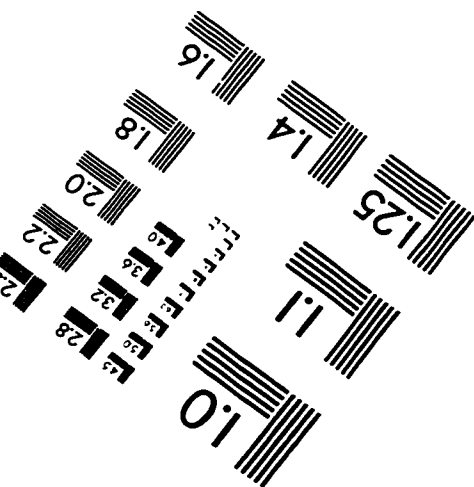
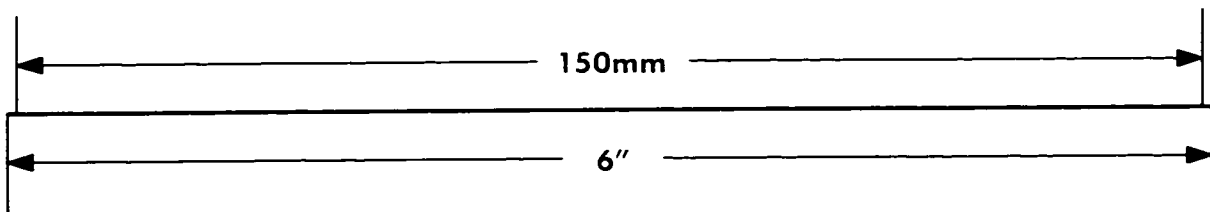
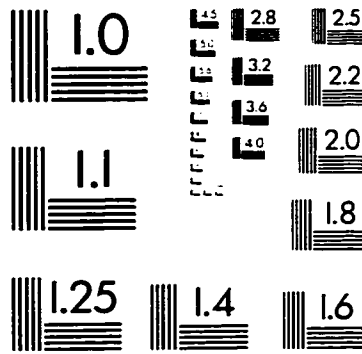
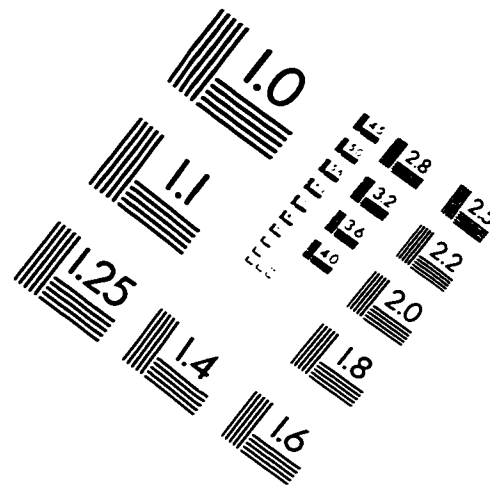
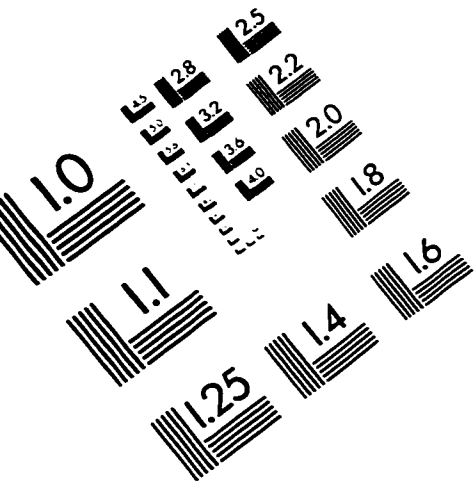
White, J.L., and W. Szydlowski, 1987, "Composite Models of Modular Intermeshing Corotating and Tangential Counter-Rotating Twin-Screw Extruders", *Adv. Polym. Tech.*, 7, #4, pp. 419-426.

Xie, Y., D. Tomayko, D.I. Bigio, and G. Batch, 1997, "Experimental and Statistical Analysis of Residence Time Distribution in Corotating Twin Screw Extruder", *SPE ANTEC Tech. Papers*, 55, pp. 89-93.

Yang, H.-H., and I. Manas-Zloczower, 1992, "Flow Field Analysis of the Kneading Disc Region in a Co-Rotating Twin-Screw Extruder", *Polym. Eng. Sci.*, 32, #19, pp. 1411-1417.

Zerafati, S., and D. Bigio, 1994, "Area Deformation as a Basis for Mixing Prediction", *SPE ANTEC Tech. Papers*, 52, pp. 310-317.

IMAGE EVALUATION TEST TARGET (QA-3)



APPLIED IMAGE, Inc
1653 East Main Street
Rochester, NY 14609 USA
Phone: 716/482-0300
Fax: 716/288-5989

© 1993, Applied Image, Inc., All Rights Reserved